



**UNIVERSIDAD NACIONAL AUTÓNOMA DE MÉXICO
POSGRADO EN CIENCIAS DE LA TIERRA
INSTITUTO DE GEOFÍSICA**

**HEAT FLOW DATA ANALYSIS IN THE CONSTRUCTION OF THE HEAT FLOW MAP
OF MEXICO**

**TESIS
QUE PARA OPTAR POR EL GRADO DE:
DOCTOR EN CIENCIAS DE LA TIERRA**

**PRESENTA:
JUAN LUIS CARRILLO DE LA CRUZ**

**ROSA MARIA PROL LEDESMA
INSTITUTO DE GEOFÍSICA**

**ANTONIO GONZÁLEZ FERNÁNDEZ¹, DIANA NÚÑEZ ESCRIBANO², MARCO
ANTONIO PÉREZ FLORES¹, GERALD GABRIEL³**

¹CENTRO DE INVESTIGACIÓN CIENTÍFICA Y DE EDUCACIÓN SUPERIOR DE
ENSENADA

²UNIVERSIDAD DE GUADALAJARA

³LEIBNIZ INSTITUTE FOR APPLIED GEOPHYSICS

CIUDAD DE MEXICO, OCTUBRE DE 2021



UNAM – Dirección General de Bibliotecas

Tesis Digitales
Restricciones de uso

DERECHOS RESERVADOS ©
PROHIBIDA SU REPRODUCCIÓN TOTAL O PARCIAL

Todo el material contenido en esta tesis está protegido por la Ley Federal del Derecho de Autor (LFDA) de los Estados Unidos Mexicanos (Méjico).

El uso de imágenes, fragmentos de videos, y demás material que sea objeto de protección de los derechos de autor, será exclusivamente para fines educativos e informativos y deberá citar la fuente donde la obtuvo mencionando el autor o autores. Cualquier uso distinto como el lucro, reproducción, edición o modificación, será perseguido y sancionado por el respectivo titular de los Derechos de Autor.

Cd. Universitaria, Ciudad de México, 04510

Of. No. PCT/CSG/235/2021.

Asunto: Aprobación de tema, asesor de tesis
y asignación de jurado para examen de grado.

CARRILLO DE LA CRUZ JUAN LUIS
ESTUDIANTE DE DOCTORADO
P R E S E N T E,

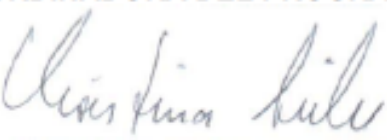
El Comité Académico de Posgrado, reunido el 23 de febrero del año en curso, aprobó el título de tesis “**Análisis e integración de datos de flujo de calor en la generación del mapa de flujo de calor de México**”. Así mismo ratificó a la Dra. Rosa María Prol Ledesma, como su asesora de tesis y designó a los siguientes investigadores como jurado para su examen de grado.

Dra. Claudia Arango Galván
Dr. Antonio González Fernández
Dra. Rosa María Prol Ledesma
Dr. Marco Antonio Pérez Flores
Dr. Gerald Gabriel

Presidente
Vocal
Secretario
Suplente
Suplente

Sin otro particular por el momento, reciba un saludo cordial.

Atentamente,
“**POR MI RAZA HABLARÁ EL ESPÍRITU**”
Ciudad Universitaria, Cd. Mx., a 24 de febrero de 2021.
COORDINADORA DEL PROGRAMA


DRA. CHRISTINA SIEBE GRABACH

CSG'gaba

Of. No. PCT/CSG/462/21

Asunto: Cambio de jurado para examen de grado.

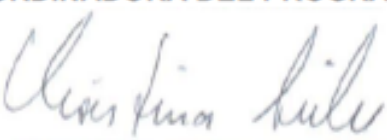
CARRILLO DE LA CRUZ JUAN LUIS
ESTUDIANTE DE DOCTORADO
P R E S E N T E,

El Comité Académico de Posgrado, reunido el 27 de abril del año en curso, **APROBÓ** su solicitud de cambio de jurado para examen de grado, de manera que la Dra. Diana Núñez Escribano sustituye a la Dra. Claudia Arango Galván, quedando el jurado designado de la siguiente manera:

Dr. Antonio González Fernández	Presidente
Dra. Diana Núñez Escribano	Vocal
Dra. Rosa María Prol Ledesma	Secretario
Dr. Marco Antonio Pérez Flores	Suplente
Dr. Gerald Gabriel	Suplente

Sin otro particular por el momento, reciba un saludo cordial.

Atentamente,
"POR MI RAZA HABLARÁ EL ESPÍRITU"
Ciudad Universitaria, a 28 de abril de 2021.
COORDINADORA DEL PROGRAMA


DRA. CHRISTINA SIEBE GRABACH

CSG*gaba

Abstract

Geothermal resources are essential during the modern energy transition. Heat flow maps are essential to explore geothermal resources because they improve a crust thermal state knowledge and show the thermal anomalies. Mexico geothermal resources need to be discovered at regional levels using heat flow maps by compiling the heat flow data from boreholes and seafloor and obtaining heat flow estimations from geophysical data. The aeromagnetic spectral analysis improves the Curie temperature-depth estimation (associated with the depth to the bottom of magnetic sources) and yields an approximation of the heat flow values where boreholes and seafloor data are unavailable. The results of this research are present on different maps: the first map is the result of the use of borehole and seafloor data, and the second map is the result of geostatistical simulations of the depth to the bottom of magnetic sources. The maps show that the ocean spreading zones and recent volcanism are closely related to heat flow anomalies and shallow depth to the bottom of magnetic sources. In the same way, geothermal zones in Mexico are in heat flow anomalies. The main chapters and outcomes are present as published papers at *Terra Digitalis*, *Tectonophysics*, *Earth Sciences Informatics*, and *Geothermics*.

“It takes something more than intelligence to act intelligently.”
— Fyodor Dostoyevsky, *Crime and Punishment*

Acknowledges

I wish to thank UNAM and the Posgrado en Ciencias de la Tierra for this opportunity to study for my Ph.D. and to CONACYT for the fellowship to carry out this research.

To my advisor, Dr. Rosa Maria, because she always was there in the darkest time, helping me to never give up. All knowledge that she shares with me and her experiences help me a lot. Without that, I have never finished this work.

To Dr. Gerald Gabriel for his help and the opportunity to be part of LIAG, my research visit to Germany was a fantastic experience. Our discussions improve an enhancement for this research.

To my committee members, Dr. Marco, Dr. Fernando, and Dr. Joel, their help was essential to aboard this problem.

To Dra. Diana and Dr. Antonio for their comments to improve better this thesis.

To my colleagues at the Instituto de Geofísica, we share experiences, papers, knowledge, and great moments.

To Rapha, Nico, and Michael, my colleagues at LIAG, for their help and friendship.

To my students (Pablo, Dario, and Katya), we had funny moments and too much coding, coding, and coding.

To my mother, my sister, and my nephews, they are always joking something about my Ph.D. and always say to me, "Never give up".

To Pólvara, my unconditional partner, she chose me when I started this, and she walks through this path with me.

To my friends, because they are always there when I really need them. Thanks, Meño, Santi, Empe, Aaron, Adrian, Xolotl, "the Trinchera", and "Cuervos soccer team".

This thesis is dedicated to Mariela. Thank you for being with me all this time, to be comprehensive, to be joyful, for these special moments, the laughs and tears, to love me so much, and to share your life with me. I really do not have words to describe my gratitude to you.

Table of Contents

	Page
Abstract	i
Acknowledges	iii
Table of Contents	iv
List of Figures.....	vi
List of Tables.....	vii
CHAPTER 1: OVERVIEW.....	1
Introduction	2
<i>1.1 Statement of the problem</i>	3
<i>1.2 Delimitation of the work</i>	3
References	4
CHAPTER 2: HEAT TRANSFER.....	6
Heat transfer mechanism in the Earth's crust	7
<i>2.1 Heat transfer mechanism</i>	7
<i>2.2 Conduction</i>	7
<i>2.3 Heat flow density at the Earth's crust</i>	9
References	14
CHAPTER 3: SPATIAL ANALYSIS	16
Map creation.....	17
<i>3.1 Isoline interpolation</i>	17
<i>3.2 Spatial estimation</i>	18
<i>3.3 Geostatistical simulations</i>	26
References	27
CHAPTER 4: HEAT FLOW MEASUREMENTS	29
Borehole temperature logging.....	30
<i>4.1 Temperature logs</i>	30
<i>4.2 Temperature logs and thermal conductivity</i>	32
<i>4.3 Temperature logs perturbation.....</i>	33
<i>4.4 Temperature measurements and heat flow calculation in Mexico</i>	37
References	40

CHAPTER 5: DEPTH TO THE BOTTOM OF THE MAGNETIC SOURCES	42
<i>5.1 MAGCPD: A MATLAB-based codes to calculate the Curie point-depth involving the spectral analysis of aeromagnetic data.....</i>	<i>43</i>
<i>5.2 Analysis of the relation between bottom hole temperature data and Curie temperature depth to calculate geothermal gradient and heat flow in Coahuila, Mexico.....</i>	<i>56</i>
CHAPTER 6: RESULTS.....	69
<i>6.1 Heat flow map and geothermal resources in Mexico.....</i>	<i>70</i>
<i>6.2 Geostatistical mapping of the depth to the bottom of magnetic sources and heat flow estimations in Mexico</i>	<i>86</i>
CONCLUSIONS.....	95
Conclusions	96
SUPPLEMENTARY MATERIAL	98

List of Figures

	Page
Figure 3.1 Variogram characteristics	20
Figure 3.2 Required parameters to calculate the experimental variogram (Leuangthon et al., 2008)	22
Figure 4.1 Temperature logging at Los Cabos, México	30
Figure 4.2 (a) Precision temperature log (> 300 temperature measurements) at water borehole and (b) BHT log at four depths during drilling operation at petroleum borehole.	31
Figure 4.3 Schematic temperature profile showing thermal conductivity changes at depth (Modified from Jorden and Campbell, 1984).	33
Figure 4.4 Temperature profile showing different heat transfer mechanisms (Modified from Grant and Bixley, 2011)	35
Figure 4.5 Temperature profile from a geothermal field (Los Humeros) in Mexico. The profile presents conduction until 1000 m, and convection caused by phase change below 1000 m and above the 250 °C	36
Figure 4.6 Schematic temperature profile showing temperature perturbation caused by aquifer connection. A) Descending flow and B) ascending flow (Modified from Beck and Balling, 1988).	36
Figure 4.7 Temperature logs measure during drilling pauses and at the end of the drilling (Modified from Lewis and Jessop, 1981)	37
Figure 4.8 Borehole MEX039. This example shows the perturbations and the constant linear increment of the geothermal gradient linear in several hundreds of meters.	38
Figure 4.9 Heat flow calculations. a) Temperature at depth profile and b) Bullard from borehole MEX060. c) Temperature at depth profile and d) Bullard from borehole MEX023.	39
Figure 4.10 (a) Temperature data used in the first heat flow measurement, (b) temperature data used in the recalculated heat flow.	40

List of Tables

	Page
Table 1 Average heat flow values from continents and oceans (complemented summary after Eppelbaum et al., 2014)	11
Table 2 Average heat flow from surface geology and age (Pollack et al., 1993; retrieved from Beardmore and Cull, 2001)	13
Table 3 Commonly used geostatistical simulations (From Díaz Viera, 2002)	26

Chapter 1: Overview

Introduction

Heat transfer studies in the Earth's crust are useful for exploring geothermal or petroleum reservoirs and plate tectonic. Within the Earth's crust, the primary heat transfer mechanism is conduction. Convection, limited in areas with fluid movement, is the second most important mechanism. The surface heat flow is calculated from direct methods (e.g., boreholes or seafloor measurements) or through temperature estimators at great depths (e.g., depth of the Curie isotherm). From a heat flow database, the map assessment studies the spatial distribution of heat flow, in which it is possible to appreciate zones with thermal anomalies associated with different geological proxies (e.g., ocean floor spreading zones, hot spots, volcanism, or others).

For this study, the surface heat flow calculation is carried out assuming a steady-state conduction heat equation with heat generation. The heat transfer mechanism knowledge is essential for calculating surface heat flow because the heat transfer mechanism modifies the borehole or ocean floor measurements. It is important to know the temperature-at-depth behavior and how different heat transfer mechanisms could affect its relationship with indirect estimators.

In most cases, direct heat flow data (borehole measurements or seafloor measurements) are not enough to construct a map. For this reason, the use of temperature-at-depth estimators is common. One of the most common technique to estimate temperature at depth is the depth to the bottom of the magnetic source (DBMS). Conventionally, the DBMS is associated with a temperature value at depth: the Curie isotherm. In this way, it is possible to estimate the surface heat flow from the DBMS calculations, considering the steady-state and conductive thermal regimes.

Different studies have made regional maps, including Mexico, of the Earth's crust surface heat flow, using direct measurement methods (Davies, 2013; Goutorbe et al. 2011; Pollack et al. 1993) or temperature-at-depth estimators (Campos-Enríquez et al., 2019; Li et al., 2017; Manea and Manea, 2011; Prol-Ledesma, 1991; Rosales-Rodríguez et al., 2014). However, it is necessary to generate a new heat flow map of Mexico due to the updated heat flow database and the new spectral methods developed for estimating DBMS. For this reason, the present work generates the heat flow map based on surface heat flow data and the estimation of the DBMS.

1.1 Statement of the problem

This research is divided into different sections, and the main result is:

- Creation of Mexico heat flow map by analyzing the heat flow database and the DBMS estimations.

To accomplish the main results, it is necessary to complete these objectives:

- Construction of the heat flow database from borehole and seafloor data.
- Heat flow map from borehole and seafloor data.
- Estimation and mapping of the DBMS using the spectral methods.
- Heat flow estimation using the DBMS as a boundary condition.
- Relationship of the DBMS and the heat flow database.

Previous works have made heat flow estimates from the DBMS for the Gulf of Mexico (Rosales-Rodríguez et al., 2014), the Chicxulub crater impact (Espinosa-Cerdeña et al., 2016), the central and southern Mexico (Manea and Manea, 2011), and Northwest Mexico (Campos-Enríquez et al., 2019). These works use different spectral analysis methodologies and do not cover the entire country. Besides, the lack of an updated heat flow database of the Mexican Republic is the main reason for carrying out this work.

1.2 Delimitation of the work

The chapters propose for this work reach the objectives presented. The chapters are:

Chapter 1 presents the generalities, the approach of the objectives, the problem statement, and the research work's delimitation.

Chapter 2 studies the heat transfer in the Earth's crust, focusing on conduction. From the equations shown, it is essential to emphasize that the heat flow estimations consider the conduction equations in steady-state with heat generation.

Chapter 3 has the map construction's generalities, explaining and discussing the most common algorithms used to construct the maps.

Chapter 4 analyzes the behavior of temperature measurements in boreholes in order to update Mexico's heat flow database. From the analysis of temperature logs in-depth, it is possible to calculate the heat flow and then construct our first map.

Chapter 5 details the calculation of the DBMS from aeromagnetic anomalies, the DBMS calculations' program and the relationship between the heat flow database and the heat flow estimations using the DBMS as a boundary condition. The chapter consists of two articles: the first one was published in *Earth Science Informatics*, and the second was published in *Tectonophysics*. Chapter 6 resumes the results obtained: the surface heat flow map using the update database and the DBMS' surface heat flow map. This chapter consists of two papers: the first as a co-authored article published in the journal *Terra Digitalis*, and the second is a paper published in the journal *Geothermics*, a result of collaboration with the Leibniz Institute for Applied Geophysics (LIAG). Chapter 7 enumerates the conclusions of the results obtained during the development of this research.

References

- Campos-Enríquez, O.C., Espinoza-Cerdeña, J.M., Oskum, O., 2019. Subduction control on the Curie isotherm around the Pacific-North America plate boundary in northwestern Mexico (Gulf of California). Preliminary results. *Journal of Volcanology and Geothermal Research* 375, 1-17. <https://doi.org/10.1016/j.jvolgeores.2019.03.005>.
- Davies, J.H., 2013. Global map of solid Earth surface heat flow. *Geochem. Geophys. Geosyst.* 14, 4608–4622. <https://doi.org/10.1002/ggpe.20271>.
- Espinosa-Cerdeña, J.M., Campos-Enríquez, J.O., Unsworth, M., 2016. Heat flow pattern at the Chicxulub impact crater, northern Yucatan, Mexico. *J. Volcanol. Geotherm. Res.* 311, 135-149. <http://dx.doi.org/10.1016/j.jvolgeores.2015.12.013>.
- Goutorbe, B., Poort, J., Lucaleau, F., Raillard, S., 2011. Global heat flow trends resolved from multiple geological and geophysical proxies. *Geophysical Journal International* 187(3), 1405-1419. <http://dx.doi.org/10.1111/j.1365-246x.2011.05228.x>.
- Li, C.F., Lu, Y., Wang, J., 2017. A global reference model of Curie-point depths based on EMAG2. *Sci. Rep.* 7, 45129. <https://doi.org/10.1038/srep45129>.

Manea, M., Manea, V.C., 2011. Curie Point Depth Estimates and Correlation with Subduction in Mexico. Pure Appl. Geophys. 168, 1489-1499. <https://doi.org/10.1007/s00024-010-0238-2>.

Pollack, H.N., Hurter, S.J., Johnson, J.R., 1993. Heat flow from the Earth's interior: Analysis of the global data set. Reviews of Geophysics 31(3), 267-280. <https://doi.org/10.1029/93RG01249>.

Prol-Ledesma, R. M., 1991. Terrestrial Heat Flow in Mexico. In: Čermák, V., Rybach, L. (Eds.), Terrestrial Heat Flow and the Lithosphere Structure. Exploration of the Deep Continental Crust. Springer Berlin Heidelberg, Berlin, Heidelberg, 475–485. https://doi.org/10.1007/978-3-642-75582-8_24.

Rosales-Rodríguez, J., Bandy, W.L., Centeno-García, E., 2014. Profundidad de la base de la fuente magnética y estructura térmica del Golfo de México. Revista Mexicana de Ciencias Geologicas, 31(2), 190–202.

Chapter 2: Heat transfer

Heat transfer mechanism in the Earth's crust

The Earth's thermal regime controls several of the geological and tectonic processes. The variation of the temperature within the Earth has great importance in recent geological time; thus, there is a close relationship between the heat flow and tectonophysical processes. There are different techniques for acquiring data related to the Earth's thermal regime. These can be associated with temperature measurements and thermophysical parameters in boreholes, temperature estimates acquired from geological observations, water's chemical analysis, or geophysical inferences. Some geological and tectonic processes are characterized by all the thermal data in the Earth's crust and have application in the energy industry: from oil to geothermal.

2.1 Heat transfer mechanism

Heat flow is known as the heat transferred through a unit area per unit time due to a difference in temperatures. Different physical mechanisms transferred the heat: conduction, convection, and radiation.

The Earth's heat is transported from the interior to the surface through conduction and convection and finally radiated into space. The primary process of heat transfer in the crust is conduction; however, convection transport occurs in areas of the crust that exhibit fluid movement (e.g., in aquifers and magmatic chambers). The general equations that describe the conduction phenomena are presented below.

2.2 Conduction

Fourier's law describes the conduction phenomenon, expressed in three dimensions as:

$$q = -\lambda \nabla T \quad (2.1)$$

where q is heat flow (W m^{-2}), λ is the thermal conductivity (W / (m K)) y ∇T geothermal gradient ($^{\circ}\text{C/m}$). The thermal conductivity λ on anisotropic media is a tensor, changing the geothermal gradient ∇T as a vector, resulting on:

$$\nabla T = \left(\frac{\partial T}{\partial x}, \frac{\partial T}{\partial y}, \frac{\partial T}{\partial z} \right) \quad (2.2)$$

Heat does not flow instantaneously since heat transfer is diffuse over time. Thermal diffusion A explains the thermal energy contained per unit volume in a mass or by the energy required to increase the mass temperature. This term is defined by:

$$A = c \rho V \frac{\partial T}{\partial t} \quad (2.3)$$

where c is specific heat capacity ($\text{J kg}^{-1} \text{ }^{\circ}\text{C}^{-1}$), ρ is density (kg m^{-3}), V is volume (m^3) and $\frac{\partial T}{\partial t}$ is the temperature change over time (Incropera et al, 2007; Beardsmore and Cull, 2001).

In addition, radioactive decay is an essential parameter in the Earth's crust thermal processes. The heat generation rate is the product of the decay of radioactive elements such as uranium, thorium, and potassium. The Earth's heat generation is not uniform and varies depending on the radioactive elements in the crust. Heat generation rate follows this equation:

$$H = 10^{-5} \rho (9.52c_U + 2.56c_{Th} + 3.48c_K) \quad (2.4)$$

where ρ is density (kg m^{-3}), c_U is uranium amount (ppm), c_{Th} is thorium amount (ppm) and c_K is potassium amount (%). The heat generation units are $\mu\text{W m}^{-3}$, and the constants 9.52, 2.56 and 3.48 are related with these units (Haenel *et al.*, 1988).

Also, heat generation rate assumes an exponential decay with the depth (Turcotte and Schubert, 2014), expressing the heat generation equation as:

$$H = H_0 e^{-z/h_r} \quad (2.5)$$

where H_0 is the generation of heat per mass unit at the Earth's surface when $z = 0$, and h_r is a length scaling for H_0 decreasing with depth. At depth $z = h_r$, H is $1/e$ of the surface heat generation rate value.

From the energy balance, the conduction heat flow equation is derived as:

$$\frac{\partial}{\partial x} \left(\lambda \frac{\partial T}{\partial x} \right) + \frac{\partial}{\partial y} \left(\lambda \frac{\partial T}{\partial y} \right) + \frac{\partial}{\partial z} \left(\lambda \frac{\partial T}{\partial z} \right) + H = c \rho \frac{\partial T}{\partial t} \quad (2.6)$$

Equation 2.6 can be simplified in isotropic and homogeneous media; therefore, the thermal conductivity λ become constant. The simplification results in:

$$k \left(\frac{\partial^2 T}{\partial x^2} + \frac{\partial^2 T}{\partial y^2} + \frac{\partial^2 T}{\partial z^2} \right) + H = c \rho \frac{\partial T}{\partial t} \quad (2.7)$$

Considering a heat generation rate with exponential decrement and neglecting the heat time dependence (steady-state), the differential equation that studies the Earth's crust temperature is (Turcotte and Schubert, 2014):

$$k \frac{\partial^2 T}{\partial z^2} + \rho H_0 e^{-z/h_r} = 0 \quad (2.8)$$

Assuming heat generation elements present below the crust and an ascending heat flow from the mantle (q_m), that is, $q \rightarrow -q_m$ in $y \rightarrow \infty$ (Turcotte and Schubert, 2014), the integration of the equation 2.8 is:

$$C_1 = k \frac{dT}{dz} - \rho H_0 e^{-\frac{z}{h_r}} = -q - \rho H_0 e^{-z/h_r} \quad (2.9)$$

The constant C_1 is the boundary condition of deep heat flow (mantle heat flow) expressed as:

$$C_1 = q_m \quad (2.10)$$

Therefore, the heat flow at depth is calculated using:

$$q = -q_m - \rho H_0 h_r e^{-z/h_r} \quad (2.11)$$

Most geophysical heat flow problems are simplified to Eq. 2.11 since they are problematic due to their geometries and boundary conditions. It is not easy to model the heat equation with exact analytical solutions (Beardmore and Cull, 2001), and it is common to use numerical solutions or problem simplifications.

2.3 Heat flow density at the Earth's crust

The Earth's interior is hotter than its surface. For this reason, the thermal energy flows through the difference in temperatures between the Earth's interior and the surface. In the Earth's crust, sources

of heat from the interior can be, for example, the cooling of hot bodies or the decay of radioactive materials contained in rocks (Beardsmore and Cull, 2001).

In practice, the heat flow is a value that can hardly be measured directly. Therefore, to calculate the corresponding heat flow values, thermal conductivity measurement from rocks and geothermal gradient measured from temperature logs are necessary. Nevertheless, in the absence of thermal conductivity and temperature logs, the heat flow values are mainly estimated using heat loss models derived from the magmatic activity and the discharge of hot fluids in the oceans (Eppelbaum *et al.*, 2014). Also, the use of temperature-at-depth estimators (e.g., silica geothermometers or Curie isotherm depth) is comprehensive. Finally, the heat flow values are associated with the geology, giving an average heat flow value depending on rock type and age.

2.3.1 Averaged Earth's surface heat flow

The heat flow values measured on the continental surface and the seafloor analyze the heat loss between different areas in the Earth's crust. Determining the average heat flow value in a region could have reference values in another region where measurements are not available (Eppelbaum *et al.*, 2014). Besides, from averaging the heat flow depending on the geological environment, it is possible to analyze the tectonic process affecting the heat transfer mechanism or the temperature anomalies.

Table 1 shows the Earth average heat flow values calculated by different authors, indicating the variations in average heat flow values caused by the new heat flow data available over the years, changing the results. Also, heat flow values variations in continents and oceans depend on multiple factors, like topography, groundwater movements, thermal waters circulation, proximity to young volcanic areas, heat production, heat flow anomalies in the mantle and lower crust, cooling effects due to sedimentation, basement structure, tectonic activity, and others (Eppelbaum *et al.*, 2014). The average heat flow in a region can serve as reference in locations with a lack of heat flow data, depending on the proxies mentioned above (i.e., ocean spreading zones could expect high heat flow values).

Table 1 Average heat flow values from continents and oceans (complemented summary after Eppelbaum *et al.*, 2014)

Continents	Oceans	References
61	61	Lee (1970)
61	93	Williams and von Herzen (1974)
53	62	Chapman and Pollack (1975)
61	87	Langseth and Anderson (1979)
53	100	Davies (1980)
55	95	Davies (1980)
57	99	Sclater <i>et al.</i> (1980)
64.4 ^a	71.8 ^a	Čermák (1984)
65	101	Pollack <i>et al.</i> (1993)
65	101	Stein (1995)
79.7 ^b	116.6 ^b	Hofmeister and Criss (2005)
66 ^c	70 ^c	Hofmeister and Criss (2005)
65	94	Jaupart <i>et al.</i> (2007)
67	100	Clauser (2009)
70.9	105.4	Davies and Davies (2010)
62 ^d	Not discussed	Gouturbe <i>et al.</i> (2011)
63.6 ^e	Not discussed	Gouturbe <i>et al.</i> (2011)
64.7	95.9	Davies (2013)
67	92	Luazeau (2019)

^a Only for Europe (continent and oceans)

^b All the data until $q = 4,183 \text{ mW m}^{-2}$

^c Data with $q > 200 \text{ mW m}^{-2}$ are omitted

^d Best combination method from Gouturbe *et al.* (2011)

^e Similarity method from Gouturbe *et al.* (2011)

2.3.2 Heat flow relationship with other geological and geophysical parameters

Pollack et al. (1993) analyze and provide average heat flow values for each geologic province (Table 2). The work of these authors is one of the first global heat flow analyses. In recent years, other authors have studied heat flow globally. For example, Goutorbe et al. (2011) estimate heat flow values from different approximations such as surface heat production, seismic waves velocities in the upper mantle, tectono-thermal age, thickness of the crust, density of the upper mantle, age of the ocean floor, topography, ages of the upper and lower edge of the sedimentary basins, age of initiation and termination of rifting, type of basin, type of rift and sedimentary thickness. On the other hand, Davies (2013) and Davies and Davies (2010) present a global map of surface heat flow and their geology relationship. Recently, Lucaleau (2019) performed the analysis of global heat flow data with the updated data for 2018, generating a map of heat flow estimates, with a resolution of $0.5^\circ \times 0.5^\circ$, from the generalized use of the Similarity method proposed by Goutorbe et al. (2011).

The authors mentioned above determine heat flow averages values per equal latitude and longitude area ($0.5^\circ \times 0.5^\circ$, $1^\circ \times 1^\circ$, $5^\circ \times 5^\circ$, and others). These methodologies have two obstacles: the first is the lack of heat flow data in some regions or inaccurate measurements; the second obstacle is the continental regions with heat flow anomalies because these regions sometimes cover an oversampled area (Eppelbaum et al., 2014). It is crucial to notice that regional heat flow studies use temperature-at-depth estimations to avoid the lack of heat flow data; such studies could use the Curie temperature-depth (Artemieva, 2006; Okubo et al., 1989) or upper mantle shear wave velocity (Shapiro and Ritzwoller, 2004).

Table 2 Average heat flow from surface geology and age (Pollack et al., 1993; retrieved from Beardmore and Cull, 2001)

Description	Average heat flow (mW m ⁻²) ^a	Standard error (mW m ⁻²)	Years range (Ma)
Oceanic			
Cenozoic undifferenced	89.3 (125.2)	2.8	0-65
Mesozoic undifferenced	44.6 (51.0)	2.8	65-251
Quaternary	139.5 (806.4)	10.1	0-1.8
Pliocene	109.1 (286.0)	5.9	1.8-5.3
Miocene	81.9 (142.2)	2.3	5.3-23.8
Oligocene	62.3 (93.4)	2.2	23.8-33.7
Eocene	61.7 (75.7)	1.6	33.7-54.8
Paleocene	65.1 (65.1)	2.8	54.8-65
Late Cretaceous	61.5 (60.0)	2.1	65-84
Middle Cretaceous	56.3 (53.9)	1.0	84-119
Lower Cretaceous	53.0 (50.5)	1.4	119-141
Late Jurassic	51.3 (49.4)	1.2	141-159
Continental			
Subaqueous undifferenced	77.7	1.9	0-65
Cenozoic (sed./met. ^b)	63.9	0.9	0-65
Cenozoic (igneous)	97.0	5.6	65-251
Mesozoic (sed./met.)	63.7	1.3	65-251
Mesozoic (igneous)	64.2	3.0	251-545
Paleozoic (sed./met.)	61.0	1.2	251-545
Paleozoic (igneous)	57.7	2.6	545-2500
Proterozoic	58.3	1.4	2500-3800
Archean	51.5	2.4	

^aValues inside the parenthesis are from Stein and Stein (1992) and are recommended by Pollack *et al.* (1993)

^b sed.= sedimentary met.= metamorphic

References

- Artemieva, I.M., 2006. Global $1^\circ \times 1^\circ$ thermal model TC1 for the continental lithosphere: Implications for lithosphere secular evolution. *Tectonophysics* 416(1-4), 245–277. <https://doi.org/10.1016/j.tecto.2005.11.022>.
- Beardmore, G., Cull, J., 2001. Crustal Heat Flow: A Guide to Measurement and Modelling. Cambridge University Press. Cambridge University Press. <https://doi.org/10.1017/S0016756803218021>.
- Clauser, C., 2009. Heat transport processes in the Earth's crust. *Surv. Geophys.* 30, 163–191.
- Clauser, C., 2003. Numerical Simulation of Reactive Flow in Hot Aquifers: Shemat and Processing Shemat. Berlin, Heidelberg: Springer Berlin Heidelberg. <https://doi.org/10.1007/978-3-642-55684-5>.
- Čermák, V., 1984. Heat flow and deep structure of Europe. In: Proceedings of 27th international geological congress, vol 8, Moscow, 94–110.
- Davies, G.F., 1980. Thermal histories of convective Earth models and constraints on radiogenic heat production in the Earth. *J. Geophys. Res.* 85, 2517–2530.
- Davies, J.H., Davies, D.R., 2010. Earth's surface heat flux. *Solid Earth* 1, 5–24.
- Davies, J.H., 2013. Global map of solid Earth surface heat flow. *Geochem. Geophys. Geosyst.* 14, 4608–4622. <https://doi.org/10.1002/ggge.20271>.
- Eppelbaum, L., Kutasov, I., Pilchin, A., 2014. Applied Geothermics. Springer Berlin Heidelberg, Berlin. <https://doi.org/10.1007/978-3-642-34023-9>.
- Goutorbe, B., Poort, J., Lucaleau, F., Raillard, S., 2011. Global heat flow trends resolved from multiple geological and geophysical proxies. *Geophysical Journal International* 187(3), 1405–1419. <http://dx.doi.org/10.1111/j.1365-246x.2011.05228.x>.
- Haenel, R., Rybach, L., Stegenga, L., 1988. Handbook of Terrestrial Heat-Flow Density Determination. Kluwer Academic Publishers, Dordrecht.
- Incropera, F.P., DeWitt, D.P., Bergman, T.L., Lavine, A.S., 2007. Fundamentals of Heat and Mass Transfer. John Wiley & Sons, Vol. 6.
- Jaupart, C., Mareschal, J.C., 2007. Heat flow and thermal structure of the lithosphere. In: Schubert G. (ed) Treatise of geophysics, vol 6. Elsevier, Oxford, 217–252.
- Lee, W.H.K., 1970. On the global variations of terrestrial heat-flow. *Phys. Earth Planet. Int.* 2, 332–341.

- Lee, M.K., Brown, G.C., Webb, P.C., Wheildon, J., Rollin, K.E., 1987. Heat flow, heat production and thermo-tectonic setting in mainland UK. *J. Geol. Soc. Lond.* 144, 35–42.
- Mottaghy, D.C., 2007. Heat transfer processes in the upper crust: influence of structure, fluid flow, and palaeoclimate. Thesis for obtain the Ph.D. degree. RWTH Aachen University.
- Okubo, Y., Tsu, H., Ogawa, K., 1989. Estimation of Curie point temperature and geothermal structure of islands arcs of Japan. *Tectonophysics* 159, 279-29.
[https://doi.org/10.1016/0040-1951\(89\)90134-0](https://doi.org/10.1016/0040-1951(89)90134-0).
- Pollack, H.N., Hurter, S.J., Johnson, J.R., 1993. Heat flow from the Earth's interior: Analysis of the global data set. *Reviews of Geophysics* 31(3), 267-280.
<https://doi.org/10.1029/93RG01249>.
- Turcotte, D., Schubert, G., 2014. *Geodynamics*. Third edition. Cambridge University Press, Cambridge.
- Sclater, J.G., Jaupart, C., Galson, D., 1980. The heat flow through oceanic and continental crust and the heat loss of the Earth. *Rev. Geophys. Space. Phys.* 18, 269–311.
- Shapiro, N.M., Ritzwoller, M.H., 2004. Inferring surface heat flux distributions guided by a global seismic model: Particular application to Antarctica. *Earth and Planetary Science Letters* 223(1-2), 213–224. <https://doi.org/10.1016/j.epsl.2004.04.011>.
- Stein, C.A., Stein, S., 1992. A model for the global variation in oceanic depth and heat flow with lithospheric age. *Nature* 359, 123-128.
- Stein, C.A., 1995. Heat flow of the Earth. *Global Earth Physics*. In: *A handbook of physical constants*. AGU Reference Shelf 1, 144–158.
- Williams, D.L., von Herzen, R.P., 1974. Heat loss from the Earth: new estimate. *Geology* 2, 327–328.

Chapter 3: Spatial analysis

Map creation

The result of data acquisition is map construction. Maps show local, regional, or global heat flow patterns. The "geothermal map" is a representation of the spatial patterns that exposes the temperature-at-depth, geothermal gradient, and (or) heat flow distribution. It is essential to complement the geothermal maps with information related to geology, tectonics, or hydrogeology (Čermak and Haenel, 1988; Eppelbaum et al., 2014). The construction of maps is carried out from interpolation methods or through spatial estimation using geostatistical methods.

3.1 Isoline interpolation

Isoline interpolations are estimates of continuous functions based on data observations at discrete points. Computational algorithms execute the interpolations methods from values within regularly or irregularly spaced data. Add geological and geophysical parameters during the algorithm's execution will improve optimal results (Davis, 2002). Tobler's first law of geography expresses the basic concept of interpolation; Tobler's law expresses that "all places are related, but nearby places are more related than distant places" (Gruver, 2018). The sections below described the generalities of some isoline interpolation methods.

3.1.1 Isolines triangulation

The method works from localized data without any regularity, connecting lines generating triangles and interpolating each triangle side, producing a contour line (Davis, 2002). The triangulation method was introduced at Geographic Information Systems by ESRI in an algorithm called Triangulated Irregular Network (TIN).

The TIN algorithm works from a triangle network formed by the Delaunay algorithm. TIN works by circumferences in each triangle, and every circumference should not contain another triangle's vertex, maximizing all triangles' minimum interior angle and avoiding long and thin triangles (ESRI, 2016). The TIN method is widely used on topographic data because the triangles are adequate to represent inclined plane plates, which result in a close approximation to a surface (Davis, 2002). This method is also used for high-precision modeling in small areas and not usually valid in angular coordinates, avoiding their use in regional studies (ESRI, 2016).

3.1.2 Polynomial function

Polynomial function (Eq. 3.1), also called trend surface analysis, is a global analysis method that fits a polynomial function to a point's values in space. The independent variables in a polynomial function are the spatial coordinates (Bonham-Carter, 1995).

$$z = f(x, y) \quad (3.1)$$

From eq. 3.1, the measured value z is a function of the coordinates x and y (Bailey and Gatrell, 1995). For example, a cubic trend surface is represented by the eq. 3.2.

$$z(x, y) = b_0 + b_1x + b_2y + b_3x^2 + b_4xy + b_5y^2 + b_6x^3 + b_7x^2y + b_8xy^2 + b_9y^3 \quad (3.2)$$

The polynomial equation (i.e., Eq. 3.2) characterizes and recognizes spatial trends, and estimate unknown values in unsampled localities (Bonham-Carter, 1995; Wang, 2015). High order models represent the complex surfaces, and the coefficient of determination (R-squared or R^2) provides some information about the goodness of fit of the polynomial model used to characterize the analyzed surface. It is essential to notice that a better model fit does not indicate better model estimations; for this reason, cross-validation is necessary to compare the model with the measured data (Wang, 2015).

3.2 Spatial estimation

Spatial estimation predicts values in locations without sampling. The estimations' quality is affected by the number of samples, the samples' location, and border effects; for example, clustered samples could generate a bias. The spatial estimation is divided into deterministic or statistical methods. Deterministic methods use a mathematical method to calculate an unsampled region's value, while statistics use statistical information and its spatial arrangement of the samples (Gruver, 2018). A brief description of the spatial estimation is presented in the following sections.

3.2.1 Inverse distance weighting

Inverse Distance Weighting (IDW) is a non-linear deterministic interpolation method that estimates values in unsampled locations based on the weighted average of nearby points, with an inverse weight of the distance raised to a power value. Tobler's first law of geography governs this

method because the closest points significantly influence the interpolation more than points at a greater distance (Brunsdon and Comber, 2015; Chang, 2004; Wang, 2015).

IDW is defined by:

$$z_u = \frac{\sum_{i=1}^s z_i d_{ui}^{-k}}{\sum_{i=1}^s d_{ui}^{-k}} \quad (3.3)$$

where z_u is the estimated value at location u , z_i is the sample value at location i , d_{ui} is the distance between the location u and location i , and k the power value.

According to Bonham-Carter (1994), greater distances produce a smaller effect on interpolated value. The power value k can be determined by a search radius, and the value can have different effects listed here (Moral García, 2003; Robeson, 1997):

- Low power values ($0 < k < 2$) highlight local anomalies.
- High power values ($3 < k < 5$) smooth local anomalies.
- When $10 \leq k$ the estimation is polygonal (flat).
- When $k = 0$ the estimation is the moving average.

The bullseyes are common in this interpolation method. The bullseye is a concentric curve around an estimated location (Moral García, 2013) and sometimes could not represent reality.

3.2.2 Structural analysis

In geostatistical modeling, structural analysis is the first step to perform spatial estimation using kriging or geostatistical simulations. The structural analysis estimates and models spatial continuity by performing the semivariogram analysis, that is, studying the main features of the regionalization; this semivariogram will be useful in subsequent spatial estimations or simulations (Díaz Viera, 2002; Moral García, 2003). The semivariogram is a statistical concept described by the mean variability of a random field $Z(x)$, defining the semivariogram of a random intrinsic function as:

$$\gamma(h) = \frac{1}{2} Var[Z(\underline{x} + h) - Z(\underline{x})] \quad (3.4)$$

If the variables are stationary and intrinsic, the mean of $Z(\underline{x} + \underline{h}) - Z(\underline{x})$ is equal to zero and the eq. 3.4 is defined by:

$$\gamma(\underline{h}) = \frac{1}{2} E \left[\{Z(\underline{x} + \underline{h}) - Z(\underline{x})\}^2 \right] \quad (3.5)$$

where $\underline{x} + \underline{h}$ and \underline{x} are points in an n -dimensional space, the semivariogram function $\gamma(\underline{h})$ finds the relationship between the semivariance and the \underline{h} vector separation, known as lag. The lag separation is the distance and the direction of any pair of values $Z(\underline{x})$ and $Z(\underline{x} + \underline{h})$ (Armstrong, 1998; Díaz Viera, 2002; Moral García, 2003).

The stationary variable's semivariogram characteristics are the sill, the range, and the nugget effect (Figure 3.1). The sill is the upper limit value and sometimes corresponds to the sample variance. The range is the distance h at the variogram that stabilizes and defines the distance sample relationship. The range could not be equal in all directions, thus because some phenomena are characterized by anisotropy. Finally, the nugget effect indicates variability at short sample distances caused by sampling errors or unknown sample variabilities (Davis, 2002; Díaz Viera, 2002; Moral García, 2003).

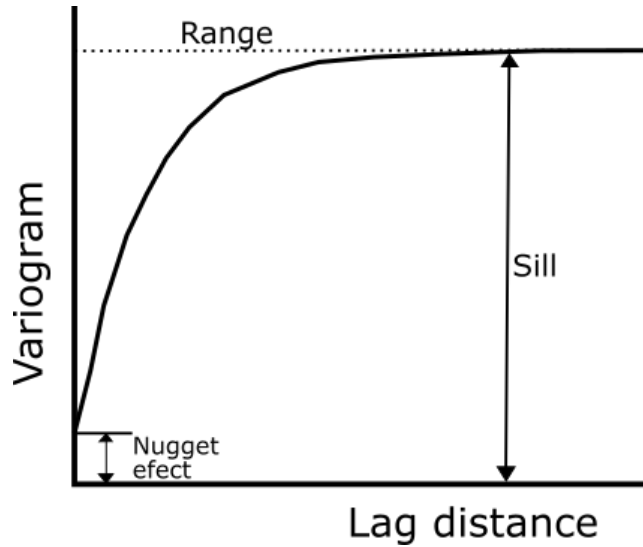


Figure 3.1 Variogram characteristics

From data sample distribution in the space, the experimental semivariogram is calculated using the following equation:

$$\gamma(\underline{h}) = \frac{1}{2N(\underline{h})} \sum_{i=1}^{N(\underline{h})} [Z(\underline{x}_i + \underline{h}) - Z(\underline{x}_i)]^2 \quad (3.4)$$

where $N(\underline{h})$ is the sample pairs number at lag \underline{h} , $Z(\underline{x}_i)$ are the sample values at location \underline{x}_i and $Z(\underline{x}_i + \underline{h})$ are the sample values at location \underline{x}_i separated by one lag.

The calculation of the experimental semivariogram parameters is by the trial-and-error method. It is essential to mention that outliers, an inappropriate coordinate system, specifying a wrong variogram direction, a small or large tolerance, or any poorly specified parameter during the experimental semivariogram estimation could inadequately result in an apparent too large nugget effect and too short range. The optimal experimental variogram calculation results when the data is in a regular mesh with a representative data sampling with a normal distribution (Díaz Viera, 2002; Leuangthon et al., 2008).

Figure 3.2 shows the parameters required for calculating the experimental semivariogram: azimuth, tolerance angle, bandwidth, lag distance, and lag numbers (Leuangthon et al., 2008). Furthermore, a theoretical model needs to be adjusted to the experimental semivariogram to any linear combination to become equal to zero (Armstrong, 1998).

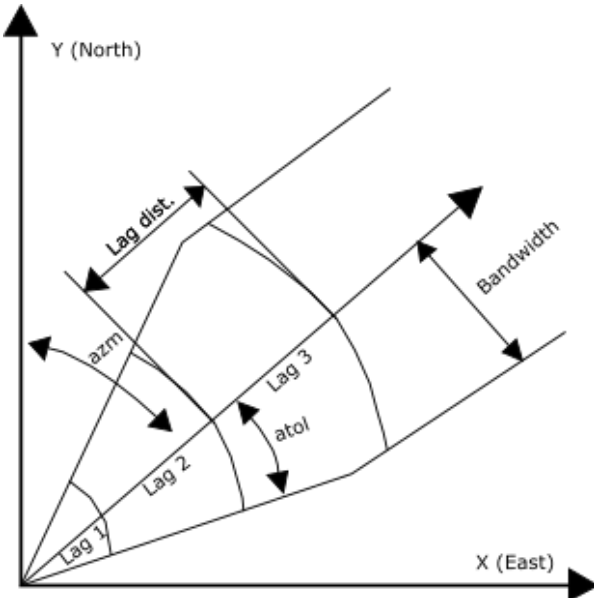


Figure 3.2 Required parameters to calculate the experimental variogram (Leuangthon et al., 2008)

$azm = \text{azimuth}$, $atol = \text{tolerance angle}$, $\text{Lag dist.} = \text{lag distance}$.

The experimental semivariogram is fit by a mathematical model of the random function and its semivariogram (Moral García, 2003). The frequent mathematical models used to fit the experimental semivariogram are listed below:

1. Nugget effect model

The nugget effect model is the simplest because the samples are random without spatial correlation. The model function is in eq. 3.5.

$$\gamma(h) = \begin{cases} 0 & \text{si } h = 0 \\ M & \text{si } h > 0 \end{cases} \quad (3.5)$$

From eq. 3.5 M is the sill value and h is the lag distance.

2. Spherical model

A simple polynomial expression represents the spherical model, and its shape has an almost linear growth until it stabilizes with distance. The tangent at the origin reaches the sill at a distance $\frac{2a}{3}$.

The function that expresses the spherical model is in eq. 3.6.

$$\gamma(h) = \begin{cases} M \left(\frac{3}{2} \frac{h}{a} - \frac{1}{2} \frac{h^3}{a^3} \right) & \text{si } h < a \\ M & \text{si } h \geq 0 \end{cases} \quad (3.6)$$

For the eq. 3.6, a is the range, M is the sill and h is the lag distance.

3. Exponential model

The exponential model has a practical range at $3a$ because this distance reaches the 95% of its limit value. The exponential model and the spherical model are linear in short distances. Nevertheless, the difference between these models is that the exponential model grows faster and gradually stabilizes. The exponential model is expressed in the eq. 3.7.

$$\gamma(h) = M \left(1 - e^{-\frac{h}{a}} \right) \text{ si } h \geq 0 \quad (3.7)$$

For the eq. 3.7, a is the range, M is the sill and h is the lag distance.

4. Gaussian model

The Gaussian model is the only stationary model with an inflection point and is used to modeling continuous phenomena. The Gaussian model considers range (a) to be the distance where the variogram reaches 95% of the sill. Eq. 3.8 represents the Gaussian model.

$$\gamma(h) = M \left(1 - e^{-\left(\frac{h}{a}\right)^2} \right) \text{ si } h \geq 0 \quad (3.8)$$

For the eq. 3.8, a is the range, M is the sill and h is the lag distance.

In geostatistics, variogram is essential for modeling continuous and categorical variables using kriging or stochastic simulations.

3.2.3 Kriging

Kriging is a local estimation technique that gives the best unbiased linear estimates (Díaz Viera, 2002). There are various types of kriging, and to use each one of them, different conditions are

necessary. Besides, before applying the kriging method, it is necessary to carry out the structural analysis and semivariogram modeling. All the kriging estimators are variants of the eq. 3.9 (Díaz Viera, 2002).

$$Z^*(\underline{x}) = \sum_{i=1}^n w_i Z(\underline{x}_i) \quad (3.9)$$

where w_i is the kriging weights, $Z(\underline{x}_i)$ is the sampled values, and $Z^*(\underline{x})$ is the estimate values derive from a linear combination of $Z(\underline{x}_i)$. The number of data n use in the estimation varies in each geographic location. The w_i values obtain provide an unbiased estimator $E[Z^*(\underline{x}) - Z(\underline{x})] = 0$ with minimum variance $Var[Z(\underline{x}) - Z^*(\underline{x})]$. The most used kriging estimators are listed below:

1. Simple Kriging

Linear kriging has constant and knew expected values throughout the studied area. This estimator is represented by:

$$Z_0^* = \sum_{i=1}^n w_i Z(\underline{x}_i) + m[1 - \sum_{i=1}^n w_i] \quad (3.10)$$

With an estimation variance as:

$$\sigma_{ks}^2 = Var[Z(\underline{x}_i) - Z_0^*] = E \left[(Z(\underline{x}_i) - Z_0^*)^2 \right] \quad (3.11)$$

where w_i is the kriging weights, $Z(\underline{x}_i)$ is the sampled values, Z_0^* is the estimation value, and m is the mean, which is a constant value for the entire sampled area.

In order to use simple kriging, the expected value (mean value) must be known for $n + 1$ and $m(\underline{x}_i) = E[Z(\underline{x}_i)]$, $\forall i = 0, \dots, n$; also, the covariance σ_{ij} of the random function $Z(x)$ is necessary to be known. The simple kriging assumes no large-scale variation being this model far from reality (Díaz Viera, 2002).

2. Ordinary Kriging

A kriging estimator with unknown mean values throughout the studied area. Ordinary kriging is expressed by:

$$Z_{K0}^* = \sum_{i=1}^n w_i Z(\underline{x}_i) \quad (3.12)$$

The ordinary kriging variance is expressed in function of the variogram, that is:

$$\sigma_{KO}^2 = \mu + \sum_{i=1}^n w_i \gamma_{ki} \quad (3.13)$$

The weights w_i minimize the error's variance and ensure that the estimate is not biased; in other words $\sum_{i=1}^n w_i = 1$. From eq. 3.13, the Lagrange multiplier is represented by μ . In ordinary kriging, random's function mean values need to be constantly following $m(\underline{x}_i) = E[Z(\underline{x}_i)]$, $\forall i = 0, \dots, n$. Also, it is necessary to know the covariance $C(\underline{h}) = E[Z(\underline{x} + \underline{h})Z(\underline{x})]$ or the semivariogram $\gamma(\underline{h}) = \frac{1}{2}Var[Z(\underline{x} + \underline{h}) - Z(\underline{x})]$ (Díaz Viera, 2002).

3. Universal Kriging

Universal kriging is an estimator with a known trend. This kriging model needs the trend expressed as a polynomial representation and the second-order moment of the random functions (covariance or semivariogram) of the data without the trend (Díaz Viera, 2002). The following equation expresses this estimator:

$$Z_{KU}^* = \sum_{i=1}^n w_i Z(\underline{x}_i) \quad (3.14)$$

And a variance estimation carried out by:

$$\sigma_{KU}^2 = \sigma^2 - \sum_{i=1}^n w_i \sigma_{i0} + \sum_{l=1}^k \mu_l \phi_l(\underline{x}_0) \quad (3.15)$$

The universal kriging presents difficulties related to the estimations of the polynomial equations that represent the trend $m(x)$. Also, the detrend semivariogram calculation (or residuals' semivariogram) could be challenging to obtain (Díaz Viera, 2002).

With the structural analysis and the kriging estimation is possible to carry out a spatial analysis of the DBMS and heat flow data. The spatial analysis of the database is fundamental to perform geostatistical simulations.

3.3 Geostatistical simulations

Kriging estimations are sometimes insufficient to describe a phenomenon's spatial distribution due to a lack of information (Méndez-Venegas, 2008). The reality can be simulated by numerical models obtained by random function simulations; for this reason, the geostatistical simulation objective is to simulate a random function's realizations to preserve the sample probability distribution of the samples. Also, a simulation needs to reproduce at least the first and second-order moments inferred from a random function sample (Díaz Viera, 2002). This chapter mentions the main geostatistical simulations, and which is suitable for simulating the DBMS and heat flow.

The simulation results must have the same mean, variance, histogram, covariance, or semivariogram. This methodology depends less on the number of samples and their spatial distribution, while the spatial estimation methods (i.e., kriging) are more affected by the number of samples and their distribution.

Geostatistical simulations main characteristics are a) using a conditional simulation, the spatial interpolation is exact, b) simulation results are not smooth because the spatial variability is the same as the sampled values, and c) the conditional simulation variance is twice the kriging variance because the error between samples and simulations does not have minimum variance (Díaz Viera, 2002). The commonly used simulation methods are mentioned in table 3, showing generalities of their characteristics.

Table 3 Commonly used geostatistical simulations (From Díaz Viera, 2002)

Simulation	Conditional	Gaussian	Regular grid
Sequential indicator	Yes	No	No
Truncated Gaussian	Yes	Yes	No
Plurigaussian	Yes	Yes	No
Boolean	No	No	No
Turning bands	No	Yes	No
Sequential Gaussian	Yes	Yes	No
Simulated annealing	Yes	No	No

For this work, the Sequential Gaussian simulation (SGS) is used due to this is a suitable method to construct maps and evaluate the spatial patterns of sampled values (e.g., Cardellini et al., 2003; Chen et al., 2012). The SGS uses a regular grid at the sampled area, and the simulations for each spatial location in the grid are done from the conditional cumulative Gaussian distribution defined from the sampled data (Cardellini et al., 2003; Chen et al., 2012). The SGS presents better results than kriging because it solves the overestimation and underestimating values produced by kriging.

All the simulations must reproduce the semivariogram and the histogram of the sampled data with some ergodicity. If there is no appropriate reproduction of the random function second-order moments, simulations are not adequately representing the sampled values; for this reason, it is crucial to verify the semivariogram and histogram. Finally, the simulation results are presented as the e-type model (average value for all simulations) and the conditional variance model (variance of all the simulations), quantifying the method's uncertainty.

References

- Armstrong, M., 1998. Basic Linear Geostatistics. Berlin, Heidelberg: Springer.
- Bailey, T.C., Gatrell, A.C., 1995. Interactive Spatial Data Analysis. Harlow, England: Longman Scientific and Technical.
- Bonham-Carter, G., 1994. Geographic Information Systems for Geoscientists: Modelling with GIS. Kent: Pergamon.
- Brunsdon, C., Comber, L., 2015. An Introduction to R for Spatial Analysis & Mapping. SAGE.
- Cardellini, C., Chiodini, G., Frondini, F., 2003. Application of stochastic simulation to CO₂ flux from soil: Mapping and quantification of gas release. J. Geophys. Res. 108(B9), 2425. <https://doi.org/10.1029/2002JB002165>.
- Chang, K.T., 2004. Introduction to Geographic Information Systems, 2nd Edition. McGraw-Hill.
- Chen, F., Chen, S., Peng, G., 2012. Using Sequential Gaussian Simulation to Assess Geochemical Anomaly Areas of Lead Element. 6th Computer and Computing Technologies in Agriculture (CCTA), Zhangjiajie, China, 69-76. https://doi.org/10.1007/978-3-642-36137-1_9.

- Čermak, V., Haenel, R., 1988. Geothermal Maps. En: Haenel R., Rybach L., Stegenga L. (eds), Handbook of Terrestrial Heat-Flow Density Determination. Solid Earth Sciences Library, vol 4. Springer, Dordrecht.
- Davis, J.C., 2002. Statistics and Data Analysis in Geology. Third Edition. Wiley.
- Díaz Viera, M.A., 2002. Geoestadística Aplicada. Universidad Nacional Autónoma de México.
- Eppelbaum, L., Kutasov, I., Pilchin, A, 2014. Applied Geothermics. Berlin, Heidelberg: Springer Berlin Heidelberg. <https://doi.org/10.1007/978-3-642-34023-9>.
- ESRI, 2016. What is a TIN surface?. Environmental Systems Research Institute, Inc. Redlands, California. Retrieved at August 20, 2019
<http://desktop.arcgis.com/en/arcmap/10.3/manage-data/tin/fundamentals-of-tin-surfaces.htm>.
- Gruver, A., 2018. Cartography and Visualization. Course notes GEOG 486. PennState, College of Earth and Mineral Sciences. Department of Geography.
- Méndez-Venegas, J., 2008. Modelación de la distribución espacial de la precipitación en el Valle de la Ciudad de México usando técnicas geoestadísticas. Thesis to obtain the Master of Sciences, Colegio de Postgraduados, Texcoco, México.
- Moral-García, F.J., 2003. La Representación Gráfica de las Variables Regionalizadas, Geoestadística Lineal. Cáceres, Universidad de Extremadura.
- Leuangthon, O., Daniel Khan, K., Deutsch, C.V., 2008. Solved Problems in Geostatistics. Hoboken, New Jersey: John Wiley & Sons.
- Pyrcz, M.J., Deutsch, C.V., 2014. Geostatistical Reservoir Modeling, 2nd Edition. Oxford University Press, New York.
- Robeson, S., 1997. Spherical Methods for Spatial Interpolation: Review and Evaluation. *Cartography and Geographic Information Systems*, 24(1), 3-20.
<https://doi.org/10.1559/152304097782438746>.
- Wang, F., 2015. Quantitative methods and socio-economic applications in GIS. Boca Raton: CRC Press.

Chapter 4: Heat flow measurements

Borehole temperature logging

It is possible to determine the surface heat flow from temperature measurements at depth and the rocks' thermal conductivity from boreholes. There are different methods to determine the heat flow; in precision temperature logs, the heat flow calculation uses the Bullard or interval method, while the Bottom Hole Temperature (BHT) measurements use the Fourier's law. It is possible to detect disturbances in the heat transfer mechanism in precision temperature logs, affecting the heat flow calculations. These disturbances could be associated with convection (caused by drilling or hydrogeological regime), heat generation, seasonal temperature changes, or others. In the following sections, we analyze the borehole heat flow calculations.

4.1 Temperature logs

Geophysical borehole logging, including the temperature logs, are measure during or at the end of the drilling. In some cases, temperature records are measure by employing thermistors connected to an electrical recording wire, as is shown in figure 4.1.



Figure 4.1 Temperature logging at Los Cabos, México

Temperature logs are mainly measured using precision temperature logs and BHT logs. Precision temperature logs are gauged at different depth intervals at the end of the borehole drilling (Fig.

4.2a). Meanwhile, the BHT logs are quantified at the maximum borehole depth during drilling intervals or at the drilling end (Fig. 4.2b).

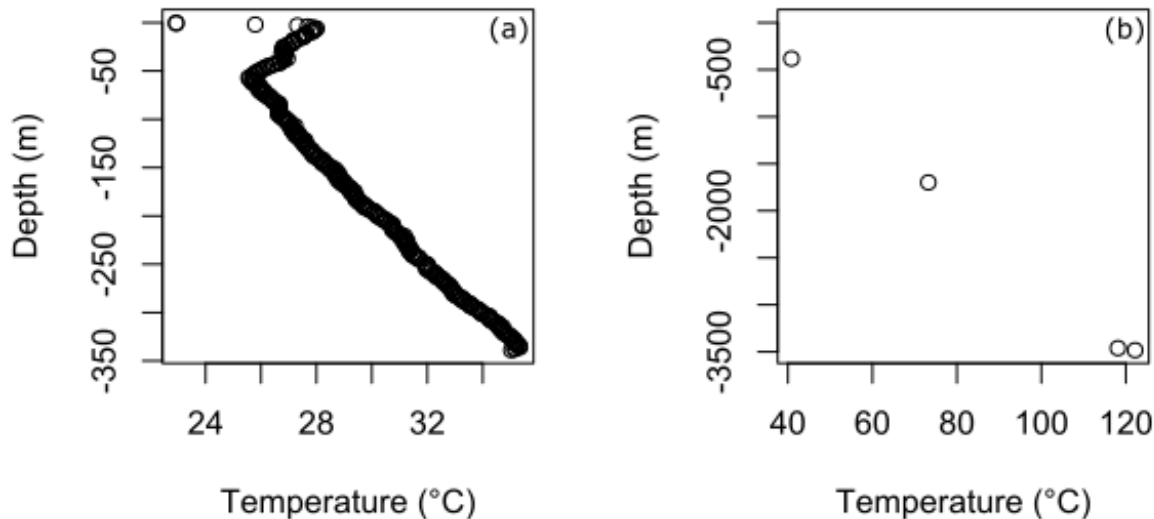


Figure 4.2 (a) Precision temperature log (> 300 temperature measurements) at water borehole and (b) BHT log at four depths during drilling operation at petroleum borehole.

The temperature log objectives are to calculate the geothermal gradient and the surface heat flow. However, borehole drilling could alter the thermal regime and result in disturbed temperature logs. For this reason, to obtain unaltered temperature logs, boreholes should be allowed to stabilize for a few months or even years; however, the stabilization time sometimes is not possible. Therefore, there are different correction methods to estimate the unaltered rock temperatures.

According to Beardsmore and Cull (2001), the temperature logs and their corrections are ranked in order of decreasing accuracy:

1. Precision temperature logs (measured in thermal equilibrium at a stabilized borehole).
2. Drill Steam Tests.
3. Corrected BHT's:
 - a. Cooper and Johns (1959) correction with reliable data.
 - b. Horner plot correction with reliable data.
 - c. Horner plot correction with less reliable data.
 - d. Other corrections.

Precision temperature logs are suitable measurements to analyze better the borehole perturbations and the heat transfer mechanisms. Precision temperature logs could show thermal conductivity changes at depth or perturbations caused by seasonal temperature changes and fluid movement (convection).

4.2 Temperature logs and thermal conductivity

The temperature increases linearly, assuming a steady-state and conductive heat transfer mechanism with constant thermal conductivity at depth and without heat generation. Any alteration to the assumptions mentioned before causes disturbances that affect the linear temperature increase. Precise temperature logs help to identify the disturbances in the linear temperature increment.

Abrupt thermal conductivity variations can be detected in precise temperature profiles, resulting in linear segments with different geothermal gradient values (Fig. 4.3). Cull and Sparksman (1977) show that thermal conductivity changes at depth could be associated with geothermal gradient linear segments. Also, they notice that abrupt changes in the thermal conductivity do not affect the Bullard plot's linearity. Schütz et al. (2018) calculate heat flow using the interval method from linear segments in the geothermal gradient to avoid possible problems related to thermal conductivity changes at depth.

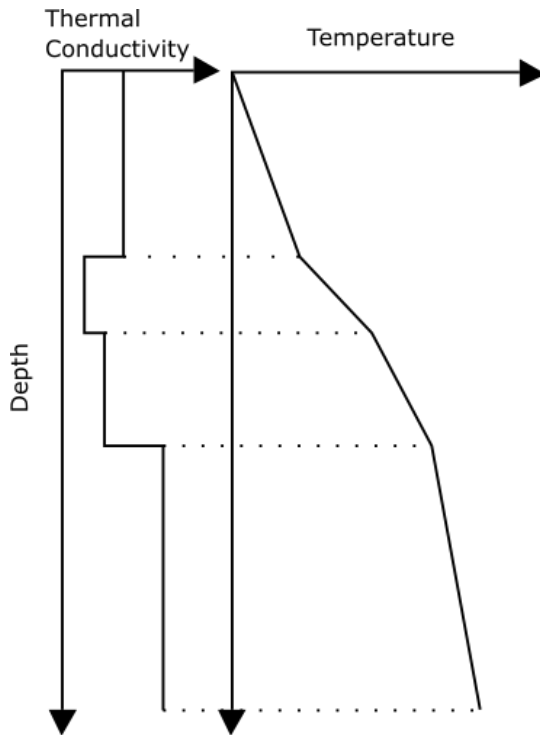


Figure 4.3 Schematic temperature profile showing thermal conductivity changes at depth (Modified from Jorden and Campbell, 1984).

4.3 Temperature logs perturbation

Temperature log perturbations are associated with irregular geothermal gradients, even negative gradients, affecting the heat flow measurements (Roy et al., 1972). Therefore, it is essential to identify irregularities in temperature logs because sometimes data become unusable if it has strong perturbations and cannot be corrected. Different temperature log perturbations are described in the following sections.

4.3.1 Shallow boreholes

Different authors suggest depths below 200 meters, the temperature logs are robust, and it is not necessary to apply corrections to them (Beck and Balling, 1988; Cull and Sparkman, 1977; Richards et al., 2012; Roy et al., 1972), although these authors agree that shallow boreholes are often disturbed by changes in the thermal regime at the surface caused by abrupt changes in vegetation, erosion, sedimentation, seasonal variations, or topography (Beck and Balling, 1988; Powell et al., 1988; Roy et al., 1972).

Lovering and Goode (1963) carried out geothermal gradient studies in shallow boreholes (shallower than 130 m) and found that the disturbances caused by daily temperature changes affect the temperatures logs at depths shallower than 1.5 m. On the other hand, periodically temperature changes with a duration of two weeks rarely penetrate deeper than 5 m, and annual temperature changes affect approximately until 20 m deep, depending on the rocks' thermal parameters.

The interpretation of shallow borehole temperature logs is extensive; nevertheless, most of the boreholes in this work have more than 200 m of depth, and the shallow perturbations are no significant.

4.3.2 Fluid movement

The fluid movement that causes perturbations on temperature logs is associated with advection or drilling. Advection (or forced convection) is the fluid movement in a porous body cause by the hydraulic regime (Beck and Balling, 1988; Cull and Beardsmore, 2001; Richards et al., 2012). Deep infiltration, circulation, or convection of fluids cause borehole sections where the temperature is constant or nearly constant with depth (isothermal profile sections). Also, shallow cold aquifers can change the borehole thermal regime, in which the cold water upward flow indicates heat loss (Grant and Bixley, 2011; Steingrímsson, 2011).

Figure 4.4 shows a temperature-depth profile with three profile sections. The first kilometer has conductive heat transport with a high gradient and linear profile. Then from 1 to 3.3 km, a convective heat transfer mechanism is identified with a geothermal gradient reduction. Finally, below 3.3 km, a transport regime is conductive (Grant and Bixley, 2011).

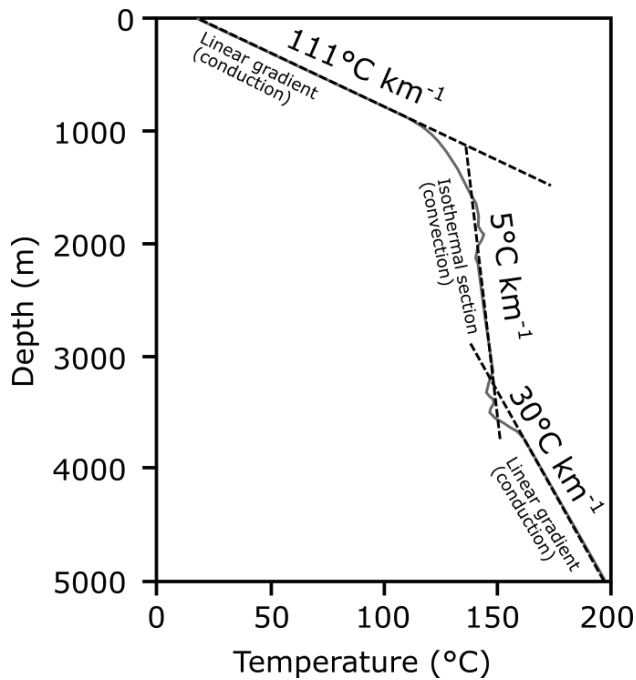


Figure 4.4 Temperature profile showing different heat transfer mechanisms (Modified from Grant and Bixley, 2011)

In geothermal systems, the temperature gradient reduction is typical due to the phase change at the reservoir. In reservoirs dominated by water, temperatures greater than 250 °C could present low or zero geothermal gradient values at temperature logs (Fig. 4.5). Meanwhile, in reservoir dominated by steam, temperatures greater than 240 °C could present low or zero geothermal gradient values at temperature logs (Steingrímsson, 2011).

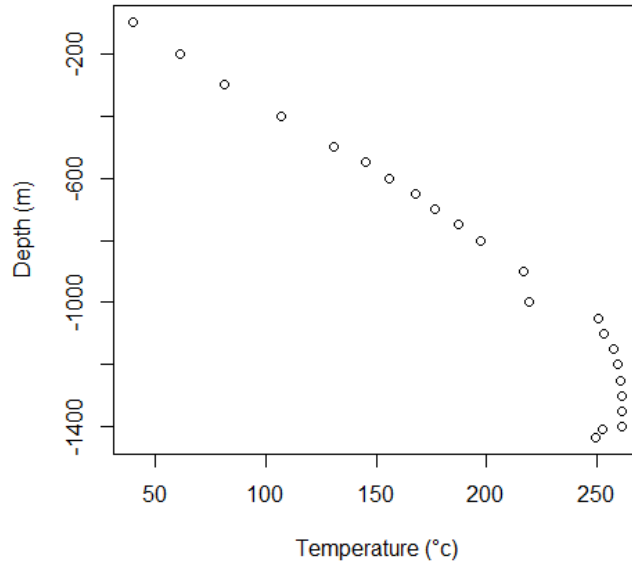


Figure 4.5 Temperature profile from a geothermal field (Los Humeros) in Mexico. The profile presents conduction until 1000 m, and convection caused by phase change below 1000 m and above the 250 °C

Meanwhile, fluid flow induced by drilling is mainly associated with aquifers' connection or drilling mud. The thermal effect caused by two aquifers' connections affects the temperature logs substantially, and the data becomes unsuitable for heat flow calculations. The aquifers' connection is illustrated in Fig. 4.6 (Beck and Balling, 1988).

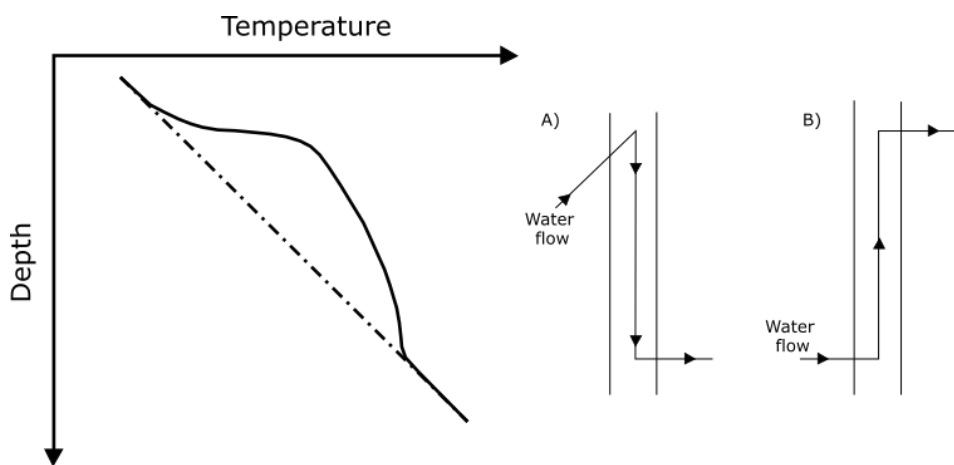


Figure 4.6 Schematic temperature profile showing temperature perturbation caused by aquifer connection. A) Descending flow and B) ascending flow (Modified from Beck and Balling, 1988).

The thermal regime of rocks is altered by drilling, nevertheless, the water at the bottom of the borehole is static during drilling pauses because there is no path opened for water movement. For this reason, BHT measurements are usually not disturbed by fluid circulation (Jessop, 1990). Recording BHT during drilling shutdowns in the morning or the evening approximates the unaltered rock temperatures and avoids disturbance caused by water movement during drilling (Fig. 3.7).

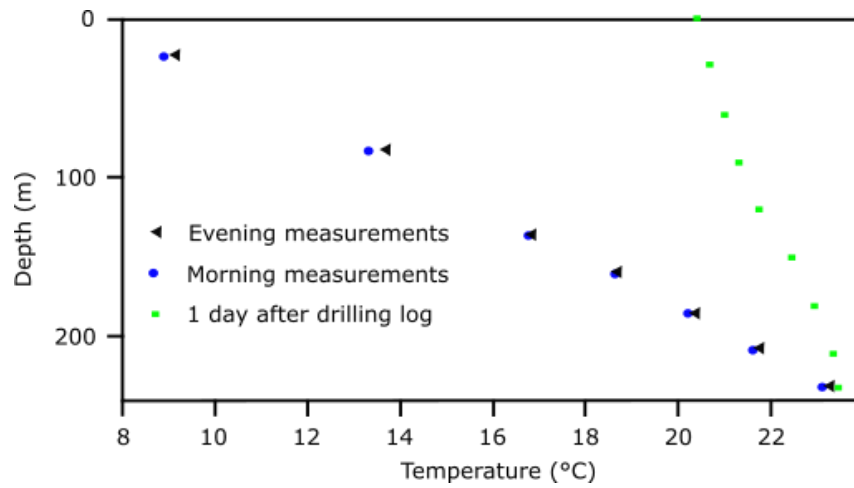


Figure 4.7 Temperature logs measure during drilling pauses and at the end of the drilling (Modified from Lewis and Jessop, 1981)

4.4 Temperature measurements and heat flow calculation in Mexico

It is essential to analyze temperature logs to detect fluid circulation or calculate the heat flow. The data quality varies on the thermal regime detected (conduction, convection, or both) and measurement methods. Depending on the thermal dominant regime in the temperature data, it is possible to decide if boreholes are usable or they need to be eliminated from the database.

Borehole depth needs to be considered because shallow boreholes are often affected by the superficial thermal regime, and corrections are necessary. Boreholes deeper than 200 m without fluid flows are suitable for heat flow calculations, and in these temperature logs, the first meters can be ignored if there are strong perturbations. Boreholes with depths shallower than 200 m have lower quality and should be removed if the log does not have a constant and unaltered geothermal

gradient for at least 50 m (Roy et al., 1972; Cull and Sparksman, 1977; Gosnold et al., 2011; Richards et al., 2012).

In this work, the heat flow calculations use the geothermal gradient's linear increment associated with conduction. For this reason, the calculation is performed only in boreholes with segments of several hundred meters of the geothermal gradient's linear increment (Fig. 4.8).

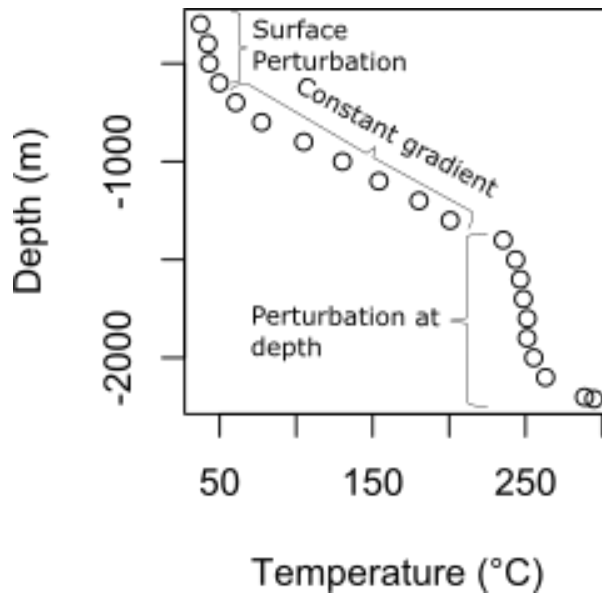


Figure 4.8 Borehole MEX039. This example shows the perturbations and the constant linear increment of the geothermal gradient linear in several hundreds of meters.

The calculation of heat flow needs the thermal conductivity values. When the thermal conductivity values from boreholes are not available, the calculation is carried out using the average values corresponding to the borehole's geological column or by using the earth's crust average. Finally, by using the Bullard method, the heat flow calculations are carried on. The Bullard method uses the linear regression between thermal resistance and temperature, calculating heat flow using eq. 4.1.

$$T_d = T_o + q_o R \quad (4.1)$$

where T_d is the temperature at depth, T_o is surface temperature, q_o is surface heat flow represented by the straight-line slope, and R is the thermal resistance.

Thermal resistance is defined by individual formations or layers with thickness Δz_i and thermal conductivity data λ_i , as is shown in eq 4.2 (Beardmore and Cull, 2001). Heat flow calculations examples are shown in Fig. 4.9.

$$R = \sum_i \left(\frac{\Delta z_i}{\lambda_i} \right) \quad (4.2)$$

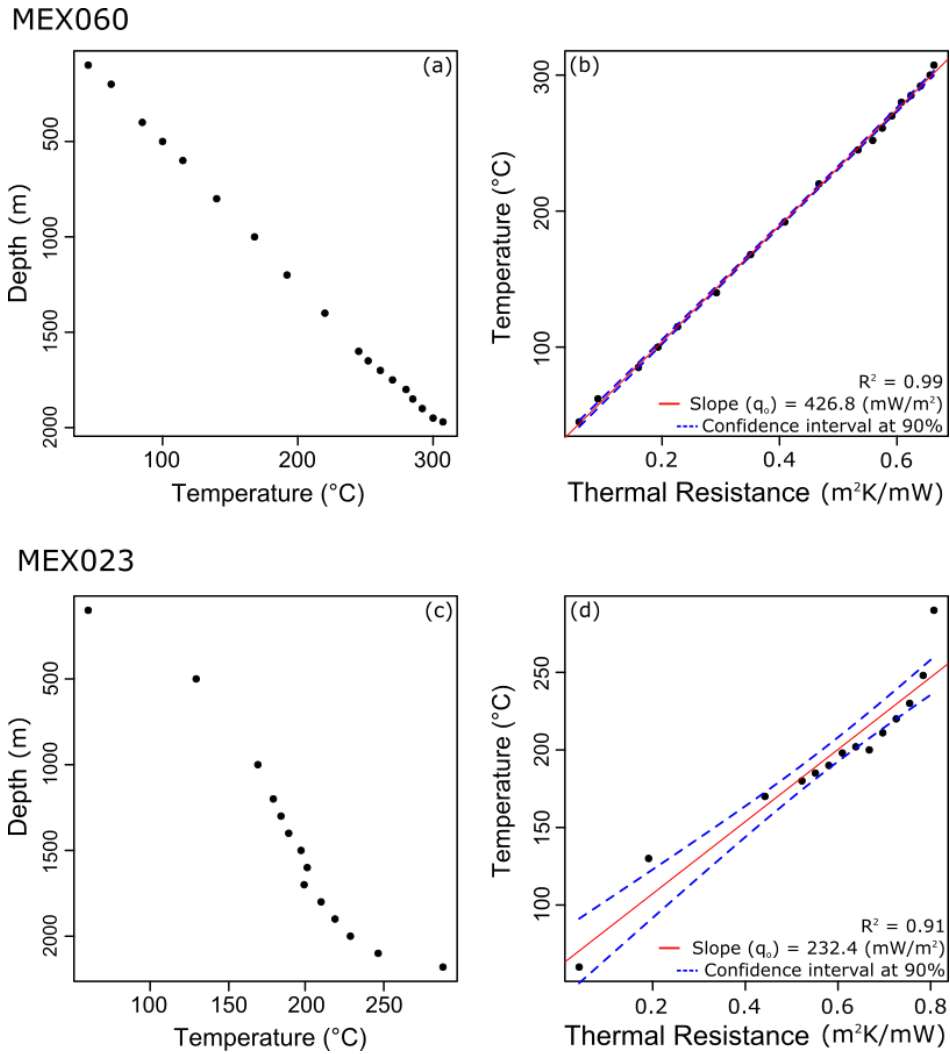


Figure 4.9 Heat flow calculations. a) Temperature at depth profile and b) Bullard from borehole MEX060. c) Temperature at depth profile and d) Bullard from borehole MEX023.

From the 108 temperature logs analyzed, only 87 temperature logs are adequate for heat flow calculations (see chapter 6.1). The heat flow calculations are an update from previous works, where

there are variations between the first heat flow calculated values (Espinoza-Ojeda et al., 2017) and the recalculated values. For example, borehole MEX057 at Los Humeros geothermal field has an initial heat flow of 10 mW m^{-2} (Fig. 4.10a), and the recalculated heat flow is 364.8 mW m^{-2} (Fig. 4.10b). Mexico's database from new data, compilations, and recalculated values has 1872 heat flow measurements.

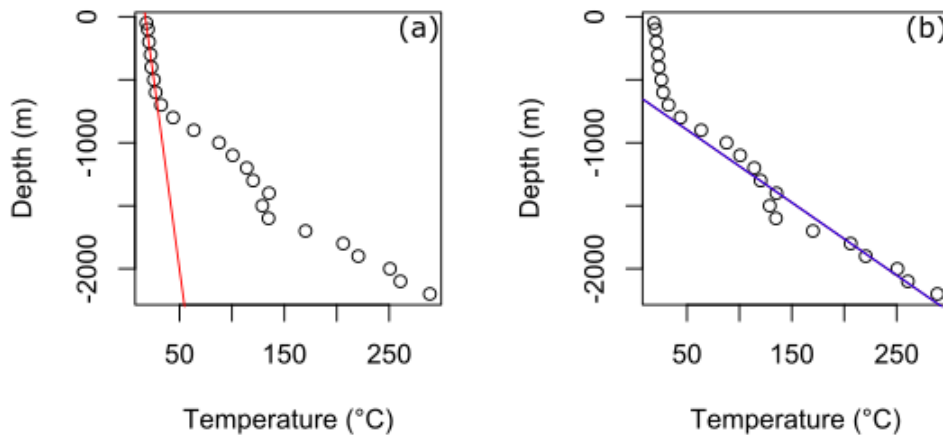


Figure 4.10 (a) Temperature data used in the first heat flow measurement, (b) temperature data used in the recalculated heat flow.

References

- Beardsmore, G., Cull, J., 2001. Crustal Heat Flow: A guide to measurement and modelling. Cambridge, UK: Cambridge University Press.
<https://doi.org/10.1017/S0016756803218021>.
- Beck, A., Balling, N., 1988. Determination of Virgin Rock Temperatures. In: Haenel R., Rybach L., Stegenga L. (Eds), Handbook of Terrestrial Heat-Flow Density Determination. Solid Earth Sciences Library, vol 4. Springer, Dordrecht.
- Cull, J., Sparksman, G., 1977. Measurements of Surface Heat Flow. Bureau of Mineral Resources Geology and Geophysics Record, 39.
- Čermák, V., Haenel, R., 1988. Geothermal Maps. In: Haenel R., Rybach L., Stegenga L. (eds), Handbook of Terrestrial Heat-Flow Density Determination. Solid Earth Sciences Library, vol 4. Springer, Dordrecht.

- Espinoza-Ojeda, O.M., Prol-Ledesma, R.M., Iglesias, E.R., Figueroa-Soto, A., 2017. Update and review of heat flow measurements in Mexico. *Energy* 121, 466-479. <https://doi.org/10.1016/j.energy.2017.01.045>.
- Gosnold, W., Majorowicz, J., Klenner, R., Hauck, S., 2011. Implications of Post-Glacial Warming for Northern Hemisphere Heat Flow. *Geothermal Resources Council Transactions* 35, 795-799.
- Grant, M., Bixley, P., 2011. *Geothermal Reservoir Engineering*. 2nd ed., Burlington, MA: Academic Press.
- Jessop, A., 1990. *Thermal geophysics*. Amsterdam: Elsevier.
- Jorden, J.R., Campbell, F.L., 1984. Well Logging I- Rock Properties, Borehole Environment, Mud and Temperature Logging. *SPE of AIME*, N.Y., Dallas, 131- 146.
- Lewis, J., Jessop, A., 1981. Heat flow in the Garibaldi volcanic belt, a possible Canadian geothermal energy resource area. *Canadian Journal of Earth Sciences* 18(2), 366-375. <https://doi.org/10.1139/e81-028>.
- Lovering, T., Goode, H., 1963. Measuring Geothermal Gradients in Drill Holes Less Than 60 Feet Deep East Tintic District, Utah. *Geological Survey Bulletin* 1172. Washington: United States Government Printing Office.
- Powell, W.G., Chapman, D.S., Balling, N., Beck, A.E., 1988. Continental Heat-Flow Density. In: Haenel R., Rybach L., Stegenga L. (Eds), *Handbook of Terrestrial Heat-Flow Density Determination*. Solid Earth Sciences Library, vol 4. Springer, Dordrecht.
- Richards, M., Blackwell, D., Williams, M., Frone, Z., Dingwall, R., Batir, J., Chickering, C., 2012. Proposed Reliability Code for Heat Flow Sites. *Geothermal Resources Council Transactions* 36, 211-218.
- Roy, R., Blackwell, D., Decker, E., 1972. Continental Heat Flow. In Robertson E. (Ed.), *The Nature of the Solid Earth*. New York: McGraw Hill.
- Schütz, F., Winterleitner, G., Huenges, E., 2018. Geothermal exploration in a sedimentary basin: new continuous temperature data and physical rock properties from northern Oman. *Geothermal Energy* 6(1). <https://doi.org/10.1186/s40517-018-0091-6>.
- Steingrimsson, B., 2013. Geothermal Well Logging: Temperature and Pressure Logs. In Short Course V on Conceptual Modelling of Geothermal System by UNU-GTP and LaGeo, El Salvador, 1-16.

Chapter 5: Depth to the bottom of the magnetic sources

5.1 MAGCPD: A MATLAB-based codes to calculate the Curie point-depth involving the spectral analysis of aeromagnetic data.

(Published paper at *Earth Science Informatics* journal)

Note: The equation number 8 is corrected using this equation:

$$\Delta Z_b = \sqrt{(2\Delta Z_0)^2 + \Delta Z_t^2}$$

This change is associated with an error on Martos et al. (2019) paper. More details at <https://doi.org/10.1007/s12145-020-00540-y>.



MAGCPD: a MATLAB-based GUI to calculate the Curie point-depth involving the spectral analysis of aeromagnetic data

Juan Luis Carrillo-de la Cruz^{1,2} · Rosa María Prol-Ledesma² · Pablo Velázquez-Sánchez³ · Dario Gómez-Rodríguez³

Received: 20 June 2020 / Accepted: 4 September 2020
© Springer-Verlag GmbH Germany, part of Springer Nature 2020

Abstract

The Curie point-depth, frequently related to the depth to the bottom of the magnetic source, is widely employed as an estimator of temperature at depth when borehole temperature data are not available. The Curie point-depth is calculated using the spectral analysis of the magnetic data derived from aeromagnetic or satellite surveys. In this paper, MATLAB user-friendly GUI are constructed to calculate the Curie Point Depth using the inversion of aeromagnetic data assuming 2D fractal magnetization and modeling the temperature at depth assuming a 1D steady-state conductive heat transfer model. The program, tested in synthetic and aeromagnetic data, is running under MATLAB 2020a or standalone application with these input parameters: Aeromagnetic data, fractal parameter, Curie temperature, surface temperature, thermal conductivity, surface radiogenic heat production and scaling length of surface radiogenic heat production. The radially averaged amplitude spectrum, scaled spectrum, modeled spectrum, Curie point-depth, and temperature profile at depth are the output parameters of the program. Finally, the program is tested with Texas aeromagnetic data, and the results of the Curie point-depth were compared with borehole data.

Keywords Magnetic data · Curie point depth · Heat flow · GUI-interface

Introduction

The study of the crustal thermal structure has essential implications in geology and tectonics due to their applications in renewable energies exploration and hydrocarbon maturity history. Some indirect estimators of the geothermal gradient and heat flow are necessary because of the lack of direct temperature measurements. One of the most commonly used estimators of temperature at depth is the Curie point-depth (CPD) that frequently marks the depth where rocks lose their

magnetic properties as a result of temperature increase; this depth is associated with the depth to the bottom of the magnetic source (DBMS), that is computed by the spectral analysis of magnetic data obtained from airborne or satellite surveys.

Different methodologies to calculate the DBMS by the analysis of the radially averaged amplitude spectrum (RAAS) have been developed. These methods can be sorted as follows: i) random and uncorrelated magnetization model (Spector and Grant 1970; Bhattacharyya and Leu 1975; Shuey et al. 1977; Connard et al. 1983; Okubo et al. 1985; Blakely 1988; Tanaka et al. 1999; Finn and Ravat 2004; Ravat 2004; Ross et al. 2006), and ii) fractal magnetization model (Pilkington and Todoeschuk 1993; Maus and Dimri 1995; Bouligand et al. 2009; Bansal et al. 2011; Li et al. 2013; Salem et al. 2014). The RAAS analyzes the long wavelengths (short wavenumber) relation with deep magnetic sources. Consequently, large size windows are required to reach the deepest magnetic signals associated with the CPD (Ross et al. 2006), nevertheless, recent studies suggest that the window size should be at least 5 times the target depth or larger (Kumar et al. 2020).

The most widely used methods for the DBMS estimations are the variations of the centroid method that consider the 2D

Communicated by: H. Babaie

Juan Luis Carrillo-de la Cruz
juanluiscc9@comunidad.unam.mx

¹ Posgrado en Ciencias de la Tierra, Instituto de Geofísica, Universidad Nacional Autónoma de México, Circuito interior s/n, Coyoacán, 04510 Ciudad de México, Mexico

² Instituto de Geofísica, Universidad Nacional Autónoma de México, Circuito interior s/n, Coyoacán, 04510 Ciudad de México, Mexico

³ División Académica de Ciencias Básicas, Universidad Juárez Autónoma de Tabasco, Carretera Cunduacán-Jalpa km. 1, 86690 Villahermosa, Tabasco, Mexico

fractal magnetization model: the modified centroid method (Li et al. 2013) and the de-fractal method (Salem et al. 2014). In this paper, a MATLAB GUI are constructed from different functions for an easy application of these methods, their results were compared, which shows that differences between methods are not significant. The codes were tested with magnetic synthetic data and aeromagnetic data from Texas. The CPD estimations from the aeromagnetic data were validated using available Bottom Hole Temperature measurements from boreholes.

Methods

The magnetism of certain minerals, like the magnetite or pyrrhotite, is manifested in rocks as remanent magnetization and ferromagnetic susceptibility. As temperature increases and the Curie temperature is reached (~580 °C for the magnetite), the remanent magnetism fades out and magnetic minerals lose their magnetic properties (Blakely 1988). The temperature increase at depth affects the magnetic susceptibility of the minerals in the crust; hence, at certain depth where the Curie temperature is attained, the magnetic materials become paramagnetic. Several studies use the amplitude (or power) spectrum of a squared windows of total field anomaly obtained by satellite or airborne data to calculate the DBMS associated with this thermal boundary. A brief description of the methods is presented below.

Random and uncorrelated magnetization model

The different methods studied by Ravat et al. (2007) to calculate the top (Z_t) and bottom (Z_b) of the magnetic sources assuming a random and uncorrelated model are: The spectral peak (Connard et al. 1983; Blakely 1995), forward modeling of the spectral peak (Ravat 2004; Finn and Ravat 2004; Ross et al. 2006) and the centroid method (Okubo et al. 1985; Tanaka et al. 1999). In these methods, the amplitude spectrum of the total magnetic field due to an infinite horizontal layer with magnetization as a random function of x and y (Blakely 1995) is defined as:

$$A(k_x, k_y) = 2\pi C_m A_m |\Theta_m| |\Theta_f| e^{-kZ_t} \left(1 - e^{-k(Z_b - Z_t)} \right) \quad (1)$$

where k_x and k_y are the x - and y -direction wavenumbers, C_m is the proportionality constant, A_m is the amplitude spectra of the magnetization, Θ_m is the directional factor related to the magnetization, Θ_f is the directional factor related to the geomagnetic field, Z_t and Z_b are the top and bottom of the magnetic source. Assuming A_m as a constant and the magnetization as a random and uncorrelated function, Eq. (1) is simplified by radial averaging as:

$$A(k) = Ce^{-kZ_t} \left(1 - e^{-k(Z_b - Z_t)} \right) \quad (2)$$

with C as non-depth dependent constant and $k = \sqrt{k_x^2 + k_y^2}$ is the wavenumber.

The spectral peak method

The method proposed by Connard et al. (1983) numerically solves the following equation:

$$\ln Z_b - \ln Z_t = k_{peak}(Z_b - Z_t) \quad (3)$$

From the Eq. (3) k_{peak} is the wavenumber related with the spectral peak. The special limitation of this method is that the spectral peak sometimes is absent and may not be applied.

Forward modeling of the spectral peak

This method uses an interactive matching, varying the values of Z_t and Z_b , to adjust the observed RAAS with a synthetic amplitude spectrum modeled by Eq. (2). In this method, the constant C in Eq. (2) is used to adjust up or down the synthetic amplitude spectrum, Z_b restrict the position of the peak at low-wavenumbers, Z_t defines the slope at high-wavenumbers and the combination of Z_t and Z_b delimit the slope immediately next to the peak. The method can be applied only if the RAAS presents a peak (Ravat 2004; Finn and Ravat 2004; Ross et al. 2006; Ravat et al. 2007).

Centroid method

This method calculates the depth to the top and centroid of the magnetic source from the RAAS and the scaled RAAS, respectively. For wavelengths less than twice the thickness of the layer (Bhattacharyya and Leu 1975; Spector and Grant 1970; Okubo et al. 1985; Tanaka et al. 1999; Li et al. 2010) Eq. (2) can be simplified to calculate Z_t as:

$$\ln[A(k)] \approx \ln C - kZ_t \quad (4)$$

Equation (2) expressed for the centroid of the magnetic source (Z_0) is:

$$A(k) = De^{-kZ_0} \left(e^{-k(Z_t - Z_0)} - e^{-k(Z_b - Z_0)} \right) \quad (5)$$

D is a constant. Eq. (5) is simplified to compute Z_0 as (Bhattacharyya and Leu 1975; Okubo et al. 1985; Tanaka et al. 1999; Li et al. 2010):

$$\ln[A(k)/k] \approx \ln D - kZ_0 \quad (6)$$

Equations (4) and (6) are straight-line equations, and in order to compute Z_t and Z_0 it is necessary to calculate the slope

of the straight line at high- and low-wavenumbers. Finally, DBMS (Z_b) is (Okubo et al. 1985):

$$Z_b = 2Z_0 - Z_t \quad (7)$$

The uncertainty associated with this method is calculated by (Martos et al. 2019):

$$\Delta Z_b = \sqrt{2 \cdot \Delta Z_0^2 + \Delta Z_t^2} \quad (8)$$

ΔZ_0 , ΔZ_t and ΔZ_b are the uncertainty of the top, the centroid, and the base of the magnetic source, respectively. The values of ΔZ_0 and ΔZ_t are computed using the standard deviation (σ_r) derived from the calculated RAAS and the linear fit in the wavenumber range used to derive the slope ($k_2 - k_1$) (Okubo and Matsunaga 1994). This uncertainty (ϵ) is:

$$\epsilon = \frac{\sigma_r}{k_2 - k_1} \quad (9)$$

Fractal magnetization model using the modified centroid approach

Ravat et al. (2007) considered that the corrections for fractal magnetization behavior (Power-law corrections) could be inappropriate due to the overcorrection of the RAAS that would yield unrealistically shallow values of the DBMS. However, new studies revealed that the DBMS calculated using a magnetization fractal model are reliable (Bouligand et al. 2009; Bansal et al. 2011; Li et al. 2013; Salem et al. 2014; Li et al. 2017; Martos et al. 2017; Andrés et al. 2018; Martos et al. 2018; Carrillo-de la Cruz et al. 2020; Kumar et al. 2020).

The methods used in this study are based on the fractal distribution of the magnetic sources (Pilkington and Todoeschuk 1993; Fedi et al. 1997; Maus et al. 1997; Bansal et al. 2011; Li et al. 2013) following the relation where the amplitude spectrum of the magnetization is proportional to the norm of the wavenumber raised to a negative fractal parameter (Eq. 10):

$$A_m(k_x, k_y, k_z) \propto k^{-\beta/2} \quad (10)$$

Modified centroid method

This method calculates the amplitude spectrum assuming a 2-D horizontal fractal magnetization model, constant vertical magnetization, and finite horizontal extension of magnetic sources, expressed (Li et al. 2013) as the following equation:

$$\ln(A(k)) = E - |k|Z_t - \frac{\beta-1}{2} \ln|k| + \ln[1 - e^{-|k|(Z_b - Z_t)}] \quad (11)$$

where, $A(k)$ is the RAAS, and E is the constant related to magnetization direction and geomagnetic field direction. To calculate Z_t , due to a large Z_b , the half-space of Eq. (11) is approximated to:

$$\ln(A(k)) \approx F - |k|Z_t - \frac{\beta-1}{2} \ln|k| \quad (12)$$

where F is constant. Li et al. (2013) scaled the amplitude spectrum in Eq. (12), following the centroid approach of Tanaka et al. (1999), calculating a modified centroid following:

$$\ln(A(k)/k) \approx G - |k|Z_0 - \frac{\beta-1}{2} \ln|k| \quad (13)$$

From this model, it is possible to calculate DBMS using the Eq. (7). In this work, we add the forward modeling of the amplitude spectrum using Eq. (11), in order to find a relationship with a β value that indicates changes in the geology. The fine-tuning between the modeled and the calculated spectrum is determined by the misfit using the following equation:

$$R = \sqrt{\frac{1}{n} \sum_{i=1}^n (A_f(k_i) - A_{syn}(k_i))^2} \quad (14)$$

where, $A_f(k)$ is the observed amplitude spectrum, and $A_{syn}(k)$ is the synthetic amplitude spectrum. For a 2-D horizontal fractal magnetization model, $\beta = 1$ corresponds to the random and uncorrelated magnetization model.

De-fractal method

Salem et al. (2014) assumed that the de-fractal method corrects the observed amplitude spectrum extracting the fractal sources using:

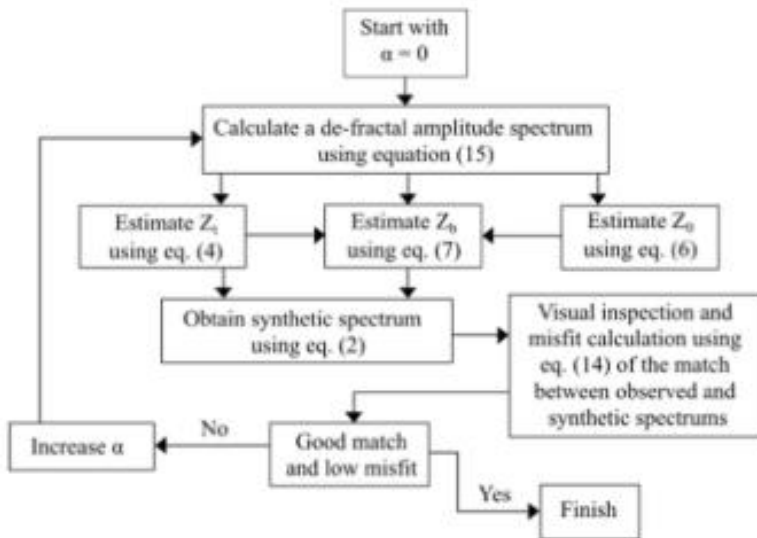
$$A_R(k_x, k_y) = A_F(k_x, k_y)k^{\alpha/2} \quad (15)$$

where, $A_R(k)$ is the amplitude spectrum assuming a random magnetization model, $A_F(k_x, k_y)$ is the calculated RAAS, k is the norm of the wavenumber, and the fractal parameter in two dimensions is $\alpha = \beta - 1$. The method evaluates Z_t , Z_b and α using forward modeling of the spectral peak on the corrected spectrum following the flowchart in Fig. 1. It is important to mention that high α values in the fractal parameter could overcorrect the spectrum.

Heat flow calculation and temperature profiles

The heat flow calculation and the temperature profile related to a conductive heat transfer model with heat generation are included in GUI. The heat flow is calculated using Fourier's Law, expressed by:

Fig. 1 Flowchart diagram to follow the processing steps (From Carrillo-de la Cruz et al. 2020; Salem et al. 2014; Martos et al. 2017)



$$q(z) = \lambda \frac{\partial T(z)}{\partial z} \quad (16)$$

If the boundary conditions are Z_b as CPD, T_c the Curie temperature ($\sim 580^\circ\text{C}$) and T_0 the surface temperature, then, the differential equation can be solved assuming conductive heat transfer (Martos et al. 2017), and the surface heat flow is:

$$q_s = \frac{\lambda(T_c - T_0)}{Z_b} + H_0 h_r - \frac{H_0 h_r^2}{Z_b} \left(1 - e^{(-Z_b/h_r)}\right) \quad (17)$$

where, λ is the thermal conductivity, H_0 is the radiogenic heat production and h_r is a scaling length for H_0 . The solution of Eq. (16) for the temperature at depth z (T_z) is the Eq. (18), taking as boundary conditions $T = T_0$ at $z = 0$ (surface), q_s is surface heat flow, and neglecting contributions from mass advection, transient cooling or temperature dependence of thermal conductivity (Ravat et al. 2016):

$$T(z) = T_s + \frac{q_s z}{\lambda} + \frac{H_0 h_r (h_r - z)}{\lambda} - \frac{H_0 h_r^2 e^{(-z/h_r)}}{\lambda} \quad (18)$$

Table 1 Synthetic data modeling using the modified centroid methods

Modified centroid method					De-fractal method				
β	Z_t	Z_b	ΔZ_b	R	α	Z_t	Z_b	ΔZ_b	R
1	1.44	36.41	2.38	0.5331	0	1.45	26.41	2.38	0.3574
2	0.88	18.36	2.02	0.3081	1	0.88	18.35	2.02	0.1598
3	0.31	10.30	1.72	0.0921	2	0.32	10.30	1.72	0.0922

It is possible to determine the temperature profile at depth from the heat flow calculated with Eq. (17) and the temperatures at depth with Eq. (18).

MAGCDP software

Software files

MAGCPD is an open source GUI developed MATLAB 2020a (The MathWorks Inc, 2020). The software files consist in two standalone applications in format .exe, running on Windows 10, for users that do not have MATLAB licenses. *Defractal.exe* calculates the CPD using the de-fractal method (Salem et al. 2014), while *modified_centroid.exe* calculates the CPD using the modified centroid method (Li et al.

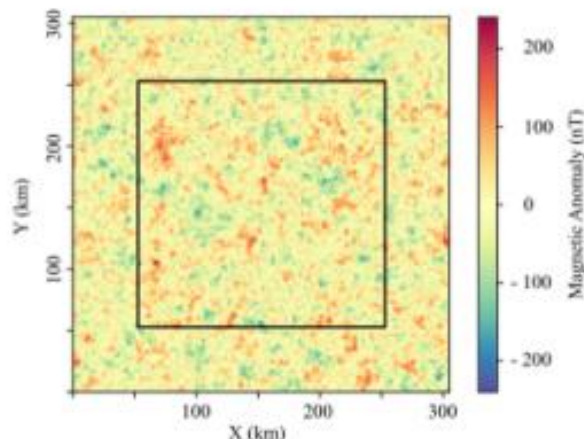


Fig. 2 Synthetic magnetic anomalies. The black square is the window used for the spectrum calculations (Bouligand et al. 2009)

2013). In addition, the files *defractal.mlapp* and *modified_centroid.mlapp* are included if the user wants to modify the code or to run the applications under MATLAB interface. The software files are hosted in GitHub.

Design and implementation

The MAGCPD GUI is implemented for the spectral analysis of aeromagnetic anomalies. The input data is the total magnetic field anomalies acquired after remove the main

magnetic field. The results of the processing are sensitive to the CPD calculations, for this reason, Ravat et al. (2007) suggest to avoid filtering in order to prevent changes at low wavenumber parts of the spectrum, nevertheless, some authors (i.e. Wang and Li 2018) use the upward continuation to suppress local signals from shallow sources and enhance regional and/or deep seated magnetic features; the user should consider that effect before calculating the total magnetic field anomaly. The total magnetic field anomaly data need to be a square

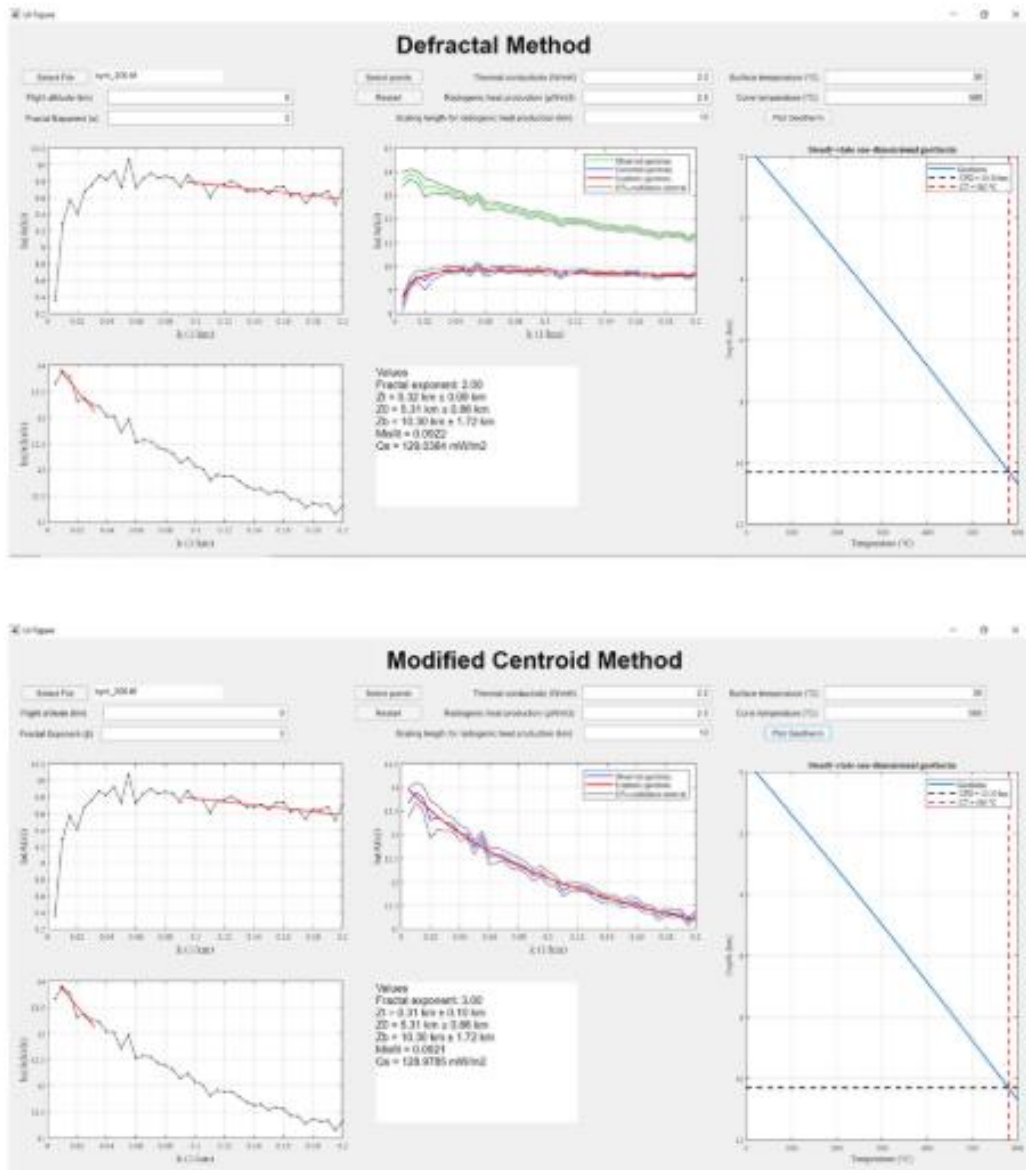


Fig. 3 Defractal method application using $\alpha = 2.0$. Modified centroid method application using $\beta = 3.0$

GeoTIFF (*.tif) grid, one band image, 32-bit floating point (float32) format, and data projection in meters. Also, old Geosoft 2-byte (signed integer) binary grids can be used in the program.

The software is constructed as follows:

- MATLAB auto-generated function to open GeoTIFF data.
- For old Geosoft 2-byte (signed integer) binary grid, the program uses `getgrd2.m` (Adam 2020) to open the data. It is important to notice that the square window need to be exported from *Oasis Montaj* as “Geosoft short” grid type.
- Detrend the data using `detrend_2d` function (Gdeisat 2011). This function removes the first order trending, because the trend could bias the calculations.
- Radially averaged amplitude spectrum is calculated by using `raPsd2d` (Ruzanski 2009). For this work, the function is adapted to compute the confidence intervals and the 1D angular frequencies of the signal with the `fcoeff` function (Ridsdill-Smith 2000). It is important to notice that the code does not work if the window is not square or do not have 100% data coverage.
- The flight height and the fractal parameter (β or α , depending on the method used) are necessary to run the algorithm.
- The slopes for the calculation of the depth to top and the centroid of the magnetic sources are interactively selected using the function `selectdata.m` (D'Errico 2007). This step

is important because the visual inspection and user selection of the slopes, instead of the automatic methods, are necessary to evaluate reliable solutions, and irregularities in the magnetic data or the amplitude spectrum (Salem et al. 2014).

- Using the obtained results, the amplitude spectrum is modeled by using eq. 2 for the de-fractal method, or eq. 11 for the modified centroid method. Finally, the temperature can be modeled with depth and the heat flow estimated (eq. 17 and 18), but the thermophysical parameters must be added: T_0 , T_c , λ , H_0 and h_r . Averaged input values for these parameters are included in the program for the modeling.

The codes were tested using synthetic data for 305×305 km size windows and the following parameters: $\beta = 3.0$, $Z_t = 0.305$ km and $Z_b = 10.305$ km (Bouligand et al. 2009). The data were clipped in a 200×200 km window, which is the appropriate size to reach DBMS at low wavenumbers (Fig. 2). The DBMS calculations were applied using different values of β and α (Fig. 1), searching the best match and a low misfit (Table 1). The wavenumber range used to model the synthetic spectra is presented in Fig. 3. In this case, it is possible to model the full spectra; nevertheless, the wavenumber range could be changed depending on the amplitude spectrum shape. The common wavenumber range used in the publications varies between 0.05 and 0.2 km^{-1} for Z_t and less than

Fig. 4 Magnetic anomaly map of the study area

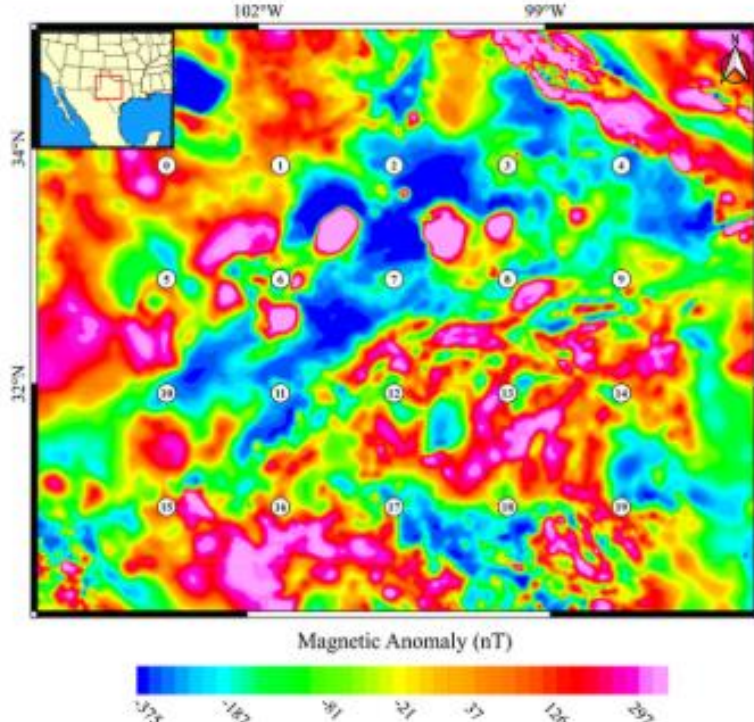


Fig. 5 Distribution and basic statistics of the geothermal gradient calculated from BHT measurements

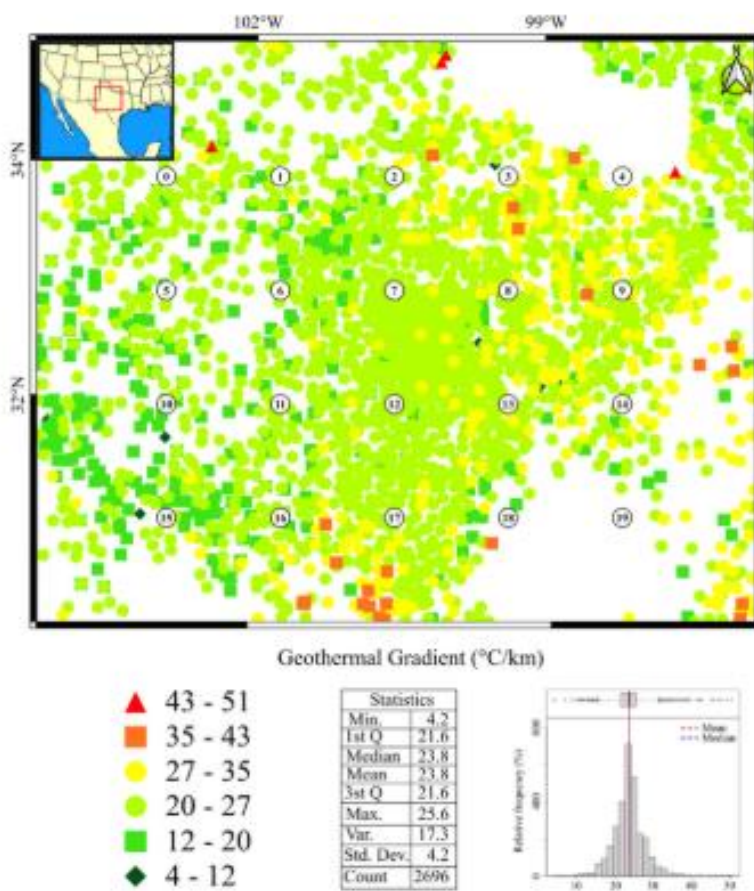


Table 2 Fractal exponents, depth to the bottom of magnetic source and misfit calculated using the modified centroid and de-fractal methods

Window number	β	CPD modified centroid method (km)	R	α	CPD de-fractal method (km)	R
0	3.4	22.82	0.118	2.4	23.28	0.148
1	3.3	22.64	0.171	2.3	22.81	0.188
2	3.3	21.50	0.216	2.3	21.69	0.162
3	3.3	23.66	0.158	2.3	23.85	0.175
4	3.0	21.80	0.138	2.0	21.80	0.138
5	3.5	20.18	0.166	2.5	20.35	0.204
6	3.5	21.41	0.180	2.5	21.41	0.180
7	3.5	19.49	0.190	2.5	19.58	0.203
8	3.0	23.74	0.152	2.0	23.62	0.157
9	3.0	21.41	0.091	2.0	21.34	0.082
10	3.5	22.04	0.198	2.5	22.08	0.210
11	3.5	22.30	0.130	2.5	22.45	0.172
12	3.0	24.32	0.141	2.0	24.31	0.148
13	3.0	20.33	0.118	2.0	20.41	0.136
14	3.0	22.84	0.101	2.0	22.78	0.096
15	3.0	24.06	0.128	2.0	24.14	0.125
16	3.5	19.02	0.108	2.5	19.16	0.137
17	3.5	21.82	0.155	2.5	21.93	0.167
18	3.5	20.57	0.101	2.5	20.62	0.103
19	3.5	20.11	0.100	2.5	20.18	0.098

0.07 km^{-1} for Z_0 (Wang and Li 2018), considering that the wavenumber ranges are variable depending on the spectrum shape. The calculations obtained using both methods are close to the depth of the synthetic data (Table 1, Fig. 3).

Application

The programs were tested in the central part of Texas due to the availability of boreholes with corrected bottom hole temperature measurements (BHT) and the North America Magnetic Anomaly Map. The aeromagnetic data used consists of a grid with 1-km spacing, DNAG projection, and upward/downward continuation to keep a standard height of 305 m above the terrain (more details in NAMAG 2002). The NAMAG data were used for calculations in the United States by Ravat et al. (2016), Bouligand et al. (2009) and Wang and Li (2015) because the grid and flight height are homogeneous (Fig. 4).

We used the geothermal gradient calculations from the SMU Heat Flow Database based on BHT Data (SMU Node of National Geothermal Data System n.d.) to compare the geothermal gradient derived from the CPD estimate. The average BHT geothermal gradient for each window is calculated and compared with the CPD estimated geothermal gradient. The SMU data are distributed in the whole study area and contain 2696 temperature data with an average geothermal gradient of $23.8 \text{ }^{\circ}\text{C}/\text{km}$, slightly below the global average of $25\text{--}30 \text{ }^{\circ}\text{C}/\text{km}$ (Fridleifsson et al. 2008). Figure 5 shows the spatial distribution of the geothermal gradient data and their basic statistics.

CPD was calculated using a $240 \times 240 \text{ km}$ window size with a 100 km distance between each window center and 100% data coverage for every window. Each window was analyzed individually to select the appropriate wavenumber range for the CPD calculation. Figure 6 displays an example of the modeled spectrum, the visual fit, and the misfit calculation, showing the variations between the two applied

methods. For the modified centroid method, the β exponent is calculated using the flowchart in Fig. 1, and the de-fractal method uses an equivalent value of α . The average CPD value for the modified centroid method is 21.8 km, and for the de-fractal method is 21.9 km (Table 2). The global model presented by Li et al. (2017) shows a bimodal distribution, where the first peak is 22.3 km: our results are slightly below this global average.

The programs presented a simple solution for the application of the fractal corrections and the calculation of the DBMS. The results of this study show that the calculations using equivalent fractal parameters (β and α) and the same wavenumber range, the results are similar (Fig. 7a). Both methods have sporadic deformations of the amplitude spectrum at low wavenumber values, for that reason, modeling at low wavenumbers is occasionally difficult and the multiple solutions for these situations need to be analyzed changing the wavenumber range and the fractal parameter. It is important to notice that the previous knowledge of the fractal parameter and changes in the wavenumber ranges (for the top and centroid) are useful to obtain better estimations.

Additionally, assuming conduction as a main heat transfer mechanism and no radiogenic heat generation, it is possible to estimate the geothermal gradient as $(T_c - T_0) / Z_b$, using the calculated CPD and the Curie temperature value of $580 \text{ }^{\circ}\text{C}$. Geothermal gradients estimated with both spectral methods is slightly higher than the geothermal gradient calculated from the BHT; nevertheless, the results are similar (Table 3 and Fig. 7b) and confirm that heat transport is mostly conductive with no significant heat generation (Fig. 7b).

Finally, temperature versus depth and heat flow are estimated, considering only a steady-state conductive heat transfer mechanism and an old basement that generates a negligible amount of heat, similar to what was observed in the neighboring region of Coahuila, México (Carrillo-de la Cruz et al. 2020). An example of the temperature profile is calculated from Eq. (18). The full example of the methodology applied using the modified centroid method is presented in Fig. 8.

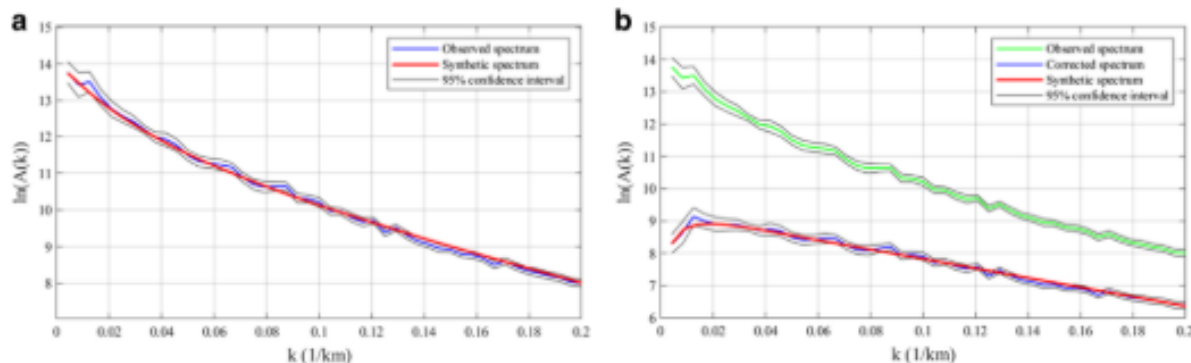


Fig. 6 Modeling of the spectrum in the window 9 using **a** modified centroid and **b** de-fractal methods

Discussion

The two methods used to calculate CPD yield similar results using the same fractal parameters and wavenumbers range. These methods are suitable to estimate the temperature at depth in regional studies of the thermal state of the crust. Nevertheless, there are multiple solutions for modeling the spectra and in some cases the low misfit values are associated with high fractal parameter values that could generate overcorrected solutions and erroneous conclusions. As observed in our results, incrementing the fractal parameter value for both methods will yield shallower DBMS and higher geothermal gradients that are not related with the actual thermal state of the study area; therefore, the calibration of the results using some actual thermal gradient measurement (i.e. BHT) could help to validate the results. Also, it is important to notice that the differences between the BHT geothermal gradients and the CPD geothermal gradients are associated with uncertainty in the values of the thermal parameters at depth, because the calculations derived from the BHT are temperature logs and measured thermal conductivities at depths between 0.35 and 6.20 km (mean value of 1.84 km) and the CPD values obtained are below 15 km, for that reason, it is important to consider a probably significant heat generation rate in the basement, possible heat sinks or a different heat transfer mechanism (convection) in some strata. Analyzing the uncertainty of the adjust and the standard deviation from Table 3, the results are similar to each other, considering that the high number of wells in the region improves the reliability of the uncertainty evaluation.

Salem et al. (2014) advocate manual analysis instead of automatic methods when analyzing the data, because the manual selection of the wavenumber range and the analysis of the modeled spectrum could reduce the uncertainty related with the fractal parameters. The processing of the data by the different centroid methods shows that the results are practically the same and modeling both mathematical approaches presents the same complexities, for this reason, it is suggested to use other geophysical and geological data to support the obtained results, considering that the CPD method is an averaging value for the entire window and the heat transport local anomalies cannot be discerned.

Conclusions

This is the first user-friendly MATLAB GUI used to calculate the CPD using the centroid methods with the fractal magnetization model approach, and this code was tested in synthetic data and aeromagnetic data from Texas. The results of both methods are similar, as the processing was performed with the same parameters and wavenumber ranges and it shows that there is no significant difference between the modified

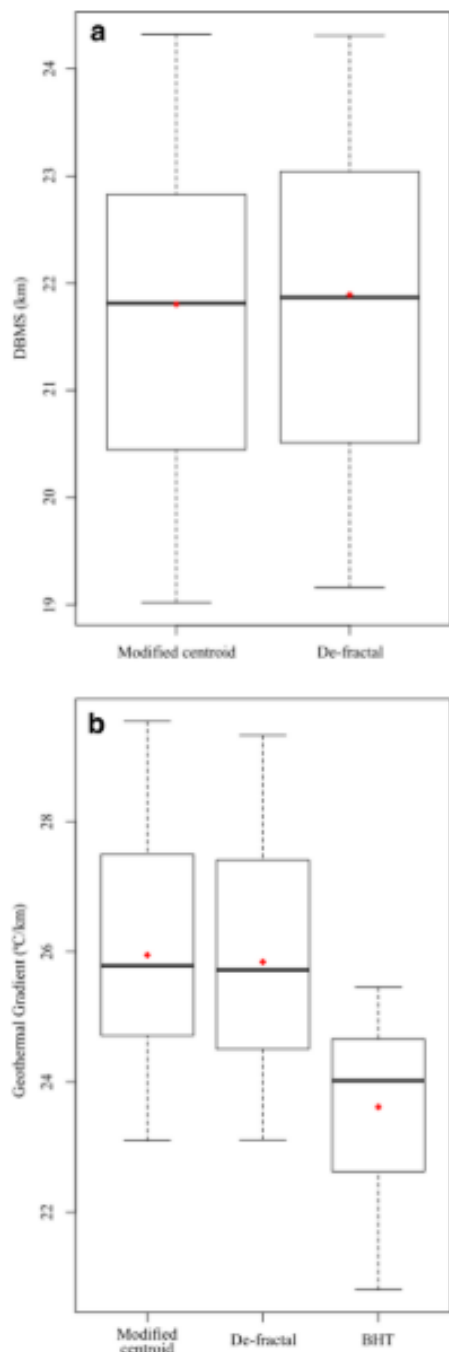


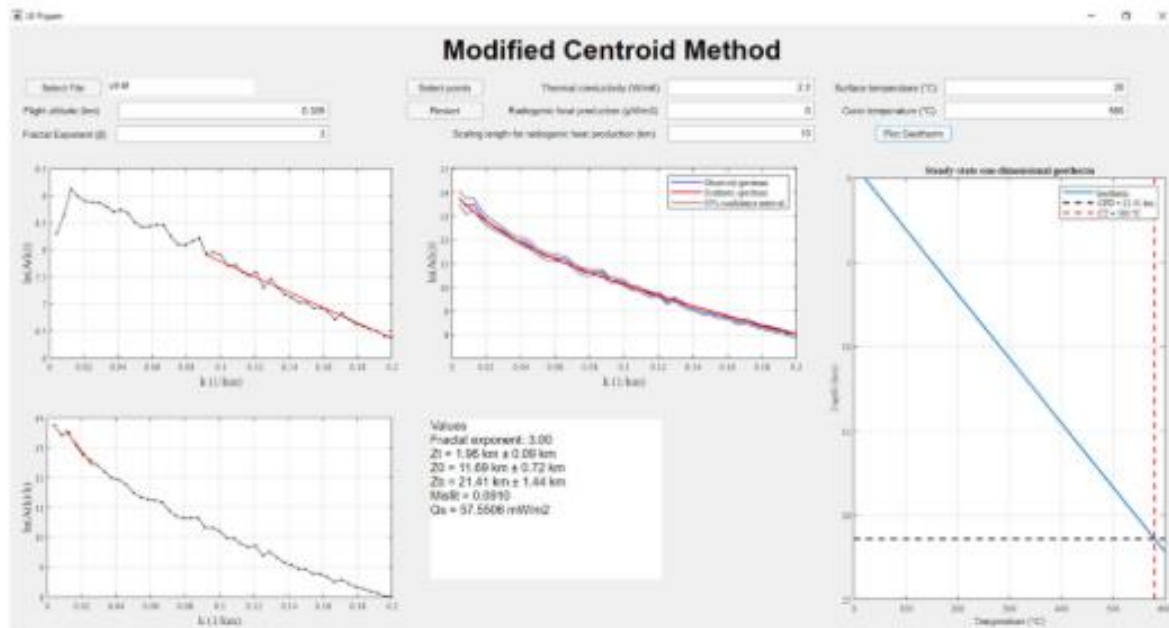
Fig. 7 Boxplot showing the comparison between **a** Depth to the bottom of magnetic source obtained with the modified centroid and the de-fractal methods; and **b** Geothermal Gradient from BHT, geothermal gradient determined with CPD calculated with modified centroid and de-fractal methods

Table 3 Geothermal gradient calculations from the CPD calculations and BHT data

Window number	Geothermal gradient modified centroid (°C/km)	Geothermal gradient de-fractal (°C/km)	Geothermal gradient BHT (°C/km)
0	24.8 ± 3.6	24.3 ± 3.5	22.3 ± 3.3
1	24.9 ± 3.3	24.7 ± 3.3	23.0 ± 3.3
2	26.2 ± 5.2	26.0 ± 5.1	24.1 ± 3.7
3	23.8 ± 2.2	23.6 ± 2.2	25.2 ± 3.6
4	25.8 ± 5.9	25.8 ± 5.9	24.7 ± 3.8
5	27.94 ± 3.8	27.7 ± 3.7	21.3 ± 3.1
6	26.3 ± 3.2	26.3 ± 3.2	22.6 ± 2.9
7	28.9 ± 4.2	28.7 ± 4.2	23.6 ± 3.2
8	23.7 ± 5.9	23.8 ± 5.9	24.7 ± 3.3
9	26.3 ± 3.5	26.3 ± 3.5	25.5 ± 3.8
10	25.5 ± 5.8	25.5 ± 5.8	20.8 ± 3.5
11	25.2 ± 3.7	25.0 ± 3.7	22.6 ± 3.1
12	23.1 ± 4.8	23.1 ± 4.8	23.4 ± 3.0
13	27.6 ± 3.9	27.5 ± 3.9	24.1 ± 3.2
14	24.7 ± 7.1	24.7 ± 7.2	25.2 ± 4.0
15	23.4 ± 3.5	23.3 ± 3.5	21.4 ± 4.1
16	29.5 ± 2.3	29.3 ± 2.2	24.0 ± 4.6
17	25.8 ± 5.9	25.6 ± 5.9	24.5 ± 4.1
18	27.4 ± 5.6	27.3 ± 5.6	24.3 ± 3.7
19	28.3 ± 7.5	28.2 ± 7.5	25.1 ± 4.8

centroid and the de-fractal methods. Also, the adjustment of the modeled spectrum has the same inconveniences at low wavenumbers for both methods.

The package also includes the calculation of the temperature profile at depth and heat flow. The CPD-estimated geothermal gradient was compared with the BHT-calculated

**Fig. 8** Example that presents the results of the application of the proposed GUI for window 9

geothermal gradient, assuming a conductive heat transfer model without heat generation, and the results are analogous for each window. Also, as commended by Salem et al. (2014), this program follows the statement of visual inspection and user selection to determine the solution, which yields better results than the automatic selection.

Acknowledgments This work was supported by Fondo de Sustentabilidad Energética SENER-CONACyT CeMIE-Geo under Grant-Project P-01: Mapas de Gradiente Geotérmico y Flujo de Calor para la República Mexicana" and to CONACyT for the PhD scholarship to the main author. QGIS software was used in the map creation. We wish to thank to Diana Nuñez and two anonymous reviewers for providing positive comments to improve the manuscript.

Code access The programs can be downloaded from <https://github.com/juanxo90/MAGCPD>.

Author contributions Juan Luis Carrillo-de la Cruz contributed to establish the basis of the codes and the application of the methodology. Also, he conceived parts of the code, developed the GIS analysis with the temperature data and wrote the manuscript.

Rosa María Prol-Ledesma contributed to manuscript writing and project scientific development.

Pablo Velázquez-Sánchez contributed to the algorithm development and the GUI interface.

Dario Gómez-Rodríguez contributed to the development of algorithm.

References

- Adam (2020) getgrd2. MATLAB Central File Exchange. <https://de.mathworks.com/matlabcentral/fileexchange/1527-getgrd2>. Accessed 20 Aug 2020
- Andrés J, Marzáin I, Ayarza P, Martí D, Palomeras I, Torné M, Campbell S, Carbonell R (2018) Curie point depth of the Iberian Peninsula and surrounding margins. A thermal and tectonic perspective of its evolution. *J Geophys Res Solid Earth* 123(3):2049–2068. <https://doi.org/10.1002/2017JB014994>
- Bansal AR, Gabriel G, Dimri VP, Krawczyk CM (2011) Estimation of depth to the bottom of magnetic sources by a modified centroid method for fractal distribution of sources: an application to aeromagnetic data in Germany. *Geophysics* 76(3):L11–L22. <https://doi.org/10.1190/1.3560017>
- Bhattacharyya BK, Leu LK (1975) Analysis of magnetic anomalies over Yellowstone National Park: mapping of curie point isothermal surface for geothermal reconnaissance. *J Geophys Res* 80(32):4461–4465. <https://doi.org/10.1029/JB080i032p04461>
- Blakely RJ (1988) Curie temperature isotherm analysis and tectonic implications of aeromagnetic data from Nevada. *J Geophys Res Solid Earth* 93(B10):11817–11832. <https://doi.org/10.1029/JB093iB10p11817>
- Blakely RJ (1995) Potential theory in gravity and magnetic applications. Cambridge University Press, Cambridge
- Bouligand C, Glen JMG, Blakely RJ (2009) Mapping curie temperature depth in the western United States with a fractal model for crustal magnetization. *J Geophys Res* 114:b11104. <https://doi.org/10.1029/2009jb006494>
- Carrillo-de la Cruz JL, Prol-Ledesma RM, Gómez-Rodríguez D, Rodríguez-Díaz AA (2020) Analysis of the relation between bottom hole temperature data and curie temperature depth to calculate geothermal gradient and heat flow in Coahuila, Mexico. *Tectonophysics* 780:228397. <https://doi.org/10.1016/j.tecto.2020.228397>
- Connard G, Couch R, Gemperle M (1983) Analysis of aeromagnetic measurements from the Cascade Range and in Central Oregon. *Geophysics* 48(3):376–390. <https://doi.org/10.1190/1.1441476>
- D'Errico J (2007) Graphical data selection tool. MATLAB Central File Exchange. <https://de.mathworks.com/matlabcentral/fileexchange/13857-graphical-data-selection-tool>. Accessed 18 May 2019
- Fedi M, Quarta T, De Santis A (1997) Improvements to the Spector and Grant method of source depth estimation using the power law decay of magnetic field power spectra. *Geophysics* 62:1143–1150
- Finn CA, Ravat D (2004) Magnetic Depth Estimates and Their Potential for Constraining Crustal Composition and Heat Flow in Antarctica. *Eos, Transactions, American Geophysical Union* 85 (47), Fall Meeting, Abstract T11A-1236
- Fridleifsson IB, Bertani R, Huenges E, Lund JW, Ragnarsson A, Rybach L (2008) The possible role and contribution of geothermal energy to the mitigation of climate change. In: Hohmeyer O, Trittin T (Eds.) IPCC scoping meeting on renewable energy sources. Proceedings, Luebeck, pp 59–80
- Gdeisat MA (2011) Flatten a data in 2D. MATLAB Central File Exchange. https://www.mathworks.com/matlabcentral/fileexchange/33192-flatten-a-data-in-2d?s_tid=prof_contriblnk. Accessed 15 Aug 2019
- Kumar R, Bansal AR, Ghods A (2020) Estimation of depth to bottom of magnetic sources using spectral methods: Application on Iran's aeromagnetic data. *J Geophys Res Solid Earth* 125: e2019JB018119. <https://doi.org/10.1029/2019JB018119>
- Li C-F, Shi X, Zhou Z, Li L, Geng J, Chen B (2010) Depths to the magnetic layer bottom in the South China Sea area and their tectonic implications. *Geophys J Int* 182(3):1229–1247. <https://doi.org/10.1111/j.1365-246X.2010.04702.x>
- Li C-F, Wang J, Lin J, Wang T (2013) Thermal evolution of the North Atlantic lithosphere: new constraints from magnetic anomaly inversion with a fractal magnetization model. *Geochem Geophys Geosyst* 14(12):5078–5105. <https://doi.org/10.1002/2013GC004896>
- Li C-F, Lu Y, Wang J (2017) A global reference model of curie-point depths based on EMAG2. *Sci Rep* 7:45129. <https://doi.org/10.1038/srep45129>
- Martos YM, Catalán M, Jordan TA, Golynsky A, Golynsky D, Eagles G, Vaughan DG (2017) Heat flux distribution of Antarctica unveiled. *Geophys Res Lett* 44(22):11,417–11,426. <https://doi.org/10.1002/2017GL075609>
- Martos YM, Jordan TA, Catalán M, Jordan TM, Bamber JL, Vaughan DG (2018) Geothermal heat flux reveals the Iceland hotspot track underneath Greenland. *Geophys Res Lett* 45(16):8214–8222. <https://doi.org/10.1029/2018GL078289>
- Martos YM, Catalán M, Galindo-Zaldívar J (2019) Curie depth, heat flux, and thermal subsidence reveal the Pacific mantle outflow through the Scotia Sea. *J Geophys Res Solid Earth* 124:10,735–10,751. <https://doi.org/10.1029/2019JB017677>
- Maus S, Dimri V (1995) Potential field power spectrum inversion for scaling geology. *J Geophys Res Solid Earth* 100(B7):12605–12616. <https://doi.org/10.1029/95JB00758>
- Maus S, Gordon D, Fairhead D (1997) Curie-temperature depth estimation using a self-similar magnetization model. *Geophys J Int* 129(1): 163–168. <https://doi.org/10.1111/j.1365-246X.1997.tb00945.x>
- NAMAG (2002) Digital data grids for the magnetic anomaly map of North America. United States Geological Survey Open File Rep. 02-414. <https://mrdata.usgs.gov/magnetic/>. Accessed 12 Jun 2019
- Okubo Y, Matsunaga T (1994) Curie point depth in Northeast Japan and its correlation with regional thermal structure and seismicity. *J Geophys Res* 99(B11):22363–22371. <https://doi.org/10.1029/94JB01336>
- Okubo Y, Graf RJ, Hansen RO, Ogawa K, Tsu H (1985) Curie point depths of the island of Kyushu and surrounding areas, Japan. *Geophysics* 50(3):481–494. <https://doi.org/10.1190/1.1441926>

- Pilkington M, Todoeschuk JP (1993) Fractal magnetization of continental crust. *Geophys Res Lett* 20(7):627–630. <https://doi.org/10.1029/92GL03009>
- Ravat D (2004) Constructing full spectrum potential field anomalies for enhanced geodynamical analysis through integration of surveys from different platforms (INVITED). *Eos, Transactions, American Geophysical Union* 85 (47), Fall Meeting, Abstract G44A-03
- Ravat D, Pignatelli A, Nicolosi I, Champagni M (2007) A study of spectral methods of estimating the depth to the bottom of magnetic sources from near surface magnetic anomaly data. *Geophys J Int* 169(2):421–434. <https://doi.org/10.1111/j.1365-246X.2007.03305.x>
- Ravat D, Morgan P, Lowry AR (2016) Geotherms from the temperature-depth-constrained solutions of 1-D steady-state heat-flow equation. *Geosphere* 12(4):1187–1197. <https://doi.org/10.1130/GES01235.1>
- Ridsdill-Smith T (2000) The application of the wavelet transform to the processing of aeromagnetic data. Dissertation, The University of Western Australia
- Ross HE, Blakely RJ, Zoback MD (2006) Testing the use of aeromagnetic data for the determination of curie depth in California. *Geophysics* 71(5):L51–L59. <https://doi.org/10.1190/1.2335572>
- Ruzanski E (2009) Radially averaged power spectrum of 2D real-valued matrix, MATLAB central file exchange. <https://de.mathworks.com/matlabcentral/fileexchange/23636-radially-averaged-power-spectrum-of-2d-real-valued-matrix>. Accessed 15 Nov 2018
- Saleem A, Green C, Ravat D, Singh KH, East P, Fairhead JD, Mogre S, Biegert E (2014) Depth to curie temperature across the Central Red Sea from magnetic data using the de-fractal method. *Tectonophysics* 624–625:75–86. <https://doi.org/10.1016/j.tecto.2014.04.027>
- Shuey RT, Schellinger DK, Tripp AC, Alley LB (1977) Curie determination from aeromagnetic spectra. *Geophys J Int* 50(1):75–101. <https://doi.org/10.1111/j.1365-246X.1977.tb01325.x>
- SMU Node of National Geothermal Data System (n.d.) SMU Heat Flow Database from BHT Data, <http://geothermal.smu.edu/static/DownloadFilesButtonPage.htm>. Accessed 10 Jun 2019
- Spector A, Grant FS (1970) Statistical models for interpreting aeromagnetic data. *Geophysics* 35(2):293–302. <https://doi.org/10.1190/1.1440092>
- Tanaka A, Okubo Y, Matsubayashi O (1999) Curie point depth based on spectrum analysis of the magnetic anomaly data in East and Southeast Asia. *Tectonophysics* 306(3–4):461–470. [https://doi.org/10.1016/S0040-1951\(99\)00072-4](https://doi.org/10.1016/S0040-1951(99)00072-4)
- The MathWorks Inc (2020) MATLAB version 9.8.0.1451342 (R2020a Update 5). Natick, Massachusetts.
- Wang J, Li C-F (2015) Crustal magmatism and lithospheric geothermal state of western North America and their implications for a magnetic mantle. *Tectonophysics* 638:112–125. <https://doi.org/10.1016/j.tecto.2014.11.002>
- Wang J, Li C-F (2018) Curie point depths in Northeast China and their geothermal implications for the Songliao Basin. *J Asian Earth Sci* 163:177–193. <https://doi.org/10.1016/j.jseas.2018.05.026>

Publisher's note Springer Nature remains neutral with regard to jurisdictional claims in published maps and institutional affiliations.

5.2 Analysis of the relation between bottom hole temperature data and Curie temperature depth to calculate geothermal gradient and heat flow in Coahuila, Mexico.

(Published paper at *Tectonophysics* journal)



Analysis of the relation between bottom hole temperature data and Curie temperature depth to calculate geothermal gradient and heat flow in Coahuila, Mexico



Juan Luis Carrillo-de la Cruz^{a,b,*}, Rosa María Prol-Ledesma^b, Darío Gómez-Rodríguez^c, Augusto Antonio Rodríguez-Díaz^b

^a Posgrado en Ciencias de la Tierra, Instituto de Geofísica, Universidad Nacional Autónoma de México, Circuito interior s/n, Coyoacán, 04510 Ciudad de México, Mexico

^b Instituto de Geofísica, Universidad Nacional Autónoma de México, Circuito interior s/n, Coyoacán, 04510 Ciudad de México, Mexico

^c División Académica de Ciencias Básicas, Universidad Jardín Autónoma de Tabasco, Carretera Cunduacán-Jalpa km. 1, 86690, Tabasco, Mexico

ARTICLE INFO

Keywords:

Geothermal gradient
Heat flow
Aeromagnetic data
Curie temperature depth

ABSTRACT

Estimations of the Curie temperature depth using aeromagnetic data are commonly employed to study the thermal structure of the crust. In this research, we estimated the Curie temperature-depth with the "de-fractal" method and calculated the geothermal gradient and the heat flow of 24 blocks uniformly distributed in the Mexican state of Coahuila. The reliability of the "de-fractal" method was evaluated by comparing the geothermal gradient results with the Bottom Hole Temperature data available from petroleum boreholes. The maps show that the regional faulting is associated with recent volcanism characterized by shallow Curie temperature-depth (~17 km); furthermore, changes of the fractal parameter have a relationship to the tectonic history of this region and the geology of each analyzed block. The results of our statistical analyses showed that the geothermal gradient estimated with the "de-fractal" method is more closely related to the Bottom Hole Temperature data than the estimations obtained with the "centroid" method. Additionally, the similarity between Bottom hole temperature and Curie temperature-depth calculated geothermal gradient indicated that conduction is the predominant heat transfer mechanism.

1. Introduction

Studies of the thermal state of the Earth's crust are useful in geothermal exploration, hydrocarbon maturity, or tectonics. Several studies compute the depth to the bottom of magnetic sources (DBMS), commonly interpreted as Curie temperature-depth (CTD), to study the thermal state of the Earth. DBMS or CTD is useful as an estimation of temperature at depth, especially in regions where no temperature logs from boreholes are available due to drilling costs, scattering, reliability, temperature stability time, or other reasons, etc.

The DBMS is computed by the spectral analysis of magnetic anomalies using the power spectrum peak (Bhattacharyya and Leu, 1975; Blakely, 1988; Connard et al., 1983; Shuey et al., 1977; Spector and Grant, 1970), the centroid method (Okubo et al., 1985; Tanaka et al., 1999), the forward modeling of the power spectrum peak (Ravat, 2004; Finn and Ravat, 2004; Ross et al., 2006), or the approach that is based on the fractal behavior of the magnetization (Bansal et al., 2011;

Bouligand et al., 2009; Li et al., 2013; Maus and Dimri, 1995; Pilkington and Todoeschuk, 1993; Salem et al., 2014). These methods use the long wavelengths part of the magnetic anomalies that are assumed to be related to the deep magnetic sources, consequently, the spectral analysis must be applied to large windows to consider the magnetic signals that are related with the rocks of the deep crust (Ross et al., 2006).

This study calculates the CTD in Coahuila, Mexico, by the spectral analysis of magnetic anomalies using a fractal approach. CTD is used to calculate the geothermal gradient and to estimate the heat flow assuming conduction as the main mechanism of heat transfer. Finally, we compared our CTD results with the Bottom Hole Temperature (BHT) data and performed statistical analyses of the geothermal gradient and the heat flow values obtained with the CTD results and the temperature measurements.

* Corresponding author at: Posgrado en Ciencias de la Tierra, Instituto de Geofísica, Universidad Nacional Autónoma de México, Circuito interior s/n, Coyoacán, 04510 Ciudad de México, Mexico.

E-mail address: juanluiscc9@comunidad.unam.mx (J.L.C.-d. la Cruz).

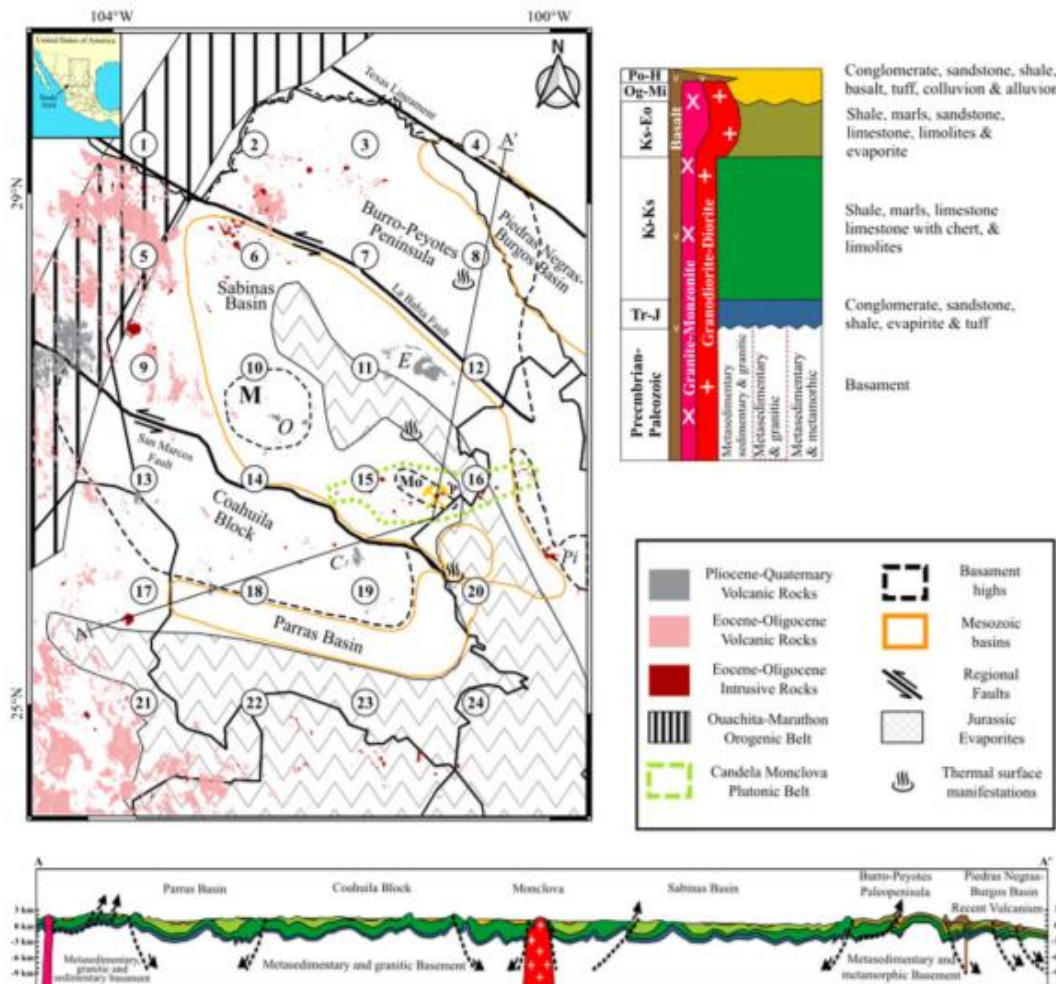


Fig. 1. Main tectonic features and recent volcanism of the study area. C = Las Coloradas Volcanic Field, E = La Esperanza Volcanic Field, M = La Mula Island, Mo = Monclova Island, O = Ocampo Volcanic Field, P = Panuco Mine, Pi = Sierra Picachos (modified from Chávez-Cabello, 2005; García-Alonso et al., 2011). White circles are the centers of the windows for which CPD are calculated from magnetic anomalies and their number denote the window number (see Table 1).

2. Geological framework

The study area is the Mexican state of Coahuila, northeastern of Mexico. This zone comprises a Mesozoic sequence of deformed sedimentary rocks deposited over a Paleozoic-Precambrian metamorphic and Paleozoic-Mesozoic intrusive rocks basement. Additionally, the main faults control the structural boundaries between blocks (Fig. 1).

The Ouachita-Marathon Orogeny (Permian-Triassic) and the rifting processes in the supercontinent Pangea (Late Triassic and Middle Jurassic), associated with the opening of the Gulf of Mexico, control the structural configuration, stratigraphy, and paleogeographic patterns of northeastern Mexico (Alemán-Gallardo et al., 2019; Anderson and Schmidt, 1983; Goldhammer, 1999; Salvador and Green, 1980; Wilson, 1990; Winkler and Buffler, 1988).

The basement uplifts of the Coahuila Block, Burro-Peyotes Peninsula, La Mula Island, and Monclova Island were formed during a rifting stage (Goldhammer, 1999) and are bounded by the Sabinas and Parras basins (Eguiluz de Antuñano, 2001). Permian-Triassic granitic-granodioritic rocks intrude the Proterozoic basement in the Coahuila block, the Upper Paleozoic basement in the Burro-Peyotes Peninsula mainly consists of metasedimentary rocks. The San Marcos and La

Babia sinistral strike-slip faults delimited these two basement uplifts (Fig. 1) (Anderson and Schmidt, 1983; Charleston, 1981; Chávez-Cabello, 2005; López et al., 2001; Wilson et al., 1984).

The basement in the Sabinas Basin is divided by Albarrán et al. (2011) into three units: the first unit is formed by Precambrian gneiss rocks intruded by diorites, the second unit is associated with Early Paleozoic metamorphic rocks (schist and metasediments) and the third unit is formed by Late Paleozoic granitic-granodioritic rocks intruded by dioritic dikes of possible Tertiary age. In addition, inside of the Sabinas Basin, Permian-Triassic granitic rocks intrude La Mula Island and Monclova Island uplifts (Jones et al., 1984; Wilson, 1990).

The sedimentary cover in the study area is very complex and has different stages, starting at Early Jurassic, in the rifting stage, with significant thickness of the Huizachal Group red beds that varies in thickness from few meters to > 1000 m (Eguiluz de Antuñano, 2001; Fastovsky et al., 2005; Goldhammer, 1999; Rueda-Gaxiola et al., 1999). During Jurassic, the structural framework supplied the conditions to deposit the Minas Viejas and Olvido evaporitic formations with little influence of volcanic deposits, over the red beds and the basement. Later, the Casita, Caja, and Pimienta formations, mainly composed of sandstones and biopelites, were deposited on the top of the evaporites

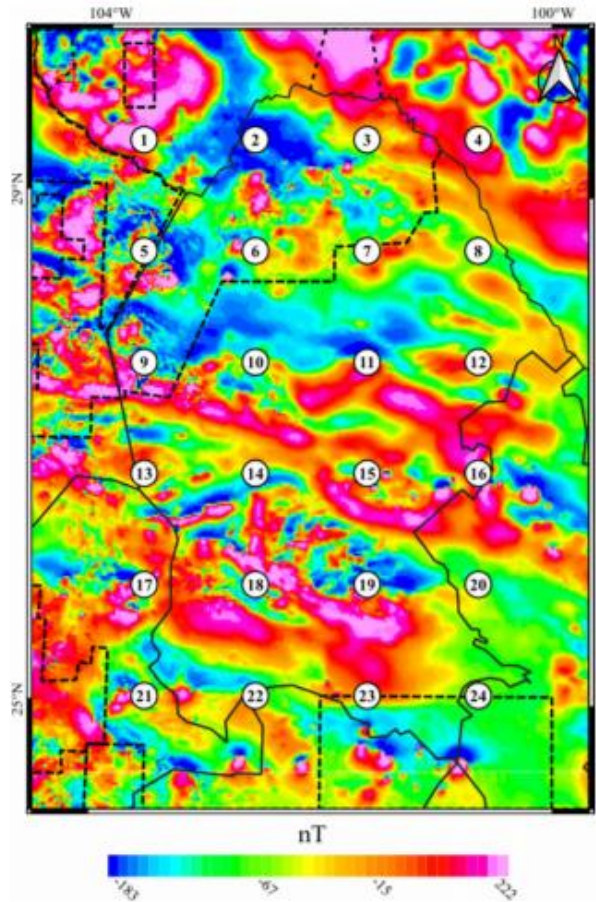


Fig. 2. Anomalies of the Earth's total magnetic field referred to an altitude of 305 m above terrain. Black lines denote state boundaries and dashed lines are different magnetic surveys. Window centers notation as in Fig. 1.

(Eguiluz de Antuñano, 2001; García-Alonso et al., 2011; Goldhammer, 1999).

During the Early Cretaceous, the deposits of different types of sediments were controlled by the end of the Gulf of Mexico opening. Thick marine platform carbonate deposits that belong to the Menchaca formation (carbonates and pelites) were identified in the central part of the Sabinas Basin. At the edge of the Coahuila Block, the red-beds of San Marcos Formation, the coral reefs (Hauterivian-Aptian) of the Cupido formation, the Lower Tamaulipas formation, and the sabkha of La Virgen Evaporitic formation are located (Eguiluz de Antuñano, 2001; García-Alonso et al., 2011; Goldhammer, 1999). During the Middle Cretaceous, pelites and micritic limestone of the La Peña and the Las Uvas Formations were deposited. After that, the Aurora Formation (platform carbonates), the Tamaulipas Superior, the Kiamichi, and the Georgetown Formations (limestone and pelites) were accumulated at the edge of the Coahuila Block. Upper Cretaceous formations are affected by the Laramide orogenesis with the accumulation of thick clastic series (La Difunta Group) with coal lens deposited in deltas and alluvial plains (García-Alonso et al., 2011; Goldhammer, 1999). According to González-Sánchez et al. (2007), the sedimentary thickness varies from ~3500 to ~4000 m in the Burro-Peyotes Peninsula and Coahuila block, and reaches about 5000 m in La Mula Island, and > 5000 m inside of the Coahuila Basin.

The Neogene is not well characterized because most sediments of this age were eroded, and Mesozoic formations are outcropping.

Nevertheless, recent volcanism and plutonism are present in some parts of the study area and an igneous suite is associated to magmatic activity of the alkaline province of northeast Mexico, Sierra Madre Occidental province and Trans-Pecos province of southwest Texas (Aranda-Gómez et al., 2005; James and Henry, 1991). Andesites, ignimbrites, rhyolites, and rhyodacite are the rocks related to the Sierra Madre Occidental in the western part of the study area (labeled in Fig. 1 as Eocene-Oligocene). The migration of the magmatic arc, caused by the variation in the subduction angle of the Farallon Plate in the Tertiary, formed these rocks. The youngest volcanic rocks related to the subduction of the Farallon plate have isotopic ages of 32.56 ± 0.08 Ma (Chávez-Cabello, 2005).

The recent igneous rocks in the study area are: the Candelaria-Monclova plutonic belt (monzodiorite, monzonite and quartz monzodiorite) with ages between 45 and 39 My, the Sierra Picachos intrusive rocks (syenite, gabbro, pyroxenite and basalt) emplaced in a basement uplift with estimated age below 30 My, and the laccolithic emplacement of La Cueva (quartz monzonite, syenite and gabbro) (Chávez-Cabello, 2005). Moreover, three main volcanic fields are found in Coahuila: (a) the La Esperanza volcanic field located in the Sabinas Basin, (b) the Ocampo volcanic field at the center of the state, and (c) the Las Coloradas volcanic field near the San Marcos Fault.

The basalt and hawaiite lava flow of the La Esperanza and the Ocampo volcanic fields, which were dated as Pliocene-Quaternary age, have relationship with intraplate volcanism. The andesites and basalts from the Las Coloradas volcanic field also have intraplate volcanism signature (Aranda-Gómez et al., 2005; Chávez-Cabello, 2005; Valdez-Moreno, 2001). An Eocene stock of variable composition (diorite, syenite, monzonite and granite), probably associated with recent volcanism, is located within the Sabinas basin in the Panuco mine (Fuentes-Guzmán, 2016).

3. Data

3.1. Magnetic data

From potential theory, it is known that the magnetic sources in the deep crust causes anomalies in the Earth's total magnetic field of large wavelength. Hence, this requires the analysis of data that covers a sufficient wide area. Usually, aeromagnetic surveys are not performed to cover wide continental areas, for this reason, it is necessary to compile different aeromagnetic surveys. In this study, we analyzed data from the Magnetic Anomaly Map of North America (Fig. 2). The Magnetic Anomaly Map of North America is the result of a compilation accomplished by the North America Magnetic Anomaly Group (NAMAG, 2002) that includes data from Canada (Geological Survey of Canada), Mexico (Consejo de Recursos Minerales, now Mexican Geological Survey) and United States (United States Geological Survey). NAMAG data have already been used in regional spectral analyses done by Bouligand et al. (2009), Manea and Manea (2011), Ravat et al. (2016) and Campos-Enriquez et al. (2019).

The data grid has 1-km spacing and is adapted to the Decade of North American Geology projection (DNAG). Before map compilation, the single data set where continued either upwards or downwards to a common level of 305 m above the terrain. In addition, to avoid wavelengths larger than 500 km, magnetic data from CHAMP satellite were used to corrected the joined data (more details in NAMAG, 2002). In general, it is possible to find artifacts caused by the merging of different surveys (Bouligand et al., 2009). As far as possible, such artifacts were avoided by the data processing scheme implemented by the NAMAG group. Nevertheless, it is important to take special caution in the windows that overlap different surveys.

3.2. Borehole data

The borehole data used in this study were published by Prol-Ledesma

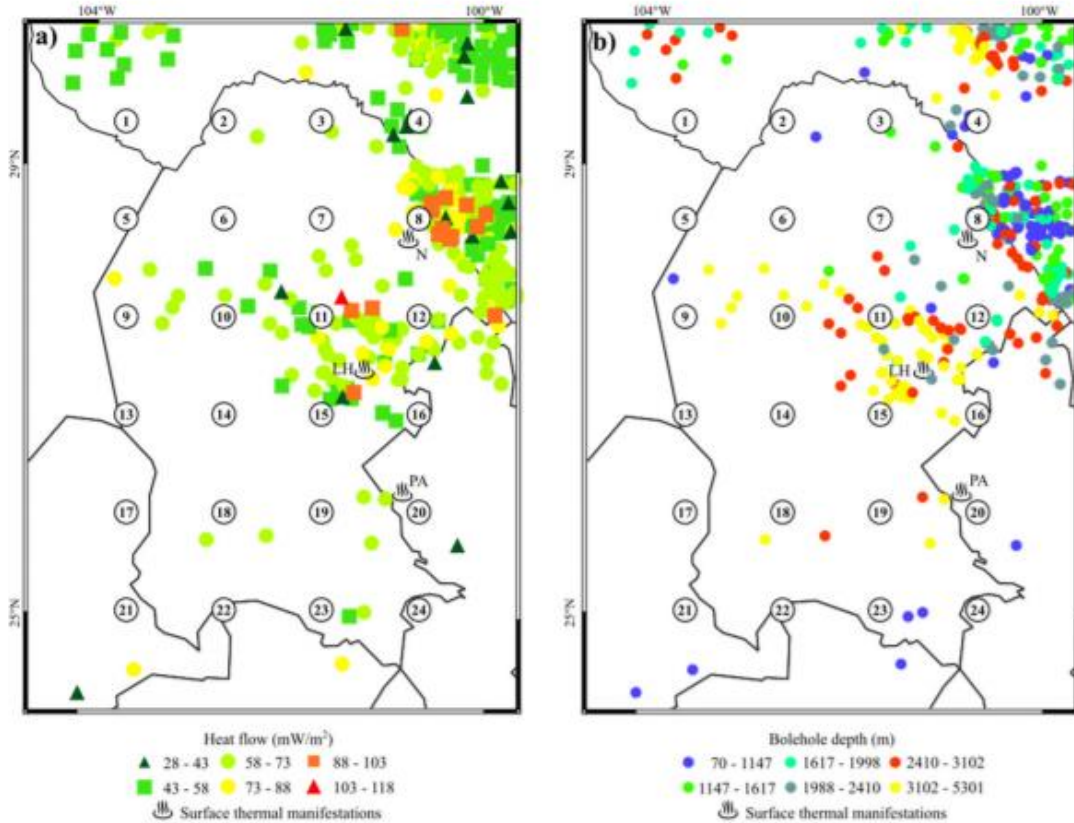


Fig. 3. a) Heat Flow data calculated from BHT and thermal surface manifestations. b) Depth of the boreholes. Window centers and state boundaries as in Fig. 2. LA = Las Hermanas, PA = El Paredon-Azufrosa, N = Navas.

et al. (2018) and by the Heat Flow Observation in Content Model Format (SMU Node of National Geothermal Data). This dataset consists of 1468 Bottom-Hole Temperature data corrected by the Harrison method (Harrison et al., 1983), thermal conductivities, and heat flow values. For this study, we retrieved all available data on the geothermal gradient, the thermal conductivity, and the heat flow data that were located in the Sabinas Basin, the Piedras Negras-Burgos Basin and the Burro Peyotes Peninsula from the database. The boreholes depth varies between 70 and 5231 m. The approximate depth of the sedimentary cover fluctuates from ~3500 m (Burro-Peyotes peninsula and Coahuila block) up to ~5000 m (Sabinas Basin); consequently, only some of the deepest boreholes reach the basement. Las Hermanas (50 °C) and El Paredón-La Azufrosa (68 °C) hot springs, and Navas (42 °C) shallow hot well are identified in the study area as surface thermal manifestations, Las Hermanas and Navas are nearby heat flow values from 73 to 88 mW m⁻² and El Paredón-La Azufrosa from 58 to 73 mW m⁻² (Fig. 3).

4. Methodology

Thermal anomalies at-depth can affect the magnetization of the rocks, and, thus, the magnetic anomalies observed at the surface. Spector and Grant (1970) determined the depth of magnetic discontinuities using spectral analysis, assuming random and uncorrelated magnetic sources. Numerous authors have used the same assumptions to associate the depth to the magnetic discontinuity directly to the CTD (Bhattacharyya and Leu, 1975; Blakely, 1988; Okubo et al., 1985; Ravat et al., 2007; Ross et al., 2006; Tanaka et al., 1999).

The Curie Temperature (CT), discovered by Pierre Curie, is defined

as the temperature where magnetic materials lose their magnetic properties. The association of the DBMS with the CTD allows estimation of the thermal state of the crust and inferring the tectonic implications, nevertheless, the DBMS may be a lithological contact because magnetic rocks (e.g. volcanic rocks) are overlying non-magnetic rocks (e.g. limestone). Frequently, this method has been uncritically applied because acquiring thermal data for regional studies is complicated and expensive. CT varies depending on the magnetic mineral association in the rocks, being magnetite the most abundant ferromagnetic mineral in the crust and its CT (~580 °C) is commonly used as the reference temperature to calculate the geothermal gradient. Ravat et al. (2007) performed a detailed study regarding the different methodologies used in the calculation of the DBMS. They found two main approaches: the spectral peak and the centroid method (Bhattacharyya and Leu, 1975; Blakely, 1988; Connard et al., 1983; Shuey et al., 1977; Spector and Grant, 1970) with the adaptations developed by Okubo et al. (1985) and Tanaka et al. (1999).

Recent studies were directed to ascertaining that the magnetization has a fractal behavior, and it is necessary to apply power-law corrections to calculate the DBMS (Andrés et al., 2018; Bansal et al., 2011; Bouligand et al., 2009; Khojamli et al., 2017; Li et al., 2013; Li et al., 2017; Martos et al., 2017; Martos et al., 2018; Salem et al., 2014). After reviewing the different methods, this study uses the de-fractal method (Salem et al., 2014) that considers the fractal behavior of the magnetization.

4.1. The centroid approach

The calculation of the DBMS using the centroid approach is

performed using the power-density spectrum $P(k_x, k_y)$ of the observed magnetic field (Okubo et al., 1985; Tanaka et al., 1999), assuming an infinite horizontal layer and that the magnetization is a random function of x and y , defined as:

$$P(k_x, k_y) = 4\pi^2 C_m^2 \phi_m |\Theta_m|^2 |\Theta_f|^2 e^{-2kZ_t} (1 - e^{-k(Z_b - Z_t)})^2 \quad (1)$$

k_x and k_y are the wavenumber in x - and y -direction, C_m is a proportionality constant, ϕ_m is the power spectrum of the magnetization, Θ_m is the directional factor related to the magnetization, Θ_f is the directional factor related to the geomagnetic field, Z_t is the depth to the top of the magnetic source and Z_b is the DBMS (Blakely, 1995; Tanaka et al., 1999). When the magnetization is random and uncorrelated, the ϕ_m is constant, thus, the annular averaging of Eq. (1) is written as:

$$P(k) = Ae^{-2kZ_t} (1 - e^{-k(Z_b - Z_t)})^2 \quad (2)$$

with A being a constant. For wavelengths less than about twice the layer thickness and the top of magnetic source dominating the power spectrum (Bhattacharyya and Leu, 1975; Okubo et al., 1985; Spector and Grant, 1970; Tanaka et al., 1999), Eq. (2) can be written as:

$$\ln[P(k)] = \ln A - 2kZ_t \quad (3)$$

For calculating the centroid of the magnetic source (Z_0), Eq. (2) transforms to:

$$P(k) = Be^{-2kZ_0} (e^{-k(Z_t - Z_0)} - e^{-k(Z_b - Z_0)})^2 \quad (4)$$

with B being a constant. The simplification of Eq. (4) to compute Z_0 is (Bhattacharyya and Leu, 1975; Okubo et al., 1985; Tanaka et al., 1999) is:

$$\ln[P(k)/k^2] = \ln B - 2kZ_0 \quad (5)$$

Eqs. (3) and (5) are linear equations; therefore, to compute Z_t and Z_0 is necessary to calculate the slope of the straight line using the high- and low-wavenumbers respectively. DBMS (Z_b) is calculated by using the approach after Okubo et al. (1985):

$$Z_b = 2Z_0 - Z_t \quad (6)$$

The uncertainties in the estimations of the DBMS are calculated after Martos et al. (2017):

$$\Delta Z_b = \sqrt{4\Delta Z_0^2 + \Delta Z_t^2} \quad (7)$$

where ΔZ_b , ΔZ_0 , and ΔZ_t are the uncertainties of Z_b , Z_0 , and Z_t respectively. The uncertainties of Z_0 and Z_t are calculated using the method proposed by Okubo and Matsunaga (1994):

$$\epsilon = \frac{\sigma_r}{k_2 - k_1} \quad (8)$$

where ϵ is the uncertainty, σ_r is the standard deviation of the radial power spectrum and the slope derived by the linear fit, and $k_2 - k_1$ is the wavenumber range used to calculate the slope. These uncertainties are always $< 15\%$ (Okubo and Matsunaga, 1994).

4.2. Forward modeling of the spectral peak

This method calculates the depth of Z_t and Z_b using an iterative matching of the observed power spectrum and the synthetic power spectrum derived by the forward modeling of Eq. (2). Forward modeling is applied only where the power spectrum has a spectral peak (Ravat, 2004; Finn and Ravat, 2004; Ross et al., 2006). From Eq. (2), the constant A is independent of depth and can be used to adjust the modeled power spectrum with the observed power spectrum. Meanwhile, Z_b adjusts the position of the spectral peak at low-wavenumbers, and Z_t controls the slope at high-wavenumbers. The combination of Z_t and Z_b controls the slope immediately next to the spectrum peak (Ravat et al., 2007).

4.3. De-fractal method

The first studies on the fractal behavior of magnetization, mainly in magnetic maps, were made by Maus and Dimri (1994, 1995) and Pilkington and Todoeschuk (1993). The first work to propose a theoretical power spectrum due to a slab with a fractal behavior of magnetization was published by Maus et al. (1997). Nevertheless, the fractal approach in DBMS calculation was not commonly used until Bouligand et al. (2009) published it. They solved analytically the radially averaged power spectrum for a fractal behavior of the magnetization and could determine three essential parameters: depth to the top and thickness of the magnetic source, and the fractal magnetization parameter, based on the shape of the radially averaged power spectrum. Subsequently, Bansal et al. (2011) developed the modified centroid method based on the fractal distributions of the magnetic sources following the relation

$$\phi_m \propto k^{-\beta} \quad (9)$$

From Eq. (9), Salem et al. (2014) determined that the random magnetization power spectrum is equivalent to the observed power spectrum multiplied by k^α when the fractal magnetization is constant in the z -direction, that is:

$$P_R(k) = P_F(k)k^\alpha \quad (10)$$

where k is the radial wavenumber, $P_F(k)$ the observed power spectrum, $P_R(k)$ the power spectrum due to the random magnetization model and α the fractal parameter related to β by $\alpha = \beta - 1$. The advantages of this method are the integration of the spectral peak and the centroid methods in a corrected power spectrum by fractal sources. The method calculates the fractal parameter as well as the top and the depth of the magnetic sources in an iterative process. Evaluation of Z_t , Z_b , and α values requires the visual inspection and calculation of the misfit between the observed power spectrum and the synthetic power spectrum (Fig. 4). To calculate the misfit R we applied the following relation:

$$R = \sqrt{\frac{1}{n} \sum_{i=1}^n (P_R(k_i) - P_{syn}(k_i))^2} \quad (11)$$

where $P_R(k)$ is the observed power spectrum, and $P_{syn}(k)$ is the synthetic power spectrum (both spectra are represented by n sampling points). However, a note of caution must be added because highest values of α could overcorrect the spectrum.

The radially averaged power spectrum was calculated using the Fast Fourier Transform (FFT) that is applied to magnetic data from windows of size of 180×180 km with a 50% overlap between adjacent windows and 100% of data coverage in every block. The edges need to be

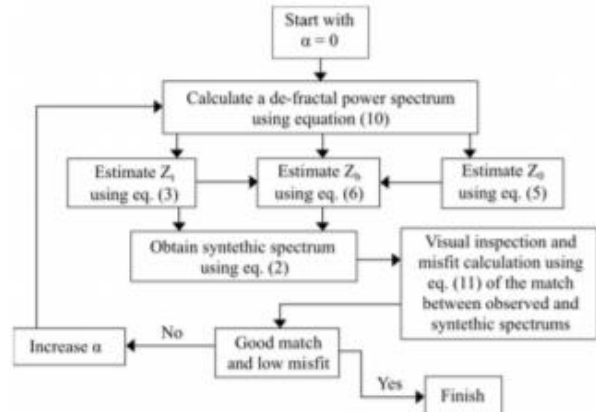


Fig. 4. Flowchart diagram to follow the steps in the processing used in this study (modified from Salem et al., 2014; Martos et al., 2017).

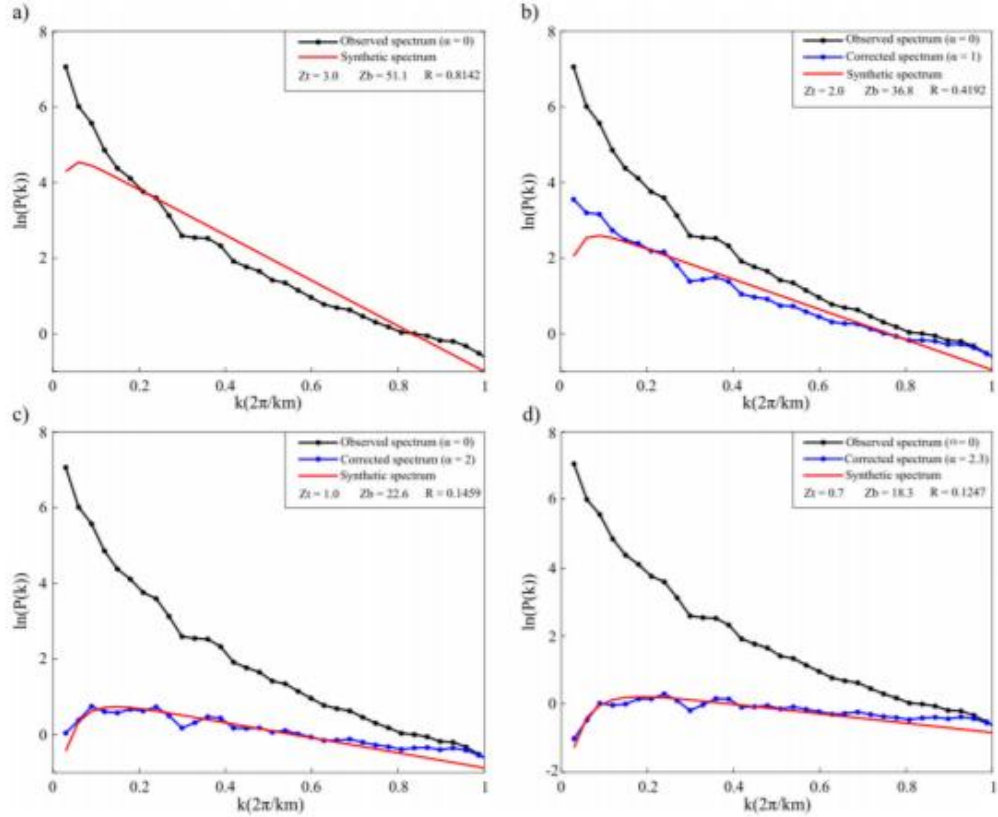


Fig. 5. Calculation of DBMS for the window 16. a) $\alpha = 0$, b) $\alpha = 1$, c) $\alpha = 2$ and d) $\alpha = 2.3$. These figures show the visual change and the misfit obtained for different values of α .

continuous in order to apply the FFT. For this reason, a first-order trend is removed in the data and the grid is expanded 10% using the maximum entropy method (Bansal et al., 2011). The selection of the related slopes and the fractal parameter is performed according to the flowchart diagram (Fig. 4) to obtain the Z_b , Z_t and α values (Fig. 5). In this work, we also calculated the DBMS using the method developed by Tanaka et al. (1999) to compare the results with those derived from the fractal correction.

4.4. Heat flow calculations

Considering conduction as the main mechanism of heat transfer, CTD can be used to estimate the geothermal gradient and the heat flow if the calculated DBMS is a thermal boundary and not a lithological boundary (e.g. magnetized rocks over non-magnetic rocks). The heat flow is obtained using the Fourier's Law (λ : thermal conductivity), expressed by:

$$q(z) = \lambda \frac{\partial T(z)}{\partial z} \quad (12)$$

Eq. (12) can be solved assuming that Z_b (DBMS) is related with the CTD, T_c is the Curie temperature, and T_0 is the temperature at the surface (Martos et al., 2017); therefore, the heat flow is calculated using:

$$q_z = \frac{\lambda(T_c - T_0)}{Z_b} + H_0 h_r - \frac{H_0 h_r^2}{Z_b} (1 - e^{(-Z_b/h_r)}) \quad (13)$$

where λ is the thermal conductivity, H_0 is the radiogenic heat production and h_r is a length scaling for H_0 decreasing with depth.

To calculate the heat flow, we assume a Curie temperature of 580 °C according to the basement studies in the Sabinas Basin that show magnetite to be the dominant magnetic mineral in the rocks (Albarrán et al., 2011) and ~20 °C for the mean surface temperature T_0 of the study area. The thermal conductivity value used in the calculation is an average value calculated from all boreholes in each window. In addition, the heat flow is calculated using an averaged thermal conductivity (2.2 W/mK). Concerning h_r , the used value is 10 km as suggested by Turcotte and Schubert (2002). We examined the concentrations of K, U, and Th from the geochemical analysis from diverse intrusive and metamorphic analogous rocks: granites, tonalites, granodiorites, monzonites, gneisses and schists to determine the radiogenic heat production of the basement rocks (Alemán-Gallardo et al., 2019; Fuentes-Guzmán, 2016; Lawlor et al., 1999; Torres-Sánchez, 2015). Geochemical analyses are available for the Huiznopalna Gneiss, Panuco intrusive rocks and Tamaulipas Paleozoic Metamorphic complex. The maximum value calculated for radiogenic heat production is related with the youngest intrusive rocks (average value 0.99 μW/m³), while the Paleozoic and Precambrian rocks have lower values (average value 0.17 and 0.22 μW/m³ respectively).

4.5. Statistical methods and mapping

Temperature data obtained from boreholes are used to validate the CTD estimations by testing statistically (*t*-student test) if the geothermal gradient population means are similar. This method is effective because numerous studies show that the *t* student method is robust to withstand non-normality and some inequality of variances. It is fundamental to compare the variances for the two data sets to find the particular *t*-

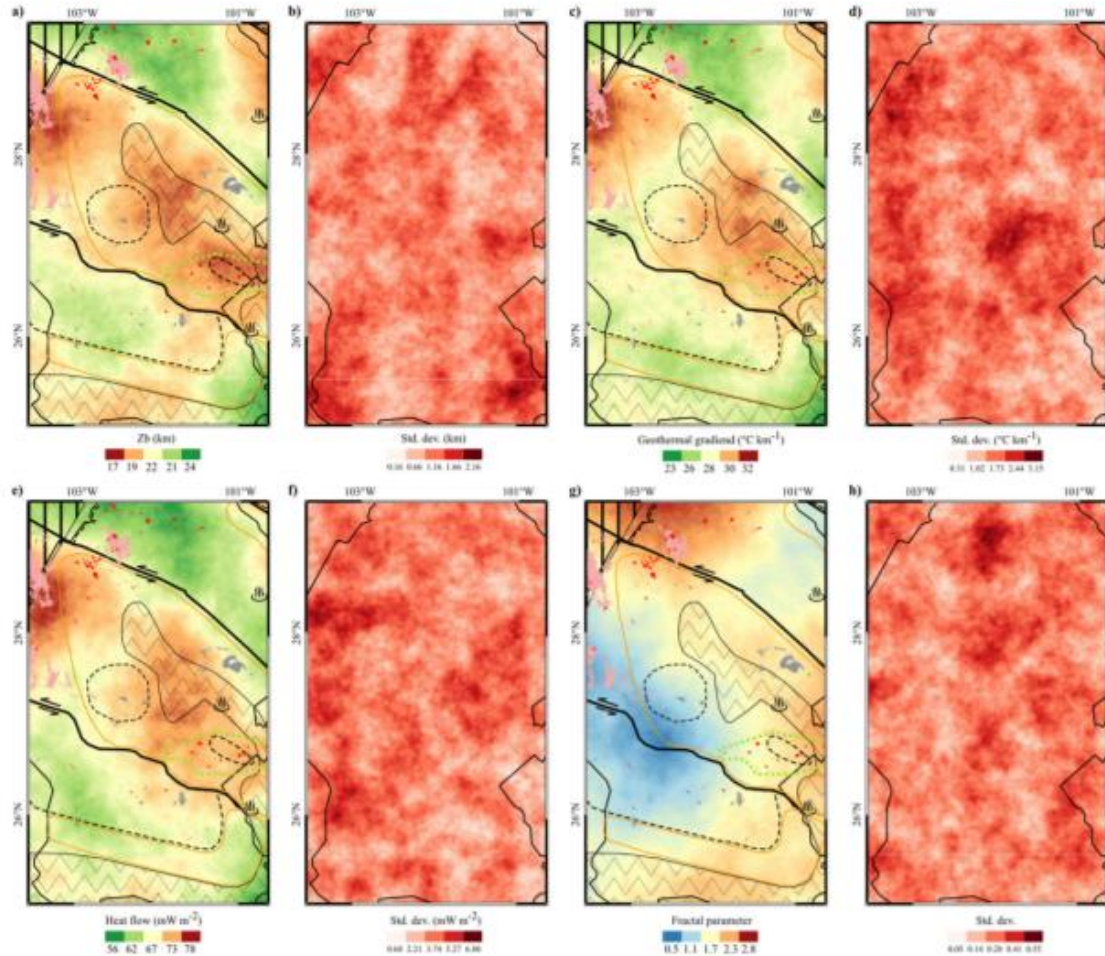


Fig. 6. Results of the SGSIM and their standard deviation for: DBMS (a,b), geothermal gradient (c,d), heat flow (e,f), and fractal parameter (g,h). Surface thermal manifestations, geological and tectonics features are from Fig. 1.

student test to be used (Zar, 2010). The statistical analysis was performed using *t*-student test with variance equality for geothermal gradient and Welch approximation for heat flow.

The CTD was calculated for 24 blocks. Considering that the CTD calculation is an average for the entire window, is necessary to calculate also the average values of the geothermal gradient, heat flow, and thermal conductivity for the boreholes inside each window in order to compare the data obtained using the spectral analysis with the borehole data.

The DBMS, geothermal gradient, heat flow and fractal parameter were mapped using the Sequential Gaussian Simulation (SGSIM) following the algorithm described by Pyrcz and Deutsch (2014) and using the Geostatistical modules provided by ArcGIS®. Application of the method requires: (i) Data transformation to a normal distribution (normal score transformation), (ii) calculation and modeling the variogram, (iii) generation of the simple kriging layer to apply the SGSIM, the back transformation of the data was carried out automatically by the module, (iv) application of the conditioned SGSIM algorithm, with a 1.5 km pixel size, using the simple kriging layer; and (v) displaying the mean and standard deviation maps of all simulated layers. This method solves some of the issues related to the underpredicted high values or overpredicted low values caused by the conditional bias of kriging.

5. Results

Fig. 6 presents the DBMS, geothermal gradient, heat flow, and fractal parameter maps obtained using the SGSIM. The standard deviation of these maps are presented showing the places where the simulation is more reliable and where it has large variations. The DBMS in the study area varies from 24 to 17 km, which yields geothermal gradients from 24 to 33 °C/km and surface heat flow from 57 to 90 mW/m². In addition, the calculated surface heat flow using an averaged thermal conductivity value yields results from 57 to 76 mW/m² (Fig. 6 and Table 1). The shallowest DBMS values and, hence, highest geothermal gradient and heat flow values are in zones with young volcanic rocks in the northwest of Coahuila and in the Sabinas Basin. These regions are associated with the two main tectonic features in the study zone: La Babia and San Marcos faults. Albarrán et al. (2011) interpreted that the continental crust close to these faults is highly fractured, enabling the intraplate volcanism, while the western volcanic rocks are more related to the volcanic events of the Sierra Madre Occidental (Fig. 6 a,c,e). Finally, the fractal parameter of the magnetization varies between 0.5 and 2.7 and its distribution is apparently related with the different geological units (Fig. 6g and Table 1).

The results from the *t*-student test are in the Table 2. The global

Table 1

Estimated values of fractal parameter (α), Depth to the bottom of magnetic source (DBMS), Geothermal Gradient (GG) and Surface Heat Flow (HF) calculated using the DBMS value and a Curie Temperature of 580 °C and surface temperature of 20 °C. HF^a is for heat flow calculated using the thermal conductivity reported from the boreholes and HF^b is for heat flow calculated using an averaged value of the rock conductivity.

Window number	α	DBMS (km)	GG (°C/km)	HF ^a (mW/m ²)	HF ^b (mW/m ²)
1	2.30	22	26	63	61
2	2.70	24	24	61	57
3	2.20	22	26	60	61
4	1.20	18	31	70	72
5	1.40	17	33	78	76
6	1.90	19	30	70	69
7	1.50	23	25	60	59
8	1.60	19	30	67	69
9	0.70	19	29	70	68
10	1.60	21	27	64	64
11	1.90	17	33	76	76
12	1.98	23	25	57	59
13	1.00	21	27	64	64
14	0.50	20	29	67	67
15	1.50	19	30	70	70
16	2.30	18	31	71	72
17	1.40	20	29	67	70
18	1.40	22	26	61	61
19	1.80	20	28	67	67
20	1.80	21	27	64	64
21	1.50	21	27	90	64
22	1.90	19	30	86	70
23	2.00	20	28	74	66
24	1.60	24	24	64	57

average values of continental heat flow and geothermal gradient are 64.4 mW/m² and 25–30 °C/km (Davies, 2013; Fridleifsson et al., 2008) and our calculated results are consistent with these global averages for regions without recent tectonic activity. The difference between the geothermal gradient estimated by DBMS and geothermal gradient calculated using BHT is 0.06 and the p-value is 0.930. For the heat flow using the thermal conductivity from wells is 4.51 and 0.018, and the heat flow using a constant thermal conductivity is 1.90 and 0.166, respectively. The p-values shows the significance of the t-student test, that is, lower p-value is related with the no association of variables, while the p-value closest to 1 indicates association between variables. The hypothesis testing indicates that the BHT geothermal gradient and the DBMS geothermal gradient are strongly related. Fig. 7 displays the box plots for the analyzed data, showing that the DBMS heat flow is slightly higher than the BHT heat flow.

For every block, the differences in the geothermal gradient results and their error bars obtained for both, the de-fractal method and the BHT, are small (Fig. 8a). Instead, variations in the heat flow results (Fig. 8b) are associated with the lack of boreholes to characterize the window (e.g. 13, 17, 21, 22, 23, and 24) or the uncertainty in thermal conductivity at depth. The thermal conductivity derived from borehole information is only representative for the first thousand meters, hence, that might explain the differences between the information from borehole measurements and the DBMS calculations. Moreover, the averaged values corresponding to the windows 17 to 24 are less reliable

because the southern part of the study area does not have enough boreholes to give representative averaged values. The windows 21 and 22 present variations in the heat flow values due to the thermal conductivity, showing that high conductivity values affect substantially the results. Finally, Fig. 8c displays the differences between the DBMS calculated using the centroid method and the DBMS using the de-fractal method. The centroid method shows an overestimation of the DBMS in all windows; consequently, the DBMS calculations after a fractal correction are more realistic.

6. Discussion

The global average of the geothermal gradient is close to the value found for our study area. For this reason, it was necessary to use a window size of 180 × 180 km to consider the deepest magnetic sources. Otherwise, the calculated DBMS cannot be related with a reliable DBMS value. However, the use of large windows reduces the spatial resolution of derived information.

For the methodological point of view, we can see that the centroid method is reliable if the fractal parameter is close or equal to zero, nevertheless, this special case is not common. The results show that DBMS calculated by the de-fractal method yields are more reliable result than the DBMS calculated by the centroid method. Hence, the de-fractal DBMS values and the derived parameters (geothermal gradient and heat flow) are better suited for further interpretation. The Fig. 8c shows the comparison between de-fractal and centroid methods, where the overestimation in the DBMS values without fractal corrections is evident.

The results of the t-student test show a similarity, with a p-value of 0.9303, between the geothermal gradient obtained by the de-fractal method and the averaged BHT. The heat flow calculation was carried out by using the thermal conductivity of the boreholes or using an average value of thermal conductivity. For both cases, the p-values (0.018 and 0.166, respectively) are lower than the geothermal gradient. These variations could be due to the uncertainty in the thermal conductivity, because values of thermal conductivity from boreholes are only representative for at most the upper five kilometers (considering the deepest borehole), and the estimations derived from the DBMS are deeper than 16 km. In addition, Fig. 8b displays how the thermal conductivity could affect the heat flow estimations (mainly in the window 21 and 22), showing that in some cases is better the use of averaged thermal conductivity values. For this study, from the geochemical analysis of analogous rocks of the basement, we found that heat generation is too low (< 1 $\mu\text{W}/\text{m}^3$) to affect significantly the geothermal gradient and heat flow results.

The deviation of the fractal parameters from zero is well known from other studies (Andrés et al., 2018; Bansal et al., 2011; Bouligand et al., 2009; Khojamli et al., 2017; Li et al., 2013; Li et al., 2017; Martos et al., 2017; Martos et al., 2018; Maus and Dimri, 1995; Pilkington and Toddeschuck, 1993; Salem et al., 2014) and is caused by the structural (geological complexity) and physical (fractal behavior of magnetization) state of the crust. The fractal parameters in our study area is variable between 2.7 and 0.5. The highest values are observed close the Ouachita marathon orogeny and at the eastern part of the Sabinas basin. Meanwhile, the lowest values are distributed mainly in the Coahuila block, and less extended in the Burro-Peyotes peninsula and

Table 2

Results of the t-student test performed to compare the values obtained using BHT (red) and DBMS (blue) to calculate geothermal gradient and the corresponding heat flow (^a for thermal conductivity from wells and ^b for averaged thermal conductivity).

Geothermal gradient	Heat flow ^a		Heat flow ^b	
P-value	0.930		P-value	0.018
Mean	(28.17, 28.11)		Mean	(63.87, 68.38)
Mean difference	0.06		Mean difference	4.51
			P-value	0.166
			Mean	(63.87, 65.77)
			Mean difference	1.90

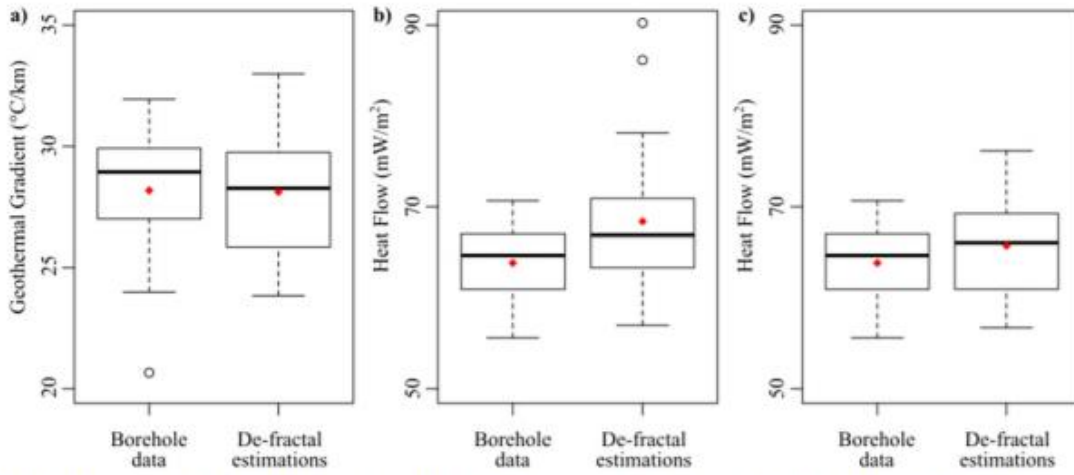


Fig. 7. Boxplots of a) geothermal gradient, b) heat flow calculated using the thermal conductivity from wells, and c) heat flow calculated using averaged thermal conductivity. Red dots denote the mean.

Piedras Negras-Burgos basin. This pattern of fractal parameters shows a striking correlation with the tectonic complexity of the study area. Fractal parameters above 2.3 are related with the remnants of the Ouachita-Marathon orogeny. Values between 1.3 and 2.3 for the fractal parameters show a correlation with the *syn-rift* sediments (influenced by evaporites) and the intraplate volcanism. Finally, values less 1.3 are apparently related with the basement uplifts and the absence of evaporitic rocks.

The anomalies displayed in the maps derived from the SGSIM (Fig. 6) show different tectonothermal processes of the study area. Heat flow values above 73 mW/m^2 in the eastern part of the Sabinas Basin are consistent with a Pliocene-Pleistocene tectonic disturbance that included extension process and volcanic activity associated with the alkaline province of northeast Mexico. The thermal anomalies mapped in the Sabinas basin by the SGSIM present a strict spatial relationship with the main faults of the basement that delimit the tectonic blocks (e.g. San Marcos and La Babia faults, Aranda-Gómez et al., 2005; Chávez-Cabello, 2005) and the basaltic type magmatism (e.g. Las Coloradas, La Esperanza and Ocampo volcanic fields, Aranda-Gómez et al., 2005). Additionally, the Eocene-Oligocene volcanic events related with the Sierra Madre Occidental in the northwest part of the study area, close to the window number 5, have a spatial distribution that coincide with the highest heat flow anomalies ($\sim 78 \text{ mW/m}^2$).

Sedimentary basins are significant to the heat flow distribution in the Sierra Madre Oriental, at the east of the study area, and Geo-preserved geothermal provinces, northeast of Mexico (Prol-Ledesma and Morán-Zenteno, 2019). Basement uplift and probably the regional groundwater movement control the heat flow patterns within the sedimentary basins (e.g. Paredón-La Azufrosa at the southeast of Coahuila, Alemán-Gallardo et al., 2019). Nevertheless, the groundwater movement has influence only in the shallow strata and the CPD estimations represent the behavior of the geothermal gradient at depths of $> 10 \text{ km}$. For this reason, mainly the tectonic framework controls the heat flow patterns estimated by the CPD (Fig. 6). For the Sabinas Basin, the emplacement of igneous rocks and the intraplate volcanism arises from La Babia and San Marcos faults are the mainly tectonic features that control the heat flow anomalies ($> 70 \text{ mW/m}^2$) in the study area (Albarrán et al., 2011; Aranda-Gómez et al., 2005). The SGSIM map marks these areas as zones of high values, supporting our results. Further availability of heat flow data from boreholes would aid in determining more precisely the average heat flow for each window to compare with the CPD estimations; however, the general heat flow pattern could not vary significantly.

7. Conclusions

In this study, we derived the depth to the bottom of the magnetic sources (or the Curie point depth) in Coahuila, Mexico. The applied method combines the two established methods, i.e. the centroid method and forward modeling of the spectral peak on a radially averaged power spectrum, after applying a power-law correction derived of the de-fractal method. Although, this study was conducted in a rather local area, some important conclusions can be derived with respect to the methodology and crustal state in this region.

- The DBMS calculated assuming random and uncorrelated magnetization model yields unrealistic values. Hence, power-law corrections are necessary to the application of the centroid method.
- For complex geological environments, fractal parameters must not be considered constant. The conducted study reveals a relationship between the fractal parameter and the geological framework. Fractal parameters higher than 2.3 found in areas that were affected by Ouachita-Marathon orogeny. Volcanic areas and regions of *syn-rift* sediments (mainly evaporites) have values between 2.3 and 1.3. Values < 1.3 are located in areas of basement uplifts and not influenced by evaporites.
- The geological history of the study zone allows to delimit the high heat flow areas. These anomalies are primarily demarcated by La Babia and San Marcos faults and are related with the recent volcanic activity.
- The statistical methods note that the geothermal gradients as calculated from the CPD and averaged BHT correlate. This is due to the predominance of conduction as a main heat transfer mechanism and the low heat generation rates. Although, the uncertainties associated with the thermal conductivity at-depth could cause the differences in the heat flow estimations.
- The analysis of aeromagnetic data to study the thermal structure of the crust is important to overcome the lack of borehole data; nevertheless, it is necessary to be careful with the DBMS estimations and their interpretation.

The findings of this study encourage a new, nation-wide calculation of the DBMS in Mexico, which seems feasible and worthwhile.

CRediT authorship contribution statement

Juan Luis Carrillo-de la Cruz: Methodology, Formal analysis, Data

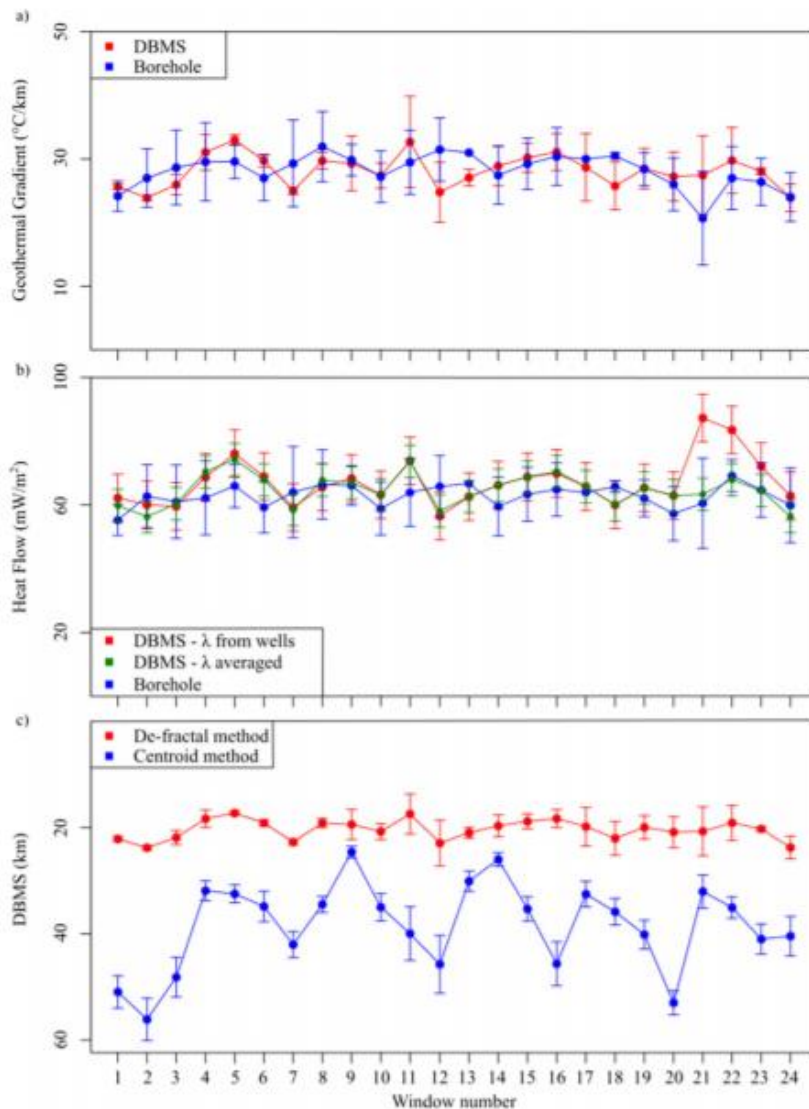


Fig. 8. Comparison between results obtained with de-fractal DBMS and BHT measured from wells: a) Geothermal gradient and b) Heat Flow. c) DBMS calculated using de-fractal and centroid method.

curation, Visualization, Writing - original draft. **Rosa María Pro-Ledesma:** Supervision, Conceptualization, Writing - review & editing. **Darío Gómez-Rodríguez:** Software, Data curation. **Augusto Antonio Rodríguez-Díaz:** Resources, Writing - review & editing.

Declaration of competing interest

The authors declare the following financial interests/personal relationships which may be considered as potential competing interests:

Acknowledgements

This work was supported by Fondo de Sustentabilidad Energética SENER-CONACyT CeMIE-Geo under Grant-Project P-01: Mapas de Gradiente Geotérmico y Flujo de Calor para la República Mexicana". Authors thank G. Gabriel, A. Bansal and V. Dimri for sharing the MATLAB codes to estimate the DBMS using the modified centroid

approach, these codes were the starting point for the new codes used in this work for the de-fractal approach. Also, we acknowledge the Manuscript Writing Training Team (CEMAI in Spanish) of CONACyT for their help with the English editing reviews and constructive criticism of the research paper and we thank to the QGIS contributors for distribute free the software used in the map creation. Finally, we thank Gerald Gabriel and two anonymous reviewers for the criticism of the work and their fruitful comments on the manuscript.

References

- Albarrán, J.J., González-Pineda, J.F., Muñoz-Cisneros, R., Rosales-Rodríguez, J., 2011. Actualización petrologica del basamento cristalino de la Cuenca de Sabina. Boletín de la Asociación Mexicana de Geólogos Petroleros 56 (1-2), 105-112.
 Alemán-Gallardo, E. A., Ramírez-Fernández, J. A., Rodríguez-Díaz, A. A.; Velasco-Tapia, F., Jenchen, U., Cruz-Gámez, E. M., De León-Barragán, Lorena, Navarro-De León, I. 2019. Evidence for an Ordovician continental arc in the pre-Mesozoic basement of the Huizachal-Peregrina Anticlinorium, Sierra Madre Oriental, Mexico: Peregrina Tonalite. Mineral. Petrol., 113 (4), 1-21. doi:<https://doi.org/10.1007/s00710-019-01107-w>

- 00660-4.
- Anderson, T.H., Schmidt, V.A., 1983. The evolution of Middle America and the Gulf of Mexico-Caribbean region during Mesozoic time. *GSA Bull.* 94 (8), 941–966. [https://doi.org/10.1130/0016-7606\(1983\)94<941:TEOMAA>2.0.CO;2](https://doi.org/10.1130/0016-7606(1983)94<941:TEOMAA>2.0.CO;2).
- Andrés, J., Marzáñ, I., Ayarza, P., Martí, D., Palomeras, L., Torné, M., Campbell, S., Carbonell, R., 2018. Curie point depth of the Iberian Peninsula and surrounding margins. A thermal and tectonic perspective of its evolution. *J. Geophys. Res. Solid Earth* 123 (3), 2049–2068. <https://doi.org/10.1002/2017JB014994>.
- Aranda-Gómez, J., Luhr, J.F., Housh, T.B., Valdez-Moreno, G., Chávez-Cabello, G., 2005. El volcanismo tipo intraplaca del Cenozoico tardío en el centro y norte de México: una revisión. *Bol. Soc. Geol. Mex.* 57 (3), 187–225. <https://doi.org/10.18268/bsgm2005v57n3s1>.
- Bansal, A.R., Gabriel, G., Dimri, V.P., Krawczyk, C.M., 2011. Estimation of depth to the bottom of magnetic sources by a modified centroid method for fractal distribution of sources: an application to aeromagnetic data in Germany. *Geophysics* 76 (3), L11–L22. <https://doi.org/10.1190/1.3560017>.
- Bhattacharyya, B.K., Leu, L.K., 1975. Analysis of magnetic anomalies over Yellowstone National Park: mapping of Curie point isothermal surface for geothermal reconnaissance. *J. Geophys. Res.* 80 (32), 4461–4465. <https://doi.org/10.1029/JB080i032p04461>.
- Blakely, R.J., 1988. Curie temperature isotherm analysis and tectonic implications of aeromagnetic data from Nevada. *J. Geophys. Res. Solid Earth* 93 (B10), 11817–11832. <https://doi.org/10.1029/JB093iB10p11817>.
- Blakely, R.J., 1995. Potential Theory in Gravity and Magnetic Applications. Cambridge University Press, Cambridge.
- Bouligand, C., Glen, J.M.G., Blakely, R.J., 2009. Mapping Curie temperature depth in the western United States with a fractal model for crustal magnetization. *J. Geophys. Res.* 114, b11104. <https://doi.org/10.1029/2009JB006494>.
- Campos-Enriquez, O.C., Espinoza-Cerdeña, J.M., Oskum, O., 2019. Subduction control on the Curie isotherm around the Pacific-North America plate boundary in northwestern Mexico (Gulf of California). Preliminary results. *J. Volcanol. Geotherm. Res.* 375, 1–17. <https://doi.org/10.1016/j.jvolgeores.2019.03.005>.
- Charleston, S., 1981. A summary of the structural geology and tectonics of the State of Coahuila. In: Schmidt, C.I., Katz, S.B. (Eds.), Lower Cretaceous Stratigraphy and Structure, Northern Mexico. West Texas Geological Society Field Trip Guidebook, Publication, Mexico, pp. 28–36.
- Chávez-Cabello, G., 2005. Deformación y magmatismo Cenozoico en el sur de la Cuenca de Sabinas, Coahuila, México. Universidad Nacional Autónoma de México, Centro de Ciencias (PhD Thesis, 226 pp.).
- Connard, G., Couch, R., Germerle, M., 1983. Analysis of aeromagnetic measurements from the Cascade Range and in central Oregon. *Geophysics* 48 (3), 376–390. <https://doi.org/10.1190/1.1441476>.
- Davies, J.T., 2013. Global map of solid Earth surface heat flow. *Geochim. Geophys. Geosyst.* 14, 4608–4622. <https://doi.org/10.1029/gg02271>.
- Eguiluz de Antuñano, S., 2001. Geologic evolution and gas resources of the Sabinas Basin in Northeastern Mexico. In: Bartolini, C., Buffer, R.T., Cantú-Chapa, A. (Eds.), The western Gulf of Mexico Basin: Tectonics, Sedimentary Basins, and Petroleum Systems. American Association of Petroleum Geologists Memoir 75, pp. 241–270.
- Fastovsky, D.E.O., Hermes, D., Strater, N.H., Bowring, S.A., Clark, J.M., Montellano, M., Hernández, R., 2005. Pre-Late Jurassic, fossil-bearing volcanic and sedimentary red beds of Huizachal Canyon, Tamaulipas, Mexico. In: Anderson, T.H., Nourse, J.A., McKee, J.W., Steiner, M.B. (Eds.), The Mojave-Sonora Megashare Hypothesis: Development, Assessment, and Alternatives. GSA Special Paper 393, pp. 259–282.
- Finn, C.A., Ravat, D., 2004. Magnetic Depth Estimates and Their Potential for Constraining Crustal Composition and Heat Flow in Antarctica. *EOS, Trans. Am. Geophys. Un.* 85 (47), Fall Meet. Suppl., Abstract T11A-1236.
- Fridleifsson, I.B., Bertani, R., Huenges, E., Lund, J.W., Ragnarsdóttir, A., Rybach, L., 2008. The possible role and contribution of geothermal energy to the mitigation of climate change. In: Hohmeyer, O., Trittm, T. (Eds.), IPCC Scoping Meeting on Renewable Energy Sources. Proceedings, Luebeck, Germany, 18–25 January 2008, pp. 59–80.
- Fuentes-Guzmán, E., 2016. Metalogia de la mina Pánuco, Coahuila. Universidad Nacional Autónoma de México, Instituto de Geología, Msc Thesis, México (111 pp.).
- García-Alonso, D., Canet, C., González-Partida, E., Villanueva-Estrada, R.E., Prol-Ledesma, R.M., Alfonso, P., Caballero-Martínez, J.A., Lozano-Santa Cruz, R., 2011. The Cretaceous sediment-hosted copper deposits of San Marcos (Coahuila, Northeastern Mexico): an approach to ore-forming processes. *J. S. Am. Earth Sci.* 31 (4), 432–443. <https://doi.org/10.1016/j.jsames.2011.02.012>.
- Goldammer, R.K., 1999. Mesozoic sequence stratigraphy and paleogeographic evolution of northeast Mexico. In: Bartolini, C., Wilson, J.L., Lawton, T.F. (Eds.), Mesozoic sedimentary and Tectonic History of North-Central Mexico. GSA Special Paper, vol. 340, pp. 1–58.
- González-Sánchez, F., Puente-Solis, R., González-Partida, E., Camprubí, A., 2007. Estratigrafía del Noreste de México y su relación con los yacimientos estratoligados de fluorita, barita, celestina y Zn-Pb. *Bol. Soc. Geol. Mex.* 1 (LIX), 43–62. <https://doi.org/10.18268/bsgm2007v59n1a4>.
- Harrison, W.E., Lutz, K.V., Prater, M.L., Cheung, P.K., 1983. Geothermal Resource Assessment in Oklahoma, Special Publication 83-1m Oklahoma Geological Survey. (42 pp.).
- James, E.W., Henry, C.D., 1991. Compositional changes in Trans-Pecos Texas magmatism coincident with Cenozoic stress realignment. *Journal Geophysical Research* 96 (13), 561–575. <https://doi.org/10.1029/91JB00203>.
- Jones, N.W., McKee, J.W., Marquez, D.B., Tovar, J., Long, L.E., Laudon, T.S., 1984. The Mesozoic La Mula Island, Coahuila, México. *GSA Bulletin* 95 (10), 1226–1241. [https://doi.org/10.1130/0016-7606\(1984\)95<1226:TMLMIC>2.0.CO;2](https://doi.org/10.1130/0016-7606(1984)95<1226:TMLMIC>2.0.CO;2).
- Khojami, A., Ardejani, F.D., Moradzadeh, A., Kalate, A.N., Kahoor, A.R., Porkhial, S., 2017. Determining fractal parameter and depth of magnetic sources for Ardabil geothermal area using aeromagnetic data by de-fractal approach. *Journal of Mining and Environment* 8 (1), 93–101. <https://doi.org/10.22044/jme.2015.481>.
- Lavelle, P.J., Ortega-Gutiérrez, F., Cameron, K.L., Ochoa-Camarillo, H., Lopez, R., Sampson, D.E., 1999. U-Pb geochronology, geochemistry, and provenance of the Grenvillian Huiznopalpa Gneiss of eastern Mexico. *Precambrian Res.* 94 (1–2), 73–99. [https://doi.org/10.1016/S0301-9268\(98\)00108-9](https://doi.org/10.1016/S0301-9268(98)00108-9).
- Li, C.-F., Wang, J., Lin, J., Wang, T., 2013. Thermal evolution of the North Atlantic lithosphere: new constraints from magnetic anomaly inversion with a fractal magnetization model. *Geochem. Geophys. Geosyst.* 14 (12), 5078–5105. <https://doi.org/10.1029/2013GC004896>.
- Li, C.-F., Lu, Y., Wang, J., 2017. A global reference model of Curie-point depths based on EMAG2. *Sci. Rep.* 7, 45129. <https://doi.org/10.1038/srep45129>.
- López, R., Cameron, K.L., Jones, N.W., 2001. Evidence for paleo-Proterozoic, Grenvillian, and Pan-African age Gondwanan crust beneath northeastern Mexico. *Precambrian Res.* 107 (3–4), 195–214. [https://doi.org/10.1016/S0301-9268\(00\)00140-6](https://doi.org/10.1016/S0301-9268(00)00140-6).
- Manea, M., Manea, V.C., 2011. Curie point depth estimates and correlation with subduction in Mexico. *Pure Appl. Geophys.* 168 (1), 489–1,499. <https://doi.org/10.1007/s00224-010-0238-2>.
- Martos, Y.M., Catalán, M., Jordan, T.A., Golynsky, A., Golynsky, D., Eagles, G., Vaughan, D.G.D., 2017. Heat flux distribution of Antarctica unveiled. *Geophys. Res. Lett.* 44 (22), 11,417–11,426. <https://doi.org/10.1002/2017GL075609>.
- Martos, Y.M., Jordan, T.A., Catalán, M., Jordán, T.M., Bamber, J.L., Vaughan, D.G., 2018. Geothermal heat flux reveals the Iceland hotspot track underneath Greenland. *Geophys. Res. Lett.* 45 (16), 8214–8222. <https://doi.org/10.1029/2018GL078289>.
- Maus, S., Dimri, V.P., 1994. Scaling properties of potential fields due to scaling sources. *Geophys. Res. Lett.* 21 (10), 891–894. <https://doi.org/10.1029/94GL00771>.
- Maus, S., Dimri, V., 1995. Potential field power spectrum inversion for scaling geology. *J. Geophys. Res. Solid Earth* 100 (B7), 12605–12616. <https://doi.org/10.1029/95JB00758>.
- Maus, S., Gordon, D., Fairhead, D., 1997. Curie-temperature depth estimation using a self-similar magnetization model. *Geophys. J. Int.* 129 (1), 163–168. <https://doi.org/10.1111/j.1365-246X.1997.tb00945.x>.
- North American Magnetic Anomaly Group (NAMAG), 2002. Digital data grids for the magnetic anomaly map of North America. <https://mrdata.usgs.gov/magnetic/> In: U.S. Geol. Surv. Open File Rep. 02–414.
- Okubo, Y., Matsunaga, T., 1994. Curie point depth in northeast Japan and its correlation with regional thermal structure and seismicity. *J. Geophys. Res.* 99 (B11), 22363–22371. <https://doi.org/10.1029/94JB01336>.
- Okubo, Y., Graf, R.J., Hansen, R.O., Ogawa, K., Tsu, H., 1985. Curie point depths of the island of Kyushu and surrounding areas, Japan. *Geophysics* 50 (3), 481–494. <https://doi.org/10.1190/1.1441926>.
- Pilkington, M., Todoeschuk, J.P., 1993. Fractal magnetization of continental crust. *Geophys. Res. Lett.* 20 (7), 627–630. <https://doi.org/10.1029/92GL03009>.
- Prol-Ledesma, R.M., Morán-Zenteno, D.J., 2019. Heat Flow and geothermal provinces in Mexico. *Geothermics* 78, 183–200. <https://doi.org/10.1016/j.geothermics.2018.12.009>.
- Prol-Ledesma, R.M., Carrillo-de la Cruz, J.L., Torres-Vera, M.A., Membrillo-Abad, A.S., Espinosa-Ojeda, O.M., 2018. Heat flow map and geothermal resources in Mexico. *Terra Digitalis* 2 (2), 1–15. <https://doi.org/10.22201/igc.25940694.2018.2.51>.
- Pyrcz, M.J., Deutsch, C.V., 2014. Geostatistical Reservoir Modeling, 2nd edition, Oxford University Press, New York.
- Ravat, D., 2004. Constructing full spectrum potential field anomalies for enhanced geodynamical analysis through integration of surveys from different platforms (INVITED). *EOS, Trans. Am. Geophys. Un.* 85 (47), (Fall Meet. Suppl., Abstract G44A-03).
- Ravat, D., Pignatelli, A., Nicolosi, I., Champagni, M., 2007. A study of spectral methods of estimating the depth to the bottom of magnetic sources from near surface magnetic anomaly data. *Geophys. J. Int.* 169 (2), 421–434. <https://doi.org/10.1111/j.1365-246X.2007.03305.x>.
- Ravat, D., Morgan, P., Lowry, A.R., 2016. Geotherms from the temperature-depth-constrained solutions of 1-D steady-state heat-flow equation. *Gemsphere* 12 (4), 1187–1197. <https://doi.org/10.1130/GES01235.1>.
- Ross, H.E., Blakely, R.J., Zoback, M.D., 2006. Testing the use of aeromagnetic data for the determination of Curie depth in California. *Geophysics* 71 (5), L51–L59. <https://doi.org/10.1190/1.2335572>.
- Rueda-Gaxiola, J., López-Ocampo, E., Dueñas, M.A., Rodríguez, J.L., Torres-Rivero, A., 1999. The palynological method: basis for defining stratigraphy and age of the Los San Pedro Allogropu, Huizachal-Peregrina anticlinorium, Mexico. In: Bartolini, C., Wilson, J., Lawton, T. (Eds.), Mesozoic Sedimentary and Tectonic History of North-Central Mexico. GSA Special Paper, vol. 340, pp. 229–269.
- Salem, A., Green, C., Ravat, D., Singh, K.H., East, P., Fairhead, J.D., Mogren, S., Biegert, E., 2014. Depth to Curie temperature across the central Red Sea from magnetic data using the de-fractal method. *Tectonophysics* 624–625, 75–96. <https://doi.org/10.1016/j.tecto.2014.04.027>.
- Salvador, A., Green, A., 1980. Opening of the Caribbean Tethys (Origin and development of the Caribbean and the Gulf of Mexico). In: Auboin, J. (Ed.), Géologie des chaînes alpines issues de la Téthys, Bureau de Recherche Géologique et Minière, Mémoires, vol. 115, pp. 224–229.
- Shuey, R.T., Schellinger, D.K., Tripp, A.C., Alley, L.B., 1977. Curie determination from aeromagnetic spectra. *Geophys. J. R. Astr. Soc.* 50 (1), 75–101. <https://doi.org/10.1111/j.1365-246X.1977.tb01325.x>.
- SMU Node of National Geothermal Data System Heat Flow Observation in Content Model Format. <http://geothermal.smu.edu/static/DownloadFilebuttonPage.htm>.
- Spector, A., Grant, F.S., 1970. Statistical models for interpreting aeromagnetic data. *Geophysics* 35 (2), 293–302. <https://doi.org/10.1190/1.1440092>.
- Tanaka, A., Okubo, Y., Matsubayashi, O., 1999. Curie point depth based on spectrum

- analysis of the magnetic anomaly data in East and Southeast Asia. *Tectonophysics* 306 (3–4), 461–470. [https://doi.org/10.1016/S0040-1951\(99\)00072-4](https://doi.org/10.1016/S0040-1951(99)00072-4).
- Torres-Sánchez, S.A., 2015. Implicaciones Geodinámicas del Complejo Metamórfico Paleozoico de la Sierra Madre Oriental en el Noreste de México. Universidad Autónoma de Nuevo León, Earth Sciences Faculty (PhD Thesis, 236 pp).
- Turcotte, D.L., Schubert, G., 2002. *Geodynamics*, second ed. Cambridge University Press, Cambridge, U. K.
- Valdez-Moreno, G., 2001. Geoquímica y petrología de los campos volcánicos Las Esperanzas y Ocampo, Coahuila, México. Universidad Nacional Autónoma de México, Instituto de Geología, (Msc. Thesis, 104 pp).
- Wilson, J.L., 1990. Basement structural controls on Mesozoic carbonates facies in northeastern Mexico: a review. In: Tucker, M.E., Wilson, J.L., Crevello, P.D., Sarg, J.R., Read, J.F. (Eds.), *Carbonate Platforms, Facies, Sequences and Evolution*. 9. International Association of Sedimentologists Special Publication, pp. 235–255.
- Wilson, J.R., Ward, W.C., Finneyan, J., 1984. A Field Guide to Upper Jurassic and Lower Cretaceous Carbonate Platform and Basin Systems. Gulf Coast Section. Society of Economic Paleontologists and Mineralogists, Monterrey-Saltillo area, northeast México, pp. 76.
- Winker, C.D., Buffler, R.T., 1988. Paleogeographic evolution of early deep-water Gulf of Mexico and margins, Jurassic to Middle Cretaceous (Comanchean). *AAPG Bull.* 72, 318–346.
- Zar, J.H., 2010. *Biostatistical Analysis*, fifth ed. Pearson, Upper Saddle River, New Jersey.

Chapter 6: Results

6.1 Heat flow map and geothermal resources in Mexico

(Published paper as second author at *Terra Digitalis* journal)

Received: 16 May 2018, Accepted: 27 Sept. 2018

Published online: 31 Oct. 2018

DOI: 10.22201/igg.25940694.2018.2.51.105

Volume: 2, Issue: 2, Pages: 1-15



Heat flow map and geothermal resources in Mexico[☆]

Mapa de flujo de calor y recursos geotérmicos de México

Rosa-Maria Prol-Ledesma^a, Juan-Luis Carrillo-de la Cruz^b, Marco-Antonio Torres-Vera^b, Alejandra-Selene Membrillo-Abad^b, Orlando-Miguel Espinoza-Ojeda^c

^aInstituto de Geofísica, Universidad Nacional Autónoma de México, Cd. Universitaria, Cd. De México, CP 04510, México.

^bPosgrado en Ciencias de la Tierra, Instituto de Geofísica, Universidad Nacional Autónoma de México, Cd. Universitaria, Cd. De México, CP 04510, México.

^cCONACYT - INICIT, Universidad Michoacana de San Nicolás de Hidalgo, Morelia, Michoacán, CP 58060, México

Abstract

Heat flow maps are a powerful tool for regional exploration of geothermal resources. Mexico is one of the main producers of geothermal energy and the search for undiscovered resources at a regional level should be based on heat flow values. Here, we present a heat flow map at 1:3,500,000 scale, produced with heat flow data compiled from open data bases and previously unpublished data. The compiled heat flow data includes bottom hole temperature, temperature logs, transient temperature measurements and measured temperature logs. The new data were calculated from temperature gradient information and estimating a mean conductivity value characteristic for the type of rock present in the stratigraphic column or assigning the mean conductivity value for the crust. Geothermal gradient and the thermal resistivity (inverse thermal conductivity) were plotted and heat flow was calculated using the Bullard method. The map covers the whole continental territory of Mexico and shows that most of the country has values higher than the world average. The highest heat flow values are concentrated in two provinces: the Gulf of California extensional province and the Trans-Mexican Volcanic Belt.

Keywords: Geothermal; recent volcanism; renewable energy, geothermal gradient, Bullard method, BHT

Resumen

Los mapas de flujo de calor son una poderosa herramienta en la exploración regional de recursos geotérmicos. México es uno de los principales productores de energía geotérmica y la búsqueda a nivel regional para descubrir nuevos recursos debería estar basada en los datos de flujo de calor. Aquí presentamos el mapa de flujo de calor a escala 1:3,500,000, que fue generado a partir de datos de flujo de calor compilados en bases de datos públicas, a los cuales se añadieron nuevos datos calculados por los autores. Los datos compilados para el cálculo del mapa de flujo de calor incluyen: temperatura de fondo de pozo (BHT), registros de temperatura en pozos (compilados y medidos en este trabajo), mediciones transientes de temperatura. Los datos que no han sido reportados previamente fueron calculados a partir de la determinación del gradiente de temperatura y la estimación de la conductividad térmica promedio para los tipos de roca reportados en la columna estratigráfica, o bien, en ausencia de la información acerca del tipo de roca, se asignó el valor promedio de la conductividad para la corteza. El gradiente geotérmico y la resistividad térmica (el inverso de la conductividad térmica) se graficaron para determinar el flujo de calor con el método de Bullard. El mapa cubre todo el territorio continental mexicano y muestra que en la mayor parte los valores de flujo de calor están por encima del flujo de calor promedio a nivel mundial. Los valores más altos de flujo de calor se concentran en la provincia extensional del Golfo de California y en la Faja Volcánica Trans-Mexicana.

Palabras clave: Geotermia; volcanismo reciente; energía renovable, gradiente geotérmico, método de Bullard, BHT

[☆]© R. M. Prol-Ledesma, J. L. Carrillo-de la Cruz, M. A. Torres-Vera, A. S. Membrillo-Abad and O. M. Espinoza-Ojeda. Published by Terra Digitalis. This is an Open Access article distributed under the terms of the Creative Commons Attribution License (<https://creativecommons.org/licenses/by-nc-sa/4.0/>).

which permits non-commercial sharing of the work and adaptions, provided the original work is properly cited and the new creations are licensed under identical terms.

*E-mail address: prol@unam.mx

1. Introduction

The total heat flux through the Earth's surface has been quantified at 47 ± 2 TW (Davies & Davies, 2010); while in 2017, the reported installed capacity in the world to produce electricity was a little more than 6 TW (<https://www.cia.gov/library/publications/the-world-factbook/rankorder/2236rank.html>). This shows that the energy irradiated by the Earth's surface is almost 8 times the world installed capacity for electricity generation and could be harnessed to supply, at least a part of the world energy needs.

The surface heat flow is an indication of the transport of heat from the interior of the Earth and its value depends greatly on the transport mechanism as well as the heat production in the crust. In most of the crust, heat is transported conductively; however, in some areas the more efficient convective heat transport predominates. To have convection in the crust, a fluid must be allowed to ascend to the surface carrying the heat in the upper crust, this fluid is often water, but magma is the dominant fluid for heat transport from the lower crust and from the mantle. The hot water can be used to produce electricity, for climatization and industrial processes.

The evaluation of the geothermal potential of a country is often linked to a heat flow map (White & Williams, 1975; Muffler & Cataldi, 1978; Muffler, 1979; Blackwell et al., 2007; van Wees et al., 2013). Heat flow values delineate the areas where the temperature at depth potentially allows exploitation of the thermal energy with the available technology. Temperatures at depth can be calculated assuming a conductive model; in this case, it is necessary to know the value of the thermal conductivity of the rocks and its chemistry to estimate the heat production by the radioactive element content. Recent tectonic and volcanic activity plays a major role in the heat flow values; heat transport models show that the maximum value of heat flow, due to an igneous intrusion in the crust, is attained after 100,000 years if convection occurs, and when conduction prevails, heat flow would decrease exponentially one order of magnitude in $\sim 200,000$ years (Norton & Knight, 1977). Therefore, a heat flow map may provide evidence about the presence of heat sources based on heat transport models.

2. Heat flow data

Heat flow measurements are scarce in Mexico, despite being one of the ten countries with the highest electricity production from geothermal energy. Published heat flow maps of the region included data calculated with temperature measurements in wells (Blackwell & Richards, 2004) but most of the heat flow reports were based on estimations, using diverse methods (Marvin, 1984; Prol-Ledesma & Juárez, 1986; Campos-Enriquez et al., 1990; Prol-Ledesma, 1990, 1991b; Beltrán-Abaunza & Quintanilla-Montoya, 2001; Prol-Ledesma & Torres-Vera, 2007; Espinosa-Cerdeña & Campos-Enriquez, 2008; Manea & Manea, 2010). Heat flow estimations are generally based on silica geothermometer, Curie Temperature Depth, and Helium isotopic

ratio (${}^3\text{He}/{}^4\text{He}$) (Swanberg & Morgan, 1978; Okubo, 1985; Poljak, 2005). More recent estimations have included geological and geophysical information (Goutorbe et al., 2011).

The heat flow map presented in this work was constructed using only data calculated with temperatures measured in wells because other estimations are less reliable. In fact, silica concentration in spring/well water is indicative of temperature at depth, provided chemical equilibrium is attained, which is not always the case. Furthermore, a parameter that remains unknown is the equilibrium depth, which hinders an accurate calculation of thermal gradient. The relation between silica geothermometer and heat flow is only qualitative, the correlation coefficient is $<50\%$ (Fig. 1) and should not be used as an exact determination to be included in thermal models.

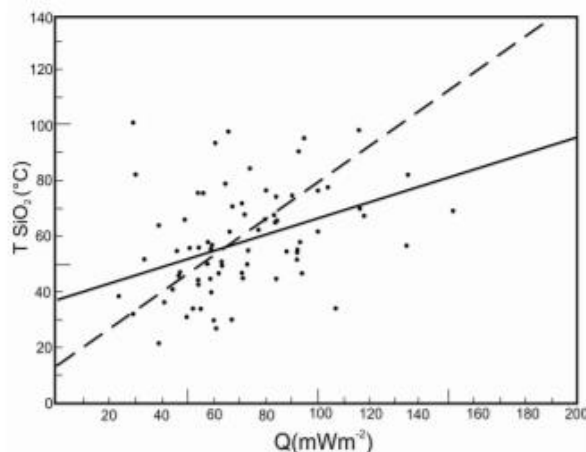


Figure 1. Plot of silica temperature vs heat flow
(Modified from Swanberg & Morgan, 1980).

Figura 1. Temperatura de sílice contra flujo de calor.

Similar ambiguity is present in heat flow estimations using the ${}^3\text{He}/{}^4\text{He}$ and Curie temperature depth (CTD). The comparison between measured heat flow and estimations calculated from CTD show significant differences in some areas (e.g. Manea & Manea, 2010). According to Bouligand et al. (2009), discrepancies between heat flow and calculated CTD arise when thermal conductivities and/or heat generation are not well constrained; additionally, 3-D variations in thermal conductivity, rapid erosion or sedimentation, variations on radioactive heat production, heat provided by recent volcanism or groundwater circulation may cause large discrepancies. More importantly, in some cases the bottom of the magnetic sources may be a lithologic contact corresponding to the base of the crust and not the actual CTD; additionally, there might be artifacts associated to the acquisition of the data. In the classic paper on CTD, Okubo (1985) did not intend to calculate heat flow, but to produce a qualitative relation between shallow CTD and the occurrence of geothermal systems; further comparison of calculated CTD with geothermal gradient measurements produced signif-

icant inconsistencies (Okubo et al., 1989). These discrepancies are also present in the estimation of the geothermal gradient of Cerro Prieto using CTD, yielding values ranging between 33 and 38 °C/km and a heat flow of 100 mW/m² (Espinosa-Cerdeña & Campos-Enríquez, 2008); while the reported well temperature (Lippmann et al., 1991) indicates a gradient higher than 100 °C/km.

The relation between heat flow and ${}^3\text{He}/{}^4\text{He}$ is based on the assumption that high ${}^3\text{He}/{}^4\text{He}$ is caused by mantle upwelling and degassing that would produce high heat flow anomalies (Polyak, 1985; Polyak & Tolstikhin, 1985; Polyak, 2005); however, the scattered data prevents a reliable quantitative correlation between both parameters (Fig. 2).

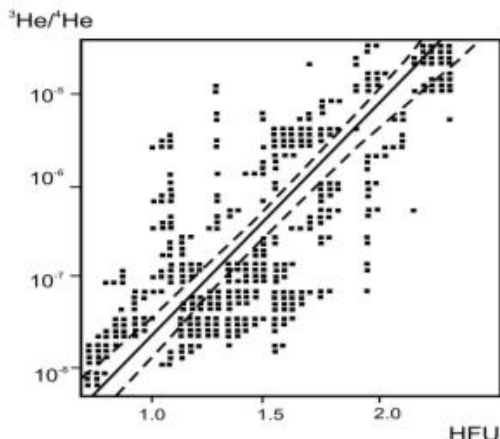


Figure 2. Plot of ${}^3\text{He}/{}^4\text{He}$ vs heat flow that shows the large scatter of the data. It also shows the best correlation between both parameters that would support calculation of heat flow with the isotopic helium ratio (after Polyak, 2005). Figura 2. ${}^3\text{He}/{}^4\text{He}$ contra flujo de calor mostrando la gran dispersión de los datos. También muestra la mejor correlación entre ambos parámetros, la cual soportaría el cálculo del flujo de calor a partir del cociente ${}^3\text{He}/{}^4\text{He}$.

At the beginning of the XXI century, the heat flow measurements reported in the continental part of Mexico (Smith, 1974; Smith et al., 1979; Reiter & Tovar, 1982; Ziegler et al., 1985; Flores-Márquez et al., 1999) were more scarce than those in the ocean bottom, where more than 700 heat flow measurements were published (Becker & Fisher, 1991; Epp et al., 1970; Fisher et al., 2001; Khutorskoy et al., 1990; Lawver & Williams, 1979; Nagihara et al., 1996; Prol-Ledesma et al., 1989; Vacquier et al., 1967; Von Herzen, 1963; Von Herzen & Uyeda, 1963). However, since the creation of the Mexican Center for Innovation in Geothermal Energy (CeMIE-Geo), a great effort has been made to compile and produce more heat flow data and construct a reliable heat flow map to assist the evaluation of the geothermal potential of the country (Espinoza-Ojeda et al., 2017 a,b; Neumann et al., 2017; Prol-Ledesma et al., 2013; Prol-Ledesma et al., 2016; Prol-Ledesma, 2018). The compilation of all available data to calculate the geothermal gradient and the measurement of temperature in wells, produced a large increase in the

number of data. Heat flow data assembled for this work are available in public data bases: Heat Flow Database (<http://www.datapages.com/gis-map-publishing-program/gis-open-files/global-framework/global-heat-flow-database>), Pangea database (<https://doi.pangaea.de/10.1594/PANGAEA.810104>), the International Heat Flow Commission [IHFC] (<http://engineering.und.edu/geology-and-geological-engineering/globe-heat-flow-data-base/index.cfm>), and the SMU Geothermal Lab database (<https://www.smu.edu/Dedman/Academics/Programs/GeothermalLab/DataMaps>).

Additionally, temperature data in wells were measured by our group to calculate heat flow using estimated values for thermal conductivity. In other cases we obtained drilling information for some previously reported data that allowed recalculating the borehole stable temperature (Appendix Table 1). When the temperature logs were available, the data were reviewed and analyzed; in some cases, they were reprocessed to calculate the borehole stable temperature and the heat flow based on the Bullard Method. In all cases the confidence of the data was estimated. The data were discarded when the correlation coefficient obtained by the Bullard Method was lower than 90%. A table of the recalculated and previously unreported data used in the map is included as supplemental online material with references to the original publications (Appendix Table 1). Here, we present the map produced by the interpolation of all heat flow data (Plate 1). The interpolation was achieved using the methodology described in this work. This map represents all heat flow data in Mexico available to date and it will be continually updated.

3. Tectonic Framework

The tectonic structure of Mexico is quite complex, as it is formed of diverse terranes (Campa & Coney, 1983; Sedlock et al., 1993), many of them allochthonous, whose relations are obscured by the widely distributed Cenozoic volcanic products (Morán-Zenteno, 1986). It is precisely the widely spread Cenozoic volcanic-tectonic activity that determines the thermal regime of most geological provinces, especially the Neogene and Quaternary volcanism (Morán-Zenteno et al., 2007). This activity is better related to the physiographic provinces (Fig. 3) than to the tectono-stratigraphic terrains, and the numerous surface hydrothermal manifestations are evidence of the extensive thermal anomalies (Appendix Figure 1). Figure 3 includes recent (<3 My) volcanism because the current models used for geothermal exploration (Moeck & Beardmore, 2014) consider that one of the geological settings for “viable” or “active” geothermal systems may be related to igneous activity with age <3 My (Pleistocene and Holocene volcanism in <https://volcano.si.edu/>, intraplate volcanism in Aranda-Gómez et al., 2005; Ferrari et al., 2005, 2007; Vidal-Solano et al., 2005).

The main Cenozoic geodynamic events (Fig. 3) are the subduction of the Farallon Plate in western Mexico, the cessation of subduction after the approaching of the oceanic ridge with

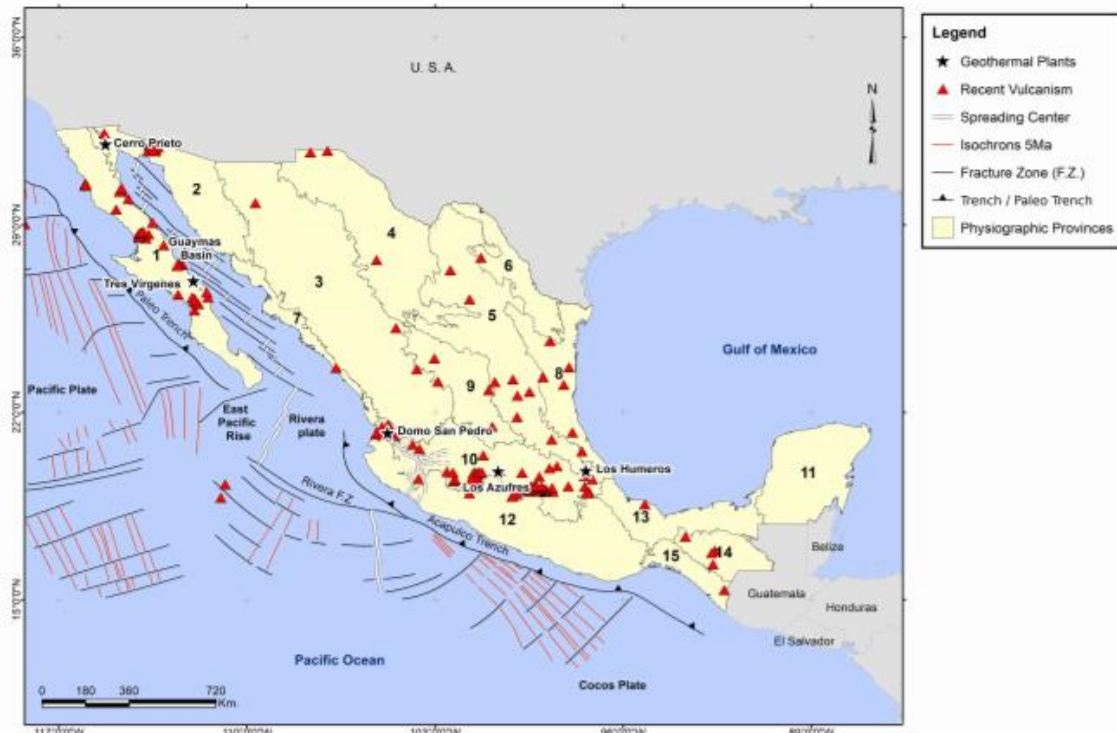


Figure 3. Main morpho-tectonic features of the pacific oceanic floor (modified after INEGI, 2001 and Padilla, 2013). The distribution of physiographic provinces of México and volcanic features < 3 My are also shown. 1. Baja California Peninsula; 2. Sonora Plains; 3. Sierra Madre Occidental; 4. Basin and range province; 5. Sierra Madre Oriental; 6. North America Plains; 7. Pacific Coastal Plains; 8. Gulf of Mexico coastal plains-north ; 9. Mesa Central Province; 10. Mexican Volcanic Belt; 11. Yucatán Peninsula; 12. Sierra Madre del Sur; 13. Gulf of Mexico coastal plains-south; 14. Sierra de Chiapas – Guatemala; 15. Central America Volcanic Belt. Volcanism with age < 3My after: <https://volcano.si.edu/>, intraplate volcanism after Aranda-Gómez et al., 2005; Ferrari et al., 2005, 2007; Vidal-Solano et al., 2005.

Figura 3. Rasgos morfotectónicos del piso oceanico del Pacífico. Distribución de las provincias fisiográficas en México y centros volcánicos de < 3 Ma. 1. Península de Baja California; 2. Planicie de Sonora; 3. Sierra Madre Occidental; 4. Provincia de cuencas y sierras; 5. Sierra Madre Oriental; 6. Planicie de Norte América; 7. Planicie de la Costa del Pacífico; 8. Planicie al norte del Golfo de México ; 9. Provincia de la Mesa Central ; 10. Cinturón Volcánico Mexicano ; 11. Península de Yucatán; 12. Sierra Madre del Sur; 13. Planicie al sur del Golfo de México; 14. Sierra de Chiapas – Guatemala; 15. Cinturón Volcánico de Centro América.

the trench and the extensional regime associated with these processes that culminate in the opening of the Gulf of California. On the other hand, subduction of the Rivera and the Cocos Plates continues beneath the central and south-western part of Mexico (Atwater, 1970). These events produced geologic provinces like the Sierra Madre Occidental, the Trans-Mexican Volcanic Belt and the formation of the continental rift, locally evolved to ocean spreading, in the Gulf of California. The Cerro Prieto geothermal field is linked to this latter geodynamic process (Fig. 3). Extensional tectonics is also observed in the western part of Mexico, where a late Cenozoic rift triple junction (Jalisco Triple Junction) delineates the Jalisco Block. These rifts are associated with Plio-Quaternary alkaline and peralka-

line volcanics, typical of continental rifting processes (Allan et al., 1991). An interesting feature in the west-central part of southern Mexico, is the Orozco Fracture Zone (OFZ) that is subducted below the Tzitzio Gap (Blatter and Hammersley, 2010), where some hydrothermal systems have been recently reported (Jácome-Paz et al., 2018). In addition to the extensional tectonics in the Gulf of California and subduction in southwestern Mexico, intraplate-type volcanism, often associated with normal faulting (late Oligocene-Quaternary), is widespread in the northern and central parts of Mexico (Aranda-Gómez et al., 2005) and to the east in the Gulf of Mexico coast (Ferrari et al., 2005). Heat flow positive anomalies appear to be linked to this type of volcanism.

4. Methodology

4.1. Heat flow calculation

Heat flow is calculated using the Fourier equation that assumes conductive heat transport:

$$q = -k(dT/dz) \quad (1)$$

where q -heat flow; k -thermal conductivity; T -temperature and z -depth. Available temperature gradient information was analyzed for data screening of geothermal gradient data. This screening was performed to remove local convective effects, especially for those measurements located within hydrothermal systems, to determine the superficial regional conductive heat flow. This was achieved by analyzing the Bullard plots to establish the linear regression between thermal resistance and temperature gradient:

$$T_d = T_o + q_o R \quad (2)$$

where T_d is temperature at depth, T_o is the temperature at surface, q_o is the surface heat flow and R is thermal resistance expressed as:

$$R = \sum_i \left(\frac{\Delta z_i}{k_i} \right) \quad (3)$$

where k_i is the thermal conductivity over the i -th stratigraphic interval at depth and Δz_i is the thickness of the interval.

As an example, Figure 4a shows temperature increases linearly with depth for well MEX060; this linear relationship is preserved in the dependence between the temperature and thermal resistance in the Bullard plot of Figure 4b.

On the other hand, Figures 4c and 4d show temperature plots for well MEX023; high resolution temperature logs are

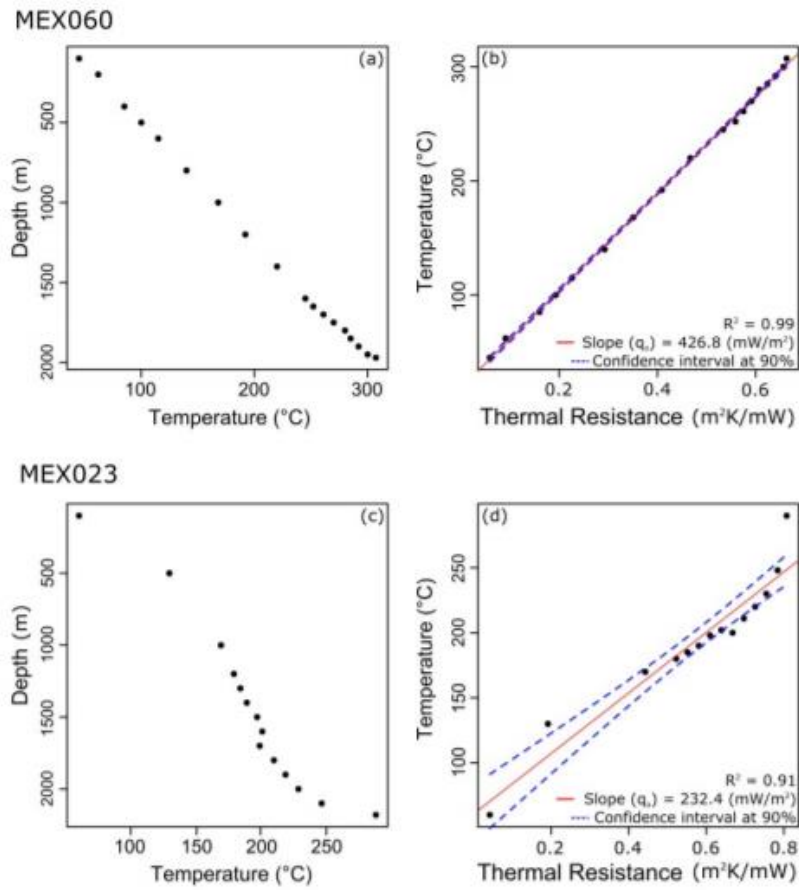


Figure 4. a) Temperature-depth profile and b) Bullard Plot from well MEX060. c) Temperature-depth profile and d) Bullard Plot from well MEX023.
Figura 4. a) Perfil temperatura-profundidad y b) Gráfico Bullard del pozo MEX060. c) Perfil temperatura-profundidad y d) Gráfico Bullard del pozo MEX023.

very useful to identify disturbances in the conductive regime within the well, but the Bullard plot allows to estimate heat flow and the confidence of the slope determination.

The well data used to calculate heat flow by the Bullard Method satisfy parameters of reliability proposed by Richards et al. (2012). Some of these parameters are: (1) the “normal” gradient conditions may be found below 200 meters depth, and (2) multiple gradient intervals are assigned to thermal conductivity values using a weighted average.

The error in the presented new heat flow data can be calculated from the correlation coefficient for each well. A well disturbed by a convection flow has a low correlation coefficient. Accordingly, disturbed wells with a correlation coefficient below 90% were discarded. Only undisturbed wells with a coefficient correlation above 90% were considered for the construction of the map. Disturbed data are easy to identify in high resolution temperature logs using a gradient-depth plot. However, wells with few data are more difficult to analyze for identification of convection disturbances (Beck & Balling, 1988; Cull & Sparksman, 1977); therefore, wells with few data and low correlation coefficients were discarded. All new heat flow data included in the Appendix Table 1, have an accuracy of more than 90% with a positional accuracy of $\pm 50\text{m}$.

4.2. Interpolation

The interpolation was performed using the Inverse Distance Weighting algorithm (IDW). IDW estimates an unknown value of z at location u as a weighted average of its surrounding points, in which the weight is the inverse of the distance raised to a power, according to Tobler's first law of geography (Chang, 2004; Wang, 2006). The observations of z at points closer to u have a higher weight in the interpolation than those at a greater distance (Brunsdon & Comber, 2015).

The algorithm is defined as:

$$z_u = \frac{\sum_{i=1}^s z_i d_{ui}^{-k}}{\sum_{i=1}^s d_{ui}^{-k}} \quad (4)$$

where:

- z_u is the unknown heat flow value to be estimated at location u .
- z_i is the heat flow value at control point i .
- d_{ui} is the distance between points i and u .
- s is the number of points used in the calculation
- k is the power the distance is raised to.

In the IDW algorithm, the power controls the weight function decrease rate with increasing distance (Bonham-Carter, 1994).

IDW is used in Earth Sciences when the data set does not present a smooth variation but contains large anomalies (Sestianto & Triandini, 2013). Other methods, like Kriging, smooth the interpolated values and the anomalies are discarded. In exploration work, the anomalies are frequently the target for the

discovery of natural resources (Shepard, 1968), as is the case in geothermal exploration; therefore, the selection of the IDW method agrees with the purpose of the map (Plate 1).

4.3. Evaluation of the error in the interpolation process

The evaluation of the error utilized the mean squared error (MSE) method to assess the differences between the actual heat flow measurements and the estimation calculated with the interpolation. The plot that represents the actual heat flow values and the associated interpolated value is shown in Figure 5.

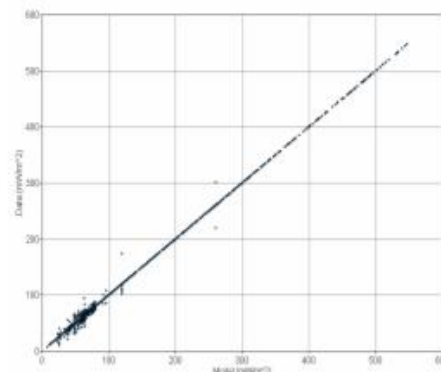


Figure 5. Error plot. The actual heat flow data values are plotted vs the modelled values in the simulation. See text for details.

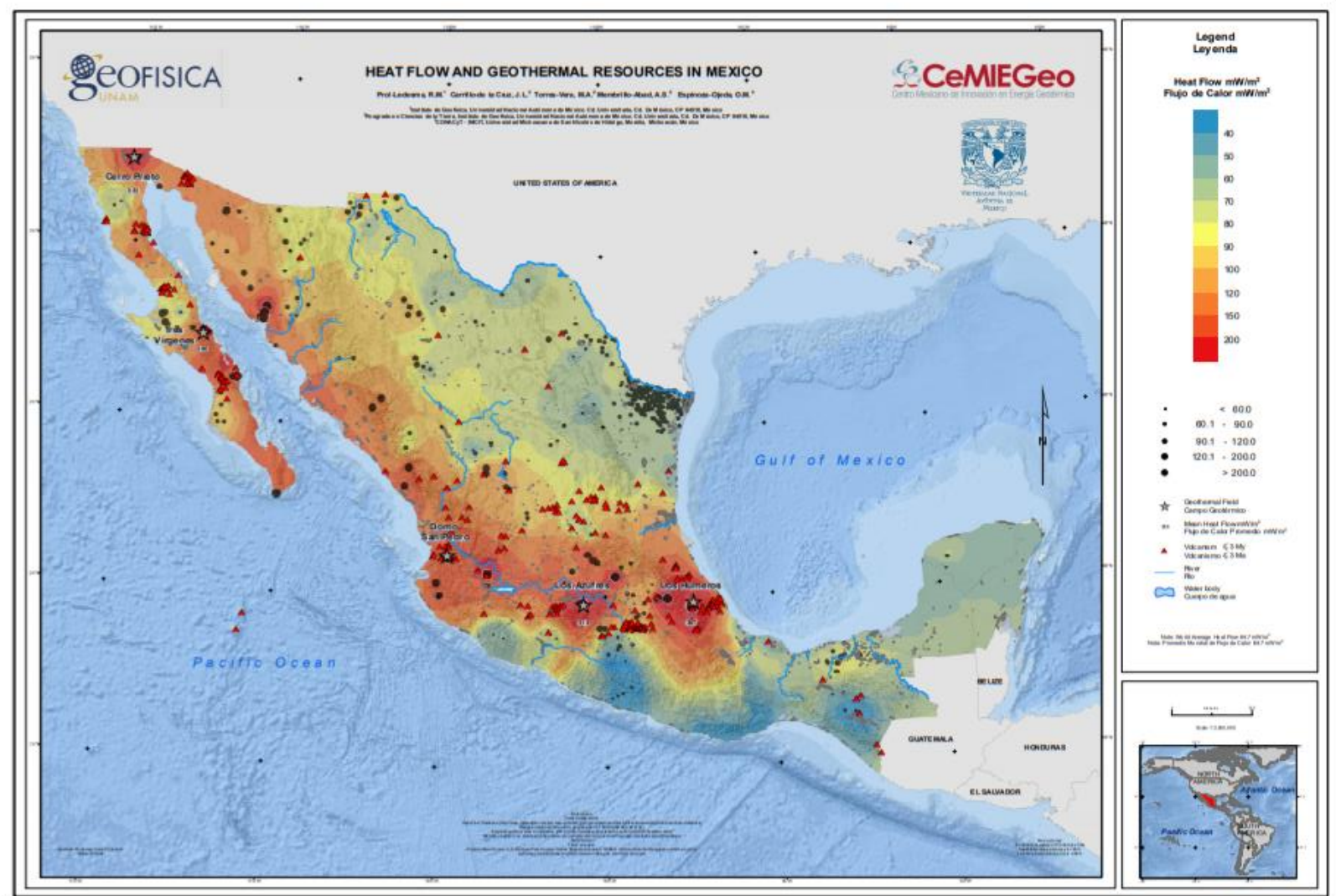
Figura 5. Gráfico de error. Los valores reales de flujo de calor están graficados contra los valores de la simulación. Ver texto para detalles.

These values were used to calculate the MSE that yields a value of 4.96% for the map, which validates the interpolation process. Figure 6 represents the error obtained for all points in the map.

5. Map Synopsis

The interpolation of all the available heat flow measurements for the continental region of Mexico indicates that high heat flow is prevalent in extensive areas in Mexico, and prospective zones are found outside of the active Mexican Volcanic Belt, where so far, most exploration work has been carried out. Three geothermal fields have been developed within the Mexican Volcanic Belt and two in the Baja California Peninsula (Fig. 3 and Plate 1). However, large areas with heat flow at least twice the world mean value have not been explored yet.

The map shows a correlation between high heat flow and recent thermal events related with volcanic-tectonic activity especially in the western and central parts of Mexico, where active subduction, sea floor spreading, and continental rifting is taking place; however, new regions where no exploration campaigns have taken place are pointed out in the map as future targets.



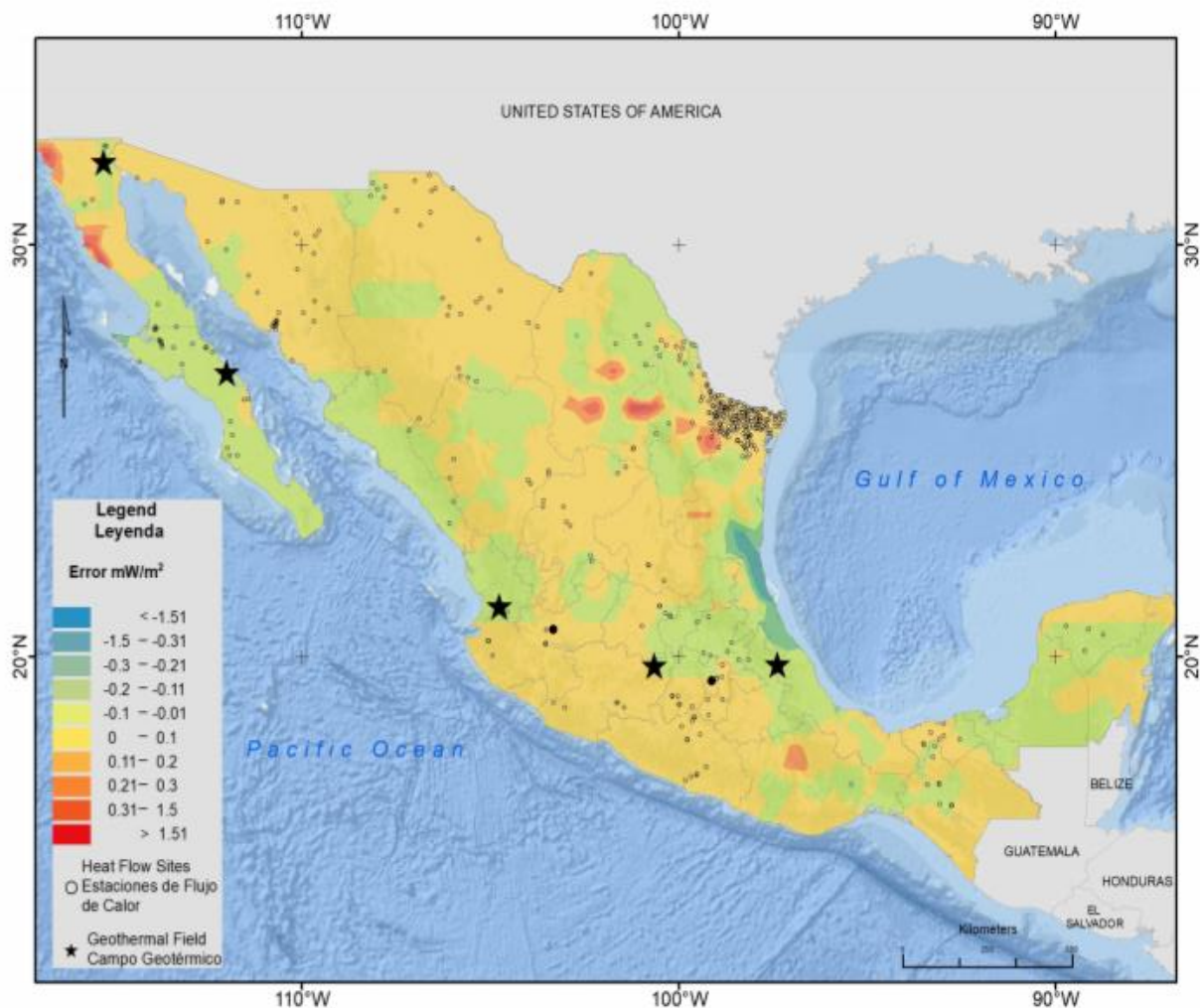


Figure 6: Map showing the error of heat flow interpolated values.
Figure 6. Mapa del error en los valores interpolados de flujo de calor.

The average heat flow for continents is $64.7 \text{ mW}\cdot\text{m}^{-2}$ (Davies, 2013), and a large part of Mexico presents heat flow values over $100 \text{ mW}\cdot\text{m}^{-2}$. This fact suggests that Mexico's geothermal potential has not been exhausted yet and that more intense exploration should be pursued in the newly appointed areas. In contrast, heat flow values, as low as $13 \text{ mW}\cdot\text{m}^{-2}$, have been measured in the Pacific coast region as a result of subduction of the oceanic plate (Ziegler et al., 1985); these areas are characterized by a deep Curie isotherm, between 16 and 24 km (Manea & Manea, 2010).

The Baja California Peninsula exhibits large areas with high heat flow above $100 \text{ mW}\cdot\text{m}^{-2}$. Two geothermal fields are currently under exploitation (Fig. 3 and Plate 1) but regional exploration indicates that the geothermal energy potential may be above 400 MWe (Arango-Galván et al., 2015), and the heat flow map confirms that large resources occur in this region. Heat flow is high along the eastern coast of the Gulf of California as evidence of the sea floor spreading processes taking place nearby.

The eastern part of central Mexico stands out with heat flow values above $150 \text{ mW}\cdot\text{m}^{-2}$. Part of this area corresponds to the limits of the Trans-Mexican Volcanic Belt, but the northern and southern sections are related to high thermal gradients within the oil fields, in some wells the thermal gradient is above $50-70^\circ\text{C}/\text{km}$ (Eguiluz-de Antuñano, 2009).

The Sierra Madre Occidental and the intraplate recent volcanic features in the central and eastern parts of Mexico represent the least studied high heat flow anomalies in Mexico (Prol-Ledesma, 2018), and a possible target for future geothermal exploration.

The southeastern part of Mexico contains the oldest provinces as the Oaxaca Terrain (Campa & Coney, 1983) and at the same time it hosts active volcanoes: El Chichón and Tacaná; the heat flow measurements have been performed in areas with predominance of the old terrains thermal regime where low heat flow values predominate; nevertheless, high heat flow data in the northern part of this area influence nearby zones as evidence of hotter than average areas.

6. Conclusions

The heat flow values indicate that a large part of Mexico contains promising areas for exploitation and direct utilization of geothermal energy. The most important result is that geothermal exploration should be continued in a regional basis focused on the heat flow anomalies revealed by this map.

The heat flow map will be indispensable for the definition of the geothermal provinces of Mexico, which will guide exploration in the future to fully develop the geothermal resources. Undoubtedly, the future increase in heat flow measurements is necessary and will reveal major high heat flow anomalies in large areas that remain uncharted.

7. Software

We developed our own programs to calculate the well stable temperature and to apply the Bullard method used to compute the new heat flow data. The interpolation process was performed with the IDW algorithm in ESRI ArcGIS.

8. Map Design

The coordinate system used for the map is WGS 84 (World Geodetic System 1984) that locates sites by Latitude, Longitude and Elevation. In this map we will use only Lat/Long to locate the heat flow sites. Geographic coordinates can be used for the whole country without much distortion. We used shape files of Countries from Wessel & Smith (2017). We used the ArcMap platform for administration of geographic data.

- Scale 1:3,500,000 and interpolation was performed in A0.
- Map is oriented to the geographic north
- The total area is $1,881,032 \text{ Km}^2$
- Grade spacing: $5^\circ 0' 0''$

Acknowledgements

The authors wish to thank J. Miguel Flores Velazquez, Marcela Errasti-Orozco, Claudia Arango, José Luis Salas, Xóchitl Flores and Juan Antonio Tapia for their help in collecting and processing the data. This work was supported by Fondo de Sustentabilidad Energética SENER-CONACyT CeMIE-Geo under Grant-Project P-01: "Mapas de Gradiente Geotérmico y Flujo de Calor para la República Mexicana". The authors thank the comments by two anonymous reviewers that greatly improve the original manuscript.

References

- Allan, J. F., Nelson, S. A., Luhr, J. F., Carmichael, I. S. E., Wopat, M., Wallace, P. J., 1991. Pliocene-Holocene Rifting and Associated Volcanism in Southwest Mexico: An Exotic Terrane in the Making: Chapter 21: Part III. Regional Geophysics and Geology 114, 425–445, doi:10.1306/M47542C21.
- Aranda-Gómez, J. J., Luhr, J. F., Housh, T. B., Valdez-Moreno, G., Chávez-Cabello, G., Aranda-Gómez, J. J., Luhr, J. F., Housh, T. B., Valdez-Moreno, G., Chávez-Cabello, G., 2005. El volcanismo tipo intraplaea del Cenozoico tardío en el centro y norte de México: una revisión. Boletín de la Sociedad Geológica Mexicana 57 (3), 187–225, doi:10.18268/hsgm2005v57n3a1.
- Arango-Galván, C., Prol-Ledesma, R. M., Torres-Vera, M. A., 2015. Geothermal prospects in the Baja California Peninsula. Geothermics 55, 39–57, doi:10.1016/j.geothermics.2015.01.005.
- Atwater, T., Dec, 1970. Implications of Plate Tectonics for the Cenozoic Tectonic Evolution of Western North America. GSA Bulletin 81 (12), 3513–3536, doi:10.1130/0016-7606(1970)81[3513:IOPTFT]2.0.CO;2.
- Beck, A. E., Balling, N., 1988. Determination of Virgin Rock Temperatures. Solid Earth Sciences Library. Springer Netherlands, Dordrecht, doi:10.1007/978-94-009-2847-3_3.
- Becker, K., Fisher, A. T., 1991. A Brief Review of Heat-Flow Studies in the Guaymas Basin, Gulf of California: Chapter 33: Part VI. Hydrothermal Processes. American Association of Petroleum Geologist Memoir 47, 709–720.

- Beltrán-Abaunza, J. M., Quintanilla-Montoya, A. L., Mar. 2001. Calculated heat flow for the ensenada region, baja california, mexico. *Ciencias Marinas* 27 (4), 619–634, doi:10.7773/cm.v27i4.497.
- Blackwell, D. D., Negraru, P. T., Richards, M. C., Dec. 2006. Assessment of the Enhanced Geothermal System Resource Base of the United States. *Natural Resources Research* 15 (4), 283–308, doi:10.1007/s11053-007-9028-7.
- Blackwell, D. D., Richards, M. C., 2004. Geothermal map of North America: Scale 1:6,500,000. Am. Assoc. Petrol. Geol., product Code 423.
- Blatter, D. L., Hammersley, L., 2010. Impact of the Orozco Fracture Zone on the central Mexican Volcanic Belt. *Journal of Volcanology and Geothermal Research* 197 (1), 67–84, doi:10.1016/j.jvolgeores.2009.08.002.
- Bonham-Carter, G. F., 1994. Geographic Information Systems for Geoscientists: Modelling with GIS. Elsevier, Canada, google-Books-ID: FkKe-BQAAQBAJ.
- Bouligand, C., Glen, J. M. G., Blakely, R. J., 2009. Mapping Curie temperature depth in the western United States with a fractal model for crustal magnetization. *Journal of Geophysical Research: Solid Earth* 114 (B11), doi:10.1029/2009JB006494.
- Brunsdon, C., Comber, L., 2015. An Introduction to R for Spatial Analysis and Mapping. SAGE, google-Books-ID: VicJCwAAQBAJ.
- Campa, M. F., Coney, P. J., Jun. 1983. Tectono-stratigraphic terranes and mineral resource distributions in Mexico. *Canadian Journal of Earth Sciences* 20 (6), 1040–1051, doi:10.1139/e83-094.
- Campos-Enriquez, J. O., Arroyo-Esquível, M. A., Urrutia-Fucugauchi, J., Jan. 1990. Basement, Curie isotherm and shallow-crustal structure of the Trans-Mexican Volcanic Belt from aeromagnetic data. *Tectonophysics* 172 (1), 77–90, doi:10.1016/0040-1951(90)90060-L.
- Chang, K.T., 2004. Introduction to geographic information systems, 2nd Edition. McGraw-Hill.
- Cull, J., Sparksman, G., 1977. Measurements of Surface Heat Flow. Bureau of Mineral Resources Geology and Geophysics Record 12 (39), 1–17.
- Davies, J. H., 2013. Global map of solid Earth surface heat flow. *Geochemistry, Geophysics, Geosystems* 14 (10), 4608–4622, doi:10.1002/ggpe.20271.
- Davies, J. H., Davies, D. R., 2010. Earth's surface heat flux. *Solid Earth* 1 (1), 5–24, doi:10.5194/se-1-5-2010.
- De Anda, L. F., Septien, J. I., Elizondo, J. R., 1964. Geothermal energy in Mexico. Proceedings of the UN Conference on New Sources of Energy 2, 149–165, new York; United Nations.
- Eguiluz-de Antuñano, S., 2009. The Yegua Formation: Gas Play in the Burgos Basin, Mexico, in C. Bartolini, and J. R. Roman Ramos, eds., Petroleum systems in the southern Gulf of Mexico.. American Association of Petroleum Geologist Memoir 90, 49–77, doi:10.1306/13191077M902621.
- Epp, D., Gnim, P. J., Langseth, M. G., Oct. 1970. Heat flow in the Caribbean and Gulf of Mexico. *Journal of Geophysical Research* 75 (29), 5655–5669, doi:10.1029/JB075i029p05655.
- Espinosa-Cardefúa, J. M., Campos-Enriquez, J. O., Oct. 2008. Curie point depth from spectral analysis of aeromagnetic data from Cerro Prieto geothermal area, Baja California, México. *Journal of Volcanology and Geothermal Research* 176 (4), 601–609, doi:10.1016/j.jvolgeores.2008.04.014.
- Espinosa-Ojeda, O. M., Prol-Ledesma, R. M., Iglesias, E. R., 2017a. Continental heat flow data update for México – Constructing a reliable and accurate heat flow map, in Proceedings of the 42nd Workshop on Geothermal Reservoir Engineering 2017: Stanford, California, USA, 13–15 February 2017SGP-TR-212.
- Espinosa-Ojeda, O. M., Prol-Ledesma, R. M., Iglesias, E. R., Figueroa-Soto, A., 2017b. Update and review of heat flow measurements in México. *Energy* 121, 466–479, doi:10.1016/j.energy.2017.01.045.
- Ferrari, L., Tagami, T., Eguchi, M., Orozco-Esquível, M. T., Petrone, C. M., Jacobo-Albarrán, J., López-Martínez, M., 2005. Geology, geochronology and tectonic setting of late Cenozoic volcanism along the southwestern Gulf of Mexico: The Eastern Alkaline Province revisited. *Journal of Volcanology and Geothermal Research* 146 (4), 284–306, doi:10.1016/j.jvolgeores.2005.02.004.
- Ferrari, L., Valencia-Moreno, M., Bryan, S., 2007. Magmatism and tectonics of the Sierra Madre Occidental and its relation with the evolution of the western margin of North America. In: Special Paper 422: Geology of México: Celebrating the Centenary of the Geological Society of México. Vol. 422. Geological Society of America, pp. 1–39, doi:10.1130/2007.2422(01).
- Fisher, A. T., Giambalvo, E., Sclater, J., Kastner, M., Ransom, B., Weinstein, Y., Lonsdale, P., 2001. Heat flow, sediment and pore fluid chemistry, and hydrothermal circulation on the east flank of Alarcon Ridge, Gulf of California. *Earth and Planetary Science Letters* 188 (3), 521–534, doi:10.1016/S0012-821X(01)00310-7.
- Flores-Márquez, E.L., Chávez-Segura, R., Campos-Enríquez, O., Pilkington, M., 1999. Preliminary 3-D structural model from the Chicxulub impact crater and its implications in the actual geothermal regime. *Trends in Heat, Mass and Momentum Transfer* 5, 19–40.
- García-Estrada, G., 2000. Modelado del estado térmico inicial del campo geotérmico de Los Azufres, Michoacán, México. PhD Thesis. Universidad Nacional Autónoma de México, Posgrado en Ciencias de la Tierra, UNAM, http://132.248.9.195/pd2000/285393/Index.html.
- Goutorbe, B., Poort, J., Lucaleau, F., Raillard, S., 2011. Global heat flow trends resolved from multiple geological and geophysical proxies. *Geophysical Journal International* 187 (3), 1405–1419, doi:10.1111/j.1365-246X.2011.05228.x.
- Iglesias, E.R., Torres, R.J., Martínez-Estreña, J.I., Reyes-Picasso, N., 2015. Summary of the 2014 Assessment of Medium- to Low-Temperature Mexican Geothermal Resources. In World Geothermal Congress, 16–24 April 2015, Australia-New Zealand: proceedingsPaper 16081, 7pp.
- Instituto Nacional de Estadística, Geografía e Informática (INEGI), 2001. Conjunto de datos vectoriales Fisiográficos. Continuo Nacional escala 1:1,000,000 serie I. Provincias fisiográficas. INEGI, http://www.beta.inegi.org.mx/temas/mapas/fisiografia/.
- Japan International Cooperation Agency (JICA), 1989. Evaluación del yacimiento geotérmico en La Primavera. JICA, 122 pp.
- Jácome-Paz, M.P., Pérez-Zárate, D., Prol-Ledesma, R.M., Rodríguez-Díaz, A.A., Estrada-Murillo, A.M., González-Romo, I. A., Magaña-Torres, E., 2018. Two new geothermal prospects in the Mexican Volcanic Belt: La Escalera and Agua Caliente-Tzitzio geothermal springs, Michoacán, México(submitted).
- Khutorskoy, M. D., Fernandez, R., Kononov, V. I., Polyak, B. G., Matveev, V. G., Rot, A. A., 1990. Heat flow through the sea bottom around the Yucatan Peninsula. *Journal of Geophysical Research: Solid Earth* 95 (B2), 1223–1237, doi:10.1029/JB095iB02p01223.
- Lawver, L. A., Williams, D. L., 1979. Heat flow in the central Gulf of California. *Journal of Geophysical Research: Solid Earth* 84 (B7), 3465–3478, doi:10.1029/JB084iB07p03465.
- Lippmann, M. J., Truesdell, A. H., Halfman-Dooley, S. E., A., M., 1991. A review of the hydrogeologic-geochemical model for Cerro Prieto. *Geothermics* 20 (1-2), 39–52, doi:10.1016/0375-6505(91)90004-F.
- Manea, M., Manea, V. C., 2010. Curie Point Depth Estimates and Correlation with Subduction in Mexico. *Pure and Applied Geophysics* 168 (8), 1489–1499, doi:10.1007/s00024-010-0238-2.
- Marvin, P.R., 1984. Regional heat flow based on the silica content of ground waters from northcentral Mexico. M.Sc. Thesis. New Mex. St. Univ., 107 p.
- Moeck, I., Beardmore, G., 2014. A New 'Geothermal Play Type' Catalog: Streamlining Exploration Decision Making. Proceedings. Thirty-Ninth Workshop on Geothermal Reservoir EngineeringStanford, California: Stanford University; p. 8.
- Morán-Zenteno, D., 1986. Breve revisión sobre la evolución tectónica de México. *Geofísica Internacional* 25 (1), 9–38.
- Morán-Zenteno, D.J., Cercu, M., Kepke, J.D., 2007. The Cenozoic tectonic and magmatic evolution of southwestern México: Advances and problems of interpretation, in Alaniz-Álvarez, S.A. & Nieto-Samaniego, A.F., eds., Geology of México: Celebrating the Centenary of the Geological Society of México. Geological Society of America Special Paper 422, 71–91, doi:10.1130/2007.2422(03).
- Muffler, P., 1979. Assessment of geothermal resources of the United States—1978. U.S.G.S. Circular 790.
- Muffler, P., Cataldi, R., 1978. Methods for regional assessment of geothermal resources. *Geothermics* 7 (2), 53–89, doi:10.1016/0375-6505(78)90002-0.
- Nagihara, S., Selater, J. G., Phillips, J. D., Behrens, E. W., Lewis, T., Lawver, L. A., Nakamura, Y., García-Abdeslem, J., Maxwell, A. E., 1996. Heat flow in the western abyssal plain of the Gulf of Mexico: Implications for thermal evolution of the old oceanic lithosphere. *Journal of Geophysical Research* 101 (B2), 2895–2913, doi:10.1029/95JB03450.
- Neumann, F., Negrete-Aranda, R., Harris, R. N., Contreras, J., Selater, J. G., González-Fernández, A., Dec. 2017. Systematic heat flow measurements

- across the Wagner Basin, northern Gulf of California. *Earth and Planetary Science Letters* 479, 340–353, doi:10.1016/j.epsl.2017.09.037.
- Norton, D., Knight, J. E., 1977. Transport phenomena in hydrothermal systems; cooling plutons. *American Journal of Science* 277 (8), 937–981, doi:10.2475/ajs.277.8.937.
- Okubo, Y., Graf, R., Hansen, R., Ogawa, K., Tsu, H., 1985. Curie point depths of the Island of Kyushu and surrounding areas, Japan. *GEOPHYSICS* 50 (3), 481–494, doi:10.1190/1.1441926.
- Okubo, Y., Tsu, H., Ogawa, K., 1989. Estimation of Curie point temperature and geothermal structure of island arc of Japan. *Tectonophysics* 159 (3), 279–290, doi:10.1016/0040-1951(89)90134-0.
- Padilla y Sánchez, R., Domínguez Trejo, L., López Azcárraga, A., Mota Nieto, J., Fuentes Menes, A., Rosique Naranjo, F., Germán Castelán, E., Campos Arriola, S., 2013. National Autonomous University of Mexico Tectonic Map of Mexico GIS Project, American Association of Petroleum Geologists GIS Open Files series.
- Polyak, B. G., 2005. Heat and mass transfer from the mantle: heat flow and He-isotope constraints. *Annals of Geophysics* 48 (1), 9–17.
- Polyak, B. G., Kononov, V. I., Kamensky, I., Prasolov, E. M., Sharkov, I. V., Prol-Ledesma, R. M., González, A., Razo, A., Molina-Berbeller, R., 1985. First estimations of terrestrial heat flow in the TMVB and adjacent areas based on isotopic composition of natural helium. *Geofísica Internacional* 24 (4), 465–476.
- Polyak, B. G., Tolstikhin, I. N., 1985. Isotopic composition of the earth's helium and the problem of the motive forces of tectogenesis. *Chemical Geology: Isotope Geoscience section* 52 (1), 9–33, doi:10.1016/0168-9622(85)90005-3.
- Prol-Ledesma, R. M., 1990. Mapa geotérmico de la República Mexicana. Atlas Nacional de México. Vol. 3. Instituto de Geografía, UNAM.
- Prol-Ledesma, R. M., 1991a. Chemical geothermometers applied to the study of thermalized aquifers in Guaymas, Sonora, Mexico: a case history. *Journal of Volcanology and Geothermal Research* 46 (1), 49–59, doi:10.1016/0377-0273(91)90075-B.
- Prol-Ledesma, R. M., 1991b. Terrestrial Heat Flow in Mexico. In: Čermák, V., Rybach, L. (Eds.), *Terrestrial Heat Flow and the Lithosphere Structure. Exploration of the Deep Continental Crust*. Springer Berlin Heidelberg, Berlin, Heidelberg, pp. 475–485, doi:10.1007/978-3-642-75582-8_24.
- Prol-Ledesma, R. M., 2018. Anomalías de flujo de calor terrestre y la definición de la provincia geotérmica asociada al volcanismo de intraplaca en México. Trabajo de Ingreso a la Academia de Ingeniería México. [Http://www.ai.org.mx/presentacion/anomalias-de-flujo-de-calor-terrestre-y-la-definicion-de-la-provincia-geotermica](http://www.ai.org.mx/presentacion/anomalias-de-flujo-de-calor-terrestre-y-la-definicion-de-la-provincia-geotermica).
- Prol-Ledesma, R. M., Arango-Galván, C., 2017. Sistemas Geotérmicos de la Península de Baja California. Vol. 21. Monografías del Instituto de Geofísica, UNAM, 233 pp.
- Prol-Ledesma, R. M., Espinoza-Ojeda, O.M., Iglesias, E.R., Arango-Galván, C., 2016. Integration of heat flow measurements and estimations in the construction of Mexico's heat flow map. *Proceedings European Geothermal Congress 2016Strasbourg, France, 19-24 Sept.*
- Prol-Ledesma, R. M., Juárez, G., 1986. Geothermal map of Mexico. *Journal of Volcanology and Geothermal Research* 28 (3), 351–362, doi:10.1016/0377-0273(86)90030-2.
- Prol-Ledesma, R. M., Sugrobov, V. M., Flores, E. L., Juárez M., G., Smirnov, Y. B., Gorshkov, A. P., Bondarenko, V. G., Rashidov, V. A., Nedopekin, L. N., Gavrilov, V. A., 1989. Heat flow variations along the Middle America Trench. *Marine Geophysical Researches* 11 (1), 69–76, doi:10.1007/BF00286248.
- Prol-Ledesma, R. M., Torres-Vera, M. A., 2007. Mapa de Recursos Geotérmicos de la República Mexicana. Atlas Nacional de México. Instituto de Geografía, UNAM. E-VI-3.
- Prol-Ledesma, R. M., Torres-Vera, M.-A., Rodolfo-Metalpa, R., Ángeles, C., Lechuga Devezze, C. H., Villanueva-Estrada, R. E., Shumilin, E., Robinson, C., 2013. High heat flow and ocean acidification at a nascent rift in the northern Gulf of California. *Nature Communications* 4, 1388, doi:10.1038/ncomms2390.
- Reiter, M., Tovar R., J. C., 1982. Estimates of terrestrial heat flow in northern Chihuahua, Mexico, based upon petroleum bottom-hole temperatures. *GSA Bulletin* 93 (7), 613–624, doi:10.1130/0016-7606(1982)93<613:EOTHFI>2.0.CO;2.
- Richards, M., Blackwell, D., Williams, M., Frone, Z., Dingwall, R., Batir, J., Chickering, C., 2012. Proposed Reliability Code for Heat Flow Sites. *GRC Transactions* 36.
- Sedlock, R.L., Ortega-Gutiérrez, F., Speed, C., 1993. Tectonostratigraphic Terranes and Tectonic Evolution of Mexico. *Geological Society of America Special Paper* 278, 153 p. doi:10.1130/SPE278-p1.
- Setianto, A., Triandini, T., 2013. COMPARISON OF KRIGING AND INVERSE DISTANCE WEIGHTED (IDW) INTERPOLATION METHODS IN LINEAMENT EXTRACTION AND ANALYSIS. *Journal of Applied Geology* 5 (1), 21–29, doi:10.22146/jag.7204.
- Shepard, D., 1968. A two-dimensional interpolation function for irregularly-spaced data. *Proceedings of the 1968 ACM National Conference*, 517–524, doi:10.1145/800186.810616.
- Smith, D. L., 1974. Heat flow, radioactive heat generation, and theoretical tectonics for northwestern Mexico. *Earth and Planetary Science Letters* 23 (1), 43–52, doi:10.1016/0012-821X(74)90028-4.
- Smith, D. L., Nuckles, C. E., Jones, R. L., Cook, G. A., 1979. Distribution of heat flow and radioactive heat generation in northern Mexico. *Journal of Geophysical Research: Solid Earth* 84 (B5), 2371–2379, doi:10.1029/JB084iB05p02371.
- Swanberg, C. A., Morgan, P., 1978. The linear relation between temperatures based on the silica content of groundwater and regional heat flow: A new heat flow map of the United States. *Pure and Applied Geophysics* 117 (1), 227–241, doi:10.1007/BF00879749.
- Swanberg, C. A., Morgan, P., 1980. The silica heat flow interpretation technique: Assumptions and applications. *Journal of Geophysical Research: Solid Earth* 85 (B12), 7206–7214, doi:10.1029/JB085iB12p07206.
- Vacquier, V., Slater, J.G., Corry, C.F., 1967. Studies of the thermal state of the Earth. 21st paper. *Heat Flow, Eastern Pacific*, 45, 375–393.
- Van Wees, J.D., Boxem, T., Calcagno, P., Dezayes, C., Lacasse, C., Manzella, A., 2013. A Methodology for Resource assessment and application to core countries. Deliverable no. 2.1 (final). GEO-ELEC project, 28 pp.
- Vidal-Solano, J.R., Paz Moreno, F.A., Demant, A., 2005. Caracterización y Cronología del Evento Volcánico Terciario Pre-Pinacate, Campo El Pinacate, Noroeste de Sonora, Mexico. Bol. Depto. Geol. UniSon 18-19, 117–140.
- Von Herzen, R. P., 1963. Geothermal Heat Flow in the Gulfs of California and Aden. *Science* 140 (3572), 1207–1208, doi:10.1126/science.140.3572.1207.
- Von Herzen, R. P., Uyeda, S., 1963. Heat flow through the eastern Pacific ocean floor. *Journal of Geophysical Research* 68 (14), 4219–4250, doi:10.1029/JZ068i014p04219.
- Wang, F., 2006. Quantitative Methods and Applications in GIS. CRC Press, doi:10.1201/9781420004281.
- White, D. E., Williams, D. L., 1975. Assessment of geothermal resources of the United States—1975. *U.S. Geological Survey Circular* 726, 155 p.
- Wilhelm, H., Heidinger, P., Safanda, J., Čermák, V., Burkhardt, H., Popov, Y., 2004. High resolution temperature measurements in the borehole Yaxcopoil-1, Mexico. *Meteoritics & Planetary Science* 39, 813–819, doi:10.1111/j.1945-5100.2004.tb00931.x.
- Ziaogos, J. P., Blackwell, D. D., Mooser, F., 1985. Heat flow in southern Mexico and the thermal effects of subduction. *Journal of Geophysical Research: Solid Earth* 90 (B7), 5410–5420, doi:10.1029/JB090iB07p05410.

This article accompanies the following material:

HTML:	DOI: 10.22201/igg.25940694.2018.2.51.103
Static map:	DOI: 10.22201/igg.25940694.2018.2.51.104

Appendix

Appendix Table 1. Data table (unpublished)

New and revised heat flow data are included in Table 1. We used published temperature logs and BHT (a – García-Estrada, 2000; b – De Anda et al., 1964; c – Prol-Ledesma, 1991a; d – JICA, 1989; e – Lippmann et al., 1991 ; f – Espinoza-Ojeda et al., 2017; g – Wilhelm et al., 2004) as well as temperature data measured by our group to calculate the geothermal gradient. Heat flow was calculated following the methodology explained in this paper. Thermal conductivity was estimated based on lithology, and when lithology was not reported for the well, we assigned the crust average conductivity value (2.5 W/m °K). All new and recalculated data presented in Table 1 were included in the heat flow map produced here. The columns of the table include: data number, original site ID, temperature data source (reference), site location in geographic coordinates, calculated geothermal gradient (°C/km), conductivity (W/m °K; estimated from lithology or average crust value “*”), heat flow (mW/m²).

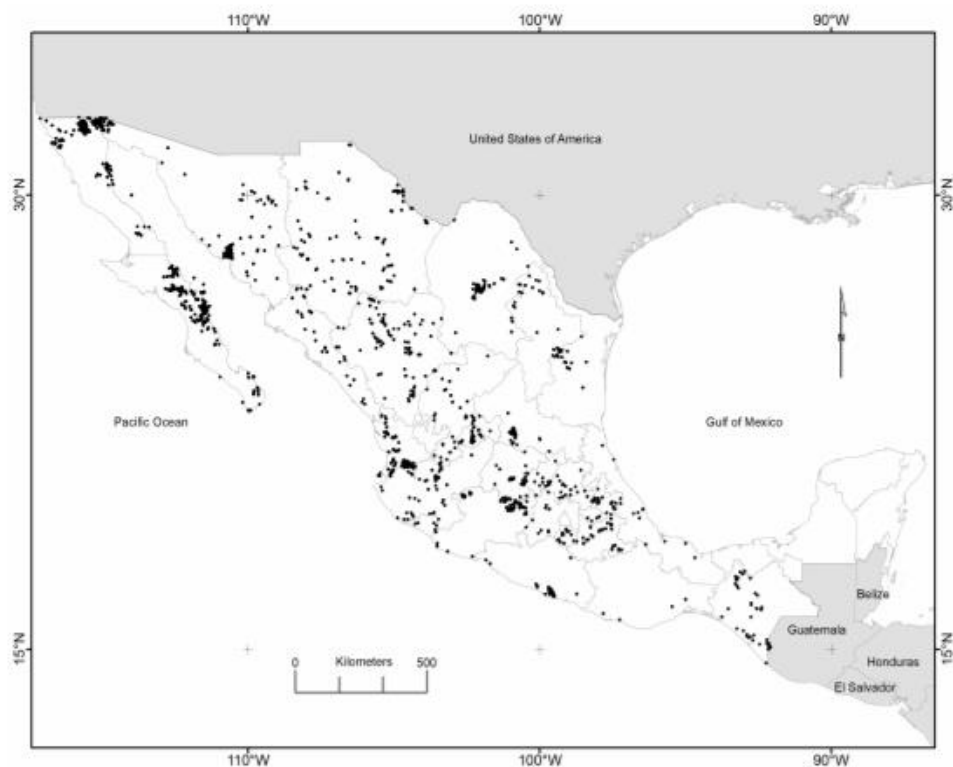
Appendix Table 1. New heat flow data produced by temperature gradient measurement (Grad-T-this work); temperature gradient from references (Grad-T-a,b,...) and recalculation of heat flow data with additional information (Rec-f). Thermal conductivity based on well lithology or crustal average (*) / Tabla 1 del apéndice. Nuevos datos de flujo de calor producidos a partir de mediciones de gradiente de temperatura (Grad-T- este trabajo); gradiente de temperatura de referencias (Grad-T-a,b,...) y nuevos cálculos de datos de flujo de calor con información adicional (Rec-f). La conductividad térmica se tomó de la litología del pozo o bien del valor promedio de la corteza(*).

Data #	Data production	Site ID	Long.	Lat.	Depth (m)	Geoth. Grad. (C/Km)	Conductivity (W/mK)	Heat Flow (mW/m ²)
1	Grad-T-this work	Fraile I	-101.33430	25.02550	334	20.0	2.50*	50.1
2	Grad-T-this work	Difunita	-101.19090	25.06305	509	28.5	2.50*	71.2
3	Grad-T-this work	Texcoco	-98.84960	19.50729	337	29.4	2.50*	73.6
4	Grad-T-a	1	-100.66489	19.79216	2159	139.7	1.87	261.3
5	Grad-T-a	3	-100.68695	19.80533	2440	99.3	1.84	182.3
6	Grad-T-a	12	-100.67013	19.79218	898	256.6	1.87	479.8
7	Grad-T-a	16	-100.67021	19.77975	2500	132.7	1.87	248.1
8	Grad-T-a	18	-100.65425	19.78473	1324	214.4	1.87	401.0
9	Grad-T-a	19	-100.66752	19.82438	1663	154.8	1.87	289.4
10	Grad-T-a	21	-100.67644	19.82662	1705	153.7	1.87	287.4
11	Grad-T-a	22	-100.66094	19.78968	1246	215.5	2.17	467.6
12	Grad-T-a	23	-100.67494	19.79773	1729	141.8	1.87	265.1
13	Grad-T-a	25	-100.66305	19.79787	1600	182.2	1.75	318.9
14	Grad-T-a	26	-100.65038	19.79787	1240	201.8	1.77	356.5
15	Grad-T-a	31	-100.64631	19.78205	1295	221.6	1.87	414.4
16	Grad-T-a	34	-100.65916	19.78459	860	292.6	1.87	547.2
17	Grad-T-a	35	-100.65424	19.79059	1225	220.4	1.87	412.1
18	Grad-T-a	37	-100.67064	19.78603	859	241.7	1.87	452.0
19	Grad-T-a	43	-100.65931	19.82277	1500	185.6	1.87	347.0
20	Grad-T-a	44	-100.68244	19.82122	2440	88.7	1.87	165.9
21	Grad-T-a	46	-100.66807	19.78246	970	258.0	1.87	482.4
22	Grad-T-a	47	-100.66438	19.78621	2957	102.9	1.89	194.5
23	Grad-T-a	48	-100.66403	19.82548	2669	93.2	1.87	174.3
24	Grad-T-a	49	-100.65831	19.81669	2400	126.1	1.87	235.9
25	Grad-T-a	51	-100.66252	19.83178	1842	158.9	1.87	297.1
26	Grad-T-a	53	-100.66228	19.82938	1201	201.0	1.87	375.8
27	Grad-T-a	54	-100.68695	19.81525	898	211.2	1.87	395.0
28	Grad-T-a	55	-100.65800	19.78985	1403	206.1	1.87	385.4
29	Grad-T-a	56	-100.67200	19.81009	2305	113.2	1.87	211.7
30	Grad-T-a	57	-100.67038	19.82422	1722	156.8	1.87	293.3
31	Grad-T-a	E1	-100.72993	19.82779	1995	94.8	1.87	177.3
32	Grad-T-a	E2	-100.71824	19.80483	1992	106.5	1.87	199.2
33	Grad-T-b	Pozo No. 4	-99.69570	20.56765	372	161.3	2.43	392.0
34	Grad-T-b	Pozo No. 5	-99.68648	20.57404	460	144.4	2.43	351.0
35	Grad-T-c	1	-110.67043	28.05821	90	28.7	2.50*	71.7
36	Grad-T-c	2	-110.70826	28.01467	71	89.5	2.50*	223.8
37	Grad-T-c	3	-110.68684	28.10318	109	79.0	2.50*	197.5
38	Grad-T-c	4	-110.67828	28.17314	136	101.4	2.50*	253.5
39	Grad-T-c	5	-110.69827	27.94543	124	41.7	2.50*	104.2
40	Grad-T-c	6	-110.61832	28.34803	147	197.4	2.50*	493.4

41	Grad-T-c	7	-110.73610	28.09105	98	49.7	2.50*	124.2
42	Grad-T-c	8	-110.77607	28.02966	61	94.6	2.50*	236.6
43	Grad-T-c	9	-110.74538	28.01253	89	36.0	2.50*	90.1
44	Grad-T-c	10	-110.67899	28.14601	149	103.1	2.50*	257.8
45	Grad-T-d	PR2	-103.53115	20.66423	1988	114.9	2.17	249.3
46	Grad-T-d	PR8	-103.52068	20.66012	1855	137.3	2.24	307.5
47	Grad-T-d	PR10	-103.51935	20.66183	2086	107.0	1.99	213.0
48	Grad-T-d	PR11	-103.52418	20.65634	2125	77.7	2.24	174.1
49	Grad-T-e	M203	-115.18686	32.39283	3958	114.4	2.42	277.0
50	Rec-f	MEX001	-115.34450	32.44840	1825	18.0	2.86	51.5
51	Rec-f	MEX002	-115.34500	32.43200	2200	11.7	2.50*	29.3
52	Rec-f	MEX003	-111.41250	26.25000	500	12.5	2.55	31.9
53	Rec-f	MEX004	-111.53500	26.24000	500	50.8	2.50*	126.9
54	Rec-f	MEX006	-103.52694	20.29167	1950	29.1	2.50*	72.8
55	Rec-f	MEX007	-103.53333	20.32278	800	49.4	2.07	102.0
56	Rec-f	MEX010	-103.51889	20.65639	2271	125.6	2.12	266.3
57	Rec-f	MEX011	-104.69500	21.11667	1911	102.5	2.50	256.3
58	Rec-f	MEX012	-104.72917	21.08333	200	53.2	2.50*	133.0
59	Rec-f	MEX013	-104.71667	21.10000	430	103.6	2.50*	259.0
60	Rec-f	MEX014	-104.54942	21.09294	2801	29.2	2.32	67.5
61	Rec-f	MEX015	-104.70167	21.18750	1911	52.4	3.05	159.7
62	Rec-f	MEX017	-112.55622	27.50772	2500	69.0	2.48	171.3
63	Rec-f	MEX018	-112.55890	27.50643	2505	94.6	2.37	224.3
64	Rec-f	MEX019	-112.53444	27.49995	1250	133.8	2.33	311.9
65	Rec-f	MEX022	-97.45561	19.66426	1810	203.0	2.09	424.0
66	Rec-f	MEX023	-97.44878	19.64046	2300	74.0	3.14	232.4
67	Rec-f	MEX024	-97.46761	19.69002	1670	230.8	2.10	484.6
68	Rec-f	MEX025	-97.45516	19.68642	1880	90.8	2.08	188.5
69	Rec-f	MEX027	-97.45619	19.67156	2310	152.7	2.22	338.8
70	Rec-f	MEX028	-97.45859	19.67629	2350	141.5	2.09	295.4
71	Rec-f	MEX030	-97.45383	19.67615	2160	123.6	2.20	272.4
72	Rec-f	MEX031	-97.44904	19.68564	2480	212.0	2.17	459.5
73	Rec-f	MEX032	-97.43770	19.64594	3100	165.9	2.41	399.4
74	Rec-f	MEX036	-97.45157	19.69623	2265	164.8	2.15	354.1
75	Rec-f	MEX037	-97.42717	19.63703	2903	98.5	2.14	210.7
76	Rec-f	MEX038	-97.44618	19.67845	2292	225.7	2.20	496.6
77	Rec-f	MEX039	-97.44182	19.68603	2402	236.6	2.12	501.5
78	Rec-f	MEX040	-97.45165	19.70603	2220	134.3	2.28	305.8
79	Rec-f	MEX041	-97.47294	19.69864	1500	189.6	2.56	485.8
80	Rec-f	MEX042	-97.43386	19.66764	2620	167.6	2.30	385.5
81	Rec-f	MEX043	-97.42156	19.64476	3270	109.7	2.23	245.1
82	Rec-f	MEX044	-97.44875	19.68839	2577	155.7	2.19	341.4
83	Rec-f	MEX045	-97.45558	19.68937	2200	120.5	2.43	293.2
84	Rec-f	MEX047	-97.45598	19.70020	1926	173.3	2.13	369.8
85	Rec-f	MEX048	-97.44844	19.69112	2200	162.3	2.09	339.9
86	Rec-f	MEX050	-97.44533	19.68354	1800	209.3	2.21	462.4
87	Rec-f	MEX051	-97.46339	19.69418	1700	234.6	2.20	515.5
88	Rec-f	MEX052	-97.44914	19.68528	1800	216.7	2.04	442.7
89	Rec-f	MEX055	-97.44185	19.64813	2500	84.3	2.21	186.2
90	Rec-f	MEX057	-97.43990	19.64801	2200	173.1	2.11	364.8
91	Rec-f	MEX058	-97.44226	19.65002	2200	184.4	2.17	400.5
92	Rec-f	MEX059	-97.46233	19.69116	2200	192.2	2.57	493.3
93	Rec-f	MEX060	-98.14294	19.92120	2000	143.5	2.98	426.8
94	Rec-f	MEX061	-98.13815	19.92339	1900	107.2	2.46	263.2
95	Rec-f	MEX064	-113.02362	25.98614	2244	25.1	2.19	55.0
96	Rec-f	MEX065	-111.84375	25.37281	3014	26.1	2.45	63.9
97	Rec-f	MEX066	-111.92245	24.88475	2500	32.4	2.36	76.5
98	Rec-f	MEX067	-111.72009	24.89025	2657	29.3	2.66	77.9
99	Rec-f	MEX068	-113.73551	27.65183	2405	34.9	1.90	66.3
100	Rec-f	MEX069	-114.88719	28.29299	2811	28.1	2.50*	70.3
101	Rec-f	MEX071	-111.88591	25.70630	3300	17.9	2.21	39.4

102	Rec-f	MEX072	-113.71727	27.63163	2325	37.1	2.36	87.7
103	Rec-f	MEX073	-114.51855	30.51737	3191	41.7	2.25	93.7
104	Rec-f	MEX074	-113.91369	27.92988	3298	30.2	2.45	74.1
105	Rec-f	MEX075	-115.03122	32.29032	3843	52.8	2.41	127.1
106	Rec-f	MEX076	-114.23769	31.38266	4799	29.9	2.57	76.7
107	Rec-f	MEX077	-114.27832	31.34619	3302	25.1	2.50*	62.7
108	Rec-f	MEX078	-114.21425	31.37561	3300	27.1	2.50*	67.7
109	Rec-f	MEX079	-113.87737	28.00498	1944	25.0	2.27	56.8
110	Rec-f	MEX080	-113.40627	27.50679	3000	19.5	2.26	44.1
111	Rec-f	MEX081	-113.84537	27.96591	2503	32.7	2.44	79.7
112	Rec-f	MEX082	-114.19665	30.83823	4930	51.3	2.50*	128.2
113	Rec-f	MEX083	-113.70833	27.51782	1363	41.8	2.48	103.7
114	Rec-f	MEX084	-113.38321	27.06762	4600	25.8	2.50*	64.5
115	Rec-f	MEX086	-111.83968	25.37540	4424	17.4	2.22	38.5
116	Rec-f	MEX087	-112.43983	25.76848	4505	25.6	2.19	56.0
117	Rec-f	MEX088	-111.98696	25.07088	3762	33.4	2.11	70.4
118	Rec-f	MEX089	-113.72808	27.58101	2750	34.3	2.29	78.6
119	Rec-f	MEX090	-114.09778	31.29304	3302	31.6	2.63	83.0
120	Rec-f	MEX091	-113.88876	31.11501	4340	47.3	2.23	105.7
121	Rec-f	MEX092	-113.79516	27.68947	3270	19.6	2.50*	49.1
122	Rec-f	MEX093	-113.18670	27.10718	3002	55.4	2.50*	138.6
123	Rec-f	MEX094	-112.87839	29.63975	4813	59.6	2.50*	149.1
124	Rec-f	MEX095	-113.75645	27.66715	2985	30.8	2.50*	77.0
125	Rec-f	MEX096	-113.90057	27.95947	2636	31.5	2.50*	78.8
126	Rec-f	MEX097	-114.65351	28.39972	4450	28.6	2.50*	71.5
127	Rec-f	MEX098	-114.76003	32.37662	2918	29.9	2.57	76.9
128	Rec-f	MEX099	-114.19423	31.26245	5591	23.3	2.47	57.4
129	Rec-f	MEX100	-110.25876	27.18580	2471	30.7	2.36	72.5
130	Rec-f	MEX101	-114.61628	31.80176	5325	27.2	2.49	67.7
131	Rec-f	MEX102	-114.94561	32.00882	4530	35.0	2.55	89.1
132	Rec-f	MEX103	-114.36411	31.62076	3872	33.3	2.50*	83.3
133	Rec-f	MEX104	-114.75972	32.00861	5152	44.1	2.50*	110.3
134	Rec-f	MEX105	-114.38430	31.79458	3887	29.4	2.42	71.2
135	Rec-f	MEX106	-104.73863	28.88995	6509	31.9	2.24	71.3
136	Rec-f	MEX107	-105.02839	28.46334	3903	30.2	2.16	65.2
137	Rec-f	MEX108	-100.97323	27.42872	3038	35.4	3.18	112.7
138	Rec-g	UNAM-5	-89.77927	20.38739	335	24.8	2.00	49.5

Appendix Figure 1



Appendix Figure 1. Map of hydrothermal manifestations in Mexico. (After: Iglesias et al., 2015; Prol-Ledesma & Arango-Galván, 2017) / Figura 1 del apéndice.
Mapa de las manifestaciones hidrotermales en México.

6.2 Geostatistical mapping of the depth to the bottom of magnetic sources and heat flow estimations in Mexico

(Published paper as second author at *Geothermics* journal)



Geostatistical mapping of the depth to the bottom of magnetic sources and heat flow estimations in Mexico

Juan Luis Carrillo-de la Cruz ^{a,b}, Rosa María Prol-Ledesma ^b, Gerald Gabriel ^{c,d,*}

^a Posgrado en Ciencias de la Tierra, Instituto de Geofísica, Universidad Nacional Autónoma de México, Circuito interior s/n, Coyoacán, 04510 Ciudad de México, México

^b Instituto de Geofísica, Universidad Nacional Autónoma de México, Circuito interior s/n, Coyoacán, 04510 Ciudad de México, México

^c Leibniz Institute for Applied Geophysics, Gilleweg 2, 30655 Hannover, Germany

^d Institut für Geologie, Leibniz Universität Hannover, Callinstrasse 30, 30167 Hannover, Germany

ARTICLE INFO

Keywords:
Curie temperature
Fractal magnetisation model
Conductive heat transfer
Geostatistical mapping
Crustal thermal structure

ABSTRACT

The depth to the bottom of magnetic sources (DBMS) is widely used as a proxy for crustal thermal structures. In this study, the DBMS is calculated using the spectral analysis of aeromagnetic data for the whole territory of Mexico. By assuming the DBMS to be related to the Curie point depth, the heat flow distribution is estimated. The DBMS and heat flow maps were constructed using geostatistical simulations to quantitatively determine standard deviation as uncertainty. The results show a good agreement with the complex geologic and tectonic setting in Mexico. Small DBMS values (high heat flow) as expected appear in areas where recent volcanism occurs and at seafloor spreading zones. In contrast, large values are present in tectonically stable zones.

1. Introduction

Different geophysical properties are studied to understand the Earth's dynamics, among them the thermal state of the crust. However, a lack of direct temperature measurements at depth hinders the knowledge of the Earth's crust thermal state. Therefore, other approaches to estimate the temperature are commonly used to evaluate the thermal regime at large depths, e.g., chemical geothermometers or Curie point depth estimations.

The estimation of the depth to the bottom of magnetic sources (DBMS), commonly used as a proxy of the Curie point depth (CPD), is a widely used approach for regional studies of the thermal structure of the Earth, when surface heat flow data are not available (Blakely, 1988; Bouligand et al., 2009; Ross et al., 2006; Tanaka et al., 1999).

In this study, the DBMS was calculated by the spectral analysis of aeromagnetic anomalies, using the modified centroid method with variable window size depending on the regional geological setting, and the construction of the DBMS map for Mexico was accomplished using geostatistical modeling, this way the uncertainties could be quantitatively determined. The resulting DBMS values were compared with surface heat flow (boreholes and seafloor) measurements to identify the relation between the borehole data and the DBMS calculation.

2. Materials and methods

To derive the depth to the bottom of magnetic sources (DBMS), the long wavelength part of the magnetic anomalies is studied in squared windows. For this reason, regional data is required that cover a sufficiently large area. Aeromagnetic data compilations or satellite magnetic data are the common datasets used for this purpose.

2.1. Aeromagnetic data

In this work, the North American Magnetic Anomaly Map (NAMAG, 2002) was used (Fig. 1). The NAMAG data is provided as 1-km grid, referred to the Decade of North American Geology projection (DNAG). For the compilation of the map, every data set was field continued to the common reference level of 305 m above terrain. Anomalies were calculated by subtracting the Definitive Geomagnetic Reference Field (DGRF), updated to every survey date, from the total magnetic field. This dataset was already used by several authors to calculate the DBMS, either for other North American countries or some isolated parts of Mexico, e.g., Bouligand et al. (2009), Campos-Enriquez et al. (2019), Carrillo-de la Cruz et al. (2020a, 2020b), Manea and Manea (2011), and Wang and Li (2015).

* Corresponding author.

E-mail address: gerald.gabriel@leibniz-liag.de (G. Gabriel).

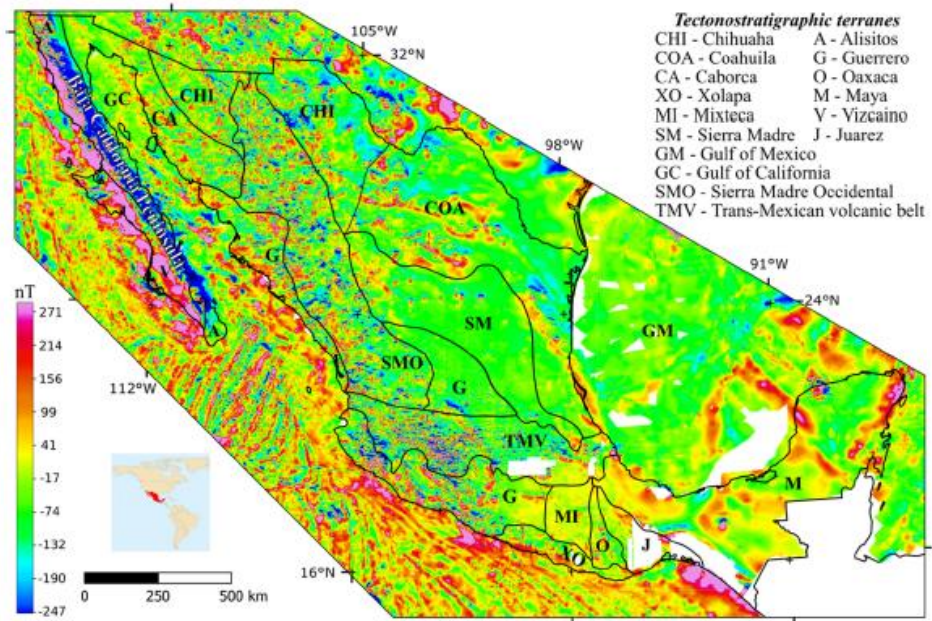


Fig. 1. Tectonostratigraphic terranes (modified after Campa and Coney, 1983) and the relevant part of the Magnetic Anomaly Map of North America (data from the North American Magnetic Anomaly Group NAMAG, 2002). White areas represent lack of magnetic data.

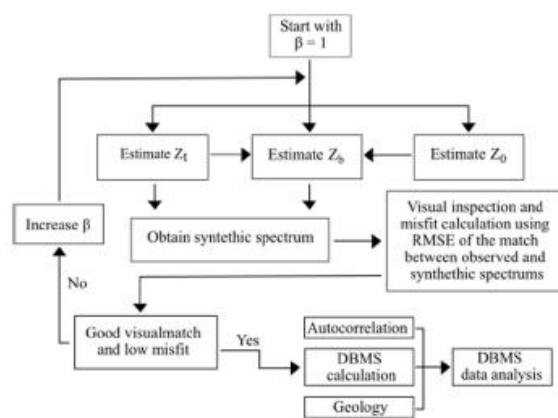


Fig. 2. Flowchart for the DBMS calculation in the present study (modified from Salem et al., 2014; Martos et al., 2017).

2.2. Depth to the bottom of magnetic sources estimations

Several methods are available for the DBMS estimation. Recent studies suggest that the fractal magnetization model methods are the most reliable (Bansal et al., 2011; Bouligand et al., 2009; Carrillo-de la Cruz et al., 2020a; Kumar et al., 2020; Li et al., 2013). For this research, the DBMS (z_b) calculation for Mexico is carried out by using the modified centroid method (Carrillo-de la Cruz et al., 2020b; Li et al., 2013) because this method considers a fractal magnetization model. DBMS was calculated using an early version of MAGCPD program (Carrillo-de la Cruz et al., 2020b).

To estimate the depth to the top (z_t) and the centroid (z_0) of the

magnetic sources, it is necessary to analyze the slope of a straight-line that fits the middle and low wavenumber parts of the amplitude spectrum and the scaled amplitude spectrum, respectively. Subsequently, the DBMS (z_b) is estimated by using Eq. (1).

$$z_b = 2z_0 - z_t \quad (1)$$

From an iterative forward modeling, z_t , z_0 and z_b are calculated by using different values of the fractal parameter (β) and wavenumber ranges of the spectra. The fractal parameter is related to the 3-D power spectrum ϕ_m of the magnetization by $\phi_m(k_x, k_y, k_z) \propto k^{-\beta}$. To get reliable DBMS results, the root-mean square error (RMSE), and the visual inspection of the similarity between the synthetic spectra (obtained by the forward modeling of the results) and the observed spectra, alongside with the autocorrelation function and the geology, are essential (Fig. 2). The method uncertainty is calculated by the approach of Martos et al. (2017) and depends on the standard deviation of the radial power spectrum (see Supplementary material).

To apply this methodology, it is mandatory to calculate the radially averaged amplitude spectrum from magnetic data within square windows. The suitable window size is still a matter of scientific discussion. For this reason, the windows size used to calculate the radially averaged amplitude spectrum is in general variable, i.e. between five to ten times the expected DBMS (Kumar et al., 2020; Ravat et al., 2007). The suitable size of every window depends on geology and the tectonic setting that affects the thermal state of the crust. Due to the complexity of the geological framework of Mexico, the present study considers the tectonostratigraphic terranes after Campa and Coney (1983) as the main generalization of the geological framework, because these terranes are closely related to the anomalies of the Earth's total magnetic field in Mexico (Fig. 1).

2.3. Heat flow estimations

DBMS is commonly used as a proxy for the Curie point depth that defines the depth where the crustal temperature exceeds the Curie

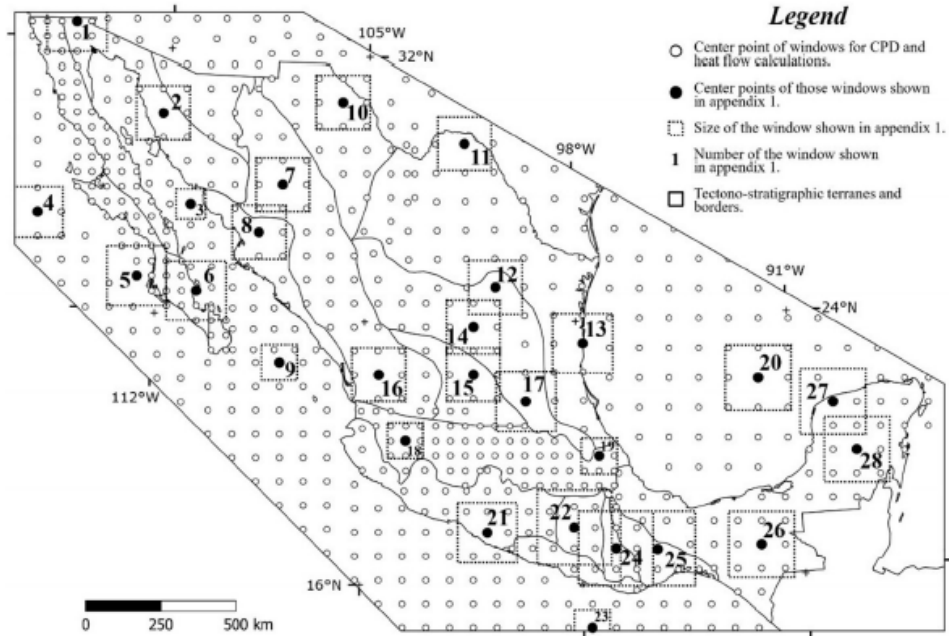


Fig. 3. Representative window size depending on the tectono-stratigraphic terranes presented in Fig. 1. Dots denote window centers and numbers indicate those windows that are part of the Supplementary material (Figure S1).

temperature of the magnetic minerals and, thus, the rocks become paramagnetic. The accepted convention is to use the Curie temperature of magnetite, which is 580 °C, as the reference Curie temperature.

The heat flow calculations in this study use a 1-D (vertical) steady-state heat conduction equation with heat production decreasing exponentially with depth (Turcotte and Schubert, 2002):

$$\lambda \frac{\partial^2 T(z)}{\partial z^2} = -H_0 e^{-(z-z_s)/h_r} \quad (2)$$

where λ is the thermal conductivity, T temperature, z_s Earth surface, z depth, H_0 heat production at the surface z_s , and h_r a scaling length for H_0 that decreases with depth.

By integrating Eq. (2) and applying the boundary conditions $z = z_b$ (CPD), $z_s = 0$ (surface), the heat flow becomes:

$$q_s = \frac{\lambda(T_c - T_0)}{z_b} + H_0 h_r - \frac{H_0 h_r^2}{z_b} (1 - e^{-(z_b/h_r)}) \quad (3)$$

with T_c being the Curie temperature at depth z_b and T_0 the temperature at the surface (Martos et al., 2017).

2.4. Stochastic simulations

The process of simulated alternative, equally probable, joint realization of the random variables in a random function model is called stochastic simulation (Deutsch and Journel, 1998). These stochastic simulations attempt to replicate reality using a model, which is the appropriate approach when constructing a map. The Sequential Gaussian Simulation (SGS) is used in this research to draw maps and assess the spatial variability of the DBMS and heat flow. SGS produces more accurate maps than kriging because it solves problems caused by the kriging method in terms of overestimated high values or underestimated low values. Details of the SGS algorithm are described by Cardellini et al. (2003), Deutsch and Journel (1998), and Pyrcz and

Deutsch (2014).

For the application of the SGS it is important to have a Gaussian distribution of the data. However, most data that describe geological processes do not fit this distribution; hence, data transformations are necessary. For this reason, the SGS algorithm follows these generalized steps (Pyrcz and Deutsch, 2014):

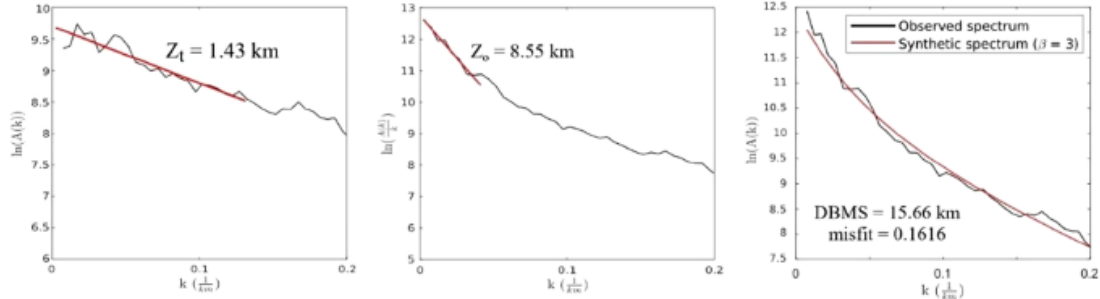
- Selection of the grid system and the coordinate system for the study area.
- Data input in the grid system.
- Normal Score Transformation, that is, the original data needs to be transformed into a normal space (Gaussian distribution).
- Calculation of the normal score semivariogram.
- Construction of the conditional distribution using kriging.
- Calculation of a simulated value using the conditional distribution.
- Simulated value input in the grid.
- Verification of all locations in the grid randomly.
- Validation of the simulated data using the histogram $N(0, 1)$ and the normal score semivariogram.
- Transformation of the data to the original Cumulative Distribution Function (CDF).
- Recalculation of the simulation using random numbers.

The results are shown as expected value models (also called e-type models) and conditional variance models pixel-by-pixel.

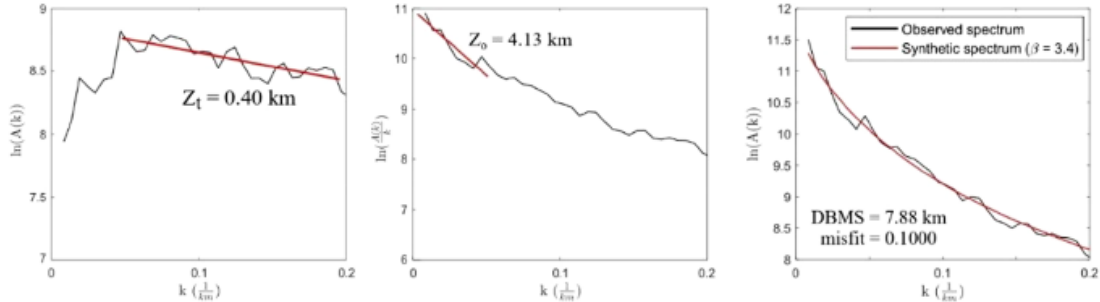
3. Applications

The methodology to construct the regional DBMS and heat flow maps of the continental and the marine region of Mexico includes the spectral analysis of aeromagnetic data, heat flow calculation and the statistical analysis of the results using the Sequential Gaussian Simulation.

Window 5



Window 16



Window 24

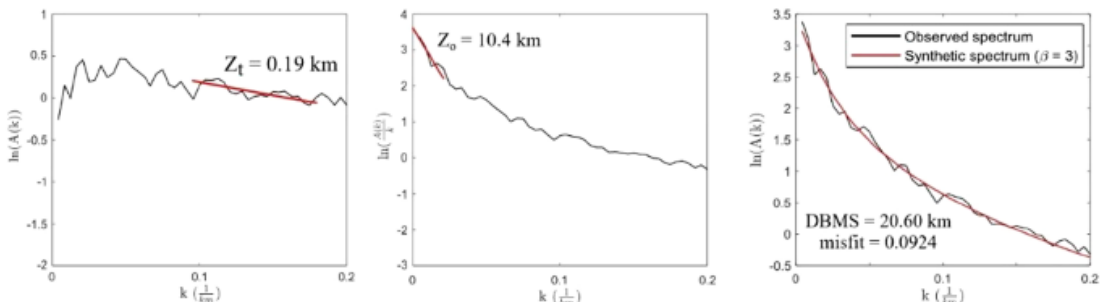


Fig. 4. Examples of windows located in different tectonostratigraphic terranes, showing the wavenumber ranges used to calculate the DBMS and the adjust between the synthetic and the observed spectra in the forward modeling; z_t top of the magnetized layer, z_0 centroid depth, β fractal parameter.

3.1. Depth to the bottom of magnetic source calculation

The calculation of the DBMS involves several subsequent steps (see Supplementary material and Fig. 2). The size of the used windows is variable, depending on the geological environment. In areas where the CPD is expected to be shallow (e.g., volcanic areas or ocean spreading zones), a small square window size in the order of 100 km - 150 km is used, whereas in zones with an expected large CPD (e.g., the tectonically stable zones) a larger window size in the order of 200 km or more is used. The window size must be large enough to reveal the magnetic signatures caused by the deepest magnetic sources for each geological province. Fig. 3 shows Mexico's tectonostratigraphic terranes, the window size for the data analysis, and the number of the windows presented as representative examples in Figure S1 at Supplementary material.

The definition of the wavenumber ranges used to calculate the slopes in the amplitude spectra and the scaled amplitude spectra vary depending on the geological setting. Additionally, the complete homogeneity of each terrain in terms of its magnetization is not a realistic assumption. Consequently, the wavenumber ranges change slightly in the various calculations to ensure a reasonable adjustment of the synthetic spectrum to the original spectrum during the forward modeling. Figs. 4 and S1 present examples for the different slopes used.

The autocorrelation function in windows 5 and 6 (Figs. 5a and S1) reveal a NW-SW oriented ellipse, related to a strong trend caused by the Peninsular Range Batholith. Similarly, windows 23, 3, and 4 (Figs. 5b and S1) show a trend related to the ocean floor spreading magnetic strip geometry. In addition, an apparent data trend in window 13 (Fig. 5c) is related to the NW-SE striking high-amplitude anomaly caused by

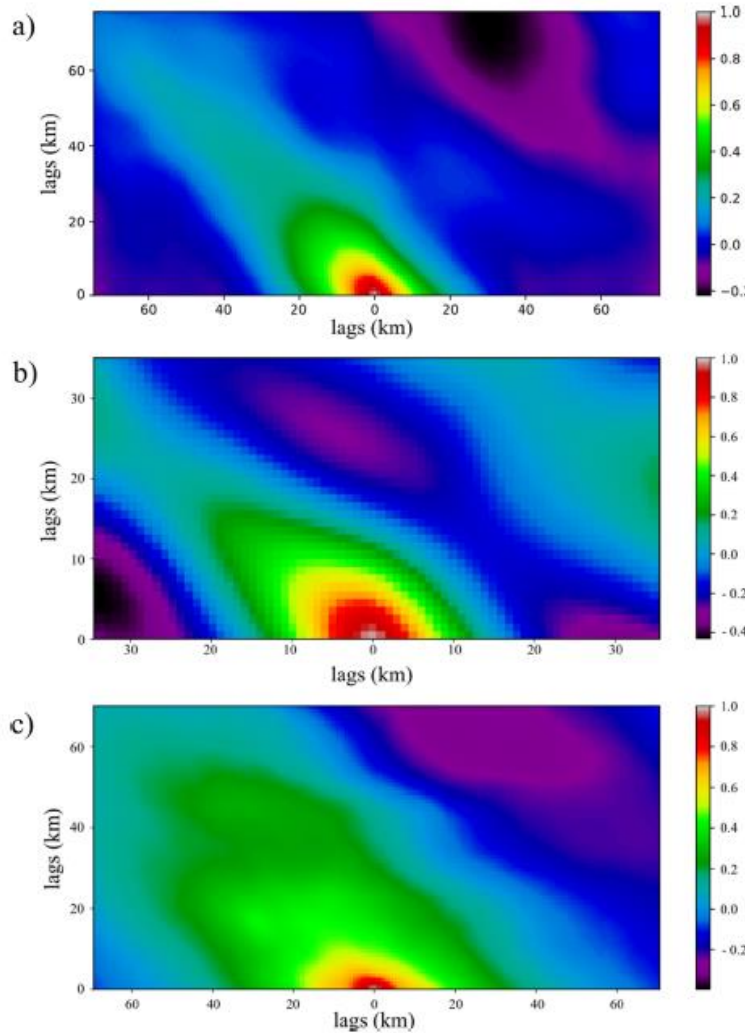


Fig. 5. Autocorrelation function: examples for a) window 5, b) window 23, and c) window 13.

basement structures of the Sierra Madre.

3.2. Heat flow estimations using the DBMS

The heat flow (Eq. (3)) is calculated using thermal parameter values as summarized in Table S2, considering the DBMS (ϕ_b) as the CPD, taking the Curie temperature of magnetite (580 °C), and a constant value for the scaling length h_r of 10 km (see Turcotte and Schubert, 2002). In Table S2, the values of thermal conductivity and heat generation rate are an average value for the representative rock types for each tectonostratigraphic terrane. To calculate the heat flow, it is necessary to subtract the reference height of the airborne data (305 m) from the DBMS results, because Eq. (3) is referred to surface.

3.3. Sequential gaussian simulation (SGS) application

The use of the geostatistical libraries (or GSLIB), published by Deutsch and Journel (1998), was essential for the realization of this

study. The simulation, using SGS, is applied using the GSLIB module *sgsim*. Following the theory behind *sgsim*, the data need to be analyzed statistically before performing each simulation. By using the semi-variogram, a regional trend was found in the data (Fig. S2 at Supplementary material). For this reason, the data need to be detrended and simulation is applied to the data residuals. From the one hundred simulations, the DBMS and heat flow map result, and by comparing the simulation models with the original data (Figs. S3 and S4 at Supplementary material), the simulations reproduce the original data with small fluctuations (see Supplementary material).

4. Results

Based on the spectral analysis of aeromagnetic anomalies and the application of the modified centroid method, DBMS and heat flow values were calculated for 722 windows of variable size. These values were analyzed using geostatistics to provide a map and examine the spatial patterns of the calculated DBMS and heat flow as well as their rela-

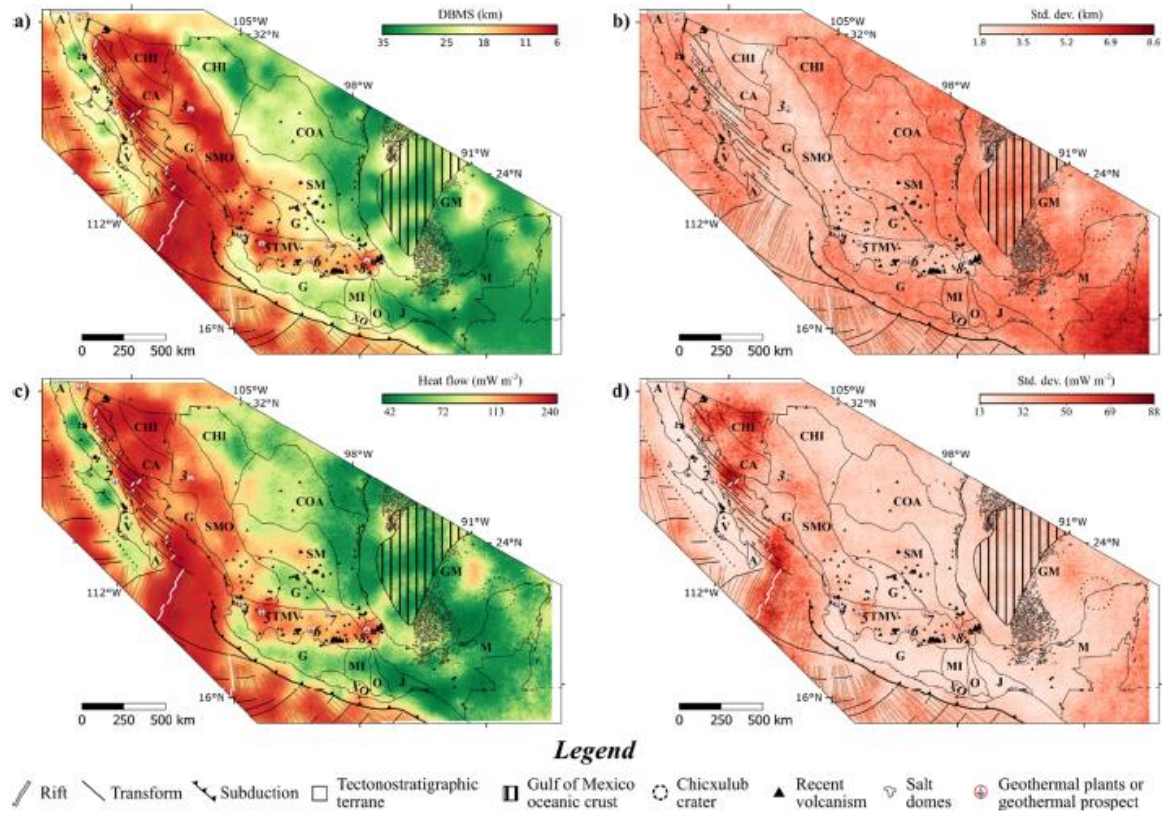


Fig. 6. a) DBMS e-type map, b) DBMS standard deviation map, c) heat flow e-type map, and d) heat flow standard deviation map with the main tectonic features. Tectonic features from the Tectonic Map of Mexico 2013 (Padilla y Sánchez et al., 2013). Geothermal plants and prospective geothermal areas: 1) Cerro Prieto, 2) Las Tres Virgenes, 3) Piedras de Lumbre-Maguarichic, 4) Domo San Pedro, 5) La Primavera-Cerritos Colorados, 6) Los Azufres, 7) Pathé, and 8) Los Humeros. Recent volcanoes (< 3 Ma) from Prol-Ledezma et al. (2018). Abbreviations from Fig. 1.

Table 1
Statistics for the entire study area.

Simulation	Original data			Simulation data		
	Mean	Std. dev.	5th–95th percentiles	Mean	Std. dev.	5th–95th percentiles
DBMS (km)	17.1	7.7	7.3–32.1	17.0	6.0	9.0–27.1
heat flow (mW m⁻²)	98.6	44.0	49.1–176.2	97.0	33.8	56.3–162.9

tionship to regional tectonics. Simulation results are presented as maps of the e-type DBMS and heat flow (Fig. 6). From the e-type models, the average heat flow of the continental part of Mexico is $85 \pm 27 \text{ mW m}^{-2}$, exceeding the global continental average of 64.7 mW m^{-2} (Davies, 2013) by more than 30%. In contrast, the average values for the oceanic part of Mexico are $103 \pm 39 \text{ mW m}^{-2}$, an average value slightly above the global oceanic average of 95.9 mW m^{-2} (Davies, 2013). Table 1 shows the statistics of the entire study area and reveals that the fluctuations between the 722 windows and the simulation results are small.

The results show that the variations of DBMS and heat flow are related to the main tectonic features, e.g., the shallower DBMS and the highest heat flow occur in spreading zones and regions of recent volcanic activity.

5. Discussion

The wavenumber ranges used to obtain ε_t and ε_0 depend on the characteristics of the slopes of the spectra and the adjustment between the observed amplitude spectra and the synthetic spectra. These considerations are different for every geological terrane, and frequently in the same terrane the wavenumber range differs between two analyzed windows. The pre-analysis of the spectra in terms of the autocorrelation function of the aeromagnetic data helps to find trends in the data. Some geological structures cause significant trends in the magnetic data, e.g., the trend related to the Peninsular Range Batholith (Baja California peninsula) and the ocean spreading zones. In both cases, the DBMS result could be biased and does not totally represent the CPD.

Active tectonic zones and the presence of recent volcanism are related with small DBMS and high heat flow values. The main volcanic terranes (Sierra Madre Occidental and Trans-Mexican Volcanic belt terranes) show a direct correlation between small DBMS (and high heat flow values) and recent volcanic activity. At Sierra Madre Occidental terrane, the thermal anomalies could be related with volcanism and the high content of radioactive elements (U, Th, and K) that contributes more than 30% to the surface heat flow (Smith et al., 1979).

For the Gulf of California, shallow DBMS is related with the rifting process, and the heat flow values derived from the DBMS are above 200 mW m^{-2} . At the center of the Baja California peninsula (Alisitos and Vizcaino terranes), the deepest DBMS values ($> 20 \text{ km}$) are possibly

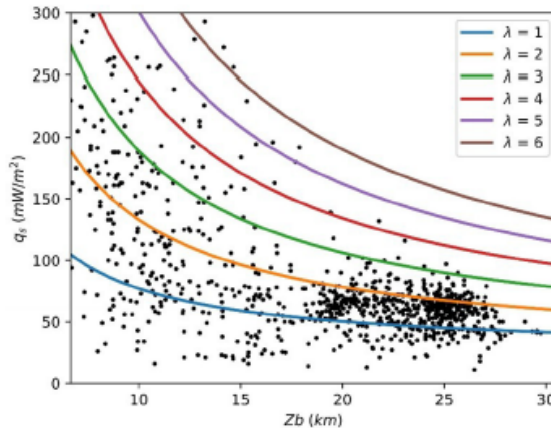


Fig. 7. Scatterplots of heat flow from boreholes and seafloor vs. DBMS ($r^2 = 0.32$). Colored lines indicate the relations when applying Eq. (3) for different thermal conductivities ($\text{in } \frac{\text{W}}{\text{m K}}$), 580 °C as Curie temperature, 20 °C as the surface temperature, $2.5 \frac{\text{dW}}{\text{m}^3}$ as heat generation rate, and h_c of 10 km. Sources: heat flow data from Prol-Ledesma et al. (2018) and SMU Node of National Geothermal Data (SMU, 2020). Boreholes and seafloor heat flow data distribution is presented in figure S5 in Supplementary material.

related to the presence of the Farallon-remnant fossil slab (Wang et al., 2013).

South of the Trans-Mexican Volcanic belt terrane, at the Guerrero, Mixteca, Oaxaca, Juarez and Xolapa terranes, the DBMS values are larger than 18 km ($< 75 \text{ mW m}^{-2}$), showing a pattern similar to that obtained by Okubo et al. (1989) for a subduction zone, where the heat flow next to the volcanic front starts to decrease. This decrease in the heat flow values is produced by the flat-slab regime in a temperature decrease caused by the plate cooling, as was also obtained in previous research (Manea and Manea, 2011).

Our DBMS results for the Gulf of California are similar to the results presented by Campos-Enríquez et al. (2019); nevertheless, our results yield deeper values for DBMS in some areas of the Baja California peninsula. Alternatively, at the Guerrero, Mixteca, Oaxaca, Juarez and Xolapa terranes, our results are in the range of ~ 20 to 30 km, that are consistently deeper than those presented by Manea and Manea (2011) (~ 16 to 24 km). In both cases, the difference between DBMS calculations could be related with the methodology and the wavenumber range employed. For example, Manea and Manea (2011) used a constant wavenumber range, while in our study it is variable depending on the geological framework. Campos et al. (2019) do not present an error estimation map, while Manea and Manea (2011) present only the map for the σ_0 error estimation. The conditional standard deviation derived from Sequential Gaussian Simulations (Fig. 5b and 5d) defines the map uncertainty; it is worth to mention that the uncertainty maps for DBMS and heat flow have not been presented by previous studies of DBMS calculations from aeromagnetic data in Mexico.

The use of geostatistical simulations in DBMS and heat flow mapping allows ascertaining the statistical variability of every estimated value in the map. The advantage of using geostatistical simulations in comparison to other interpolation methods (e.g., kriging) is the uncertainty quantification as standard deviation maps.

The heat transfer mechanism is the most important parameter in the calculation of the heat flow. Guerrero-Martínez et al. (2020) used the DBMS as a boundary condition to simulate heat transfer in the Acoculco caldera, located at the Trans-Mexican Volcanic Belt. Their results show that local heat sources would not be evident in a regional model, i.e., on the scale on which the DBMS is calculated. Similarly, the intense

convection in the Cerro Prieto hydrothermal system that promotes a more efficient heat transport and the DBMS values calculated for Cerro Prieto (~15 km) do not reproduce the 79–90 °C/km geothermal gradient (expected DBMS ~7 km) measured from wells (Prol-Ledesma et al., 2016). The convection effects in the geothermal gradient are not expressed in the results of heat flow estimation using DBMS/CPD, as observed in other DBMS/CPD calculations for Cerro Prieto (Campos-Enríquez et al., 2019).

Heat flow calculations based on DBMS values were compared with heat flow data from boreholes and seafloor data (Figure S5 in Supplementary material); the theoretical curves in Fig. 7 result from Eq. (3). The in-situ data have a wide scattering, showing a similar trend than those presented in other studies (Li et al., 2010, 2013; Wang and Li, 2015). Fig. 7 shows that most data cluster on theoretical curves that corresponds to thermal conductivities between 1 and $3 \frac{\text{W}}{\text{m K}}$. The data scattering in relation with the presented theoretical curves is consistent with changes of the thermal parameters at depth (Curie temperature, thermal conductivity, and/or heat generation rate) or different heat transfer mechanisms.

6. Conclusions

The depths to the bottom of the magnetic sources (DBMS) of Mexico were calculated by using a combination of the modified centroid method and forward modeling of the radially averaged amplitude spectrum. Heat flow is estimated based on the DBMS derived from magnetic anomaly data. Finally, the DBMS and heat flow maps of Mexico were generated by applying for the first-time geostatistical simulations. The most important conclusions derived with respect to the methodology and geological interpretations are:

- The autocorrelation function characteristics turned out to be an important tool to analyze trends in magnetic data that could affect the DBMS calculations.
- The lower and middle wavenumber range used to calculate the top and centroid of the magnetic sources are selected depending on the detectable slopes in the spectra; the spectra change, depending on the geological setting. The selection of wavenumber ranges affects the forward modeling.
- Geostatistical simulations, firstly applied in this study in the context of the DBMS, provide a robust quantification of the spatial patterns and the spatial uncertainties.
- The effective thermal conductivity of Mexico is between 1 and $3 \frac{\text{W}}{\text{m K}}$, and the presence of different heat transfer mechanism at local scale affect the relation between DBMS and heat flow from borehole and seafloor data (Fig. 7).
- For hydrothermal reservoirs, the DBMS values differ significantly from the borehole data due to heat being transferred convectively as well as conductively in the hydrothermal reservoirs. This is shown for two active geothermal fields (Cerro Prieto and Acoculco).
- For this study, the estimated average heat flow value for the continental part of Mexico is significantly higher than the global continental average, whereas the averaged estimated heat flow value for the oceanic part of the study area is only slightly higher than the global average. This is interpreted as a consequence of two effects: active sea floor spreading in extensive areas in the western Pacific areas nearby Mexico and the low heat flow and large DBMS in the Gulf of Mexico.

CREDIT authorship contribution statement

Juan Luis Carrillo-de la Cruz: Methodology, Formal analysis, Writing – original draft. Rosa María Prol-Ledesma: Conceptualization, Supervision, Writing – review & editing. Gerald Gabriel: Supervision, Methodology, Writing – review & editing.

Declaration of Competing Interest

The authors declare that they have no known competing financial interests or personal relationships that could have appeared to influence the work reported in this paper.

Role of the funding source

The funding source was the SENER-CONACyT (Mexico) Fondo de Sustentabilidad through the project CeMIE-Geo P-01. It was neither involved in the project activities nor in the decision to submit this article for publication in Geothermics.

Funding

Funding source was the SENER-CONACyT (Mexico) Fondo de Sustentabilidad Grant 207032 of the Centro Mexicano de Innovación en Energía Geotérmica (CeMIE-Geo) project P-01 to R.M. Prol-Ledesma and the CONACyT PhD fellowship 478768. Part of the work was conducted during a seven-month research visit (Juan Luis Carrillo-de la Cruz) at the Leibniz Institute for Applied Geophysics.

Acknowledgments

The authors thank Augusto Rodriguez, Diana Nuñez and two anonymous reviewers for their positive comments that helped to improve the manuscript. The QGIS contributors are thanked for the free distribution of the software that was used in the map creation. Funding by CONACyT of the PhD fellowship of the first author is much appreciated.

Supplementary materials

Supplementary material associated with this article can be found, in the online version, at [doi:10.1016/j.geothermics.2021.102225](https://doi.org/10.1016/j.geothermics.2021.102225).

References

- Bansal, A.R., Gabriel, G., Dini, V.P., Krawczyk, G.M., 2011. Estimation of depth to the bottom of magnetic sources by a modified centroid method for fractal distribution of sources: an application to aeromagnetic data in Germany. *Geophysics* 76 (3), L11–L22. <https://doi.org/10.1190/1.3560017>.
- Blakely, R.J., 1988. Curie temperature isotherm analysis and tectonic implications of aeromagnetic data from Nevada. *J. Geophys. Res. Solid Earth* 93 (B10), 11817–11832. <https://doi.org/10.1029/JB093B10p11817>.
- Bouligand, C., Glen, J.M.G., Blakely, R.J., 2009. Mapping Curie temperature depth in the western United States with a fractal model for crustal magnetization. *J. Geophys. Res.* 114, B11104. <https://doi.org/10.1029/2009jb006494>.
- Campa, M.P., Coney, P.J., 1993. Tectono-stratigraphic terranes and mineral resource distributions in Mexico. *Can. J. Earth Sci.* 20, 1040–1051. <https://doi.org/10.1139/e93-094>.
- Campos-Enriquez, O.C., Espinosa-Cardeña, J.M., Osukum, O., 2019. Subduction control on the Curie isotherm around the Pacific-North America plate boundary in northwestern Mexico (Gulf of California). Preliminary results. *J. Volcanol. Geothermal Res.* 375, 1–17. <https://doi.org/10.1016/j.volgeores.2019.03.005>.
- Cardellini, C., Chioldini, G., Frondini, F., 2003. Application of stochastic simulation to CO₂ flux from soil: mapping and quantification of gas release. *J. Geophys. Res.* 108 (B9), 2425. <https://doi.org/10.1029/2002JB002165>.
- Carrillo-de la Cruz, J.L., Prol-Ledesma, R.M., Gómez-Rodríguez, D., Rodríguez-Díaz, A. A., 2020a. Analysis of the relation between bottom hole temperature data and Curie temperature depth to calculate geothermal gradient and heat flow in Coahuila, Mexico. *Tectonophysics* 700, 220397. <https://doi.org/10.1016/j.tecto.2020.220397>.
- Carrillo-de la Cruz, J.L., Prol-Ledesma, R.M., Velázquez-Sánchez, P., Gómez-Rodríguez, D., 2020b. MAGCPD: a MATLAB-based GUI to calculate the Curie point-depth involving the spectral analysis of aeromagnetic data. *Earth Sci. Inf.* <https://doi.org/10.1007/s12145-020-00526-x>.
- Davies, J.H., 2013. Global map of solid Earth surface heat flow. *Geochem. Geophys. Geosyst.* 14 (10), 4600–4622. <https://doi.org/10.1029/ggpe.20271>.
- Deutsch, C.V., Journel, A.G., 1998. *GSLIB: Geostatistical Software Library and User Guide*. Oxford Univ. Press, New York, p. 369.
- Guerrero-Martínez, F.J., Prol-Ledesma, R.M., Carrillo-de la Cruz, J.L., Rodríguez-Díaz, A. A., González-Romo, I.A., 2020. A Three-Dimensional Temperature Model of the Acoculco caldera complex, Puebla, Mexico, from the Curie isotherm as a Boundary Condition, 86. *Geothermics*, 101794. <https://doi.org/10.1016/j.geothermics.2019.101794>.
- Kumar, R., Banal, A.R., Ghosh, A., 2020. Estimation of depth to bottom of magnetic sources using spectral methods: application on Iran's aeromagnetic data. *J. Geophys. Res. Solid Earth* 125, e2019JB018119. <https://doi.org/10.1029/2019JB018119>.
- Li, C.-F., Shi, X., Zhou, Z., Li, J., Geng, J., Chen, B., 2010. Depths to the magnetic layer bottom in the South China Sea area and their tectonic implications. *Geophys. J. Int.* 182 (3), 1229–1247. <https://doi.org/10.1111/j.1365-246X.2010.04702.x>.
- Li, C.-F., Wang, J., Lin, J., Wang, T., 2013. Thermal evolution of the North Atlantic lithosphere: new constraints from magnetic anomaly inversion with a fractal magnetization model. *Geochim. Geophys. Geosyst.* 14 (12), 5078–5105. <https://doi.org/10.1002/2013GC004096>.
- Manea, M., Manea, V.C., 2011. Curie point depth estimates and correlation with subduction in Mexico. *Pure Appl. Geophys.* 168, 1439–1499. <https://doi.org/10.1007/s00224-010-0230-2>.
- Martoo, Y.M., Catalán, M., Jordan, T.A., Golynsky, A., Golynsky, D., Eagles, O., Vaughan, D.O.D.C., 2017. Heat flux distribution of antarctica unveiled. *Geophys. Res. Lett.* 44 (22), 11417–11426. <https://doi.org/10.1029/2017GL075609>.
- North American Magnetic Anomaly Group (NAMAG), 2002. Digital Data Grids for the Magnetic Anomaly Map of North America. U.S. Geol. Surv. Open File Rep., pp. 02–414. <http://mrdata.usgs.gov/magnetic/>.
- Okubo, Y., Tsu, H., Ogawa, K., 1989. Estimation of Curie point temperature and geothermal structure of island arcs of Japan. *Tectonophysics* 159, 279–290.
- Padilla y Sánchez, R.J., Domínguez Trejo, I., López Ascárraga, A.G., Mota Nieto, J., Fuentes Menes, A.O., Roigique Narango, P., Germán Castellán, E.A., Campos Ariolla, S. E., 2013. National Autonomous University of Mexico Tectonic Map of Mexico GIS Project. American Association of Petroleum Geologists GIS Open Files series.
- Prol-Ledesma, R.M., Arango-Galván, C., Torres-Vera, M.A., 2016. Rigorous analysis of available data from cerro prieto and las tres virgenes geothermal fields with calculations for expanded electricity generation. *Nat. Resour. Res.* 25, 445–458. <https://doi.org/10.1007/s11053-016-9295-2>.
- Prol-Ledesma, R.M., Carrillo-de la Cruz, J.L., Torres-Vera, M.A., Membrillo-Abad, A.S., Espinoza-Ojeda, O.M., 2018. Heat flow map and geothermal resources in Mexico. *Terra Digitalis* 2 (2), 1–15. <https://doi.org/10.22301/igg.25940694.2018.2.51>.
- Pryce, M.J., Deutach, C.V., 2014. *Geostatistical Reservoir Modeling*, 2nd Ed. Oxford University Press, New York.
- Ravat, D., Pignatelli, A., Nicolosi, I., Champagni, M., 2007. A study of spectral methods of estimating the depth to the bottom of magnetic sources from near surface magnetic anomaly data. *Geophys. J. Int.* 169 (2), 421–434. <https://doi.org/10.1111/j.1365-246X.2007.03305.x>.
- Ross, H.E., Blakely, R.J., Zoback, M.D., 2006. Testing the use of aeromagnetic data for the determination of Curie depth in California. *Geophysica* 71 (5), L51–L59. <https://doi.org/10.1190/1.2335572>.
- Salem, A., Green, C., Ravat, D., Singh, K.H., East, P., Fairhead, J.D., Mogren, S., Biegert, E., 2014. Depth to Curie temperature across the central Red Sea from magnetic data using the de-fracta method. *Tectonophysics* 75–86. <https://doi.org/10.1016/j.tecto.2014.04.027>, 624–625.
- Smith, D.L., Nuckles III, C.E., Jones, R.L., Cook, G.A., 1979. Distribution of heat flow and radioactive heat generation in northern Mexico. *J. Geophys. Res.* 84 (B5), 2371–2379. <https://doi.org/10.1029/JB0041B05p02371>.
- SMU Node of national geothermal data system heat flow observation in content model format. <http://geothermal.smu.edu/static/DownloadFilesButtonPage.htm>. Accessed on February 25, 2020.
- Tanaka, A., Okubo, Y., Matubayashi, O., 1999. Curie point depth based on spectrum analysis of the magnetic anomaly data in East and Southeast Asia. *Tectonophysics* 306 (3–4), 461–470. [https://doi.org/10.1016/S0040-1951\(99\)00072-4](https://doi.org/10.1016/S0040-1951(99)00072-4).
- Turcotte, D.L., Schubert, G., 2002. *Geodynamics*. Cambridge University Press, p. 863.
- Wang, J., Li, C.-F., 2015. Crustal magnetism and lithospheric geothermal state of the western North America and their implications for magnetic mantle. *Tectonophysics* 630, 112–125. <https://doi.org/10.1016/j.tecto.2014.11.002>.
- Wang, Y., Forsyth, D.W., Ran, C.J., Carriero, N., Schmandt, B., Gaherty, J.B., Savage, B., 2013. Fossil slab attached to unsubducted fragments of the Farallon plate. *Proc. Nat. Acad. Sci.* 110, 5342–5347.

Conclusions

Conclusions

The main result of this thesis work is that two heat flow maps of Mexico were obtained. The first map was constructed with borehole and seafloor heat flow data, and the second map is the result of heat flow estimations using the depth to the bottom of magnetic sources (DBMS) calculation. An updated surface heat flow database was created using data compilations and analyzing temperatures profiles in this work. Finally, to obtain heat flow measurements in zones where boreholes were scarce or absent, geostatistical simulations of the heat flow estimations using the DBMS were computed. From the results obtained and considering the methodologies applied, the main conclusions are:

- The heat flow map made with the actual temperature gradient measurements in boreholes shows a good correlation with the main tectonic features and provides an excellent data base to calibrate the heat flow estimations based on DBMS calculations.
- The DBMS estimations by assuming random and uncorrelated magnetization yields unreal values. A fractal magnetization model is necessary to yield realistic DBMS calculations.
- The patterns of heat flow and geothermal gradient estimations from the DBMS and the average borehole data show correlation when the conduction is the primary heat transfer mechanism, and the heat generation rates are low or negligible.
- Wavenumber ranges used to calculate the centroid and the top of the magnetic source are strictly related to detectable slopes in the amplitude (or power) spectrum. The slope selections depend directly on the magnetic signal related to the geological setting. Forward modeling is essential to help in wavenumber range use.
- Geostatistical methods provide maps to analyze spatial patterns and quantify the uncertainties.
- The DBMS geostatistical simulation results are compared with the heat flow database, showing that Mexico's effective thermal conductivity is between 1 and $3 \frac{W}{mK}$. Besides, local changes in the heat transfer mechanisms affect the relationship between the DBMS the heat flow.
- In geothermal fields with intense hydrothermal convection, the estimated DBMS heat flow differs significantly from borehole heat flow measurements because the convection or the

combination of convection and conduction throughout an entire geothermal reservoir generate a more efficient heat transfer regime. Cerro Prieto and Acoculco geothermal fields are examples of this.

- Increasing the number of surface heat flow measurements in Mexico will improve better heat flow maps, supporting the estimations obtained from DBMS and delineating new geothermal prospects.
- Small DBMS values and high heat flow values are related to ocean floor spreading zones and recent volcanism. From the results obtained, it is possible to conclude that the main tectonic features control the heat flow patterns and DBMS distribution.

Supplementary Material

Content of this file

Methods to calculate Depth to the Bottom of Magnetic Sources.

Application of the Sequential Gaussian Simulation.

Figures S1 to S5.

Tables S1 and S2.

Introduction

This supplementary material file contains the description of the estimations of the depth to the bottom of magnetic sources (DBMS) and the statistical analysis using Sequential Gaussian Simulation. The tables compile the wavenumber ranges used to calculate the DBMS from different studies and the thermal parameters used to calculate heat flow depending on the tectonostratigraphic provinces. Moreover, this file contains examples of the autocorrelation function, the corrected amplitude spectra, the corrected scaled-amplitude spectra, the wavenumber ranges for calculating the top (z_t) and centroid (z_0) depth of the magnetic sources, the modeled spectra versus the original spectra and the results for the windows labeled in Figure 3. Finally, the spatial distribution of the heat flow data (boreholes and seafloor) used to compare the DBMS results in Figure 7 is presented.

Depth to the bottom of magnetic sources calculation

The calculation of the DBMS is carried out using the radially averaged amplitude spectrum of magnetic anomalies. Diverse methods have been developed and applied: the analysis of the peak of the amplitude spectrum (Bhattacharyya and Leu, 1975; Blakely, 1988; Connard et al., 1983; Shuey et al., 1977; Spector and Grant, 1970), the centroid method (Okubo et al., 1985; Tanaka et al., 1999), modeling the peak of the amplitude spectrum (Ross et al., 2006), and using a fractal magnetization model of the amplitude spectrum (Bansal et al., 2011; Bouligand et al., 2009; Li et al., 2013; Maus and Dimri, 1995; Pilkington and Todoeschuck, 1993; Salem et al., 2014).

The DBMS is calculated using the amplitude spectrum $A(k)$ of the magnetic anomalies. After Blakely (1995), the amplitude spectrum of a total magnetic field anomaly that is caused by an infinite horizontal layer of random magnetization is:

$$A(k_x, k_y) = 2\pi C_m A_m |\theta_m| |\theta_f| e^{-kz_t} (1 - e^{-k(z_b - z_t)}) \quad (1)$$

where k_x and k_y are the wavenumbers in x- and y-direction, C_m is a proportionality constant, A_m is the amplitude-density spectrum of the magnetization, θ_m is the directional factor related to the magnetization, θ_f is the directional factor related to the geomagnetic field, and Z_t and Z_b are the top and bottom of the magnetized horizontal layer, resp.

The 3-D fractal magnetization model has a power spectrum of magnetization proportional to the norm of the wavenumber raised to power $-\beta$ (Li et al., 2013):

$$\phi_m(k_x, k_y, k_z) \propto k^{-\beta} \quad (2)$$

in which $\phi_m(k_x, k_y, k_z)$ is the 3-D power spectrum of the magnetization and k_x , k_y , and k_z are the x-, y- and z- components of the wavenumber.

Following equation 2, for a 2-D horizontal fractal magnetization, constant vertical magnetization, and finite horizontal extension of the magnetic sources equation 1 becomes (Li et al., 2013; Kumar et al., 2020):

$$A(k) = C_1 |2\pi k|^{-\frac{\beta-1}{2}} e^{-|2\pi k|z_t} (1 - e^{-|2\pi k|(z_b - z_t)}) \quad (3)$$

where C_1 is a constant and β is the 3-D fractal exponent related to the crustal lithology. For this study, the DBMS is calculated using the centroid method for a fractal magnetization model. This method determines the depth to the top and the centroid of a magnetic slab. If the considered wavelengths are less than twice the thickness of the magnetic layer, equation 3 can be approximated by (after Li et al., 2013):

$$\ln(A(k)) \approx C_2 - |2\pi k|z_t - \frac{\beta-1}{2} \ln|2\pi k| \quad (4)$$

where C_2 is a constant. Thus, the estimation of the top of the magnetic sources, z_t , is based on the slope of that part of the amplitude spectrum that contains information about the medium to high wavenumbers. In contrast, the centroid depth, z_0 , is derived from the part of the amplitude spectrum that represents the smaller wavenumbers.

Following the centroid methodology (Tanaka et al., 1999), it is possible to approximate equation (3) by the following formula that relates the depth of the centroid of the magnetic layer z_0 with the amplitude spectrum (Li et al., 2013):

$$\ln\left(\frac{A(k)}{|2\pi k|}\right) \approx C_3 - |2\pi k|z_0 - \frac{\beta-1}{2} \ln|2\pi k| \quad (5)$$

where C_3 is a constant. Finally, the depth to the bottom of the magnetic source, z_b , is calculated as:

$$z_b = 2z_0 - z_t \quad (6)$$

Table S1 summarizes the different wavenumber ranges that have been used in other published DBMS estimations that used the centroid and modified centroid methods. In the cited studies, these wavenumbers are evaluated regarding the reasonability of the obtained results in relation to the tectonic and geological environment. However, the summary reveals a wide range of wavenumbers that probably depends on the specific nature of the magnetic sources and the geological environment.

The depths to the top, the centroid, and the bottom of the magnetic sources are calculated for different values of β using the equations 4, 5, and 6, respectively (Carrillo-de la Cruz et al., 2020b). From an iterative forward modeling, using different values of β and wavenumber ranges, the differences between synthetic spectra and observed spectra are analyzed. To get reliable DBMS calculations, the root-mean square error, and the visual inspection of the similarity between the synthetic spectra and the observed spectra, alongside with autocorrelation function and geology, are essential (Fig. 2 at main manuscript). The root-mean square error is calculated by:

$$R = \sqrt{\frac{1}{n} \sum_{i=1}^n (A_f(k) - A_{syn}(k))^2} \quad (7)$$

in which $A_f(k)$ is the observed amplitude spectrum and $A_{syn}(k)$ is the synthetic amplitude spectrum. The evaluation of β must be done carefully because high values of β could result in an overestimation of the DBMS.

The uncertainty estimation related with the modified centroid method was proposed by Okubo and Matsunaga (1994). The uncertainty, ϵ , in z_0 and z_t is always less than 15% of the corresponding estimated depth, and is calculated with the following equation:

$$\epsilon = \frac{\sigma}{(k_u - k_l)} \quad (8)$$

where σ is the standard deviation between the logarithm of the radially average amplitude spectrum and the linear fit of the least squares adjust. The difference $(k_u - k_l)$ is the wavenumber range used.

From the uncertainty of z_0 and z_t , the depth to the bottom of magnetic source (z_b) uncertainty is calculated by using (Martos et al., 2017):

$$\Delta z_b = \sqrt{(2\Delta z_0)^2 + \Delta z_t^2} \quad (9)$$

where Δz_b , Δz_0 and Δz_t are the uncertainties for z_b , z_0 and z_t , respectively. The uncertainty of the method only represents the error in each window centers.

Finally, the strong trends in the aeromagnetic data caused by regional geological units could affect the spectra used to calculate the DBMS. Ravat et al. (2007) and Shuey et al. (1977) suggest application of the autocorrelation function (AF) analysis to detect trends. A near-circular AF is associated with reliable DBMS calculations, while not near-circular AF is related to strong trends that may control the shape of the spectrum and produced biased results. The AF is calculated by:

$$AF = F^{-1}[F(X)F^*(X)] \quad (10)$$

where $F(X)$ is the fast Fourier transform of the magnetic data of the analyzed window, $F^*(X)$ is the complex conjugate and F^{-1} is the back transformation to the space domain. From the results of equation (10), it is necessary to take the real part and shift the zero-frequency components to the center of the spectrum. Finally, the autocorrelation function is normalized between -1 and 1.

Figure S1 shows examples of the applied methodology and demonstrates that the different windows from different geological environments changes the fractal parameter and the wavenumber ranges. In addition, the autocorrelation functions show which geological structures cause trends that could bias the results.

Sequential Gaussian Simulation application

The Sequential Gaussian Simulation (SGS) assess the spatial variability of an attribute (e.g., Cardellini et al., 2003; Chen et al., 2012), considering the realization of an attribute as a stationary multivariate Gaussian random function (Cardellini et al., 2003). The attribute is simulated in each location following a regularly spaced grid of an area of interest by sampling a Gaussian conditional cumulative distribution function defined on the original data (Cardellini et al., 2003; Chen et al., 2012).

Before the simulation, an analysis and modeling of the semivariogram is mandatory. First, the normal score transformation is applied before the semivariogram calculation. Figure S2a displays the semivariogram of the DBMS normal score and shows the trend in the data. This trend is caused by the small DBMS values in the west of Mexico and by large DBMS values in the east. A linear

trend is removed from the DBMS and heat flow datasets in order to model the semivariogram and to apply the SGS. The residuals are exported for subsequent processing with GSLIB (Pyrcz and Deutsch, 2014).

The semivariogram model fitted to the DBMS normal score residuals is an exponential model, following the expression

$$\gamma = c_0 + c \left[1 - \exp\left(-\frac{h}{a}\right) \right] \text{ for } 0 < h \quad (11)$$

whereas a spherical model was fitted to the normal score residuals of the heat flow values:

$$\gamma = c_0 + c \left[\frac{3}{2} \left(\frac{h}{a} \right) - \frac{1}{2} \left(\frac{h}{a} \right)^3 \right] \text{ for } 0 < h \leq a \quad (12)$$

In equations 11 and 12, γ is the semivariogram, c_0 is the nugget effect, c is the sill, a is the range and h is the lag distance between samples (Oliver and Webster, 2015). It is important to notice that the quantity $c_0 + c$ is the sill variance. To model the normal scores semivariogram, this quantity is defined to be 1. Semivariogram modeling is presented in figures S2a, and S2b.

After that, one hundred simulations of the DBMS and the heat flow were performed on 9 x 9 km pixels using the semivariogram models of figures S2a and S2b. The SGS simulations 25, 50, 75, and 100 are used by chance to verify if the normal score semivariograms and back-transformed Cumulative Distribution Function (CDF) of the simulated residuals reproduce the original residual data.

Figure S3 shows the fluctuations between the calculated, modeled, and simulated semivariograms. The normal scores show fluctuations in all semivariograms. These fluctuations are stronger at larger lag distances. Meanwhile, Figure S4 shows the comparison between the CDF of the simulated residuals with the CDF of the residuals. The simulations reproduce the original residual data but exhibit fluctuations in the mean and the standard deviation (Tables in Figure S4). The fluctuations between the original data and the simulated residuals are small, hence the simulated and the original data are similar, and simulations can be used.

Since all the realizations are equiprobable, it is necessary to simplify the model by averaging the values of each location (or pixel) using (Pyrcz and Deutsch, 2014):

$$\bar{z}(u_\alpha) = \frac{1}{L} \sum_{l=1}^L z_l(u_\alpha) \quad (13)$$

where L is the number of realizations of the attribute z at the location u_α . The e-type model is the best estimate of all data and local statistics. From the e-type model, the conditional variance can be calculated for each location in the model by:

$$\sigma^2(u_\alpha) = \frac{1}{L} \sum_{l=1}^L [z_l(u_\alpha) - \bar{z}(u_\alpha)]^2 \quad (14)$$

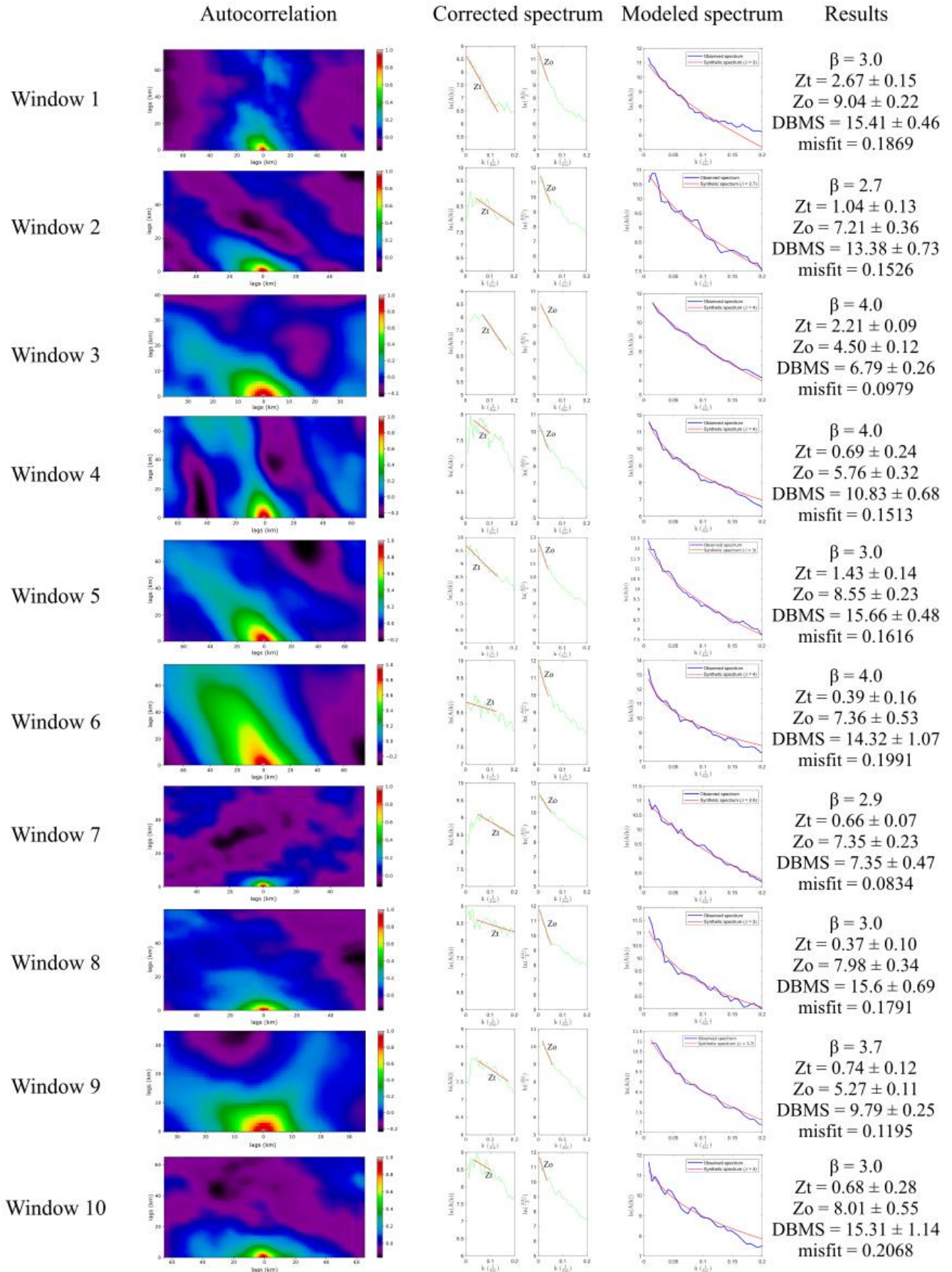
The conditional standard deviation is:

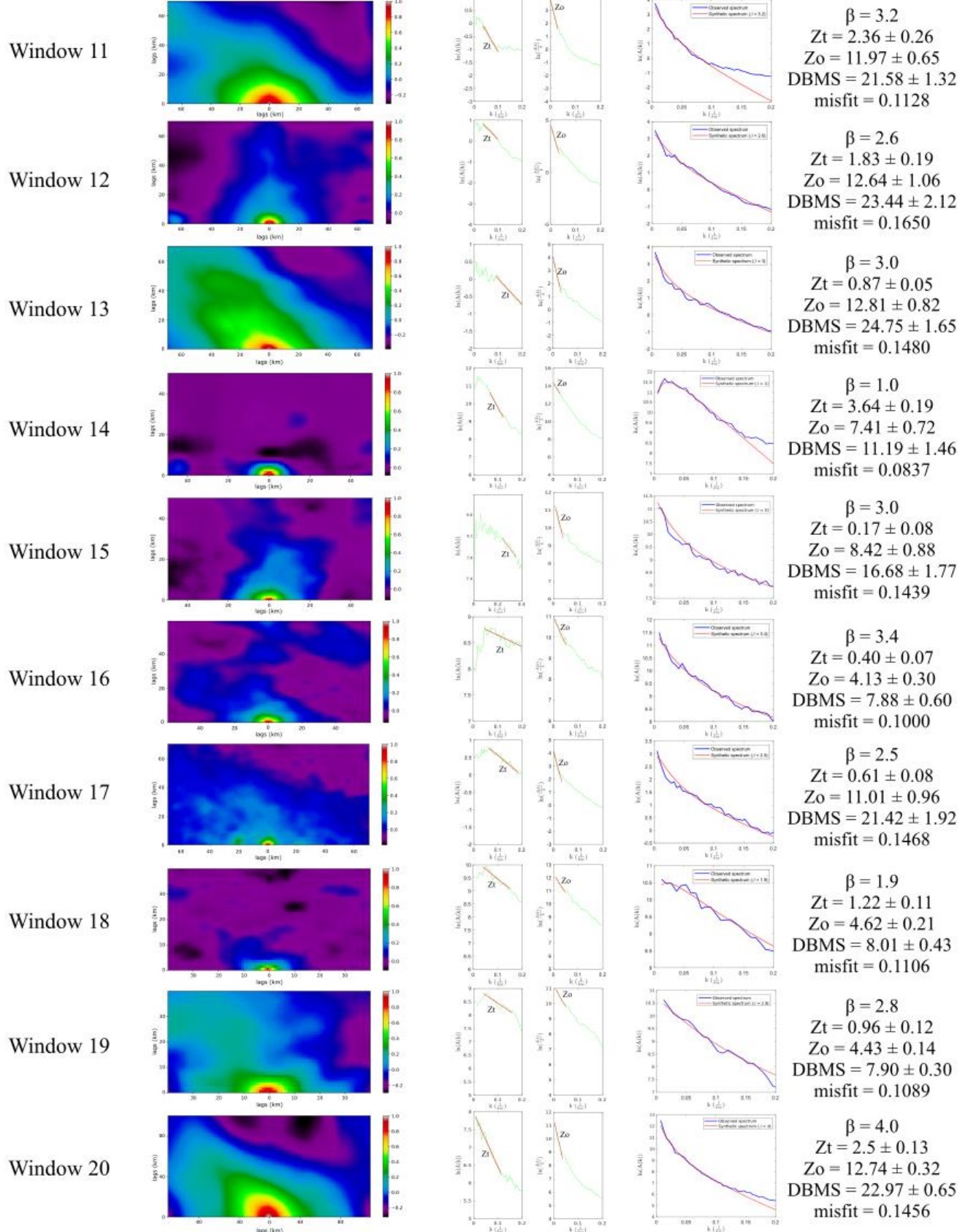
$$\sigma(u_\alpha) = \sqrt{\sigma^2(u_\alpha)} \quad (15)$$

The conditional standard deviation is a useful to represent local uncertainty. In order to apply equations 13 and 15 to the simulated residuals, the removed trend in the semivariogram analysis needs to be added to the simulated residuals again.

Fig. S1. Examples for the autocorrelation function and amplitude spectrum of those windows

labeled in Figure 3.





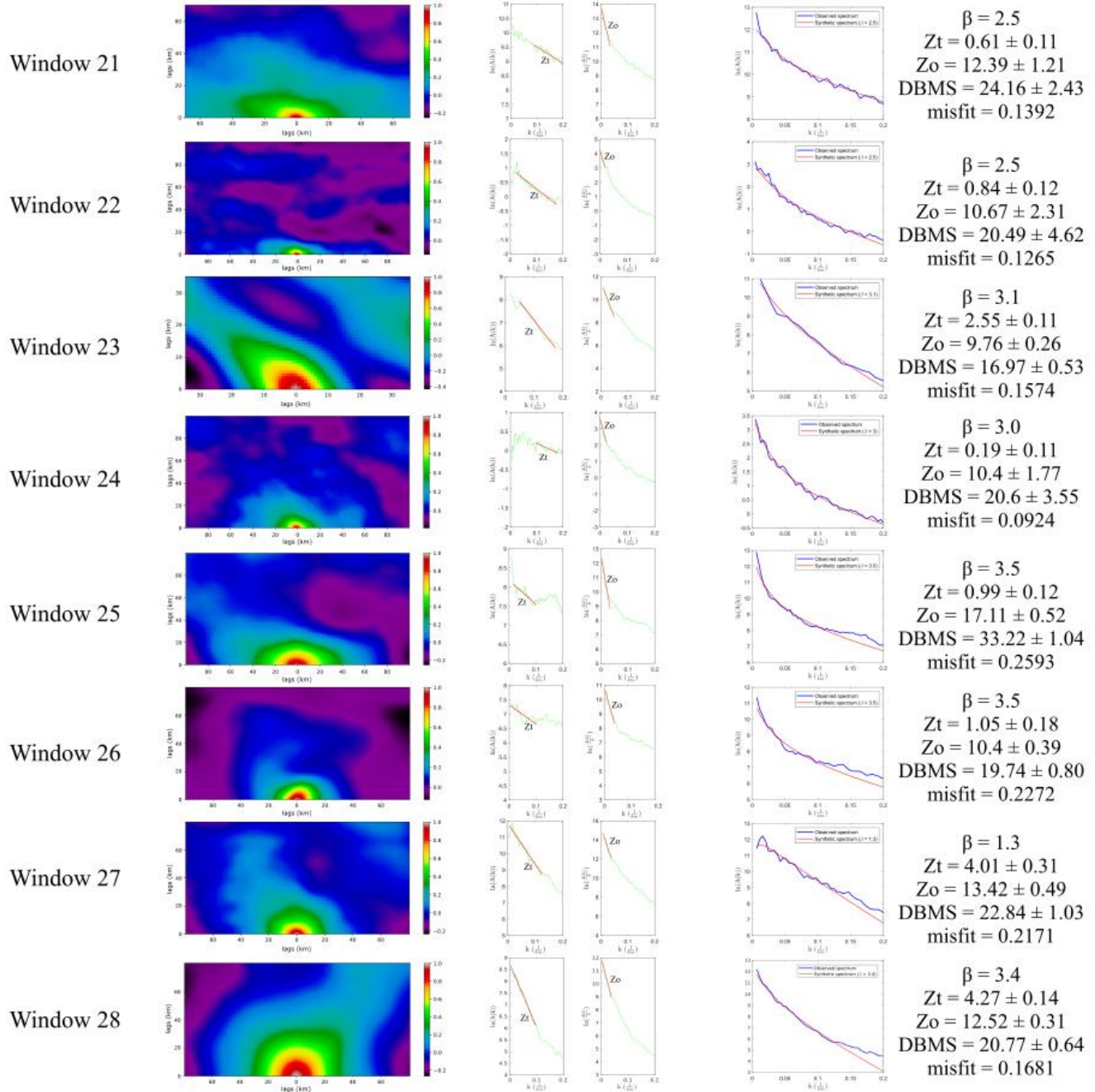


Fig. S2. Semivariogram analysis of a) DBMS, b) heat flow.

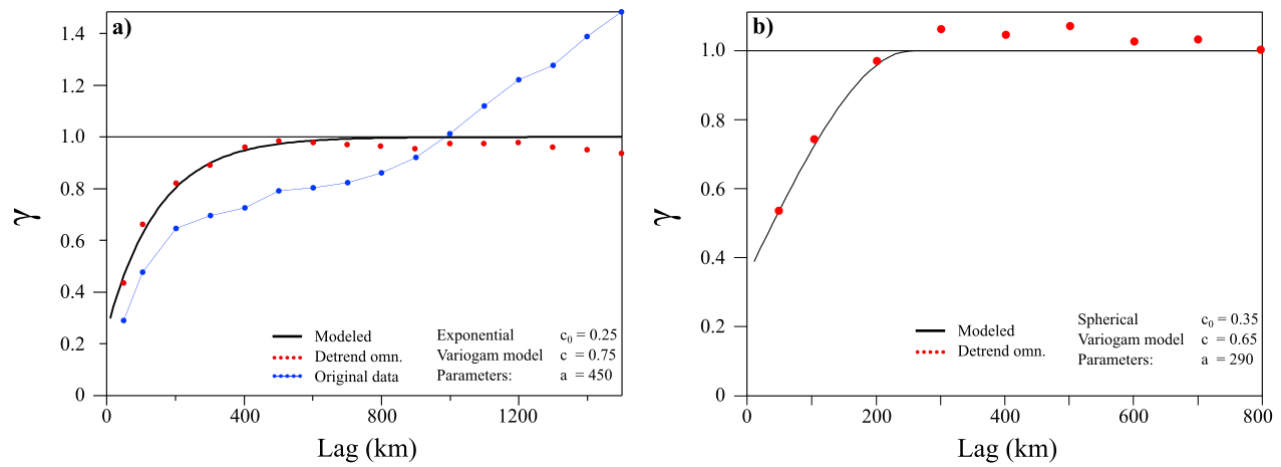


Fig. S3. Normal score semivariograms of the simulations and original residual data of a) DBMS and b) heat flow.

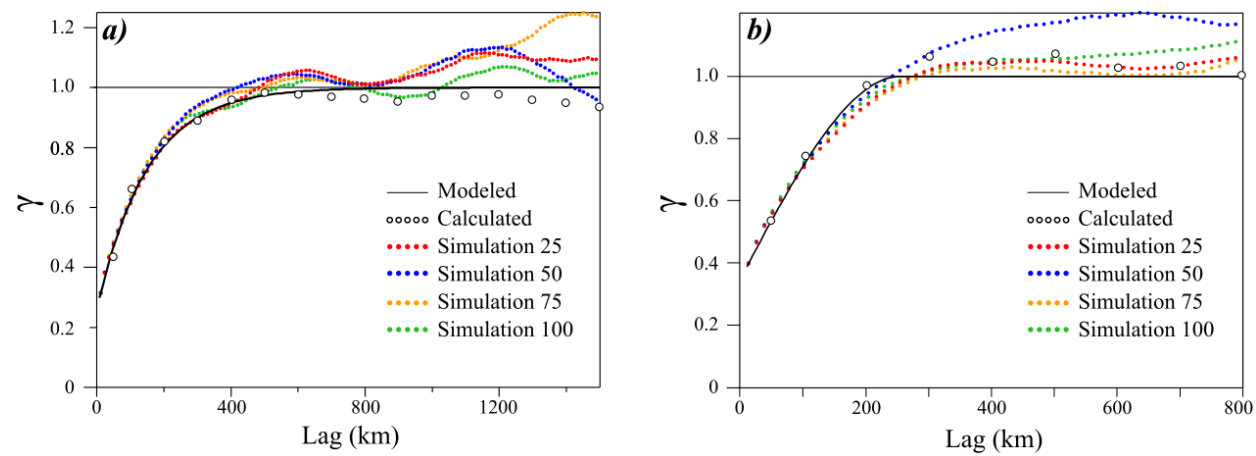
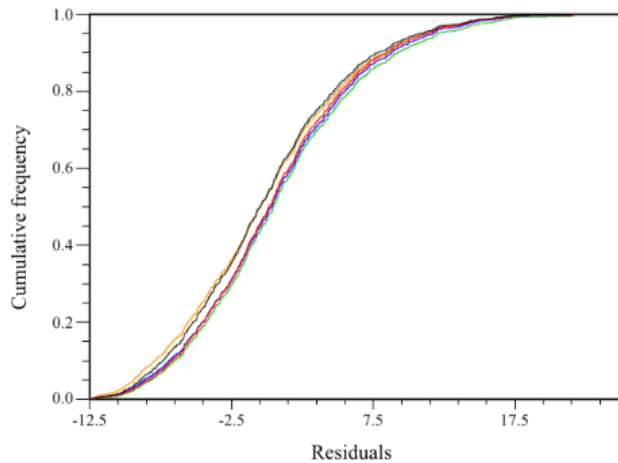


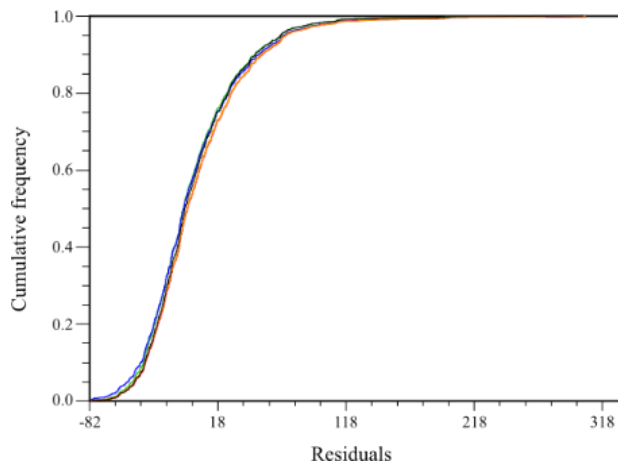
Fig. S4. Cumulative Distribution Function and basic statistics of the residuals.

***Depth to the bottom of
magnetic sources***



	mean	min.	max.	std. dev.
data	0.00	-12.47	21.74	5.89
sim. 25	0.60	-12.47	21.74	5.82
sim. 50	0.67	-12.47	21.74	5.98
sim. 75	-0.05	-12.47	21.74	6.14
sim. 100	1.00	-12.47	21.74	6.12

Heat flow



	mean	min.	max.	std. dev.
data	0.00	-81.13	304.24	37.90
sim. 25	2.00	-81.13	304.24	39.66
sim. 50	-0.79	-81.13	304.24	41.40
sim. 75	2.17	-81.13	304.24	40.74
sim. 100	-1.55	-81.13	304.24	37.93

Fig. S5. Heat flow data (borehole and seafloor) and main tectonic features (from Prol-Ledesma et al., 2018; SMU Node of National Geothermal Data, accessed on February 25, 2020). Tectonic features, geothermal fields and prospects, recent volcanism, and abbreviations as in Figures 1 and 6.

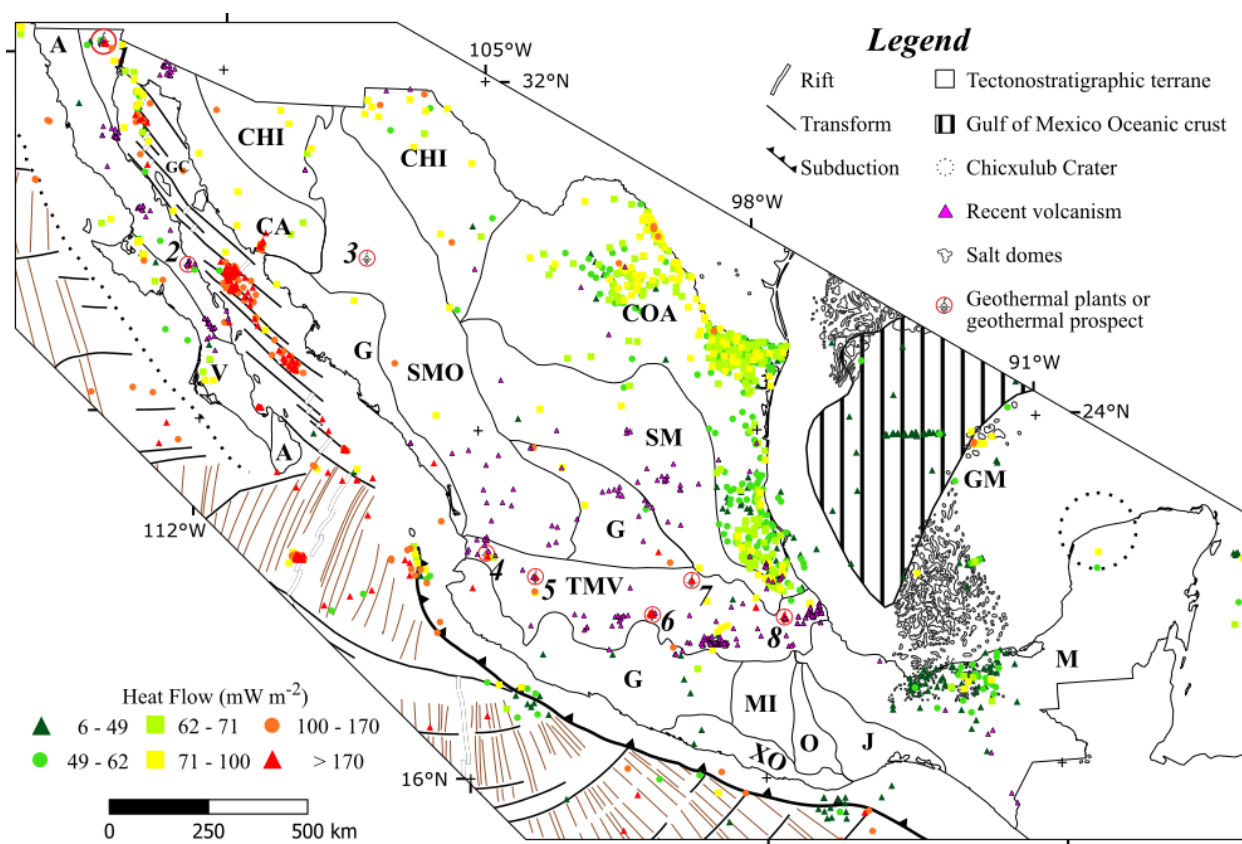


Table S1. Summary of wavenumber ranges (1/km) used to calculate the DBMS (complemented summary after Wang and Li, 2018).

region	z_t wavenumber range	z_0 wavenumber range	reference
East and Southeast Asia	~0.050-0.100	~0.005-0.030	Tanaka et al. (1999)
Western Argentina	~0.020-0.060	~0.005-0.020	Ruiz and Introcaso (2004)
Central-Southern Europe	0.050-0.100	0.005-0.050	Chiozzi et al. (2005)
Eastern China	~0.050-0.100	~0.005-0.050	Li et al. (2009)
Bulgaria	0.050-0.100	0.005-0.045	Trifonova et al. (2009)
Central Turkey	~0.050-0.800	~0.050-0.250	Maden (2010)
Germany	~0.008-0.080*	~0.002-0.035*	Bansal et al. (2011)
Nankai subduction zone	~0.050-0.100	~0.005-0.050	Li (2011)
Mexican Subduction Zone	~0.095-0.140*	~0.008-0.032*	Manea and Manea (2011)
Central India	~0.002-0.100*	~0.002-0.020*	Bansal et al. (2013)
North Atlantic	~0.030-0.080	~0.005-0.030	Li et al. (2013)
Taiwan	~0.040-0.070	~0.005-0.030	Hsieh et al. (2014)
Southeast Tibet	~0.040-0.080*	~0.006-0.070*	Gao et al. (2015a)
Tarim Basin	0.050-0.100	0.005-0.050	Gao et al. (2015b)
Western North America	~0.030-0.080	~0.005-0.030	Wang and Li (2015)
Arabian Shield	~0.003-0.036	~0.003-0.027	Aboud et al. (2016)
Western Turkey	~0.010-0.025*	~0.003-0.010*	Bilim et al. (2016)
SW Indian Ocean	~0.098-0.286	~0.008-0.092	Gailler et al. (2016)
E & SE Asia	~0.030-0.080	~0.005-0.030	Li and Wang (2016)

South California	~0.010-0.020*	~0.003-0.010*	Mickus and Hussein (2016)
Northern Yucatan, Mexico	~0.020-0.150	~0.010-0.070	Espinosa-Cerdeña et al. (2016)
Alps & Po Plain	~0.040-0.160	~0.010-0.070	Speranza et al. (2016)
Lesser Antilles Arc	~0.096-0.178	~0.012-0.088	Gailler et al. (2017)
West Himalayan syntaxis	~0.040-0.100*	~0.016-0.040*	Gao et al. (2017)
Antarctica	~0.180-0.400	~0.030-0.150	Martos et al. (2017)
Global	~0.030-0.080	~0.005-0.030	Li et al. (2017)
SW Caribbean	~0.030-0.080*	~0.005-0.030*	Salazar et al. (2017)
Pacific	~0.030-0.080	~0.003-0.030	Li and Wang (2018)
Greenland	~0.180-0.400	~0.030-0.150	Martos et al. (2018)
Iberian Peninsula	~0.350-0.480	~0.004-0.020	Andrés et al. (2018)
Coahuila, Mexico	~0.025-0.100*	~0.005-0.040*	Carrillo et al. (2020a)
Iran	~0.050-0.120*	~0.005-0.032*	Kumar et al. (2020)

* converted from rad/km

Table S2. Thermal conductivities (Robertson, 1988; Lee and Deming, 1998; Beardsmore and Cull, 2001; Eppelbaum et al., 2014; Pasquale et al., 2014; Dalla Santa et al., 2020) and heat generation rate (Smith, 1974; Smith et al. 1979; Hasterok et al., 2018) for tectonostratigraphic provinces of Mexico.

Terrane	Thermal conductivity λ $(\frac{W}{mK})$	Heat production rate at surface $H_0 (\frac{\mu W}{m^3})$	Main rock type
Trans-Mexican volcanic belt	2.10	1.56	volcanic rocks
Sierra Madre	2.34	1.53	sedimentary rocks over metamorphic basement
Maya	2.48	0.88	sedimentary rocks over igneous and metamorphic basement
Sierra Madre Occidental	1.61	2.15	volcanic rocks (andesites, ignimbrites, and rhyolites)
Caborca	2.45	1.38	metamorphic rocks intruded by igneous rocks
Chihuahua	2.33	2.24	sedimentary rocks over basement, affected by volcanism
Coahuila	2.24	1.6	sedimentary rocks over igneous-

			metamorphic basement
Guerrero	2.24	1.78	igneous, metamorphic, and sedimentary rocks
Juarez	2.26	0.83	sedimentary rocks
Mixteco	2.07	1.05	igneous basement covered by sedimentary rocks
Oaxaca	2.26	1.4	metamorphic rocks covered by sedimentary rocks
Alisitos	2.27	0.99	Peninsular Ranges Batholith with influence of volcano- sedimentary and ocean floor rocks
Vizcaino	2.11	1.27	Peninsular Ranges Batholith and ocean floor rocks

References

- Aboud, E., Alotaibi, A.M., Saud, R., 2016. Relationship between Curie isotherm surface and Moho discontinuity in the Arabian shield, Saudi Arabia. *J. Asian Earth Sci.* 128, 42–53. <https://doi.org/10.1016/j.jseaes.2016.07.025>.
- Andrés, J., Marzán, I., Ayarza, P., Martí, D., Palomeras, I., Torné, M., Campbell, S., Carbonell, R., 2018. Curie Point Depth of the Iberian Peninsula and Surrounding Margins. A Thermal and Tectonic Perspective of its Evolution. *J. Geophys. Res. Solid Earth* 123 (3), 2049-2068. <https://doi.org/10.1002/2017JB014994>.
- Bansal, A.R., Anand, S.P., Rajaram, M., Rao, V.K., Dimri, V.P., 2013. Depth to the bottom of magnetic sources (DBMS) from aeromagnetic data of Central India using modified centroid method for fractal distribution of sources. *Tectonophysics* 603, 155–161. <https://doi.org/10.1016/j.tecto.2013.05.024>.
- Bansal, A.R., Gabriel, G., Dimri, V.P., Krawczyk, C.M., 2011. Estimation of depth to the bottom of magnetic sources by a modified centroid method for fractal distribution of sources: an application to aeromagnetic data in Germany. *Geophysics* 76 (3), L11–L22. <https://doi.org/10.1190/1.3560017>.
- Beardsmore, G., Cull, J., 2001. Crustal Heat Flow: A Guide to Measurement and Modelling. Cambridge University Press. <https://doi.org/10.1017/S0016756803218021>.
- Bilim, F., Akay, T., Aydemir, A., Kosaroglu, S., 2016. Curie point depth, heat-flow and radiogenic heat production deduced from the spectral analysis of the aeromagnetic data for geothermal investigation on the Menderes Massif and the Aegean Region, western Turkey. *Geothermics* 60, 44–57. <https://doi.org/10.1016/j.geothermics.2015.12.002>.
- Bhattacharyya, B.K., Leu, L.K., 1975. Analysis of magnetic anomalies over Yellowstone National Park: Mapping of Curie point isothermal surface for geothermal reconnaissance. *J. Geophys. Res.* 80 (32), 4461-4465. <https://doi.org/10.1029/JB080i032p04461>.
- Blakely, R.J., 1988. Curie temperature Isotherm Analysis and Tectonic Implications of Aeromagnetic Data from Nevada. *J. Geophys. Res. Solid Earth* 93 (B10), 11817-11832. <https://doi.org/10.1029/JB093iB10p11817>.
- Blakely, R.J., 1995. Potential Theory in Gravity and Magnetic Applications. Cambridge University Press, Cambridge.

- Bouligand, C., Glen, J.M.G., Blakely, R.J., 2009. Mapping Curie temperature depth in the western United States with a fractal model for crustal magnetization. *J. Geophys. Res.* 114, B11104. <http://dx.doi.org/10.1029/2009jb006494>.
- Cardellini, C., Chiodini, G., Frondini, F., 2003. Application of stochastic simulation to CO₂ flux from soil: Mapping and quantification of gas release. *J. Geophys. Res.* 108(B9), 2425. <https://doi.org/10.1029/2002JB002165>.
- Carrillo-de la Cruz, J.L., Prol-Ledesma, R.M., Gómez-Rodríguez, D., Rodríguez-Díaz, A.A., 2020a. Analysis of the relation between bottom hole temperature data and Curie temperature depth to calculate geothermal gradient and heat flow in Coahuila, Mexico. *Tectonophysics* 780, 228397. <https://doi.org/10.1016/j.tecto.2020.228397>.
- Carrillo-de la Cruz, J.L., Prol-Ledesma, R.M., Velázquez-Sánchez, P., Gómez-Rodríguez, D., 2020b. MAGCPD: A MATLAB-based GUI to calculate the Curie point-depth involving the spectral analysis of aeromagnetic data. *Earth Sciences Informatics* 13, 1539-1550. <https://doi.org/10.1007/s12145-020-00525-x>.
- Chen, F., Chen, S., Peng, G., 2012. Using Sequential Gaussian Simulation to Assess Geochemical Anomaly Areas of Lead Element. 6th Computer and Computing Technologies in Agriculture (CCTA), Zhangjiajie, China. pp. 69-76. https://doi.org/10.1007/978-3-642-36137-1_9.
- Chiozzi, P., Matsushima, J., Okubo, Y., Pasquale, V., Verdoya, M., 2005. Curie-point depth from spectral analysis of magnetic data in central-southern Europe. *Phys. Earth Planet. In.* 152, 267–276. <https://doi.org/10.1016/j.pepi.2005.04.005>.
- Connard, G., Couch, R., Gemperle, M., 1983. Analysis of aeromagnetic measurements from the Cascade Range and in central Oregon. *Geophysics* 48 (3), 376–390. <https://doi.org/10.1190/1.1441476>.
- Dalla Santa, G., Galgaro, A., Sassi, R., Cultrera, M., Scotton, P., Mueller, J., Bertermann, D., Mendrinos, D., Pasquali, R., Prego, R., Pera, S., Di Sipio, E., Cassiani, G., De Carli, M., Bernardi, A., (2020). An updated ground thermal properties database for GSHP applications. *Geothermics*, 85. <https://doi.org/10.1016/j.geothermics.2019.101758>.
- Eppelbaum, L., Kutasov, I., Pilchin, A., 2014. Applied Geothermics. Springer Berlin Heidelberg, Berlin. <https://doi.org/10.1007/978-3-642-34023-9>.

- Espinosa-Cerdeña, J.M., Campos-Enríquez, J.O., Unsworth, M., 2016. Heat flow pattern at the Chicxulub impact crater, northern Yucatan, Mexico. *J. Volcanol. Geotherm. Res.* 311, 135–149. <http://dx.doi.org/10.1016/j.jvolgeores.2015.12.013>.
- Gailler, L., Arcay, D., Münch, P., Martelet, G., Thinon, I., Lebrun, J.-F., 2017. Forearc structure in the Lesser Antilles inferred from depth to the Curie temperature and thermo-mechanical simulations. *Tectonophysics* 706–707, 71–90. <https://doi.org/10.1016/j.tecto.2017.03.014>.
- Gailler, L.S., Lenat, J.F., Blakely, R.J., 2016. Depth to Curie temperature or bottom of the magnetic sources in the volcanic zone of la Reunion hot spot. *J. Volcanol. Geotherm. Res.* 324, 169–178. <https://doi.org/10.1016/j.jvolgeores.2016.06.005>.
- Gao, G.M., Kang, G.F., Bai, C.H., Wen, L.M., 2015a. Study on crustal magnetic anomalies and Curie surface in Southeast Tibet. *J. Asian Earth Sci.* 97, 169–177. <https://doi.org/10.1016/j.jseaes.2014.10.035>.
- Gao, G.M., Kang, G.F., Li, G.Q., Bai, C.H., 2015b. Crustal magnetic anomaly and Curie surface beneath Tarim Basin, China, and its adjacent area. *Can. J. Earth Sci.* 52, 357–367. <https://doi.org/10.1139/cjes-2014-0204>.
- Gao, G., Kang, G., Li, G., Bai, C., Wu, Y., 2017. An analysis of crustal magnetic anomaly and Curie surface in west Himalayan syntaxis and adjacent area. *Acta Geod. Geophys.* 52, 407–420. <https://doi.org/10.1007/s40328-016-0179-z>.
- Hasterok, D., Gard, M., Webb, J., 2018. On the radiogenic heat production of metamorphic, igneous, and sedimentary rocks. *Geoscience Frontiers* 9, 1777–1794. <https://doi.org/10.1016/j.gsf.2017.10.012>.
- Hsieh, H.H., Chen, C.H., Lin, P.Y., Yen, H.Y., 2014. Curie point depth from spectral analysis of magnetic data in Taiwan. *J. Asian Earth Sci.* 90, 26–33. <https://doi.org/10.1016/j.jseaes.2014.04.007>.
- Kumar, R., Bansal, A.R., Ghods, A., 2020. Estimation of depth to bottom of magnetic sources using spectral methods: Application on Iran's aeromagnetic data. *J. Geophys. Res. Solid Earth* 125, e2019JB018119. <https://doi.org/10.1029/2019JB018119>.
- Lee, Y., Deming, D., 1998. Evaluation of thermal conductivity temperature corrections applied in terrestrial heat flow studies, *J. Geophys. Res. Solid Earth* 103 (B2), 2447–2454. <https://doi.org/10.1029/97JB03104>.

- Li, C.-F., 2011. An integrated geodynamic model of the Nankai subduction zone and neighboring regions from geophysical inversion and modeling. *J. Geodyn.* 51, 64–80. <https://doi.org/10.1016/j.jog.2010.08.003>.
- Li, C.-F., Chen, B., Zhou, Z.Y., 2009. Deep crustal structures of eastern China and adjacent seas revealed by magnetic data. *Sci. China Ser. D* 52, 984–993. <https://doi.org/10.1007/s11430-009-0096-x>.
- Li, C.-F., Lu, Y., Wang, J., 2017. A global reference model of Curie-point depths based on EMAG2. *Sci. Rep.* 7, 45129. <https://doi.org/10.1038/srep45129>.
- Li, C.-F., Wang, J., 2016. Variations in Moho and Curie depths and heat flow in Eastern and Southeastern Asia. *Mar. Geophys. Res.* 37, 1–20. <https://doi.org/10.1007/s11001-016-9265-4>.
- Li, C.-F., Wang, J., 2018. Thermal structures of the Pacific lithosphere from magnetic anomaly inversion. *Earth Planet. Phys.* 2, 52–66.
- Li, C.-F., Wang, J., Lin, J., Wang, T., 2013. Thermal evolution of the North Atlantic lithosphere: New constraints from magnetic anomaly inversion with a fractal magnetization model. *Geochem. Geophys. Geosyst.* 14 (12), 5078-5105. <https://doi.org/10.1002/2013GC004896>.
- Maden, N., 2010. Curie-point depth from spectral analysis of magnetic data in Erciyes stratovolcano (central Turkey). *Pure Appl. Geophys.* 167, 349–358. <https://doi.org/10.1007/s00024-009-0017-0>.
- Manea, M., Manea, V.C., 2011. Curie Point Depth Estimates and Correlation with Subduction in Mexico. *Pure Appl. Geophys.* 168, 1489-1499. <https://doi.org/10.1007/s00024-010-0238-2>.
- Martos, Y. M., Catalán, M., Jordan, T. A., Golynsky, A., Golynsky, D., Eagles, G., Vaughan, D.G. D.G., 2017. Heat Flux Distribution of Antarctica Unveiled. *Geophys. Res. Lett.* 44 (22), 11,417-11,426. <https://doi.org/10.1002/2017GL075609>.
- Martos, Y.M., Jordan, T.A., Catalán, M., Jordan, T.M., Bamber, J.L., Vaughan, D.G., 2018. Geothermal Heat Flux Reveals the Iceland Hotspot Track Underneath Greenland. *Geophys. Res. Lett.* 45 (16), 8214–8222. <https://doi.org/10.1029/2018GL078289>.
- Maus, S., Dimri, V., 1995. Potential field power spectrum inversion for scaling geology. *J. Geophys. Res. Solid Earth* 100 (B7), 12605–12616. <https://doi.org/10.1029/95JB00758>.

- Mickus, K., Hussein, M., 2016. Curie depth analysis of the Salton Sea Region, Southern California. *Pure Appl. Geophys.* 173, 537–554. <https://doi.org/10.1007/s00024-015-1100-3>.
- Okubo, Y., Graf, R.J., Hansen, R.O., Ogawa, K., Tsu, H., 1985. Curie point depths of the island of Kyushu and surrounding areas, Japan. *Geophysics* 50 (3), 481-494. <https://doi.org/10.1190/1.1441926>.
- Okubo, Y., Matsunaga, T., 1994. Curie point depth in Northeast Japan and its correlation with regional thermal structure and seismicity. *J. Geophys. Res.* 99(B11), 22363–22371. <https://doi.org/10.1029/94JB01336>.
- Oliver, M.A., Webster, R., 2015. Basic steps in Geostatistics: The variogram and Kriging. Springer Briefs in Agriculture, Springer International Publisher, pp. 100. <https://doi.org/10.1007/978-3-319-15865-5>.
- Pasquale, V., Verdoya, M., Chiozzi, P., 2014. Geothermics: Heat Flow in the Lithosphere. Springer Briefs in Earth Sciences. Springer International Publishing. <https://doi.org/10.1007/978-3-319-02511-7>.
- Pilkington, M., Todoeschuck, J.P., 1993. Fractal magnetization of continental crust. *Geophys. Res. Lett.* 20 (7), 627–630. <https://doi.org/10.1029/92GL03009>.
- Prol-Ledesma, R.M., Carrillo-de la Cruz, J.L., Torres-Vera, M.A., Membrillo-Abad, A.S., Espinosa-Ojeda, O.M., 2018. Heat flow map and geothermal resources in Mexico. *Terra Digitalis* 2 (2), 1–15. <https://doi.org/10.22201/igg.25940694.2018.2.51>.
- Pyrcz, M.J., Deutsch, C.V., 2014. Geostatistical Reservoir Modeling, 2nd Edition. Oxford University Press, New York.
- Ravat, D., Pignatelli, A., Nicolosi, I., Champpini, M., 2007. A study of spectral methods of estimating the depth to the bottom of magnetic sources from near surface magnetic anomaly data. *Geophys. J. Int.* 169 (2), 421-434. <https://doi.org/10.1111/j.1365-246X.2007.03305.x>.
- Robertson, E.C., 1988. Thermal Properties of Rocks. US Department of the Interior: Geological Survey, 88–441.
- Ross, H.E., Blakely, R.J., Zoback, M.D., 2006. Testing the use of aeromagnetic data for the determination of Curie depth in California. *Geophysics* 71 (5), L51-L59. <https://doi.org/10.1190/1.2335572>.

- Ruiz, F., Introcaso, A., 2004. Curie point depths beneath Precordillera cuyana and sierras Pampeanas obtained from spectral analysis of magnetic anomalies. *Gondwana Res.* 7(4), 1133–1142. [https://doi.org/10.1016/S1342-937X\(05\)71089-3](https://doi.org/10.1016/S1342-937X(05)71089-3).
- Salazar, J.M., Vargas, C.A., Leon, H., 2017. Curie point depth in the SW Caribbean using the radially averaged spectra of magnetic anomalies. *Tectonophysics* 694, 400–413.
- Salem, A., Green, C., Ravat, D., Singh, K.H., East, P., Fairhead, J.D., Mogren, S., Biegert, E., 2014. Depth to Curie temperature across the central Red Sea from magnetic data using the de-fractal method. *Tectonophysics* 624–625, 75–86. <https://doi.org/10.1016/j.tecto.2014.04.027>.
- Shuey, R.T., Schellinger, D.K., Tripp, A.C., Alley, L.B., 1977. Curie determination from aeromagnetic spectra. *Geophys. J. R. Astr. Soc.* 50 (1), 75–101. <https://doi.org/10.1111/j.1365-246X.1977.tb01325.x>.
- Smith, D.L., 1974. Heat flow, radioactive heat generation, and theoretical tectonics for northwestern Mexico. *Earth and Planetary Science Letters* 23, 43-52. [https://doi.org/10.1016/0012-821X\(74\)90028-4](https://doi.org/10.1016/0012-821X(74)90028-4).
- Smith, D.L., Nuckles III, C.E., Jones, R.L., Cook, G.A., 1979. Distribution of heat flow and radioactive heat generation in northern Mexico. *J. Geophys. Res.* 84(B5), 2371-2379. <https://doi.org/10.1029/JB084iB05p02371>.
- [dataset] SMU Node of National Geothermal Data System Heat Flow Observation in Content Model Format. <http://geothermal.smu.edu/static/DownloadFilesButtonPage.htm>. Accessed on February 25, 2020.
- Spector, A., Grant, F.S., 1970. Statistical models for interpreting aeromagnetic data. *Geophysics* 35(2), 293-302. <https://doi.org/10.1190/1.1440092>.
- Speranza, F., Minelli, L., Pignatelli, A., Gilardi, M., 2016. Curie temperature depths in the Alps and the Po Plain (northern Italy): Comparison with heat flow and seismic tomography data. *J. Geodyn.* 98, 19–30. <https://doi.org/10.1016/j.jog.2016.03.012>.
- Tanaka, A., Okubo, Y., Matsubayashi, O., 1999. Curie point depth based on spectrum analysis of the magnetic anomaly data in East and Southeast Asia. *Tectonophysics* 306 (3-4), 461-470. [https://doi.org/10.1016/S0040-1951\(99\)00072-4](https://doi.org/10.1016/S0040-1951(99)00072-4).
- Trifonova, P., Zhelev, Z., Petrova, T., Bojadzieva, K., 2009. Curie point depths of Bulgarian territory inferred from geomagnetic observations and its correlation with regional

thermal structure and seismicity. *Tectonophysics* 473(3-4), 362–374.
<https://doi.org/10.1016/j.tecto.2009.03.014>.

Wang, J., Li, C.-F., 2015. Crustal magmatism and lithospheric geothermal state of the western North America and their implications for magnetic mantle. *Tectonophysics* 638, 112-125. <https://doi.org/10.1016/j.tecto.2014.11.002>.

Wang, J., Li, C-F., 2018. Curie point depths in Northeast China and their geothermal implications for the Songliao Basin. *Journal of Asian Earth Sciences* 163, 177-193.
<https://doi.org/10.1016/j.jseaes.2018.05.026>

MAGCPD codes

Content

Defractal and modified centroid

Introduction

This section presents the codes for the GUI published. The version is the 2.0 uploaded at <https://github.com/juanxo90/MAGCPD> at Feb 5, 2021. There are 3 files, the first two (*modified_centroid.mlapp* and *defractal.mlapp*) are written in *MATLAB 2020a* using the *App Designer*. It could be difficult paste the code in the *App Designer*, please go to GitHub and download it. Also, the file *selectdata.m* need to be in the same folder before to run the program, because is a fundamental part of it, if the file is not in the same folder, the app will crash.

```

modified_centroid.mlapp

classdef modified_centroid < matlab.apps.AppBase

% Properties that correspond to app components
properties (Access = public)
UIFigure matlab.ui.Figure
UIAxes matlab.ui.control.UIAxes
UIAxes2 matlab.ui.control.UIAxes
UIAxes3 matlab.ui.control.UIAxes
UIAxes4 matlab.ui.control.UIAxes
FractalExponentLabel matlab.ui.control.Label
FractalExponentEditField matlab.ui.control.NumericEditField
SelectpointsButton matlab.ui.control.Button
ValuesLabel matlab.ui.control.Label
SurfacetemperatureCEditFieldLabel matlab.ui.control.Label
SurfacetemperatureCEditField matlab.ui.control.NumericEditField
CurietemperatureCEditFieldLabel matlab.ui.control.Label
CurietemperatureCEditField matlab.ui.control.NumericEditField
SurfaceheatproductionmicroWm3EditFieldLabel matlab.ui.control.Label
SurfaceheatproductionmicroWm3EditField matlab.ui.control.NumericEditField
EmpiricalheatproductiondepthdistributionparameterkmEditField
matlab.ui.control.NumericEditField
ThermalconductivityWmKEditFieldLabel matlab.ui.control.Label
ThermalconductivityWmKEditField matlab.ui.control.NumericEditField
PlotGeothermButton matlab.ui.control.Button
RestartButton matlab.ui.control.Button
SelectFileButton matlab.ui.control.Button
Label matlab.ui.control.Label
FlightaltitudekmEditFieldLabel matlab.ui.control.Label
FlightaltitudekmEditField matlab.ui.control.NumericEditField
EmpiricalheatproductiondepthdistributionparameterkmLabel matlab.ui.control.Label
ModifiedCentroidMethodLabel matlab.ui.control.Label
ResolutionkmEditFieldLabel matlab.ui.control.Label
ResolutionkmEditField matlab.ui.control.NumericEditField
end

methods (Access = public)
function [w,pw,ps,ci] = fractal_correction(~,x,b1)
w = x(:,1);
ps = x(:,2) - log( 2*pi*w ) + (0.5*(b1-1))*log( 2*pi*w );% for Z0
pw = x(:,2) + (0.5*(b1-1))*log( 2*pi*w );% for Zt
ci = x(:,3);
end
function b = data_aero(~,fileToRead1)
%IMPORTFILE(FILETOREAD1)
% Imports data from the specified file
% FILETOREAD1: file to read
% Auto-generated by MATLAB on 23-May-2019 17:59:12
% Import the file

```

```

rawData1 = importdata(fileToRead1);
% For some simple files (such as a CSV or JPEG files), IMPORTDATA might
% return a simple array. If so, generate a structure so that the output
% matches that from the Import Wizard.
[~,name] = fileparts(fileToRead1);
newData1.(matlab.lang.makeValidName(name)) = rawData1;
% Create new variables in the base workspace from those fields.
vars = fieldnames(newData1);
for i = 1:length(vars)
assignin('base', vars{i}, newData1.(vars{i}));
end
b = rawData1;
end
function Z_f = detrend_2d(~,Z)
% This function is written by Munther Gdeisat-The General Engineering
% Research Institute (GERI) at Liverpool John Moores University.
% This program is written on 9th October 2011
% This function is the 2D equivalent of detrend function in Matlab
% Z_f = DETREND(Z) removes the best plane fit trend from the data
% in the 2D array Z and returns the residual in the 2D array Z_f
if size(Z,2) < 2
disp('Z must be a 2D array')
return
end
M = size(Z,2);
N = size(Z,1);
[X,Y] = meshgrid(1:M,1:N);
%Make the 2D data as 1D vector
Xcolv = X(:); % Make X a column vector
Ycolv = Y(:); % Make Y a column vector
Zcolv = Z(:); % Make Z a column vector
Const = ones(size(Xcolv)); % Vector of ones for constant term
% find the coefficients of the best plane fit
Coefficients = [Xcolv Ycolv Const]\Zcolv; % Find the coefficients
XCoef = Coefficients(1); % X coefficient
YCoef = Coefficients(2); % Y coefficient
CCoef = Coefficients(3); % constant term
% detrend the data
Z_p = XCoef * X + YCoef * Y + CCoef;
Z_f = Z - Z_p;
end
function cv3 = raas(~,anom,d1)
% function raps(img)
% Computes and plots radially a power spectrum of magnetic data in
% a GEOTif image of the amplitude spectrum
% Based and modified on (C) E. Ruzanski, RCG, 2009 and
% Tom Ridsdill-Smith March 2000
%% Process image size information
[ny, nx] = size(anom);
N = max(nx,ny);
if mod(N,2) ~= 0
N = N + 1;
end
TFA = fftshift(fft2(anom,N,N));
EA = 2*abs(TFA)/(ny*nx); % Espectro de amplitud 2D

```

```

% Compute radially average amplitude spectrum
n = -N/2:N/2-1;
[NX, NY] = meshgrid(n,n);
[~, rho] = cart2pol(NX, NY); % Convert to polar coordinate axes
rho = round(rho);
i = cell(N/2+1, 1);
Pf = zeros(N/2+1,1);
CF = zeros(N/2+1,1);
nm = zeros(N/2+1,1);
for r = 0:N/2
i{r + 1} = find(rho == r);
Pf(r + 1) = nanmean(log(EA(i{r+1}))); %Amplitude spectra
CF(r + 1) = 1.96*(nanstd(log(EA(i{r+1}))))...
/sqrt(length(EA(i{r+1}))); %confidence interval
end
% Calculate the 1D wavenumber for a signal of even length
kn = 1/(2*d1); % Frecuencia de Nyquist
k0 = 1/(N*d1); % Frecuencia fundamental
w = (0:k0:kn)';
cv2=[w(2:end),Pf(2:end),CF(2:end),nm(2:end)];
cv3 =cv2(cv2(:,3) <= 1, :);
end
function results = func18(~)
[pointlist,xs,ys] = selectdata(Input);
results = [pointlist,xs,ys];
end
function [x, y] = ind(~,xi,yi,dx)

n = length(dx);
x = ones(n,1);
y = ones(n,1);
for i = 1:n
c = find(xi ==dx(i));
x(i) = xi(c);
y(i) = yi(c);
end
end
function x = fileid(~,data)
% This program identifies the input file extension. If the files
% have a *.grd extention one the return value is 0. If the file has
% a *.tif extension, the return value is 1.
[~,~,ext] = fileparts(data);
if (strcmpi(trim(ext), '.grd'))
x=0;
elseif (strcmpi(trim(ext), '.tif'))
x=1;
else
disp('Error: Unexpected file')
return
end
end
function [D,varargout] = getgrd2(~,filename)
% Read a Geosoft 2-byte binary grid
% Syntax: [D,varargout] = getgrd2(filename);

```

```

% Import: filename = string of grid filename, eg. 'mag.grd'
% Use full path if grid is not in current directory
% eg. 'd:\data\mag.grd'
% Export: D = 2D array of real data
% varargout = Xaxis,Yaxis,dummy
% Xaxis,Yaxis = x- and y-axis coordinates
% dummy = dummy value as a real in D
% Usage : D = getgrd2(filename); % Array only
% [D,X,Y] = getgrd2(filename); % Data and coordinates
% To locate dummy pixels and image use:
% [D,X,Y,dummy] = getgrd2(filename);
% dummypos = find(D<=dummy);
% D(dummypos) = NaN;
% imagesc(D,'XData',[min(X),max(X)],'YData',[min(Y),max(Y)]);
% set(gca,'YDir','normal');
% Notes : Requires files grdheadset.m and grdelemset.m
% Geosoft short (2-byte, signed integer) grids ONLY
% Author: Adam O'Neill, 31/1/02
% Set some constants
%griddummy = -32767;
grdhead = struct(
    'es',0,...,
    'sf',4,...,
    'ne',8,...,
    'nv',12,...,
    'kx',16,...,
    'de',20,...,
    'dv',28,...,
    'x0',36,...,
    'y0',44,...,
    'rot',52,...,
    'zbase',60,...,
    'zmult',68,...,
    'label',76,...,
    'mapno',124,...,
    'proj',140,...,
    'unitx',144,...,
    'unity',148,...,
    'unitz',152,...,
    'nvpts',156,...,
    'izmin',160,...,
    'izmax',164,...,
    'izmed',168,...,
    'izmea',172,...,
    'zvar',176,...,
    'prcs',184,...,
    'totallength',512); % Geosoft 2 byte grids ONLY
grdelem = struct(
    'es','int32',... % Data storage
    'sf','int32',...
    'ne','int32',...
    'nv','int32',...
    'kx','int32',...
    'de','float64',... % Geographic information
    'dv','float64',...

```

```

'x0','float64',...
'y0','float64',...
'rot','float64',...
'zbase','float64',...
% Data (Z) scaling
'zmult','float64',...
'label','char*48',...
'mapno','char*16',...
'proj','int32',...
% Optional parameters
'unitx','int32',...
'unity','int32',...
'unitz','int32',...
'nvpnts','int32',...
'izmin','int32',...
'izmax','int32',...
'izmed','int32',...
'izmea','int32',...
'zvar','float64',...
'prcs','int32',...
'datasize','int16'); % Geosoft 2 byte grids ONLY;

% Open data file and get necessary header info
fid = fopen(filename,'r','n');
% Data storage
% fseek(fid,grdhead.es,'bof');
% es = fread(fid,1,grdelem.es);
% fseek(fid,grdhead.sf,'bof');
% sf = fread(fid,1,grdelem.sf);
fseek(fid,grdhead.ne,'bof');
ne = fread(fid,1,grdelem.ne); % No. of elements per vector
fseek(fid,grdhead.nv,'bof');
nv = fread(fid,1,grdelem.nv); % No. of vectors
fseek(fid,grdhead.kx,'bof');
kx = fread(fid,1,grdelem.kx); % Orientation sense
% kx = 1, vectors run left-right
% kx = -1, vectors run up-down
% Geographic information
fseek(fid,grdhead.de,'bof');
de = fread(fid,1,grdelem.de);
fseek(fid,grdhead.dv,'bof');
dv = fread(fid,1,grdelem.dv);
fseek(fid,grdhead.x0,'bof');
x0 = fread(fid,1,grdelem.x0);
fseek(fid,grdhead.y0,'bof');
y0 = fread(fid,1,grdelem.y0);
% fseek(fid,grdhead.rot,'bof');
% rot = fread(fid,1,grdelem.rot);
% Data (Z) scaling
fseek(fid,grdhead.zbase,'bof');
zbase = fread(fid,1,grdelem.zbase);
fseek(fid,grdhead.zmult,'bof');
zmult = fread(fid,1,grdelem.zmult);
% Go to start of data stream and read into array
fseek(fid,grdhead.totallength,'bof');
TEMP = fread(fid,[ne nv],grdelem.datasize);

```

```

% Make the output array
if eq(kx,1)
TEMP2 = TEMP';
elseif eq(kx,-1)
TEMP2 = TEMP;
else
disp('kx not valid')
return
end
% Convert to reals
D = (TEMP2./zmult) + zbase;
clear TEMP TEMP2
% Optional outputs
switch nargout
case {1,2}
case {3,4}
Xaxis = (x0 : de : x0+de*(ne-1));
Yaxis = (y0 : dv : y0+dv*(nv-1));
dummy = min(min(D));
varargout{1} = Xaxis;
varargout{2} = Yaxis;
otherwise
error('Require 1 or 4 outputs')
end
if nargout>3
varargout{3} = dummy;
end
fclose(fid);
end
end

% Callbacks that handle component events
methods (Access = private)

% Value changed function: FractalExponentEditField
function Fractal(app, event)
xsi = getappdata(app.UIFigure, 'xs');
xs2i = getappdata(app.UIFigure, 'xs2');
a2 = getappdata(app.UIFigure, 'data');
Zc = app.FlightaltitudekmEditField.Value;
b2 = app.FractalExponentEditField.Value;
[w2,pw2,ps2,ci1] = fractal_correction(app,a2,b2);
n = length(xsi);
if n == 0
% Plot 1
plot(app.UIAxes,w2,pw2,'k.-');
ylabel(app.UIAxes,'$\ln(A(k))$', 'Interpreter','latex','FontSize',12)
xlabel(app.UIAxes,'$k\backslash;(\frac{1}{km})$', 'Interpreter','latex','FontSize',12)
app.UIAxes.XLim = [0 w2(end)];
app.UIAxes.YLimMode = 'auto';
% Plot 2

```

```

plot(app.UIAxes2,w2,ps2,'k.-');
ylabel(app.UIAxes2,'$\ln(\frac{A(k)}{2\pi k})$','Interpreter','latex','FontSize',12)
xlabel(app.UIAxes2,'$k;(\frac{1}{km})$','Interpreter','latex','FontSize',12)
app.UIAxes2.XLim = [0 w2(end)];
app.UIAxes2.YLimMode = 'auto';
else
%fm1 = getappdata(app.UIFigure,'fm1');
% Calculations
[xs2, ys2] = ind(app,w2,pw2,xs2i);
p2=polyfit(xs2,ys2,1); %slope Zt and intercept
wh2=min(xs2)-0.001:0.001:max(xs2)+0.001; %wavenumber to graphs
kk2=polyval(p2,wh2); %values for files
Zt=(-1)*(p2(1)/(2*pi));
sd2=sqrt(sum((ys2-polyval(p2,xs2)).^2)/(length(xs2))); %standart deviation
Zt_error= sd2/((2*pi)*(max(xs2)-min(xs2)));
% Plot 1
plot(app.UIAxes,w2,pw2,'k.-');
ylabel(app.UIAxes,'$\ln(A(k))$','Interpreter','latex','FontSize',12)
xlabel(app.UIAxes,'$k;(\frac{1}{km})$','Interpreter','latex','FontSize',12)
hold(app.UIAxes,'on')
plot(app.UIAxes,wh2,kk2,'-r','Linewidth',1,'Markersize',12)
hold(app.UIAxes,'off')
app.UIAxes.XLim = [0 0.2];
% Calculations
[xs, ys] = ind(app,w2,ps2,xsi);
pl = polyfit(xs,ys,1); %slope Z0 and intercept
w1 = min(xs)-0.002:0.001:max(xs)+0.002; %wavenumber to graphs
kk = polyval(pl,w1); %values for files
Z0 = (-1)*(pl(1)/(2*pi));
sd1 = sqrt(sum((ys-polyval(pl,xs)).^2)/(length(xs))); %standart deviation
p1_err = sd1/((2*pi)*(max(xs)-min(xs)));
Zb = ((2*Z0)-Zt); %depth to the bottom of the magnetic source (DBMS)
Zb_err = sqrt((4*(p1_err^2)+(Zt_error^2)); %DBMS uncertainty (Martos et al., 2017)
% Plot 2
plot(app.UIAxes2,w2,ps2,'k.-');
ylabel(app.UIAxes2,'$\ln(\frac{A(k)}{2\pi k})$','Interpreter','latex','FontSize',12)
xlabel(app.UIAxes2,'$k;(\frac{1}{km})$','Interpreter','latex','FontSize',12)
hold(app.UIAxes2,'on')
plot(app.UIAxes2,w1, kk,'-r','Linewidth',1,'Markersize',12)
hold(app.UIAxes2,'off')
app.UIAxes2.XLim = [0 0.2];
app.UIAxes2.YLim = [floor(min(ps2(w2<0.2))) ceil(max(ps2) + 1)];
%% Forward model
c1 = find(pw2==ys2(end));
g2=a2(:,2); %Amplitude spectrum
sx=w2(1:c1);
sy=g2(1:c1);
d = exp(sy);
G = ((2*pi*sx).^( -0.5*(b2-1))).*exp(-2*pi*sx*Zt).* (1-exp(-2*pi*sx*(Zb-Zt)));
x0 = log((G'*G)\G'*d);
func = @(x0,x)x0 - (2*pi*x*Zt)- 0.5*(b2-1)*log(2*pi*x)...
+ log((1-exp(-2*pi*x*(Zb-Zt)))); 
[xc,resnorm] = lsqcurvefit(func,x0,sx,sy);
mf=sqrt(resnorm/length(sx));
wn=linspace(w2(1),w2(end));

```

```

fm1=func(xc,wn); %Synthetic Spectrum
fit_fm=mf; %Misfit
% Plot 3
% Confidence intervals
p3 = plot(app.UIAxes3,w2,a2(:,2) + ci1,'k');
hold(app.UIAxes3, 'on')
plot(app.UIAxes3,w2,a2(:,2) - ci1,'k')
%Plots
p1 = plot(app.UIAxes3,w2,a2(:,2),'b-','Linewidth',1,'Markersize',12);
p2 = plot(app.UIAxes3,wn,fm1,'-r','Linewidth',1.5,'Markersize',12);
ylabel(app.UIAxes3,'$\ln(A(k))$','Interpreter','latex','FontSize',12)
xlabel(app.UIAxes3,'$k\frac{1}{km}$','Interpreter','latex','FontSize',12)
hold(app.UIAxes3, 'off')
app.UIAxes3.XLim = [0 0.2];
legend(app.UIAxes3,[p1 p2 p3 ],{'Observed spectrum','Synthetic spectrum','95% confidence interval'})
app.ValuesLabel.Text = sprintf('Values\nFractal exponent  $\beta$ : %0.2f\nZt = %0.2f km\n%0.2f km\nZ0 = %0.2f km\n%0.2f km\nZb = %0.2f km\n%0.2f km\nMisfit = %0.4f',...
b2,Zt-Zc,Zt_error,Z0-Zc,p1_err,Zb-Zc,Zb_err,fit_fm);
setappdata(app.UIFigure,'b2',b2)
setappdata(app.UIFigure,'Zt',Zt)
setappdata(app.UIFigure,'Zt_error',Zt_error)
setappdata(app.UIFigure,'Z0',Z0)
setappdata(app.UIFigure,'p1_err',p1_err)
setappdata(app.UIFigure,'Zb',Zb)
setappdata(app.UIFigure,'Zb_err',Zb_err)
setappdata(app.UIFigure,'fit_fm',fit_fm)
setappdata(app.UIFigure,'xs',xs)
setappdata(app.UIFigure,'xs2',xs2)
end
setappdata(app.UIFigure,'b2',b2)
setappdata(app.UIFigure,'w2',w2)
setappdata(app.UIFigure,'pw2',pw2)
setappdata(app.UIFigure,'ps2',ps2)
setappdata(app.UIFigure,'ci1',ci1)
setappdata(app.UIFigure,'Zc',Zc)
end

% Callback function: CurietemperatureCEditField,
% EmpiricalheatproductiondepthdistributionparameterkmEditField,
% PlotGeothermButton,
% Surfaceheatproductionmicrowm3EditField,
% SurfacetemperatureCEditField,
% ThermalconductivityWmKEditField
function Geotherm(app, event)
Zc = app.FlightaltitudekmEditField.Value;
Ts = app.SurfacetemperatureCEditField.Value;
Tc = app.CurietemperatureCEditField.Value;
A = app.Surfaceheatproductionmicrowm3EditField.Value*1e-6;
b = app.EmpiricalheatproductiondepthdistributionparameterkmEditField.Value*1e3;
k = app.ThermalconductivityWmKEditField.Value;
Zb = 1000*(getappdata(app.UIFigure,'Zb'))-Zc);

```

```

qs = k*(Tc-Ts)/Zb + A*b - ((A*b^2)/Zb)*(1-exp(-Zb/b)); %Martos et al., 2017 %heat
flow at the surface (W/m2)
zb=Zb/1000;
if zb < 20
dlim=ceil(zb/2)*2;
else
dlim=ceil(zb/5)*5;
end
z=0:1000*dlim;
Tcrust=Ts + z*qs/k + A*b*(b-z)/k - A*b^2*exp(-z/b)/k; %Ravat et al., 2016
% tm=max(Tcrust); %Tlim=ceil(tm/100)*100;
% Geotherm
plot(app.UIAxes4,Tcrust,z'/1000,'LineWidth',1.5)
hold(app.UIAxes4,'on')
plot(app.UIAxes4,[0, max(Tcrust)], [zb, zb],'--k','LineWidth',1.5) %Curie Point Depth
plot(app.UIAxes4,[Tc, Tc], [0, dlim],'-r','LineWidth',1.5) %Curie temperature
axis(app.UIAxes4,'ij')
app.UIAxes4.XLim = [0,max(Tcrust)];
app.UIAxes4.YLim = [0,dlim];
legend(app.UIAxes4,['Geotherm',[' CPD = ' num2str(zb,'%.2f') ' km'],[' CT = '
num2str(Tc) ' °C']]);
hold(app.UIAxes4,'off')
b2 = app.FractalExponentEditField.Value;
Zt = getappdata(app.UIFigure,'Zt');
Zt_error = getappdata(app.UIFigure,'Zt_error');
Z0 = getappdata(app.UIFigure,'Z0');
p1_err = getappdata(app.UIFigure,'p1_err');
Zb = getappdata(app.UIFigure,'Zb');
Zb_err = getappdata(app.UIFigure,'Zb_err');
fit_fm = getappdata(app.UIFigure,'fit_fm');
app.ValuesLabel.Text = sprintf('Values\nFractal exponent β: %0.2f\nZt = %0.2f km
\x00B1 %0.2f km\nZ0 = %0.2f km \x00B1 %0.2f km\nZb = %0.2f km \x00B1 %0.2f km\nMisfit
= %0.4f\nnqs = %.4f mW/m2\n',...
b2,Zt-Zc,Zt_error,Z0-Zc,p1_err,Zb-Zc,Zb_err,fit_fm,qs*1e3);
end

```

```

% Button pushed function: SelectFileButton
function Readdata(app, event)
Restart(app,event)
[file, path] = uigetfile({'*.grd';'*.tif'});
app.Label.Text = sprintf(file);
if fileid(app,file) == 1
b = data_aero(app,fullfile(path, file));
elseif fileid(app,file) == 0
b = getgrd2(app,fullfile(path, file));
end
setappdata(app.UIFigure,'b',b)
set(app.ResolutionkmEditField, 'Enable', 'on');
set(app.ResolutionkmEditFieldLabel, 'Enable', 'on');
dl = app.ResolutionkmEditField.Value;
b = getappdata(app.UIFigure,'b');
dt = detrend_2d(app,b); % Polynomial Trend Surface Estimation (degree = 1)
a2 = raas(app,dt,dl); % Radially average power spectrum
plot(app.UIAxes,a2(:,1),a2(:,2),'k.-');

```

```

ylabel(app.UIAxes,'$\ln(A(k))$', 'Interpreter', 'latex', 'FontSize',12)
xlabel(app.UIAxes,'$k\left(\frac{1}{km}\right)$', 'Interpreter', 'latex', 'FontSize',12)
app.UIAxes.XLim = [0 a2(end,1)];
app.UIAxes.YLimMode = 'auto';
plot(app.UIAxes2,a2(:,1),a2(:,2)-log(2*pi*a2(:,1)), 'k.-');
ylabel(app.UIAxes2,'$\ln(\frac{A(k)}{2\pi})$', 'Interpreter', 'latex', 'FontSize',12)
xlabel(app.UIAxes2,'$k\left(\frac{1}{km}\right)$', 'Interpreter', 'latex', 'FontSize',12)
app.UIAxes2.XLim = [0 a2(end,1)];
app.UIAxes2.YLimMode = 'auto';
setappdata(app.UIFigure, 'data',a2)
xs = []; % Data not selected yet
xs2 = []; % Data not selected yet
setappdata(app.UIFigure, 'xs',xs)
setappdata(app.UIFigure, 'xs2',xs2)
% Initial value
[w2,pw2,ps2,ci1] = fractal_correction(app,a2,1);
set(app.FractalExponentEditField, 'Enable', 'on'); set(app.FractalExponentLabel,
'Enable', 'on')
set(app.FlightlatitudekmEditField, 'Enable', 'on');
set(app.FlightlatitudekmEditFieldLabel, 'Enable', 'on')
set(app.SelectpointsButton,'Enable','on')
set(app.RestartButton,'Enable','on')
setappdata(app.UIFigure,'w2',w2)
setappdata(app.UIFigure,'pw2',pw2)
setappdata(app.UIFigure,'ps2',ps2)
setappdata(app.UIFigure,'ci1',ci1)
end

% Button pushed function: RestartButton
function Restart(app, event)
cla(app.UIAxes)
cla(app.UIAxes2)
cla(app.UIAxes3)
cla(app.UIAxes4)
app.ValuesLabel.Text = sprintf('Values');
app.Label.Text = sprintf('');
legend(app.UIAxes3,'off')
legend(app.UIAxes4,'off')
app.FractalExponentEditField.Value = 1;
set(app.FractalExponentEditField, 'Enable', 'off'); set(app.FractalExponentLabel,
'Enable', 'off')
set(app.FlightlatitudekmEditField, 'Enable', 'off');
set(app.FlightlatitudekmEditFieldLabel, 'Enable', 'off')
set(app.SelectpointsButton,'Enable','off')
set(app.RestartButton,'Enable','off')
set(app.SurfacetemperatureCEditField, 'Enable', 'off');
set(app.SurfacetemperatureCEditFieldLabel, 'Enable', 'off')
set(app.CurietemperatureCEditField,'Enable','off');
set(app.CurietemperatureCEditFieldLabel,'Enable','off')
set(app.Surfaceheatproductionmicrowm3EditField,'Enable','off');
set(app.Surfaceheatproductionmicrowm3EditFieldLabel,'Enable','off')
set(app.EmpiricalheatproductiondepthdistributionparameterkmEditField,'Enable','off');
set(app.EmpiricalheatproductiondepthdistributionparameterkmLabel,'Enable','off')

```

```

set(app.ThermalconductivityWmKEditField, 'Enable', 'off');
set(app.ThermalconductivityWmKEditFieldLabel, 'Enable', 'off')
set(app.PlotGeothermButton, 'Enable', 'off')
set(app.ResolutionkmEditField, 'Enable', 'off');
set(app.ResolutionkmEditFieldLabel, 'Enable', 'off');
end

% Button pushed function: SelectpointsButton
function Selectpoints(app, event)
a2 = getappdata(app.UIFigure, 'data');
b2 = app.FractalExponentEditField.Value;
w2 = getappdata(app.UIFigure, 'w2');
pw2 = getappdata(app.UIFigure, 'pw2');
ps2 = getappdata(app.UIFigure, 'ps2');
ci1 = getappdata(app.UIFigure, 'ci1');
Zc = app.FlightlatitudekmEditField.Value;
% Figura 1
f1 = figure;
plot(w2,pw2, 'k.-')
ylabel('$\ln(A(k))$', 'Interpreter', 'latex', 'FontSize', 12);
xlabel('$k; (\frac{1}{km})$', 'Interpreter', 'latex', 'FontSize', 12)
xlim([0 w2(end)])
ylim([floor(min(pw2)) ceil(max(pw2)+1)]);
[~,xs2,ys2] = selectdata('sel','br','BrushShape','rect','BrushSize',0.01);
close(f1)
p2=polyfit(xs2,ys2,1); %slope Zt and intercept
wh2=min(xs2)-0.001:0.001:max(xs2)+0.001; %wavenumber to graphs
kk2=polyval(p2,wh2); %values for files
Zt=(-1)*(p2(1)/(2*pi));
sd2=sqrt(sum((ys2-polyval(p2, xs2)).^2)/(length(xs2))); %standart deviation
Zt_error= sd2/((2*pi)*(max(xs2)-min(xs2)));
% Figura 2
f2=figure;
plot(w2,ps2, 'k.-');
ylabel('$\ln(\frac{A(k)}{2\pi k})$', 'Interpreter', 'latex', 'FontSize', 12)
xlabel('$k; (\frac{1}{km})$', 'Interpreter', 'latex', 'FontSize', 12)
xlim([0 w2(end)])
ylim([floor(min(ps2)) ceil(max(ps2)+1)]);
[~,xs,ys] = selectdata('sel','br','BrushShape','rect','BrushSize',0.01);
close(f2)
pl = polyfit(xs,ys,1); %slope Z0 and intercept
w1 = min(xs)-0.002:0.001:max(xs)+0.002; %wavenumber to graphs
kk = polyval(pl,w1); %values for files
Z0 = (-1)*(pl(1)/(2*pi));
sd1 = sqrt(sum((ys-polyval(pl, xs)).^2)/(length(xs))); %standart deviation
p1_err = sd1/((2*pi)*(max(xs)-min(xs)));
Zb = ((2*Z0)-Zt); %depth to the bottom of the magnetic source (DBMS)
Zb_err = sqrt((4*(p1_err^2)+(Zt_error^2)); %DBMS uncertainty (Martos et al., 2017)
%% Forward model
c1 = find(pw2==ys2(end));
g2=a2(:,2); %Amplitude spectrum
sx=w2(1:c1);
sy=g2(1:c1);
d = exp(sy);

```

```

G = ((2*pi*sx).^(-0.5*(b2-1))).*exp(-2*pi*sx*Zt).*(1-exp(-2*pi*sx*(Zb-Zt)));
x0 = log((G'*G)\G'*d);
func = @(x0,x)x0 - 2*pi*x*Zt- 0.5*(b2-1)*log(2*pi*x)...
+ log((1-exp(-2*pi*x*(Zb-Zt)))); 
[xc,resnorm] = lsqcurvefit(func,x0,sx,sy);
mf=sqrt(resnorm/length(sx));
wn=linspace(w2(1),w2(end));
fm1=func(xc,wn); %Synthetic Spectrum
fit_fm=mf; %Misfit
% Plot 1
plot(app.UIAxes,w2,pw2,'k.-');
ylabel(app.UIAxes,'$\ln(A(k))$', 'Interpreter', 'latex', 'FontSize',12);
xlabel(app.UIAxes,'$k\backslash;(\frac{1}{km})$', 'Interpreter', 'latex', 'FontSize',12)
hold(app.UIAxes, 'on')
plot(app.UIAxes,wh2,kk2,'-r','Linewidth',1,'Markersize',12)
hold(app.UIAxes, 'off')
app.UIAxes.XLim = [0 0.2];
% Plot 2
plot(app.UIAxes2,w2,ps2,'k.-');
ylabel(app.UIAxes2,'$\ln(\frac{A(k)}{2\pi k})$', 'Interpreter', 'latex', 'FontSize',12)
xlabel(app.UIAxes2,'$k\backslash;(\frac{1}{km})$', 'Interpreter', 'latex', 'FontSize',12)
hold(app.UIAxes2, 'on')
plot(app.UIAxes2,w1,kk,'-r','Linewidth',1,'Markersize',12)
hold(app.UIAxes2, 'off')
app.UIAxes2.XLim = [0 0.2];
app.UIAxes2.YLim = [floor(min(ps2(w2<0.2))) ceil(max(ps2) + 1)];
% Plot3
% Confidence intervals
p3 = plot(app.UIAxes3,w2,a2(:,2) + ci1,'k');
hold(app.UIAxes3, 'on')
plot(app.UIAxes3,w2,a2(:,2) - ci1,'k')
%Plots
p1 = plot(app.UIAxes3,w2,a2(:,2),'b-','Linewidth',1,'Markersize',12);
p2 = plot(app.UIAxes3,wn,fm1,'-r','Linewidth',1.5,'Markersize',12);
ylabel(app.UIAxes3,'$\ln(A(k))$', 'Interpreter', 'latex', 'FontSize',12);
xlabel(app.UIAxes3,'$k\backslash;(\frac{1}{km})$', 'Interpreter', 'latex', 'FontSize',12)
hold(app.UIAxes3, 'off')
app.UIAxes3.XLim = [0 0.2];
legend(app.UIAxes3,[p1 p2 p3],{'Observed spectrum','Synthetic spectrum','95% confidence interval'})
% Values
app.ValuesLabel.Text = sprintf('Values\nFractal exponent  $\beta$ : %0.2f\n $Z_t = %0.2f \text{ km}$ \n $Z_0 = %0.2f \text{ km}$ \n $Z_b = %0.2f \text{ km}$ \n $\text{Misfit} = %0.4f$ ',...
b2,Zt-Zc,Zt_error,Z0-Zc,p1_err,Zb-Zc,Zb_err,fit_fm);
% Enables buttons
set(app.SurfacetemperatureCEditField, 'Enable', 'on');
set(app.SurfacetemperatureCEditFieldLabel, 'Enable', 'on')
set(app.CurietemperatureCEditField, 'Enable', 'on');
set(app.CurietemperatureCEditFieldLabel, 'Enable', 'on')
set(app.Surfaceheatproductionmicrowm3CEditField, 'Enable', 'on');
set(app.Surfaceheatproductionmicrowm3CEditFieldLabel, 'Enable', 'on')
set(app.EmpiricalheatproductiondepthdistributionparameterkmEditField, 'Enable', 'on');set(app.EmpiricalheatproductiondepthdistributionparameterkmLabel, 'Enable', 'on')

```

```

set(app.ThermalconductivityWmKEditField, 'Enable', 'on');
set(app.ThermalconductivityWmKEditFieldLabel, 'Enable', 'on')
set(app.PlotGeothermButton, 'Enable', 'on')
setappdata(app.UIFigure, 'b2', b2)
setappdata(app.UIFigure, 'Zt', Zt)
setappdata(app.UIFigure, 'Zt_error', Zt_error)
setappdata(app.UIFigure, 'Z0', Z0)
setappdata(app.UIFigure, 'p1_err', p1_err)
setappdata(app.UIFigure, 'Zb', Zb)
setappdata(app.UIFigure, 'Zb_err', Zb_err)
setappdata(app.UIFigure, 'fit_fm', fit_fm)
setappdata(app.UIFigure, 'xs', xs)
setappdata(app.UIFigure, 'xs2', xs2)
setappdata(app.UIFigure, 'Zc', Zc)
end

% Value changed function: ResolutionkmEditField
function Resolutionandraas(app, event)
dl = app.ResolutionkmEditField.Value;
b = getappdata(app.UIFigure, 'b');
dt = detrend_2d(app,b); % Polynomial Trend Surface Estimation (degree = 1)
a2 = raas(app,dt,dl); % Radially average power spectrum
plot(app.UIAxes,a2(:,1),a2(:,2), 'k.-');
ylabel(app.UIAxes, '$\ln(A(k))$', 'Interpreter', 'latex', 'FontSize',12);
xlabel(app.UIAxes, '$k \cdot (\frac{1}{km})$', 'Interpreter', 'latex', 'FontSize',12)
app.UIAxes.XLim = [0 a2(end,1)];
app.UIAxes.YLimMode = 'auto';
plot(app.UIAxes2,a2(:,1),a2(:,2)-log(2*pi*a2(:,1)), 'k.-');
ylabel(app.UIAxes2, '$\ln(\frac{A(k)}{2\pi k})$', 'Interpreter', 'latex', 'FontSize',12);
xlabel(app.UIAxes2, '$k \cdot (\frac{1}{km})$', 'Interpreter', 'latex', 'FontSize',12)
app.UIAxes2.XLim = [0 a2(end,1)];
app.UIAxes2.YLimMode = 'auto';
setappdata(app.UIFigure, 'data', a2)
xs = []; % Data not selected yet
xs2 = []; % Data not selected yet
setappdata(app.UIFigure, 'xs', xs)
setappdata(app.UIFigure, 'xs2', xs2)
% Initial value
[w2,pw2,ps2,ci1] = fractal_correction(app,a2,1);
set(app.FractalExponentEditField, 'Enable', 'on'); set(app.FractalExponentLabel, 'Enable', 'on')
set(app.FlightlatitudekmEditField, 'Enable', 'on');
set(app.FlightlatitudekmEditFieldLabel, 'Enable', 'on')
set(app.SelectpointsButton, 'Enable', 'on')
set(app.RestartButton, 'Enable', 'on')
app.FractalExponentEditField.Value = 1;
setappdata(app.UIFigure, 'w2', w2)
setappdata(app.UIFigure, 'pw2', pw2)
setappdata(app.UIFigure, 'ps2', ps2)
setappdata(app.UIFigure, 'ci1', ci1)
end
end

```

```

% Component initialization
methods (Access = private)

% Create UIFigure and components
function createComponents(app)

% Create UIFigure and hide until all components are created
app.UIFigure = uifigure('Visible', 'off');
app.UIFigure.Position = [100 100 1010.75 672];
app.UIFigure.Name = 'UI Figure';

% Create UIAxes
app.UIAxes = uiaxes(app.UIFigure);
xlabel(app.UIAxes, 'k (1/km)')
ylabel(app.UIAxes, 'ln(A(k))')
app.UIAxes.FontName = 'Times New Roman';
app.UIAxes.GridAlpha = 0.15;
app.UIAxes.MinorGridAlpha = 0.25;
app.UIAxes.Box = 'on';
app.UIAxes.XGrid = 'on';
app.UIAxes.YGrid = 'on';
app.UIAxes.Position = [11 263 320 230];

% Create UIAxes2
app.UIAxes2 = uiaxes(app.UIFigure);
xlabel(app.UIAxes2, 'k (1/km)')
ylabel(app.UIAxes2, 'ln(A(k)/k)')
app.UIAxes2.FontName = 'Times New Roman';
app.UIAxes2.GridAlpha = 0.15;
app.UIAxes2.MinorGridAlpha = 0.25;
app.UIAxes2.Box = 'on';
app.UIAxes2.XGrid = 'on';
app.UIAxes2.YGrid = 'on';
app.UIAxes2.Position = [11 13 320 220];

% Create UIAxes3
app.UIAxes3 = uiaxes(app.UIFigure);
xlabel(app.UIAxes3, 'k (1/km)')
ylabel(app.UIAxes3, 'ln(A(k))')
app.UIAxes3.FontName = 'Times New Roman';
app.UIAxes3.GridAlpha = 0.15;
app.UIAxes3.MinorGridAlpha = 0.25;
app.UIAxes3.Box = 'on';
app.UIAxes3.XGrid = 'on';
app.UIAxes3.YGrid = 'on';
app.UIAxes3.Position = [361 263 320 230];

% Create UIAxes4
app.UIAxes4 = uiaxes(app.UIFigure);

```

```

title(app.UIAxes4, 'Steady-state one-dimensional geotherm')
xlabel(app.UIAxes4, 'Temperature (°C)')
ylabel(app.UIAxes4, 'Depth (km)')
app.UIAxes4.FontName = 'Times New Roman';
app.UIAxes4.GridAlpha = 0.15;
app.UIAxes4.MinorGridAlpha = 0.25;
app.UIAxes4.Box = 'on';
app.UIAxes4.XGrid = 'on';
app.UIAxes4.YGrid = 'on';
app.UIAxes4.Position = [711 13 288 480];

% Create FractalExponentLabel
app.FractalExponentLabel = uilabel(app.UIFigure);
app.FractalExponentLabel.HorizontalAlignment = 'right';
app.FractalExponentLabel.VerticalAlignment = 'top';
app.FractalExponentLabel.Enable = 'off';
app.FractalExponentLabel.Position = [4 518 114 22];
app.FractalExponentLabel.Text = 'Fractal Exponent ( $\beta$ )';

% Create FractalExponentEditField
app.FractalExponentEditField = uieditfield(app.UIFigure, 'numeric');
app.FractalExponentEditField.Limits = [1 Inf];
app.FractalExponentEditField.ValueChangedFcn = createCallbackFcn(app, @Fractal,
true);
app.FractalExponentEditField.Enable = 'off';
app.FractalExponentEditField.Position = [131 521 97 22];
app.FractalExponentEditField.Value = 1;

% Create SelectpointsButton
app.SelectpointsButton = uibutton(app.UIFigure, 'push');
app.SelectpointsButton.ButtonPushedFcn = createCallbackFcn(app, @Selectpoints, true);
app.SelectpointsButton.Enable = 'off';
app.SelectpointsButton.Position = [340 581 100 22];
app.SelectpointsButton.Text = 'Select points';

% Create ValuesLabel
app.ValuesLabel = uilabel(app.UIFigure);
app.ValuesLabel.BackgroundColor = [1 1 1];
app.ValuesLabel.VerticalAlignment = 'top';
app.ValuesLabel.FontName = 'Arial';
app.ValuesLabel.FontSize = 16;
app.ValuesLabel.Position = [371 13 303 210];
app.ValuesLabel.Text = 'Values';

% Create SurfaceTemperatureCEditFieldLabel
app.SurfaceTemperatureCEditFieldLabel = uilabel(app.UIFigure);
app.SurfaceTemperatureCEditFieldLabel.HorizontalAlignment = 'right';
app.SurfaceTemperatureCEditFieldLabel.VerticalAlignment = 'top';
app.SurfaceTemperatureCEditFieldLabel.Enable = 'off';
app.SurfaceTemperatureCEditFieldLabel.Position = [741 585 141 15];

```

```

app.SurfacetemperatureCEditFieldLabel.Text = 'Surface temperature (°C)';

% Create SurfacetemperatureCEditField
app.SurfacetemperatureCEditField = uieditfield(app.UIFigure, 'numeric');
app.SurfacetemperatureCEditField.ValueChangedFcn = createCallbackFcn(app, @Geotherm,
true);
app.SurfacetemperatureCEditField.Enable = 'off';
app.SurfacetemperatureCEditField.Position = [891 581 50 22];
app.SurfacetemperatureCEditField.Value = 20;

% Create CurietemperatureCEditFieldLabel
app.CuriетemperatureCEditFieldLabel = uilabel(app.UIFigure);
app.CuriетemperatureCEditFieldLabel.HorizontalAlignment = 'right';
app.CuriетemperatureCEditFieldLabel.VerticalAlignment = 'top';
app.CuriетemperatureCEditFieldLabel.Enable = 'off';
app.CuriетemperatureCEditFieldLabel.Position = [751 555 129 15];
app.CuriетemperatureCEditFieldLabel.Text = 'Curie temperature (°C)';

% Create CurietemperatureCEditField
app.CuriетemperatureCEditField = uieditfield(app.UIFigure, 'numeric');
app.CuriетemperatureCEditField.ValueChangedFcn = createCallbackFcn(app, @Geotherm,
true);
app.CuriетemperatureCEditField.Enable = 'off';
app.CuriетemperatureCEditField.Position = [891 551 50 22];
app.CuriетemperatureCEditField.Value = 580;

% Create Surfaceheatproductionmicrowm3CEditFieldLabel
app.Surfaceheatproductionmicrowm3CEditFieldLabel = uilabel(app.UIFigure);
app.Surfaceheatproductionmicrowm3CEditFieldLabel.HorizontalAlignment = 'right';
app.Surfaceheatproductionmicrowm3CEditFieldLabel.VerticalAlignment = 'top';
app.Surfaceheatproductionmicrowm3CEditFieldLabel.Enable = 'off';
app.Surfaceheatproductionmicrowm3CEditFieldLabel.Position = [461 555 208 15];
app.Surfaceheatproductionmicrowm3CEditFieldLabel.Text = 'Surface heat production
(microw/m3)';

% Create Surfaceheatproductionmicrowm3CEditField
app.Surfaceheatproductionmicrowm3CEditField = uieditfield(app.UIFigure, 'numeric');
app.Surfaceheatproductionmicrowm3CEditField.ValueChangedFcn = createCallbackFcn(app,
@Geotherm, true);
app.Surfaceheatproductionmicrowm3CEditField.Enable = 'off';
app.Surfaceheatproductionmicrowm3CEditField.Position = [681 551 40 22];
app.Surfaceheatproductionmicrowm3CEditField.Value = 2.5;

% Create EmpiricalheatproductiondepthdistributionparameterkmEditField
app.EmpiricalheatproductiondepthdistributionparameterkmEditField =
uieditfield(app.UIFigure, 'numeric');
app.EmpiricalheatproductiondepthdistributionparameterkmEditField.ValueChangedFcn =
createCallbackFcn(app, @Geotherm, true);
app.EmpiricalheatproductiondepthdistributionparameterkmEditField.Enable = 'off';

```

```

app.EmpiricalheatproductiondepthdistributionparameterkmEditField.Position = [682 521
39 22];
app.EmpiricalheatproductiondepthdistributionparameterkmEditField.Value = 10;

% Create ThermalconductivityWmKEditFieldLabel
app.ThermalconductivityWmKEditFieldLabel = uilabel(app.UIFigure);
app.ThermalconductivityWmKEditFieldLabel.HorizontalAlignment = 'right';
app.ThermalconductivityWmKEditFieldLabel.VerticalAlignment = 'top';
app.ThermalconductivityWmKEditFieldLabel.Enable = 'off';
app.ThermalconductivityWmKEditFieldLabel.Position = [511 585 160 15];
app.ThermalconductivityWmKEditFieldLabel.Text = 'Thermal conductivity (W/mK)';

% Create ThermalconductivityWmKEditField
app.ThermalconductivityWmKEditField = uieditfield(app.UIFigure, 'numeric');
app.ThermalconductivityWmKEditField.ValueChangedFcn = createCallbackFcn(app,
@Geotherm, true);
app.ThermalconductivityWmKEditField.Enable = 'off';
app.ThermalconductivityWmKEditField.Position = [681 581 40 22];
app.ThermalconductivityWmKEditField.Value = 2.2;

% Create PlotGeothermButton
app.PlotGeothermButton = uibutton(app.UIFigure, 'push');
app.PlotGeothermButton.ButtonPushedFcn = createCallbackFcn(app, @Geotherm, true);
app.PlotGeothermButton.Enable = 'off';
app.PlotGeothermButton.Position = [801 521 100 22];
app.PlotGeothermButton.Text = 'Plot Geotherm';

% Create RestartButton
app.RestartButton = uibutton(app.UIFigure, 'push');
app.RestartButton.ButtonPushedFcn = createCallbackFcn(app, @Restart, true);
app.RestartButton.Enable = 'off';
app.RestartButton.Position = [340 551 100 22];
app.RestartButton.Text = 'Restart';

% Create SelectFileButton
app.SelectFileButton = uibutton(app.UIFigure, 'push');
app.SelectFileButton.ButtonPushedFcn = createCallbackFcn(app, @Readdata, true);
app.SelectFileButton.Position = [14 617 100 22];
app.SelectFileButton.Text = 'Select File';

% Create Label
app.Label = uilabel(app.UIFigure);
app.Label.BackgroundColor = [1 1 1];
app.Label.VerticalAlignment = 'top';
app.Label.Position = [128 618 191 20];
app.Label.Text = '';

% Create FlightaltitudekmEditFieldLabel

```

```

app.FlightaltitudekmEditFieldLabel = uilabel(app.UIFigure);
app.FlightaltitudekmEditFieldLabel.HorizontalAlignment = 'right';
app.FlightaltitudekmEditFieldLabel.VerticalAlignment = 'top';
app.FlightaltitudekmEditFieldLabel.Enable = 'off';
app.FlightaltitudekmEditFieldLabel.Position = [11 555 105 15];
app.FlightaltitudekmEditFieldLabel.Text = 'Flight altitude (km)';

% Create FlightaltitudekmEditField
app.FlightaltitudekmEditField = uieditfield(app.UIFigure, 'numeric');
app.FlightaltitudekmEditField.Enable = 'off';
app.FlightaltitudekmEditField.Position = [131 551 97 22];

% Create EmpiricalheatproductiondepthdistributionparameterkmLabel
app.EmpiricalheatproductiondepthdistributionparameterkmLabel =
uilabel(app.UIFigure);

app.EmpiricalheatproductiondepthdistributionparameterkmLabel.HorizontalAlignment =
'right';

app.EmpiricalheatproductiondepthdistributionparameterkmLabel.VerticalAlignment =
'top';
app.EmpiricalheatproductiondepthdistributionparameterkmLabel.Enable =
'off';
app.EmpiricalheatproductiondepthdistributionparameterkmLabel.Position =
[335 525 334 15];
app.EmpiricalheatproductiondepthdistributionparameterkmLabel.Text =
'Empirical heat-productiondepth-distribution parameter (km)';

% Create ModifiedCentroidMethodLabel
app.ModifiedCentroidMethodLabel = uilabel(app.UIFigure);
app.ModifiedCentroidMethodLabel.VerticalAlignment = 'top';
app.ModifiedCentroidMethodLabel.FontSize = 36;
app.ModifiedCentroidMethodLabel.FontWeight = 'bold';
app.ModifiedCentroidMethodLabel.Position = [387 617 457 47];
app.ModifiedCentroidMethodLabel.Text = 'Modified Centroid Method';

% Create ResolutionkmEditFieldLabel
app.ResolutionkmEditFieldLabel = uilabel(app.UIFigure);
app.ResolutionkmEditFieldLabel.HorizontalAlignment = 'right';
app.ResolutionkmEditFieldLabel.Enable = 'off';
app.ResolutionkmEditFieldLabel.Position = [23 578 90 22];
app.ResolutionkmEditFieldLabel.Text = 'Resolution (km)';

% Create ResolutionkmEditField
app.ResolutionkmEditField = uieditfield(app.UIFigure, 'numeric');
app.ResolutionkmEditField.Limits = [0 Inf];
app.ResolutionkmEditField.ValueChangedFcn = createCallbackFcn(app,
@Resolutionandraas, true);
app.ResolutionkmEditField.Enable = 'off';
app.ResolutionkmEditField.Position = [128 578 100 22];

```

```

app.ResolutionkmEditField.Value = 1;

    % Show the figure after all components are created
    app.UIFigure.Visible = 'on';
end
end

% App creation and deletion
methods (Access = public)

    % Construct app
    function app = modified_centroid

        % Create UIFigure and components
        createComponents(app)

        % Register the app with App Designer
        registerApp(app, app.UIFigure)

        if nargout == 0
            clear app
        end
    end

    % Code that executes before app deletion
    function delete(app)

        % Delete UIFigure when app is deleted
        delete(app.UIFigure)
    end
end

```

```

defractal.mlapp

classdef defractal < matlab.apps.AppBase

% Properties that correspond to app components
properties (Access = public)
UIFigure matlab.ui.Figure
UIAxes matlab.ui.control.UIAxes
UIAxes2 matlab.ui.control.UIAxes
UIAxes3 matlab.ui.control.UIAxes
UIAxes4 matlab.ui.control.UIAxes
FractalExponentLabel matlab.ui.control.Label
FractalExponentEditField matlab.ui.control.NumericEditField
SelectpointsButton matlab.ui.control.Button
ValuesLabel matlab.ui.control.Label
SurfacetemperatureCEditFieldLabel matlab.ui.control.Label
SurfacetemperatureCEditField matlab.ui.control.NumericEditField
CurietemperatureCEditFieldLabel matlab.ui.control.Label
CurietemperatureCEditField matlab.ui.control.NumericEditField
SurfaceheatproductionmicroWm3EditFieldLabel matlab.ui.control.Label
SurfaceheatproductionmicroWm3EditField matlab.ui.control.NumericEditField
EmpiricalheatproductiondepthdistributionparameterkmEditField
matlab.ui.control.NumericEditField
ThermalconductivityWmKEditFieldLabel matlab.ui.control.Label
ThermalconductivityWmKEditField matlab.ui.control.NumericEditField
PlotGeothermButton matlab.ui.control.Button
RestartButton matlab.ui.control.Button
SelectFileButton matlab.ui.control.Button
Label matlab.ui.control.Label
FlightaltitudekmEditFieldLabel matlab.ui.control.Label
FlightaltitudekmEditField matlab.ui.control.NumericEditField
EmpiricalheatproductiondepthdistributionparameterkmLabel matlab.ui.control.Label
DefractalMethodLabel matlab.ui.control.Label
ResolutionkmEditFieldLabel matlab.ui.control.Label
ResolutionkmEditField matlab.ui.control.NumericEditField
end

methods (Access = public)
function [w,pw,ps,ci] = fractal_correction(~,x,b1)
w=x(:,1);
ps=(x(:,2)- log( 2*pi*w )) + log(( 2*pi*w ).^( 0.5*(b1) ) );% for Z0
pw=x(:,2)+log(( 2*pi*w ).^(0.5*(b1)));% for Zt
ci=x(:,3);
end
function b = data_aero(~,fileToRead1)
%IMPORTFILE(FILETOREAD1)
% Imports data from the specified file
% FILETOREAD1: file to read
% Auto-generated by MATLAB on 23-May-2019 17:59:12
% Import the file

```

```

rawData1 = importdata(fileToRead1);
% For some simple files (such as a CSV or JPEG files), IMPORTDATA might
% return a simple array. If so, generate a structure so that the output
% matches that from the Import Wizard.
[~,name] = fileparts(fileToRead1);
newData1.(matlab.lang.makeValidName(name)) = rawData1;
% Create new variables in the base workspace from those fields.
vars = fieldnames(newData1);
for i = 1:length(vars)
assignin('base', vars{i}, newData1.(vars{i}));
end
b = rawData1;
end
function Z_f = detrend_2d(~,Z)
% This function is written by Munther Gdeisat-The General Engineering
% Research Institute (GERI) at Liverpool John Moores University.
% This program is written on 9th October 2011
% This function is the 2D equivalent of detrend function in Matlab
% Z_f = DETREND(Z) removes the best plane fit trend from the data
% in the 2D array Z and returns the residual in the 2D array Z_f
if size(Z,2) < 2
disp('Z must be a 2D array')
return
end
M = size(Z,2);
N = size(Z,1);
[X,Y] = meshgrid(1:M,1:N);
%Make the 2D data as 1D vector
Xcolv = X(:); % Make X a column vector
Ycolv = Y(:); % Make Y a column vector
Zcolv = Z(:); % Make Z a column vector
Const = ones(size(Xcolv)); % Vector of ones for constant term
% find the coefficients of the best plane fit
Coefficients = [Xcolv Ycolv Const]\Zcolv; % Find the coefficients
XCoeff = Coefficients(1); % X coefficient
YCoeff = Coefficients(2); % Y coefficient
CCoeff = Coefficients(3); % constant term
% detrend the data
Z_p = XCoeff * X + YCoeff * Y + CCoeff;
Z_f = Z - Z_p;
end
function cv3 = raas(~,anom,d1)
% function raps(img)
% Computes and plots radially a power spectrum of magnetic data in
% a GEOTif image of the amplitude spectrum
% Based and modified on (C) E. Ruzanski, RCG, 2009 and
% Tom Ridsdill-Smith March 2000
%% Process image size information
[ny, nx] = size(anom);
N = max(nx,ny);
if mod(N,2) ~= 0
N = N + 1;
end

```

```

TFA = fftshift(fft2(anom,N,N));
EA = 2*abs(TFA)/(ny*nx); % Espectro de amplitud 2D
% Compute radially average amplitude spectrum
n = -N/2:N/2-1;
[NX, NY] = meshgrid(n,n);
[~, rho] = cart2pol(NX, NY); % Convert to polar coordinate axes
rho = round(rho);
i = cell(N/2+1, 1);
Pf = zeros(N/2+1,1);
CF = zeros(N/2+1,1);
nm = zeros(N/2+1,1);
for r = 0:N/2
i{r + 1} = find(rho == r);
Pf(r + 1) = nanmean(log(EA(i{r+1}))); %Amplitude spectra
CF(r + 1) = 1.96*(nanstd(log(EA(i{r+1}))))...
/sqrt(length(EA(i{r+1}))); %confidence interval
end
% Calculate the 1D wavenumber for a signal of even length
kn = 1/(2*d1); % Nyquist wavenumber
k0 = 1/(N*d1); % Fundamental wavenumber
w = (0:k0:kn)';
cv2=[w(2:end),Pf(2:end),CF(2:end),nm(2:end)];
cv3 =cv2(cv2(:,3) <= 1, :);
end
function results = func18(~)
[pointlist, xs, ys] = selectdata(Input);
results = [pointlist, xs, ys];
end
function [x, y] = ind(~, xi, yi, dx)

n = length(dx);
x = ones(n,1);
y = ones(n,1);
for i = 1:n
c = find(xi == dx(i));
x(i) = xi(c);
y(i) = yi(c);
end
end
function x = fileid(~,data)
% This program identifies the input file extension. If the files
% have a *.grd extention one the return value is 0. If the file has
% a *.tif extension, the return value is 1.
[~,~,ext] = fileparts(data);
if (strcmpi(trim(ext), '.grd'))
x=0;
elseif (strcmpi(trim(ext), '.tif'))
x=1;
else
disp('Error: Unexpected file')
return
end
end
function [D,varargout] = getgrd2(~,filename)

```

```

% Read a Geosoft 2-byte binary grid
% Syntax: [D,varargout] = getgrd2(filename);
% Import: filename = string of grid filename, eg. 'mag.grd'
% Use full path if grid is not in current directory
% eg. 'd:\data\mag.grd'
% Export: D = 2D array of real data
% varargout = Xaxis,Yaxis,dummy
% Xaxis,Yaxis = x- and y-axis coordinates
% dummy = dummy value as a real in D
% Usage : D = getgrd2(filename); % Array only
% [D,X,Y] = getgrd2(filename); % Data and coordinates
% To locate dummy pixels and image use:
% [D,X,Y,dummy] = getgrd2(filename);
% dummypos = find(D<=dummy);
% D(dummypos) = NaN;
% imagesc(D,'XData',[min(X),max(X)],'YData',[min(Y),max(Y)]);
% set(gca,'YDir','normal');
% Notes : Requires files grdheadset.m and grdelemset.m
% Geosoft short (2-byte, signed integer) grids ONLY
% Author: Adam O'Neill, 31/1/02
% Set some constants
%griddummy = -32767;
grdhead = struct(...  

    'es',0,...  

    'sf',4,...  

    'ne',8,...  

    'nv',12,...  

    'kx',16,...  

    'de',20,...  

    'dv',28,...  

    'x0',36,...  

    'y0',44,...  

    'rot',52,...  

    'zbase',60,...  

    'zmult',68,...  

    'label',76,...  

    'mapno',124,...  

    'proj',140,...  

    'unitx',144,...  

    'unity',148,...  

    'unitz',152,...  

    'nvpts',156,...  

    'izmin',160,...  

    'izmax',164,...  

    'izmed',168,...  

    'izmea',172,...  

    'zvar',176,...  

    'prcs',184,...  

    'totallength',512); % Geosoft 2 byte grids ONLY
grdelem = struct(...  

    'es','int32',...
    '% Data storage  

    'sf','int32',...
    'ne','int32',...
    'nv','int32',...
    'kx','int32',...

```

```

'de','float64',...
'dv','float64',...
'x0','float64',...
'y0','float64',...
'rot','float64',...
'zbase','float64',... % Data (Z) scaling
'zmult','float64',...
'label','char*48',...
'mapno','char*16',...
'proj','int32',... % Optional parameters
'unitx','int32',...
'unity','int32',...
'unitz','int32',...
'nvpts','int32',...
'izmin','int32',...
'izmax','int32',...
'izmed','int32',...
'izmea','int32',...
'zvar','float64',...
'prcs','int32',...
'datasize','int16'); % Geosoft 2 byte grids ONLY;

% Open data file and get necessary header info
fid = fopen(filename,'r','n');
% Data storage
% fseek(fid,grdhead.es,'bof');
% es = fread(fid,1,grdelem.es);
% fseek(fid,grdhead.sf,'bof');
% sf = fread(fid,1,grdelem.sf);
fseek(fid,grdhead.ne,'bof');
ne = fread(fid,1,grdelem.ne); % No. of elements per vector
fseek(fid,grdhead.nv,'bof');
nv = fread(fid,1,grdelem.nv); % No. of vectors
fseek(fid,grdhead.kx,'bof');
kx = fread(fid,1,grdelem.kx); % Orientation sense
% kx = 1, vectors run left-right
% kx = -1, vectors run up-down
% Geographic information
fseek(fid,grdhead.de,'bof');
de = fread(fid,1,grdelem.de);
fseek(fid,grdhead.dv,'bof');
dv = fread(fid,1,grdelem.dv);
fseek(fid,grdhead.x0,'bof');
x0 = fread(fid,1,grdelem.x0);
fseek(fid,grdhead.y0,'bof');
y0 = fread(fid,1,grdelem.y0);
% fseek(fid,grdhead.rot,'bof');
% rot = fread(fid,1,grdelem.rot);
% Data (Z) scaling
fseek(fid,grdhead.zbase,'bof');
zbase = fread(fid,1,grdelem.zbase);
fseek(fid,grdhead.zmult,'bof');
zmult = fread(fid,1,grdelem.zmult);
% Go to start of data stream and read into array

```

```

fseek(fid,grdhead.totallength,'bof');
TEMP = fread(fid,[ne nv],grdelem.datasize);
% Make the output array
if eq(kx,1)
TEMP2 = TEMP';
elseif eq(kx,-1)
TEMP2 = TEMP;
else
disp('kx not valid')
return
end
% Convert to reals
D = (TEMP2./zmult) + zbase;
clear TEMP TEMP2
% Optional outputs
switch nargout
case {1,2}
case {3,4}
Xaxis = (x0 : de : x0+de*(ne-1));
Yaxis = (y0 : dv : y0+dv*(nv-1));
dummy = min(min(D));
varargout{1} = Xaxis;
varargout{2} = Yaxis;
otherwise
error('Require 1 or 4 outputs')
end
if nargout>3
varargout{3} = dummy;
end
fclose(fid);
end
end

% Callbacks that handle component events
methods (Access = private)

% Value changed function: FractalExponentEditField
function Fractal(app, event)
xsi = getappdata(app.UIFigure, 'xs');
xs2i = getappdata(app.UIFigure, 'xs2');
a2 = getappdata(app.UIFigure, 'data');
Zc = app.FlightaltitudekmEditField.Value;
b2 = app.FractalExponentEditField.Value;
[w2,pw2,ps2,ci1] = fractal_correction(app,a2,b2);
n = length(xsi);
if n == 0
% Plot 1
plot(app.UIAxes,w2,pw2,'k.-');
ylabel(app.UIAxes,$'\ln(A(k))$', 'Interpreter', 'latex', 'FontSize',12)
xlabel(app.UIAxes,$'k\backslash(\frac{1}{km})$', 'Interpreter', 'latex', 'FontSize',12)
app.UIAxes.XLim = [0 w2(end)];

```

```

app.UIAxes.YLimMode = 'auto';
% Plot 2
plot(app.UIAxes2,w2,ps2,'k.-');
ylabel(app.UIAxes2,'$\ln(\frac{A(k)}{2\pi k})$', 'Interpreter', 'latex', 'FontSize',12)
xlabel(app.UIAxes2,'$k;(\frac{1}{km})$', 'Interpreter', 'latex', 'FontSize',12)
app.UIAxes2.XLim = [0 w2(end)];
app.UIAxes2.YLimMode = 'auto';
else
%fm1 = getappdata(app.UIFigure,'fm1');
% Calculations
[xs2, ys2] = ind(app,w2,pw2,xs2i);
p2=polyfit(xs2,ys2,1); %slope Zt and intercept
wh2=min(xs2)-0.001:0.001:max(xs2)+0.001; %wavenumber to graphs
kk2=polyval(p2,wh2); %values for files
Zt=(-1)*(p2(1)/(2*pi));
sd2=sqrt(sum((ys2-polyval(p2,xs2)).^2)/(length(xs2))); %standart deviation
Zt_error= sd2/((2*pi)*(max(xs2)-min(xs2)));
% Plot 1
plot(app.UIAxes,w2,pw2,'k.-');
ylabel(app.UIAxes,'$\ln(A(k))$', 'Interpreter', 'latex', 'FontSize',12)
xlabel(app.UIAxes,'$k;(\frac{1}{km})$', 'Interpreter', 'latex', 'FontSize',12)
hold(app.UIAxes, 'on')
plot(app.UIAxes,wh2, kk2, '-r', 'Linewidth',1, 'Markersize',12)
hold(app.UIAxes, 'off')
app.UIAxes.XLim = [0 0.2];
% Calculations
[xs, ys] = ind(app,w2,ps2,xsi);
pl = polyfit(xs,ys,1); %slope Z0 and intercept
w1 = min(xs)-0.002:0.001:max(xs)+0.002; %wavenumber to graphs
kk = polyval(pl,w1); %values for files
Z0 = (-1)*(pl(1)/(2*pi));
sd1 = sqrt(sum((ys-polyval(pl,xs)).^2)/(length(xs))); %standart deviation
p1_err = sd1/((2*pi)*(max(xs)-min(xs)));
Zb = ((2*Z0)-Zt); %depth to the bottom of the magnetic source (DBMS)
Zb_err = sqrt((4*(p1_err^2))+(Zt_error^2)); %DBMS uncertainty (Martos et al., 2019)
% Plot 2
plot(app.UIAxes2,w2,ps2,'k.-');
ylabel(app.UIAxes2,'$\ln(\frac{A(k)}{2\pi k})$', 'Interpreter', 'latex', 'FontSize',12)
xlabel(app.UIAxes2,'$k;(\frac{1}{km})$', 'Interpreter', 'latex', 'FontSize',12)
hold(app.UIAxes2, 'on')
plot(app.UIAxes2,w1, kk, '-r', 'Linewidth',1, 'Markersize',12)
hold(app.UIAxes2, 'off')
app.UIAxes2.XLim = [0 0.2];
app.UIAxes2.YLim = [floor(min(ps2(w2<0.2))) ceil(max(ps2) + 1)];
%% Forward model
c1 = find(ps2==ys2(end));
sx=w2(1:c1);
sy=pw2(1:c1); %Amplitude spectrum
d = exp(sy);
G = exp(-2*pi*sx*Zt).*(1-exp(-2*pi*sx*(Zb-Zt)));
x0 = log((G'*G)\G'*d);
func = @(x0,x)x0 - ((2*pi*x)*Zt) + log((1-exp(-2*pi*x*(Zb-Zt))));
[xc,resnorm] = lsqcurvefit(func,x0,sx,sy);
mf=sqrt(resnorm/length(sx));
wn=linspace(w2(1),w2(end));

```

```

fm1=func(xc,wn); %Synthetic Spectrum
fit_fm=mf; %Misfit
% Plot 3
% Confidence intervals
p4 = plot(app.UIAxes3,w2,pw2 + ci1, 'k');
hold(app.UIAxes3, 'on')
plot(app.UIAxes3,w2,pw2 - ci1, 'k')
plot(app.UIAxes3,w2,a2(:,2) + ci1, 'k')
plot(app.UIAxes3,w2,a2(:,2) - ci1, 'k')
%Plots
p2 = plot(app.UIAxes3,w2,pw2, 'b-', 'LineWidth',1,'MarkerSize',12);
p1 = plot(app.UIAxes3,w2,a2(:,2), 'g-', 'LineWidth',1,'MarkerSize',12);
p3 = plot(app.UIAxes3,wn,fm1, '-r', 'LineWidth',1.5,'MarkerSize',12);
ylabel(app.UIAxes3,'$\ln(A(k))$', 'Interpreter', 'latex', 'FontSize',12)
xlabel(app.UIAxes3,'$k\frac{1}{km}$', 'Interpreter', 'latex', 'FontSize',12)
hold(app.UIAxes3, 'off')
app.UIAxes3.XLim = [0 0.2];
legend(app.UIAxes3,[p1 p2 p3 p4],{'Observed spectrum', 'Corrected spectrum',...
'Synthetic spectrum', '95% confidence interval'})
app.ValuesLabel.Text = sprintf('Values\nFractal exponent  $\alpha$ : %0.2f\nZt = %0.2f km
\x00B1 %0.2f km\nZ0 = %0.2f km \x00B1 %0.2f km\nZb = %0.2f km \x00B1 %0.2f km\nMisfit
= %0.4f', ...
b2,Zt-Zc,Zt_error,Z0-Zc,p1_err,Zb-Zc,Zb_err,fit_fm);
setappdata(app.UIFigure, 'b2',b2)
setappdata(app.UIFigure, 'Zt',Zt)
setappdata(app.UIFigure, 'Zt_error',Zt_error)
setappdata(app.UIFigure, 'Z0',Z0)
setappdata(app.UIFigure, 'p1_err',p1_err)
setappdata(app.UIFigure, 'Zb',Zb)
setappdata(app.UIFigure, 'Zb_err',Zb_err)
setappdata(app.UIFigure, 'fit_fm',fit_fm)
setappdata(app.UIFigure, 'xs',xs)
setappdata(app.UIFigure, 'xs2',xs2)
end
setappdata(app.UIFigure, 'b2',b2)
setappdata(app.UIFigure, 'w2',w2)
setappdata(app.UIFigure, 'pw2',pw2)
setappdata(app.UIFigure, 'ps2',ps2)
setappdata(app.UIFigure, 'ci1',ci1)
setappdata(app.UIFigure, 'Zc',Zc)
end

% Callback function: CurietemperatureCEditField,
% EmpiricalheatproductiondepthdistributionparameterkmEditField,
% PlotGeothermButton,
% SurfaceheatproductionmicroWm3EditField,
% SurfacetemperatureCEditField,
% ThermalconductivityWmKEditField
function Geotherm(app, event)
Zc = app.FlightlatitudekmEditField.Value;
Ts = app.SurfacetemperatureCEditField.Value;
Tc = app.CurietemperatureCEditField.Value;
A = app.SurfaceheatproductionmicroWm3EditField.Value*1e-6;
b = app.EmpiricalheatproductiondepthdistributionparameterkmEditField.Value*1e3;

```

```

k = app.ThermalconductivityWmKEditField.Value;
Zb = 1000*(getappdata(app.UIFigure, 'Zb'))-Zc;
qs = k*(Tc-Ts)/Zb + A*b - ((A*b^2)/Zb)*(1-exp(-Zb/b)); %Martos et al., 2017 %heat
flow at the surface (W/m2)
zb=Zb/1000;
if zb < 20
dlim=ceil(zb/2)*2;
else
dlim=ceil(zb/5)*5;
end
z=0:1000*dlim;
Tcrust=Ts + z*qs/k + A*b*(b-z)/k - A*b^2*exp(-z/b)/k; %Ravat et al., 2016
% tm=max(Tcrust); %Tlim=ceil(tm/100)*100;
% Geotherm
plot(app.UIAxes4,Tcrust,z'/1000, 'LineWidth',1.5)
hold(app.UIAxes4, 'on')
plot(app.UIAxes4,[0, max(Tcrust)], [zb, zb], '--k', 'LineWidth',1.5) %Curie Point Depth
plot(app.UIAxes4,[Tc, Tc], [0, dlim], '--r', 'LineWidth',1.5) %Curie temperature
axis(app.UIAxes4, 'ij')
app.UIAxes4.XLim = [0,max(Tcrust)];
app.UIAxes4.YLim = [0,dlim];
legend(app.UIAxes4,{'Geotherm',' CPD = ' num2str(zb,'%.2f') ' km',' CT = '
num2str(Tc) ' °C'});
hold(app.UIAxes4, 'off')
b2 = app.FractalExponentEditField.Value;
Zt = getappdata(app.UIFigure, 'Zt');
Zt_error = getappdata(app.UIFigure, 'Zt_error');
Z0 = getappdata(app.UIFigure, 'Z0');
p1_err = getappdata(app.UIFigure, 'p1_err');
Zb = getappdata(app.UIFigure, 'Zb');
Zb_err = getappdata(app.UIFigure, 'Zb_err');
fit_fm = getappdata(app.UIFigure, 'fit_fm');
app.ValuesLabel.Text = sprintf('Values\nFractal exponent a: %0.2f\nZt = %0.2f km
\x00B1 %0.2f km\nZ0 = %0.2f km \x00B1 %0.2f km\nZb = %0.2f km \x00B1 %0.2f km\nMisfit
= %0.4f\nqs = %.4f mW/m2\n',...
b2,Zt-Zc,Zt_error,Z0-Zc,p1_err,Zb-Zc,Zb_err,fit_fm,qs*1e3);
end

% Button pushed function: SelectFileButton
function Readdata(app, event)
Restart(app,event)
[file, path] = uigetfile({'*.grd'; '*.tif'});
app.Label.Text = sprintf(file);
if fileid(app,file) == 1
b = data_aero(app,fullfile(path, file));
elseif fileid(app,file) == 0
b = getgrd2(app,fullfile(path, file));
end
setappdata(app.UIFigure, 'b',b)
set(app.ResolutionkmEditField, 'Enable', 'on');
set(app.ResolutionkmEditFieldLabel, 'Enable', 'on');
dl = app.ResolutionkmEditField.Value;
b = getappdata(app.UIFigure, 'b');
dt = detrend_2d(app,b); % Polynomial Trend Surface Estimation (degree = 1)

```

```

a2 = raas(app,dt,d1); % Radially average power spectrum
plot(app.UIAxes,a2(:,1),a2(:,2), 'k.-');
ylabel(app.UIAxes,'$\ln(A(k))$', 'Interpreter', 'latex', 'FontSize',12)
xlabel(app.UIAxes,'$k\;(\frac{1}{km})$', 'Interpreter', 'latex', 'FontSize',12)
app.UIAxes.XLim = [0 a2(end,1)];
app.UIAxes.YLimMode = 'auto';
plot(app.UIAxes2,a2(:,1),a2(:,2)-log(2*pi*a2(:,1)), 'k.-');
ylabel(app.UIAxes2,'$\ln(\frac{A(k)}{2\pi k})$', 'Interpreter', 'latex', 'FontSize',12)
xlabel(app.UIAxes2,'$k\;(\frac{1}{km})$', 'Interpreter', 'latex', 'FontSize',12)
app.UIAxes2.XLim = [0 a2(end,1)];
app.UIAxes2.YLimMode = 'auto';
setappdata(app.UIFigure, 'data',a2)
xs = []; % Data not selected yet
xs2 = []; % Data not selected yet
setappdata(app.UIFigure, 'xs',xs)
setappdata(app.UIFigure, 'xs2',xs2)
% Initial value
[w2,pw2,ps2,ci1] = fractal_correction(app,a2,0);
set(app.FractalExponentEditField, 'Enable', 'on'); set(app.FractalExponentLabel,
'Enable', 'on')
set(app.FlightlatitudekmEditField, 'Enable', 'on');
set(app.FlightlatitudekmEditFieldLabel, 'Enable', 'on')
set(app.SelectpointsButton,'Enable','on')
set(app.RestartButton,'Enable','on')
setappdata(app.UIFigure, 'w2',w2)
setappdata(app.UIFigure, 'pw2',pw2)
setappdata(app.UIFigure, 'ps2',ps2)
setappdata(app.UIFigure, 'ci1',ci1)
end

% Button pushed function: RestartButton
function Restart(app, event)
cla(app.UIAxes)
cla(app.UIAxes2)
cla(app.UIAxes3)
cla(app.UIAxes4)
app.ValuesLabel.Text = sprintf('Values');
app.Label.Text = sprintf('');
legend(app.UIAxes3,'off')
legend(app.UIAxes4,'off')
app.FractalExponentEditField.Value = 0;
set(app.FractalExponentEditField, 'Enable', 'off'); set(app.FractalExponentLabel,
'Enable', 'off')
set(app.FlightlatitudekmEditField, 'Enable', 'off');
set(app.FlightlatitudekmEditFieldLabel, 'Enable', 'off')
set(app.SelectpointsButton,'Enable','off')
set(app.RestartButton,'Enable','off')
set(app.SurfaceTemperatureCEditField, 'Enable', 'off');
set(app.SurfaceTemperatureCEditFieldLabel, 'Enable', 'off')
set(app.CurietemperatureCEditField, 'Enable', 'off');
set(app.CurietemperatureCEditFieldLabel, 'Enable', 'off')
set(app.Surfaceheatproductionmicrowm3EditField,'Enable','off');
set(app.Surfaceheatproductionmicrowm3EditFieldLabel,'Enable','off')

```

```

set(app.EmpiricalheatproductiondepthdistributionparameterkmEditField, 'Enable', 'off');
set(app.EmpiricalheatproductiondepthdistributionparameterkmLabel, 'Enable', 'off')
set(app.ThermalconductivityWmKEditField, 'Enable', 'off');
set(app.ThermalconductivityWmKEditFieldLabel, 'Enable', 'off')
set(app.PlotGeothermButton, 'Enable', 'off')
set(app.ResolutionkmEditField, 'Enable', 'off');
set(app.ResolutionkmEditFieldLabel, 'Enable', 'off');
end

% Button pushed function: SelectpointsButton
function Selectpoints(app, event)
a2 = getappdata(app.UIFigure, 'data');
b2 = app.FractalExponentEditField.Value;
w2 = getappdata(app.UIFigure, 'w2');
pw2 = getappdata(app.UIFigure, 'pw2');
ps2 = getappdata(app.UIFigure, 'ps2');
ci1 = getappdata(app.UIFigure, 'ci1');
Zc = app.FlightlatitudekmEditField.Value;
% Figura 1
f1 = figure;
plot(w2,pw2, 'k.-')
ylabel('$\ln(A(k))$', 'Interpreter', 'latex', 'FontSize', 12)
xlabel('$k; (\frac{1}{km})$', 'Interpreter', 'latex', 'FontSize', 12)
xlim([0 w2(end)]);
ylim([floor(min(pw2)) ceil(max(pw2)+1)]);
[~,xs2,ys2] = selectdata('sel','br','BrushShape','rect','BrushSize',0.01);
close(f1)
p2=polyfit(xs2,ys2,1); %slope Zt and intercept
wh2=min(xs2)-0.001:0.001:max(xs2)+0.001; %wavenumber to graphs
kk2=polyval(p2,wh2); %values for files
Zt=(-1)*(p2(1)/(2*pi));
sd2=sqrt(sum((ys2-polyval(p2, xs2)).^2)/(length(xs2))); %standart deviation
Zt_error= sd2/((2*pi)*(max(xs2)-min(xs2)));
% Figura 2
f2=figure;
plot(w2,ps2, 'k.-');
ylabel('$\ln(\frac{A(k)}{k})$', 'Interpreter', 'latex', 'FontSize', 12)
xlabel('$k; (\frac{1}{km})$', 'Interpreter', 'latex', 'FontSize', 12)
xlim([0 w2(end)]);
ylim([floor(min(ps2)) ceil(max(ps2)+1)]);
[~,xs,ys] = selectdata('sel','br','BrushShape','rect','BrushSize',0.01);
close(f2)
pl = polyfit(xs,ys,1); %slope Z0 and intercept
w1 = min(xs)-0.002:0.001:max(xs)+0.002; %wavenumber to graphs
kk = polyval(pl,w1); %values for files
Z0 = (-1)*(pl(1)/(2*pi));
sd1 = sqrt(sum((ys-polyval(pl, xs)).^2)/(length(xs))); %standart deviation
p1_err = sd1/((2*pi)*(max(xs)-min(xs)));
Zb = ((2*Z0)-Zt); %depth to the bottom of the magnetic source (DBMS)
Zb_err = sqrt((4*(p1_err^2)+(Zt_error^2)); %DBMS uncertainty (Martos et al., 2019)
%% Forward model
c1 = find(pw2==ys2(end));
sx=w2(1:c1);
sy=pw2(1:c1); %Amplitude spectrum

```

```

d = exp(sy);
G = exp(-2*pi*sx*Zt).*(1-exp(-2*pi*sx*(Zb-Zt)));
x0 = log((G'*G)\G'*d);
func = @(x0,x) x0 - ((2*pi*x)*Zt) + log((1-exp(-2*pi*x*(Zb-Zt))));
[xc,resnorm] = lsqcurvefit(func,x0,sx,sy);
mf=sqrt(resnorm/length(sx));
wn=linspace(w2(1),w2(end));
fm1=func(xc,wn); %Synthetic Spectrum
fit_fm=mf; %Misfit
% Plot 1
plot(app.UIAxes,w2,pw2,'k.-');
ylabel(app.UIAxes,'$\ln(A(k))$', 'Interpreter', 'latex', 'FontSize',12)
xlabel(app.UIAxes,'$k\;(\frac{1}{km})$', 'Interpreter', 'latex', 'FontSize',12)
hold(app.UIAxes, 'on')
plot(app.UIAxes,wh2,kk2,'-r','Linewidth',1,'Markersize',12)
hold(app.UIAxes, 'off')
app.UIAxes.XLim = [0 0.2];
% Plot 2
plot(app.UIAxes2,w2,ps2,'k.-');
ylabel(app.UIAxes2,'$\ln(\frac{A(k)}{\pi k})$', 'Interpreter', 'latex', 'FontSize',12)
xlabel(app.UIAxes2,'$k\;(\frac{1}{km})$', 'Interpreter', 'latex', 'FontSize',12)
hold(app.UIAxes2, 'on')
plot(app.UIAxes2,w1,kk,'-r','Linewidth',1,'Markersize',12)
hold(app.UIAxes2, 'off')
app.UIAxes2.XLim = [0 0.2];
app.UIAxes2.YLim = [floor(min(ps2(w2<0.2))) ceil(max(ps2) + 1)];
% Plot3 3
% Confidence intervals
p4 = plot(app.UIAxes3,w2,pw2 + ci1,'k');
hold(app.UIAxes3, 'on')
plot(app.UIAxes3,w2,pw2 - ci1,'k')
plot(app.UIAxes3,w2,a2(:,2) + ci1,'k')
plot(app.UIAxes3,w2,a2(:,2) - ci1,'k')
%Plots
p2 = plot(app.UIAxes3,w2,pw2,'b-','Linewidth',1,'Markersize',12);
p1 = plot(app.UIAxes3,w2,a2(:,2),'g-','Linewidth',1,'Markersize',12);
p3 = plot(app.UIAxes3,wn,fm1,'-r','Linewidth',1.5,'Markersize',12);
ylabel(app.UIAxes3,'$\ln(A(k))$', 'Interpreter', 'latex', 'FontSize',12)
xlabel(app.UIAxes3,'$k\;(\frac{1}{km})$', 'Interpreter', 'latex', 'FontSize',12)
hold(app.UIAxes3, 'off')
app.UIAxes3.XLim = [0 0.2];
legend(app.UIAxes3,[p1 p2 p3 p4],{'Observed spectrum', 'Corrected spectrum',...
'Synthetic spectrum', '95% confidence interval'})
% Values
app.ValuesLabel.Text = sprintf('Values\nFractal exponent a: %0.2f\nZt = %0.2f km
\x00B1 %0.2f km\nZ0 = %0.2f km \x00B1 %0.2f km\nZb = %0.2f km \x00B1 %0.2f km\nMisfit
= %0.4f',...
b2,Zt-Zc,Zt_error,Z0-Zc,p1_err,Zb-Zc,Zb_err,fit_fm);
% Enables buttons
set(app.SurfaceTemperatureCEditField, 'Enable', 'on');
set(app.SurfaceTemperatureCEditFieldLabel, 'Enable', 'on')
set(app.CurieTemperatureCEditField, 'Enable', 'on');
set(app.CurieTemperatureCEditFieldLabel, 'Enable', 'on')
set(app.Surfaceheatproductionmicrowm3EditField, 'Enable', 'on');
set(app.Surfaceheatproductionmicrowm3EditFieldLabel, 'Enable', 'on')

```

```

set(app.EmpiricalheatproductiondepthdistributionparameterkmEditField, 'Enable', 'on');s
et(app.EmpiricalheatproductiondepthdistributionparameterkmLabel, 'Enable', 'on')
set(app.ThermalconductivityWmKEeditField, 'Enable', 'on');
set(app.ThermalconductivityWmKEeditFieldLabel, 'Enable', 'on')
set(app.PlotGeothermButton, 'Enable', 'on')
setappdata(app.UIFigure, 'b2',b2)
setappdata(app.UIFigure, 'Zt',Zt)
setappdata(app.UIFigure, 'Zt_error',Zt_error)
setappdata(app.UIFigure, 'Z0',Z0)
setappdata(app.UIFigure, 'p1_err',p1_err)
setappdata(app.UIFigure, 'Zb',Zb)
setappdata(app.UIFigure, 'Zb_err',Zb_err)
setappdata(app.UIFigure, 'fit_fm',fit_fm)
setappdata(app.UIFigure, 'xs',xs)
setappdata(app.UIFigure, 'xs2',xs2)
setappdata(app.UIFigure, 'zc',zc)
end

% Value changed function: ResolutionkmEditField
function Resolutionandraas(app, event)
dl = app.ResolutionkmEditField.Value;
b = getappdata(app.UIFigure, 'b');
dt = detrend_2d(app,b); % Polynomial Trend Surface Estimation (degree = 1)
a2 = raas(app,dt,dl); % Radially average power spectrum
plot(app.UIAxes,a2(:,1),a2(:,2), 'k.-');
ylabel(app.UIAxes,'$\ln(A(k))$', 'Interpreter', 'latex', 'FontSize',12)
xlabel(app.UIAxes,'$k\backslash;(\frac{1}{km})$', 'Interpreter', 'latex', 'FontSize',12)
app.UIAxes.XLim = [0 a2(end,1)];
app.UIAxes.YLimMode = 'auto';
plot(app.UIAxes2,a2(:,1),a2(:,2)-log(2*pi*a2(:,1)), 'k.-');
ylabel(app.UIAxes2,'$\ln(\frac{A(k)}{2\pi k})$', 'Interpreter', 'latex', 'FontSize',12)
xlabel(app.UIAxes2,'$k\backslash;(\frac{1}{km})$', 'Interpreter', 'latex', 'FontSize',12)
app.UIAxes2.XLim = [0 a2(end,1)];
app.UIAxes2.YLimMode = 'auto';
setappdata(app.UIFigure, 'data',a2)
xs = []; % Data not selected yet
xs2 = []; % Data not selected yet
setappdata(app.UIFigure, 'xs',xs)
setappdata(app.UIFigure, 'xs2',xs2)
% Initial value
[w2,pw2,ps2,ci1] = fractal_correction(app,a2,0);
set(app.FractalExponentEditField, 'Enable', 'on'); set(app.FractalExponentLabel,
'Enable', 'on')
set(app.FlightlatitudekmEditField, 'Enable', 'on');
set(app.FlightlatitudekmEditFieldLabel, 'Enable', 'on')
set(app.SelectpointsButton, 'Enable', 'on')
set(app.RestartButton, 'Enable', 'on')
app.FractalExponentEditField.Value = 0;
setappdata(app.UIFigure, 'w2',w2)
setappdata(app.UIFigure, 'pw2',pw2)
setappdata(app.UIFigure, 'ps2',ps2)
setappdata(app.UIFigure, 'ci1',ci1)
end
end

```

```

% Component initialization
methods (Access = private)

% Create UIFigure and components
function createComponents(app)

% Create UIFigure and hide until all components are created
app.UIFigure = uifigure('Visible', 'off');
app.UIFigure.Position = [100 100 1010.75 672];
app.UIFigure.Name = 'UI Figure';

% Create UIAxes
app.UIAxes = uiaxes(app.UIFigure);
xlabel(app.UIAxes, 'k (1/km)')
ylabel(app.UIAxes, 'ln(A(k))')
app.UIAxes.FontName = 'Times New Roman';
app.UIAxes.GridAlpha = 0.15;
app.UIAxes.MinorGridAlpha = 0.25;
app.UIAxes.Box = 'on';
app.UIAxes.XGrid = 'on';
app.UIAxes.YGrid = 'on';
app.UIAxes.Position = [11 263 320 230];

% Create UIAxes2
app.UIAxes2 = uiaxes(app.UIFigure);
xlabel(app.UIAxes2, 'k (1/km)')
ylabel(app.UIAxes2, 'ln(A(k)/k)')
app.UIAxes2.FontName = 'Times New Roman';
app.UIAxes2.GridAlpha = 0.15;
app.UIAxes2.MinorGridAlpha = 0.25;
app.UIAxes2.Box = 'on';
app.UIAxes2.XGrid = 'on';
app.UIAxes2.YGrid = 'on';
app.UIAxes2.Position = [11 13 320 220];

% Create UIAxes3
app.UIAxes3 = uiaxes(app.UIFigure);
xlabel(app.UIAxes3, 'k (1/km)')
ylabel(app.UIAxes3, 'ln(A(k))')
app.UIAxes3.FontName = 'Times New Roman';
app.UIAxes3.GridAlpha = 0.15;
app.UIAxes3.MinorGridAlpha = 0.25;
app.UIAxes3.Box = 'on';
app.UIAxes3.XGrid = 'on';
app.UIAxes3.YGrid = 'on';
app.UIAxes3.Position = [361 263 320 230];

```

```

% Create UIAxes4
app.UIAxes4 = uiaxes(app.UIFigure);
title(app.UIAxes4, 'Steady-state one-dimensional geotherm')
xlabel(app.UIAxes4, 'Temperature (°C)')
ylabel(app.UIAxes4, 'Depth (km)')
app.UIAxes4.FontName = 'Times New Roman';
app.UIAxes4.GridAlpha = 0.15;
app.UIAxes4.MinorGridAlpha = 0.25;
app.UIAxes4.Box = 'on';
app.UIAxes4.XGrid = 'on';
app.UIAxes4.YGrid = 'on';
app.UIAxes4.Position = [711 13 288 480];

% Create FractalExponentLabel
app.FractalExponentLabel = uilabel(app.UIFigure);
app.FractalExponentLabel.HorizontalAlignment = 'right';
app.FractalExponentLabel.VerticalAlignment = 'top';
app.FractalExponentLabel.Enable = 'off';
app.FractalExponentLabel.Position = [4 518 114 22];
app.FractalExponentLabel.Text = 'Fractal Exponent ( $\alpha$ )';

% Create FractalExponentEditField
app.FractalExponentEditField = uieditfield(app.UIFigure, 'numeric');
app.FractalExponentEditField.Limits = [0 Inf];
app.FractalExponentEditField.ValueChangedFcn = createCallbackFcn(app, @Fractal,
true);
app.FractalExponentEditField.Enable = 'off';
app.FractalExponentEditField.Position = [131 521 97 22];

% Create SelectpointsButton
app.SelectpointsButton = uibutton(app.UIFigure, 'push');
app.SelectpointsButton.ButtonPushedFcn = createCallbackFcn(app, @Selectpoints, true);
app.SelectpointsButton.Enable = 'off';
app.SelectpointsButton.Position = [340 581 100 22];
app.SelectpointsButton.Text = 'Select points';

% Create ValuesLabel
app.ValuesLabel = uilabel(app.UIFigure);
app.ValuesLabel.BackgroundColor = [1 1 1];
app.ValuesLabel.VerticalAlignment = 'top';
app.ValuesLabel.FontName = 'Arial';
app.ValuesLabel.FontSize = 16;
app.ValuesLabel.Position = [371 13 303 210];
app.ValuesLabel.Text = 'Values';

% Create SurfaceTemperatureCEditFieldLabel
app.SurfaceTemperatureCEditFieldLabel = uilabel(app.UIFigure);
app.SurfaceTemperatureCEditFieldLabel.HorizontalAlignment = 'right';
app.SurfaceTemperatureCEditFieldLabel.VerticalAlignment = 'top';
app.SurfaceTemperatureCEditFieldLabel.Enable = 'off';

```

```

app.SurfaceTemperatureCEditFieldLabel.Position = [741 585 141 15];
app.SurfaceTemperatureCEditFieldLabel.Text = 'Surface temperature (°C)';

% Create SurfaceTemperatureCEditField
app.SurfaceTemperatureCEditField = uieditfield(app.UIFigure, 'numeric');
app.SurfaceTemperatureCEditField.ValueChangedFcn = createCallbackFcn(app, @Geotherm,
true);
app.SurfaceTemperatureCEditField.Enable = 'off';
app.SurfaceTemperatureCEditField.Position = [891 581 50 22];
app.SurfaceTemperatureCEditField.Value = 20;

% Create CurieTemperatureCEditFieldLabel
app.CurieTemperatureCEditFieldLabel = uilabel(app.UIFigure);
app.CurieTemperatureCEditFieldLabel.HorizontalAlignment = 'right';
app.CurieTemperatureCEditFieldLabel.VerticalAlignment = 'top';
app.CurieTemperatureCEditFieldLabel.Enable = 'off';
app.CurieTemperatureCEditFieldLabel.Position = [751 555 129 15];
app.CurieTemperatureCEditFieldLabel.Text = 'Curie temperature (°C)';

% Create CurieTemperatureCEditField
app.CurieTemperatureCEditField = uieditfield(app.UIFigure, 'numeric');
app.CurieTemperatureCEditField.ValueChangedFcn = createCallbackFcn(app, @Geotherm,
true);
app.CurieTemperatureCEditField.Enable = 'off';
app.CurieTemperatureCEditField.Position = [891 551 50 22];
app.CurieTemperatureCEditField.Value = 580;

% Create SurfaceHeatProductionMicroWm3CEditFieldLabel
app.SurfaceHeatProductionMicroWm3CEditFieldLabel = uilabel(app.UIFigure);
app.SurfaceHeatProductionMicroWm3CEditFieldLabel.HorizontalAlignment = 'right';
app.SurfaceHeatProductionMicroWm3CEditFieldLabel.VerticalAlignment = 'top';
app.SurfaceHeatProductionMicroWm3CEditFieldLabel.Enable = 'off';
app.SurfaceHeatProductionMicroWm3CEditFieldLabel.Position = [461 555 208 15];
app.SurfaceHeatProductionMicroWm3CEditFieldLabel.Text = 'Surface heat production
(microW/m³)';

% Create SurfaceHeatProductionMicroWm3CEditField
app.SurfaceHeatProductionMicroWm3CEditField = uieditfield(app.UIFigure, 'numeric');
app.SurfaceHeatProductionMicroWm3CEditField.ValueChangedFcn = createCallbackFcn(app,
@Geotherm, true);
app.SurfaceHeatProductionMicroWm3CEditField.Enable = 'off';
app.SurfaceHeatProductionMicroWm3CEditField.Position = [681 551 40 22];
app.SurfaceHeatProductionMicroWm3CEditField.Value = 2.5;

% Create EmpiricalHeatProductionDepthDistributionParameterkmCEditField
app.EmpiricalHeatProductionDepthDistributionParameterkmCEditField =
uieditfield(app.UIFigure, 'numeric');
app.EmpiricalHeatProductionDepthDistributionParameterkmCEditField.ValueChangedFcn =
createCallbackFcn(app, @Geotherm, true);

```

```

app.EmpiricalheatproductiondepthdistributionparameterkmEditField.Enable = 'off';
app.EmpiricalheatproductiondepthdistributionparameterkmEditField.Position = [682 521
39 22];
app.EmpiricalheatproductiondepthdistributionparameterkmEditField.Value = 10;

% Create ThermalconductivityWmKEditFieldLabel
app.ThermalconductivityWmKEditFieldLabel = uilabel(app.UIFigure);
app.ThermalconductivityWmKEditFieldLabel.HorizontalAlignment = 'right';
app.ThermalconductivityWmKEditFieldLabel.VerticalAlignment = 'top';
app.ThermalconductivityWmKEditFieldLabel.Enable = 'off';
app.ThermalconductivityWmKEditFieldLabel.Position = [511 585 160 15];
app.ThermalconductivityWmKEditFieldLabel.Text = 'Thermal conductivity (W/mK)';

% Create ThermalconductivityWmKEditField
app.ThermalconductivityWmKEditField = uieditfield(app.UIFigure, 'numeric');
app.ThermalconductivityWmKEditField.ValueChangedFcn = createCallbackFcn(app,
@Geotherm, true);
app.ThermalconductivityWmKEditField.Enable = 'off';
app.ThermalconductivityWmKEditField.Position = [681 581 40 22];
app.ThermalconductivityWmKEditField.Value = 2.2;

% Create PlotGeothermButton
app.PlotGeothermButton = uibutton(app.UIFigure, 'push');
app.PlotGeothermButton.ButtonPushedFcn = createCallbackFcn(app, @Geotherm, true);
app.PlotGeothermButton.Enable = 'off';
app.PlotGeothermButton.Position = [801 521 100 22];
app.PlotGeothermButton.Text = 'Plot Geotherm';

% Create RestartButton
app.RestartButton = uibutton(app.UIFigure, 'push');
app.RestartButton.ButtonPushedFcn = createCallbackFcn(app, @Restart, true);
app.RestartButton.Enable = 'off';
app.RestartButton.Position = [340 551 100 22];
app.RestartButton.Text = 'Restart';

% Create SelectFileButton
app.SelectFileButton = uibutton(app.UIFigure, 'push');
app.SelectFileButton.ButtonPushedFcn = createCallbackFcn(app, @Readdata, true);
app.SelectFileButton.Position = [18 616 100 22];
app.SelectFileButton.Text = 'Select File';

% Create Label
app.Label = uilabel(app.UIFigure);
app.Label.BackgroundColor = [1 1 1];
app.Label.VerticalAlignment = 'top';
app.Label.Position = [131 617 191 20];
app.Label.Text = '';

```

```

% Create FlightaltitudekmEditFieldLabel
app.FlightaltitudekmEditFieldLabel = uilabel(app.UIFigure);
app.FlightaltitudekmEditFieldLabel.HorizontalAlignment = 'right';
app.FlightaltitudekmEditFieldLabel.VerticalAlignment = 'top';
app.FlightaltitudekmEditFieldLabel.Enable = 'off';
app.FlightaltitudekmEditFieldLabel.Position = [11 555 105 15];
app.FlightaltitudekmEditFieldLabel.Text = 'Flight altitude (km)';

% Create FlightaltitudekmEditField
app.FlightaltitudekmEditField = uieditfield(app.UIFigure, 'numeric');
app.FlightaltitudekmEditField.Enable = 'off';
app.FlightaltitudekmEditField.Position = [131 551 97 22];

% Create EmpiricalheatproductiondepthdistributionparameterkmLabel
app.EmpiricalheatproductiondepthdistributionparameterkmLabel =
uilabel(app.UIFigure);

app.EmpiricalheatproductiondepthdistributionparameterkmLabel.HorizontalAlignment =
'right';

app.EmpiricalheatproductiondepthdistributionparameterkmLabel.VerticalAlignment =
'top';
app.EmpiricalheatproductiondepthdistributionparameterkmLabel.Enable =
'off';
app.EmpiricalheatproductiondepthdistributionparameterkmLabel.Position =
[335 525 334 15];
app.EmpiricalheatproductiondepthdistributionparameterkmLabel.Text =
'Empirical heat-productiondepth-distribution parameter (km)';

% Create DefractalMethodLabel
app.DefractalMethodLabel = uilabel(app.UIFigure);
app.DefractalMethodLabel.VerticalAlignment = 'top';
app.DefractalMethodLabel.FontSize = 36;
app.DefractalMethodLabel.FontWeight = 'bold';
app.DefractalMethodLabel.Position = [401 616 302 47];
app.DefractalMethodLabel.Text = 'Defractal Method';

% Create ResolutionkmEditFieldLabel
app.ResolutionkmEditFieldLabel = uilabel(app.UIFigure);
app.ResolutionkmEditFieldLabel.HorizontalAlignment = 'right';
app.ResolutionkmEditFieldLabel.Enable = 'off';
app.ResolutionkmEditFieldLabel.Position = [23 578 90 22];
app.ResolutionkmEditFieldLabel.Text = 'Resolution (km)';

% Create ResolutionkmEditField
app.ResolutionkmEditField = uieditfield(app.UIFigure, 'numeric');
app.ResolutionkmEditField.Limits = [0 Inf];
app.ResolutionkmEditField.ValueChangedFcn = createCallbackFcn(app,
@Resolutionandraas, true);
app.ResolutionkmEditField.Enable = 'off';

```

```

app.ResolutionkmEditField.Position = [128 578 100 22];
app.ResolutionkmEditField.Value = 1;

% Show the figure after all components are created
app.UIFigure.Visible = 'on';
end
end

% App creation and deletion
methods (Access = public)

    % Construct app
    function app = defractal

        % Create UIFigure and components
        createComponents(app)

        % Register the app with App Designer
        registerApp(app, app.UIFigure)

        if nargout == 0
            clear app
        end
    end

    % Code that executes before app deletion
    function delete(app)

        % Delete UIFigure when app is deleted
        delete(app.UIFigure)
    end
end
end

```

Selectdata.m

```
function [pointslist,xselect,yselect] = selectdata(varargin)
% selectdata: graphical selection of data points on a plot using the mouse
% usage: pointslist = selectdata           % uses all default options
% usage: pointslist = selectdata(prop1,val1,prop2,val2,...)
%
% SELECTDATA allows the user to select data points on a given plot
% using the mouse, in a variety of modes. 'Lasso' mode allows the
% selection by a user directed lasso around the points. 'Brush' mode
% selects points as you brush over them with the mouse. 'Rect' mode
% draws a rectangle, selecting any points inside the rectangle.
% 'Closest' mode looks for a aingle mouse click, finding the closest
% point to the mouse.
%
% Returned is a list of the point indexes selected, additionally you
% can specify that the points be deleted from the plot.
%
% Arguments: (input)
% The input arguments to SELECTDATA are all property/value pairs.
% (See PARSE_pv_PAIRS for more details.)
%
http://www.mathworks.com/matlabcentral/fileexchange/loadFile.do?objectId=9082&objectType=FILE
%
% Property names and character values can be shortened as long as
% the shortening is unambiguous. Capitalization is ignored.
%
% Valid Properties: 'Action', 'Axes', 'BrushSize', 'Identify',
%                   'Ignore' , 'Pointer', 'SelectionMode'
%
% 'Action' - {'list', 'delete'}
%             'delete' causes the selected points to be deleted from
%             the figure after their selection is final.
%
%             DEFAULT VALUE: 'List'
%
% 'Axes' - denotes the axes from which to select points
%
%             DEFAULT VALUE: gca
%
% 'BrushShape' - {'rect', 'circle'}
%
%             DEFAULT VALUE: 'circle'
%
%             Sets the shape of the brush to be used. Both brush
%             shapes are relative to the figure axes, so a nominally
%             "circular" brush is actually elliptical if the axis
%             units/lengths are unequal.
%
%             Only used when SelectionMode is 'brush'.
%
% 'BrushSize' - Only used when SelectionMode is 'brush'.
%
%             DEFAULT VALUE: 0.05
```

```

%
% The default value will specify a rectangular brush
% that has dimensions of 5% of the current axes. Note
% that on a set of square axes, the brush will always
% look square, even if the axes have very different
% units.
%
% 0 < brushsize <= 0.25
%
% 'Identify' - {'on', 'off'}
% Causes the selected points to be temporarily over-plotted
% with a new filled red marker ('o') as they are selected.
%
% Points selected with a lasso, or rect may be deselected
% as the tool is modified. Brush selections are cumulative.
%
% DEFAULT VALUE: 'on'
%
% 'Ignore' - a data handle, or []
%
% A list of data handles to be ignored. This allows you to
% use selectdata on only some sets of points, while others
% in the same figure are ignored. This is a useful option
% when you may have plotted some data points but also a
% curve fit through your data. You can then cause the plotted
% curve to be ignored by selectdata.
%
% DEFAULT VALUE: []
%
% 'Label' - {'off', 'on'}
%
% Causes text labels with their (x,y) coordinates to appear
% next to each point selected.
%
% Beware that selecting large numbers of points and creating
% and displaying the label for them can be time consuming.
% This option is a great one for single point selection,
% but I have seen system-related problems when rapidly
% selecting & deselecting large numbers of points with the
% rect tool.
%
% DEFAULT VALUE: 'off'
%
% 'Pointer' - {'crosshair' | 'fullcrosshair' | 'arrow' | 'ibeam' |
% 'watch' | 'topl' | 'topr' | 'botl' | 'botr' | 'left' |
% 'top' | 'right' | 'bottom' | 'circle' | 'cross' | 'fleur' |
% 'hand' }
%
% Changes the cursor pointer while selection is active.
% After selection terminates, the figure pointer is
% restored to its old setting.
%
% DEFAULT VALUE: 'crosshair'
%
% 'Return' - {'selected' | 'unselected' }

```

```

%
% Selection of data points, perhaps if used to indicate
% outliers in data, would normally return that set of
% points selected. But some users may prefer to see the
% list of points returned to be those points which were
% NOT selected.
%
% DEFAULT VALUE: 'selected'
%
% 'SelectionMode' - {'Lasso', 'Brush', 'Rect', 'Closest'}
%
% DEFAULT VALUE: 'Lasso'
%
% If 'Brush' is used, then the brush will be a rectangular
% brush, with a size as defined by the 'BrushSize' property.
% The brush will be centered at the current mouse coordinates.
% Brush size will be a fraction of the axis limits for the
% current axes. Click inside the axes, then drag the "brush"
% around. Any points the brush crosses over will be selected.
%
% If 'Lasso' is chosen, then click inside the axes to define
% one end of the lasso, then drag with the mouse still down,
% causing the mouse to define a general curvilinear region.
% The polygon will close automatically when the mouse button
% is released. A point is "inside" the lasso if inpolygon
% identifies it as so. BEWARE of convoluted lassos that
% intersect themselves.
%
% If 'Rect' is chosen, then click inside the axes to define
% one corner of the rect, dragging to specify the opposite
% corner, just as rbbox would do.
%
% If 'Closest' was chosen, then a single mouse click in the
% figure window is used, then that point which is closest in
% Euclidean distance (in window units) is chosen. You
% can move the cursor around (don't release the mouse until
% you are done) and the currently selected point will be
% highlighted.
%
% 'Verify' - { 'off' | 'on' }
%
% If set to 'on', this causes a dialog box to pop up after
% selection. The user can then accept the selection, redo
% it, or cancel out, causing no points to be selected.
%
% Note, if cancel is chosen from the dialog, and 'return'
% was specified to return those points 'unselected', then ALL
% the points will actually be returned.
%
% DEFAULT VALUE: 'off'
%
%
% Note: other properties are available for use, but I've chosen to
% leave them semi-hidden because they don't seem terribly useful to
% most users. These properties allow you to specify the colors of the

```

```

% selection tool itself, the colors of the selected point markers,
% the transparency of the selection tool, the marker itself, etc.
% Default values for these parameters are:
%
%     FlagMarker      = 'o'
%     FlagColor       = 'r'
%     Fill            = 'on'
%     FillColor       = 'y'
%     FillEdgeColor   = 'b'
%     FillTrans       = 0.5
%     MaxBrush        = 0.25
%     RemoveTool      = 'on'
%     RemoveFlagged   = 'on'
%     RemoveLabels    = 'on'
%
% Further documentation on these parameters can be found by editting
% selectdata.m itself.
%
%
% Arguments: (output)
% pointslist - list of points that were selected. If only one
% dataset was found, then points list is a simple vector.
% If multiple sets of points were found in the axes, then
% points list will be a cell array.
%
% NOTE: Each set of points is peeled off the stack in the
% matlab stores it.
%
% xselect - array (or cell array) containing the x coordinates of
% those points identified in the selection
%
% yselect - array (or cell array) containing the y coordinates of
% those points identified in the selection
%
%
% Example:
% Plot a set of points, then select some with the mouse
% using a rectangular brush, return the indices of those
% points selected. (Note: user interaction on the plot
% will be necessary.)
%
%     x = 0:.1:1;
%     y = x.^2;
%     plot(x,y,'o')
%     pl = selectdata('selectionmode','brush');
%
% Example:
% Select a single point with the mouse, then delete that
% selected point from the plot.
%
%     pl = selectdata('selectionmode','closest','action','delete');
%
% Example:
% Select some points using a rect(rbbox) tool, also return
% the (x,y) coordinates from multiple curves plotted. Use

```

```

% shortened versions of the properties and values.
%
% plot(rand(5,2),rand(5,2),'o')
% [pl,xs,ys] = selectdata('sel','r');
%
% Example:
% Plot a curve and some data points on one plot, select
% some points from the data plotted, but ignore the
% smooth curve, even if the lasso passes over it.
% x = 0:.01:1;
% y = exp(x);
% ynoisy = y + randn(size(y))/2;
% h1 = plot(x,y,'-');
% hold on
% h2 = plot(x,ynoisy,'o');
% [pl,xs,ys] = selectdata('sel','lasso','ignore',h1);
%
% See also:
%
%
% Author: John D'Errico
% E-mail: woodchips@rochester.rr.com
% Release: 3.0
% Release date: 2/19/07
% defaults for the parameters
params.Axes = gca;
params.SelectionMode = 'lasso';
params.Action = 'list';
params.BrushShape = 'circle';
params.BrushSize = .05;
params.Identify = 'on';
params.Ignore = [];
params.Pointer = 'cross';
params.Return = 'selected';
params.Verify = 'off';
params.Label = 'off';
%
% Undocumented options, also unchecked for validity.
% These parameters control the marker used to identify
% those points which are currently selected.
% FlagMarker must be a valid plot marker, FlagColor
% must be a valid color spec. The default values are...
params.FlagMarker = 'o';
params.FlagColor = 'r';
%
% More (unchecked) options that are yours to fiddle with
% (or not.) These control the fill color to be applied
% to the interior of the lasso, rect, and brush. Also
% controlled are the degree of transparency to be applied.
params.Fill = 'on';
params.FillColor = 'y';
params.FillEdgeColor = 'b';
params.FillTrans = 0.5; % must be in the interval [0,1]
%
% The maximum relative brushsize allowed is also
% controlled here, just in case I ever wanted to allow
% the brush to be a bit larger.
params.MaxBrush = 0.25;

```

```

% After selection has been accomplished, the flagged points
% and the selection tool itself are normally deleted. But
% in some circumstances it may be useful to not delete
% those objects. 'off' will cause these objects to remain.
params.RemoveTool = 'on';
params.RemoveFlagged = 'on';
params.RemoveLabels = 'on';
% save this to restore later
axissize = axis;
% process any Property/value pairs.
if nargin>0
    params = parse_pv_pairs(params,varargin);
end
% check the supplied parameters for validity
params = check_params(params);
% bring the focus to the figure containing the
% designated axes
fighandle = get(params.Axes,'parent');
figure(fighandle)
% get the current figure pointer, so we can
% restore it later on
oldpointer = get(fighandle,'Pointer');
% extract xdata and ydata from the specified axes
% get the children of the axes
hc = get(params.Axes,'children');
% are any of the data handles to be ignored?
if ~isempty(params.Ignore)
    hc = setdiff(hc,params.Ignore);
end
% strip out xdata and ydata
xdata = get(hc,'xdata');
ydata = get(hc,'ydata');
% if we must highlight the points as they are
% selected, then for efficiency we need to know
% how many we may expect.
flaghandle = [];
if ~iscell(xdata)
    xdata = xdata(:);
    ydata = ydata(:);
    % total number of data points
    npoints = length(xdata);
else
    for i = 1:length(xdata)
        xdata{i} = xdata{i}(:);
        ydata{i} = ydata{i}(:);
    end
    % total number of data points
    npoints = cellfun('length',xdata);
end
% for textlabels if desired
texthandles = [];
% set up a while loop in case we need to verify
% satisfaction
selectionflag = true;
while selectionflag

```

```

% and the total number currently selected
nSel = 0;

% what SelectionMode was specified
switch params.SelectionMode
case 'closest'
    % Find the single closest point (in Euclidean distance)
    % to the mouse click

    % set the figure pointer
    if ~isempty(params.Pointer)
        set(figHandle, 'Pointer', params.Pointer)
    end

    % mouse click?
    waitForButtonPress;

    % Button Motion and Button Up
    set(figHandle, 'WindowButtonMotionFcn', @CPmotion);
    set(figHandle, 'WindowButtonUpFcn', @selectDone);

    % dx, dy to scale the distance
    dx = (axisSize(2) - axisSize(1));
    dy = (axisSize(4) - axisSize(3));

    % current closest point is
    cc = get(gca, 'CurrentPoint');
    xy = cc(1, 1:2);

    % what point was closest?
    [pointsList, xSelect, ySelect] = closestPoint(xy, xData, yData, dx, dy);
    nSel = 1;

    % identify any points?
    if strcmp(params.Identify, 'on')
        flagPoints
    end

    % label them?
    if strcmp(params.Label, 'on')
        makeTextLabels
    end

    % selectHandle is not needed for this mode of operation
    selectHandle = [];

    % wait until the mouse button was released
    uiWait

    % .....

    % resume.

    % all we need to do here is restore the figure pointer
    % if we changed it before

```

```

if ~isempty(params.Pointer)
    set(fighandle,'Pointer',oldpointer)
end

case 'rect'
    % Selection rect as a polygon
    % mouse click?
    waitforbuttonpress;
    % set the figure pointer
    if ~isempty(params.Pointer)
        set(fighandle,'Pointer',params.Pointer)
    end
    % button down detected
    cc = get(gca,'CurrentPoint');
    rectxy1 = cc(1,1:2);
    rectxy2 = rectxy1 + eps(rectxy1);
    % make a polygon of the box, initially of nil area
    xv = [rectxy1(1), rectxy2(1), rectxy2(1), rectxy1(1), rectxy1(1)];
    yv = [rectxy1(2), rectxy1(2), rectxy2(2), rectxy2(2), rectxy1(2)];
    % no points should been selected
    [pointslist,xselect,yselect,nsel] = testpoly(xv,yv,xdata,ydata);
    % and plot it, filled or not
    hold on
    if strcmp(params.Fill,'on')
        % filled
        selecthandle = fill(xv,yv,params.FillColor);
        set(selecthandle,'facealpha',params.FillTrans, ...
            'linestyle','--','edgecolor',params.FillEdgeColor)
    else
        % unfilled
        selecthandle = plot(xv,yv,'r:');
    end
    % we can undo the hold now
    hold off
    % Button Motion and Button Up
    set(fighandle,'WindowButtonMotionFcn',@rectmotion);
    set(fighandle,'WindowButtonUpFcn',@selectdone);
    % wait until the selection is done
    uiwait
    % ....
    % resume.
    % The rect already is a polygon, stored in (xv,yv)
case 'lasso'
    % Selection lasso as a polygon
    % mouse click?
    waitforbuttonpress;
    % set the figure pointer
    if ~isempty(params.Pointer)
        set(fighandle,'Pointer',params.Pointer)
    end
    % button down detected
    cc = get(gca,'CurrentPoint');
    xlasso = cc(1,1);
    ylasso = cc(1,2);
    % form the polygon

```

```

xv = xlasso;
yv = ylasso;
% and plot it, filled or not
hold on
if strcmp(params.Fill, 'on')
    % filled
    selecthandle = fill(xv,yv,params.FillColor);
    set(selecthandle, 'facealpha', params.FillTrans, ...
        'linestyle', '--', 'edgecolor', params.FillEdgeColor)
else
    % unfilled
    selecthandle = plot(xv,yv, 'r:');
end
% we can undo the hold now
hold off
% Button Motion and Button Up
set(fighandle, 'WindowButtonMotionFcn', @lassomotion);
set(fighandle, 'WindowButtonUpFcn', @selectdone);
% wait until the selection is done
uiwait
% ....
% resume.
% The lasso already is a polygon, stored in (xv,yv)
case 'brush'
    % paint over the data, with a rectangular brush
    % mouse click?
    waitforbuttonpress;
    % set the figure pointer
    if ~isempty(params.Pointer)
        set(fighandle, 'Pointer', params.Pointer)
    end
    % button down detected
    bc = get(gca, 'CurrentPoint');
    brushcenter = bc(1,1:2);
    % dx, dy for the brush
    bdx = params.BrushSize*(axissize(2) - axissize(1));
    bdy = params.BrushSize*(axissize(4) - axissize(3));
    if strcmpi(params.BrushShape, 'rect')
        % make the brush polygon as a fixed size rectangle
        % that we can slide around
        xv = brushcenter(1) + [-1, 1, 1, -1, -1]*bdx/2;
        yv = brushcenter(2) + [-1, -1, 1, 1, -1]*bdy/2;
    else
        % a circle was specified
        theta = linspace(0, 2*pi, 100);
        xv = cos(theta)*bdx/2 + brushcenter(1);
        yv = sin(theta)*bdy/2 + brushcenter(2);
    end
    % draw the initial brush polygon, filled or not
    hold on
    if strcmp(params.Fill, 'on')
        % filled
        selecthandle = fill(xv,yv,params.FillColor);
        set(selecthandle, 'facealpha', params.FillTrans, ...
            'linestyle', '-', 'edgecolor', params.FillEdgeColor)
    end
end

```

```

else
    % unfilled
    selecthandle = plot(xv,yv,'r:');
end
hold off
% have any points been selected?
[pointslist,xselect,yselect,nSel] = testpoly(xv,yv,xdata,ydata);
% identify any points?
if strcmp(params.Identify,'on') && (nSel>0)
    flagpoints
end

% label them?
if strcmp(params.Label,'on') && (nSel>0)
    makeTextLabels
end

% Button Motion and Button Up
set(figHandle,'WindowButtonMotionFcn',@brushMotion);
set(figHandle,'WindowButtonUpFcn',@selectDone);
% wait until the selection is done
uiwait
% ....
% resume.
end

% verify?
if strcmpi(params.Verify,'on')
    % pop up a dialog
    ButtonName = questdlg( ...
        'Are you satisfied with the points selected?', '???' , ...
        'Yes','Redo Selection','Cancel Selection','Yes');

switch ButtonName
    case 'Yes'
        % we can drop through
        selectionFlag = false;

    case 'Cancel Selection'
        % drop out, with nothing selected
        if ~iscell(xdata)
            pointslist = [];
            xselect = [];
            yselect = [];
        else
            for i = 1:numel(xdata)
                pointslist{i} = [];
                xselect{i} = [];
                yselect{i} = [];
            end
        end
        selectionFlag = false;
    end

```

```

    case 'Redo Selection'
        % or try again. The while loop will cycle
        % until happy or canceled

    end

else
    % no verification was requested, so we want to
    % terminate the while loop after only one pass through.
    selectionflag = false;
end

end
% pointslist and xselect, yselect are already complete.
% Do we delete the selected points?
if strcmpi(params.Action,'delete')
    if ~iscell(xdata)
        % only one set, so xdata and ydata are not cell arrays

        % Which points from the data fall in the selection polygon?
        xdata(pointslist) = [];
        ydata(pointslist) = [];

        % drop those points from the plot
        set(hc,'xdata',xdata,'ydata',ydata)
    else
        % it was a cell array, so there were multiple sets.
        for i = 1:numel(xdata)

            xdata{i}(pointslist{i}) = [];
            ydata{i}(pointslist{i}) = [];

            % drop those points from the plot
            set(hc(i),'xdata',xdata{i}, 'ydata',ydata{i})
        end
    end
end
% was 'return' set to be the selected list or the unselected one?
% Do nothing if 'selected', we are already done.
if strcmpi(params.Return,'unselected')
    if ~iscell(xdata)
        % only one set, so xdata and ydata are not cell arrays
        pointslist = setdiff((1:npoints)',pointslist);
        xselect = xdata(pointslist);
        yselect = ydata(pointslist);
    else
        % it was a cell array, so there were multiple sets.
        for i = 1:numel(xdata)
            pointslist{i} = setdiff((1:npoints(i))',pointslist{i});

            xselect{i} = xdata{i}(pointslist{i});
            yselect{i} = ydata{i}(pointslist{i});
        end
    end
end

```

```

% =====
% begin nested functions
% =====
function brushmotion(src,evt) %#ok
    % nested function for motion of the brush

    % get the new mouse position
    mousenew = get(params.Axes,'CurrentPoint');
    mousenew = mousenew(1,1:2);

    % make sure the axes are fixed
    axis(axissize)

    % how far did it move
    brushoffset = mousenew - brushcenter;
    brushcenter = mousenew;

    xv = xv + brushoffset(1);
    yv = yv + brushoffset(2);

    % did we brush over any new points
    [pl,xselect,yselect,nsel] = testpoly(xv,yv,xdata,ydata);

    % for a brush, we need to append any selected points to
    % the already selected list
    if ~iscell(xdata)
        % only one set, so xdata and ydata are not cell arrays
        pointslist = union(pointslist,pl);
        xselect = xdata(pointslist);
        yselect = ydata(pointslist);
        nsel = length(pointslist);
    else
        % it was a cell array, so there were multiple sets.
        for j = 1:numel(pointslist)
            pointslist{j} = union(pointslist{j},pl{j}); %#ok
            pointslist{j} = pointslist{j}(:); %#ok

            if ~isempty(pointslist{j})
                xselect{j} = xdata{j}(pointslist{j});
                yselect{j} = ydata{j}(pointslist{j});
            end
        end

        % total of points selected
        nsel = sum(cellfun('length',pointslist));
    end

    % identify any points?
    if strcmp(params.Identify,'on')
        flagpoints
    end

    % label them?
    if strcmp(params.Label,'on')
        maketextlabels
    end

```

```

end

% replot the brush in its new position
set(selecthandle,'xdata',xv,'ydata',yv)

end
% =====
% =====
function CPmotion(src,evnt) %#ok
    % nested function to select the closest point

    % get the new mouse position
    mousenew = get(params.Axes,'CurrentPoint');
    xy = mousenew(1,1:2);

    % make sure the axes stay fixed
    axis(axissize)

    % what point was closest?
    [pointslist,xselect,yselect] = closestpoint(xy,xdata,ydata,dx,dy);
    nsel = 1;

    % identify any points?
    if strcmp(params.Identify,'on')
        flagpoints
    end

    % label them?
    if strcmp(params.Label,'on')
        maketextlabels
    end

end
% =====
% =====
function rectmotion(src,evnt) %#ok
    % nested function for expansion or contraction of the rect

    % get the new mouse position
    mousenew = get(params.Axes,'CurrentPoint');
    rectxy2 = mousenew(1,1:2);

    % make sure the axes are fixed
    axis(axissize)

    % update the rect polygon of the box, changing the second corner
    xv = [rectxy1(1), rectxy2(1), rectxy2(1), rectxy1(1), rectxy1(1)];
    yv = [rectxy1(2), rectxy1(2), rectxy2(2), rectxy2(2), rectxy1(2)];

    % did we brush over any new points
    [pointslist,xselect,yselect,nsel] = testpoly(xv,yv,xdata,ydata);

    % identify any points?
    if strcmp(params.Identify,'on')
        flagpoints

```

```

    end
    % label them?
    if strcmp(params.Label, 'on')
        maketextlabels
    end

    % replot the rect in its new position
    set(selecthandle, 'xdata', xv, 'ydata', yv)

end
% =====
% =====
function lassomotion(src,evt) %#ok
    % nested function for expansion of the lasso

    % get the new mouse position
    mousenew = get(params.Axes, 'CurrentPoint');
    mousenew = mousenew(1,1:2);
    % append the new point on the end of the last lasso
    xlasso = [xlasso,mousenew(1,1)];
    ylasso = [ylasso,mousenew(1,2)];

    % and close it to form the polygon
    xv = [xlasso,xlasso(1)];
    yv = [ylasso,ylasso(1)];
    % replot the newly extended lasso
    set(selecthandle, 'xdata', xv, 'ydata', yv)

    % did we enclose any new points?
    [pointslist,xselect,yselect,nse] = testpoly(xv,yv,xdata,ydata);

    % identify any points?
    if strcmp(params.Identify, 'on')
        flagpoints
    end
    % label them?
    if strcmp(params.Label, 'on')
        maketextlabels
    end

    % make sure the axes are maintained in size
    axis(axissize)

end
% =====
% =====
function selectdone(src,evt) %#ok
    % nested function for mouse up

    % do we remove the selection tool?
    if strcmpi(params.RemoveTool, 'on')
        % delete the selection object from the plot
        delete(selecthandle)
        selecthandle = [];
    end

```

```

% do we remove the flagged points?
if strcmpi(params.RemoveFlagged,'on')
    % also remove the flagged/plotted points
    if ~isempty(flaghandle)
        delete(flaghandle)
        flaghandle = [];
    end
end

% do we remove the flagged points?
if strcmpi(params.RemoveLabels,'on')
    % also remove the labels
    delete(texthandles)
    texthandles = [];
end

% cancel the WindowButtonFcn's that we had set
set(fighandle,'WindowButtonMotionFcn',[]);
set(fighandle,'WindowButtonUpFcn',[]);

% restore the figure pointer to its original setting
if ~isempty(params.Pointer)
    set(fighandle,'Pointer',oldpointer)
end

% and resume execution, back in the mainline
uiresume
end
% =====
% =====
function flagpoints
    % nested function for flagging the selected points

    % Are these the first points flagged? If so,
    % we need to plot them and set the marker, etc.
    if isempty(flaghandle) && (nse1 > 0)
        % hold the figure, so we can add the flagged points
        hold on

        if ~iscell(xselect)
            flaghandle = plot(xselect,yselect,params.FlagMarker);
            set(flaghandle,'Color',params.FlagColor,'MarkerFaceColor',params.FlagColor)
        else
            flaghandle = plot(vertcat(xselect{:}),vertcat(yselect{:}),params.FlagMarker);
            set(flaghandle,'Color',params.FlagColor,'MarkerFaceColor',params.FlagColor)
        end

        % now release the hold
        hold off
    elseif ~isempty(flaghandle)
        % otherwise, we just need to update xdata and ydata

        if nse1 == 0
            set(flaghandle,'xdata',[],'ydata',[]);

```

```

elseif ~iscell(xselect)
    set(flaghandle,'xdata',xselect,'ydata',yselect);
else
    set(flaghandle,'xdata',vertcat(xselect{:}),'ydata',vertcat(yselect{:})));
end
end
end
% =====
% =====
function maketextlabels
    % nested function for generation of text labels
    % over each point selected

    % We need to remove the last set of text labels
    delete(texthandles)

    % creat a new set of handles
    if ~iscell(xselect)
        xtext = xselect;
        ytext = yselect;
    else
        xtext = vertcat(xselect{:});
        ytext = vertcat(yselect{:});
    end

    % anything selected?
    if ~isempty(xtext)
        textlabels = cell(1,nsel);
        for L = 1:nsl
            textlabels{L} = [ '(',num2str(xtext(L)),',',num2str(ytext(L)),')'];
        end
        texthandles = text(xtext,ytext,textlabels);
    end
end
% =====
end % mainline end
% =====
%         end main function
% =====
% =====
%         subfunctions
% =====
function [pl,xsel,ysel,nsl] = testpoly(xv,yv,xdata,ydata)
% checks which points are inside the given polygon
% was there more than one set of points found in the plot?
if ~iscell(xdata)
    % only one set, so xdata and ydata are not cell arrays

    % Which points from the data fall in the selection polygon?
    pl = find(inpolygon(xdata,ydata,xv,yv));
    nsl = length(pl);

    xsel = xdata(pl);
    ysel = ydata(pl);

```

```

else
    % it was a cell array, so there were multiple sets.
    pl = cell(size(xdata));
    xsel = pl;
    ysel = pl;
    nsel = 0;
    for i = 1:numel(xdata)
        pl{i} = find(inpolygon(xdata{i},ydata{i},xv,yv));
        nsel = nsel + length(pl{i});

        if ~isempty(pl{i})
            xsel{i} = xdata{i}(pl{i});
            ysel{i} = ydata{i}(pl{i});
        end
    end
end
end % subfunction end
% =====
%           subfunction
% =====
function [pointslist,xselect,yselect] = closestpoint(xy,xdata,ydata,dx,dy)
% find the single closest point to xy, in scaled units
if ~iscell(xdata)
    % just one set of points to consider
    D = sqrt(((xdata - xy(1))/dx).^2 + ((ydata - xy(2))/dy).^2);
    [junk,pointslist] = min(D(:)); %#ok
    xselect = xdata(pointslist);
    yselect = ydata(pointslist);
else
    % there is more than one set of points
    Dmin = inf;
    pointslist = cell(size(xdata));
    for i = 1:numel(xdata)
        D = sqrt(((xdata{i} - xy(1))/dx).^2 + ((ydata{i} - xy(2))/dy).^2);
        [mind,ind] = min(D(:)); %#ok

        if mind < Dmin
            % searching for the closest point
            Dmin = mind;

            pointslist = cell(size(xdata));
            xselect = cell(size(xdata));
            yselect = cell(size(xdata));

            pointslist{i} = ind;
            xselect{i} = xdata{i}(ind);
            yselect{i} = ydata{i}(ind);
        end
    end
end
end % subfunction end
% =====
%           subfunction
% =====

```

```

% =====
% subfunction - check_params
% =====
function par = check_params(par)
% check the parameters for acceptability
%
% Defaults
% Axes = gca;
% SelectionMode = 'lasso';
% Action = 'list';
% BrushSize = .05;
% Axes == gca by default
if isempty(par.Axes)
    par.Axes = gca;
else
    if ~ishandle(par.Axes)
        error 'Axes must be the handle to a valid set of axes.'
    end
end
% SelectionMode == 'brush' by default
if isempty(par.SelectionMode)
    par.SelectionMode = 'brush';
else
    valid = {'rect', 'brush', 'lasso', 'closest'};
    if ~ischar(par.SelectionMode)
        error 'Invalid Style: Must be character'
    end

    ind = strmatch(lower(par.SelectionMode),valid); %#ok
    if isempty(ind) || (length(ind)>1)
        error(['Invalid SelectionMode: ',par.SelectionMode])
    end
    par.SelectionMode = valid{ind};
end
% BrushShape == 'circle' by default
if isempty(par.BrushShape)
    par.BrushShape = 'circle';
else
    valid = {'rect', 'circle'};
    if ~ischar(par.BrushShape)
        error 'Invalid Style: Must be character'
    end

    ind = strmatch(lower(par.BrushShape),valid); %#ok
    if isempty(ind) || (length(ind)>1)
        error(['Invalid SelectionMode: ',par.BrushShape])
    end
    par.BrushShape = valid{ind};
end
% Action == 'list' by default
if isempty(par.Action)
    par.Action = 'list';
else
    valid = {'list', 'delete'};
    if ~ischar(par.Action)

```

```

    error 'Invalid Action: Must be character'
end

ind = strmatch(lower(par.Action),valid); %#ok
if isempty(ind) || (length(ind)>1)
    error(['Invalid Action: ',par.Action])
end
par.Action = valid{ind};

% Pointer == 'crosshair' by default, but
% if empty, will not change the pointer.
if ~isempty(par.Pointer)
    valid = {'crosshair', 'fullcrosshair', 'arrow', 'ibeam', ...
        'watch', 'topl', 'topr', 'botl', 'botr', 'left', 'top', ...
        'right', 'bottom', 'circle', 'cross', 'fleur', ...
        'custom', 'hand'};

if ~ischar(par.Pointer)
    error 'Invalid Pointer: Must be character'
end

ind = strmatch(lower(par.Pointer),valid,'exact');
if isempty(ind)
    ind = strmatch(lower(par.Pointer),valid); %#ok
    if isempty(ind) || (length(ind)>1)
        error(['Invalid Pointer: ',par.Pointer])
    end
end
par.Pointer = valid{ind};

% Identify == 'on' by default
if isempty(par.Identify)
    par.Identify = 'on';
else
    valid = {'on', 'off'};
    if ~ischar(par.Identify)
        error 'Value for Identify is invalid: Must be character'
    end

    ind = strmatch(lower(par.Identify),valid); %#ok
    if isempty(ind) || (length(ind)>1)
        error(['Invalid Action: ',par.Identify])
    end
    par.Identify = valid{ind};
end

% Label == 'off' by default
if isempty(par.Label)
    par.Label = 'off';
else
    valid = {'on', 'off'};
    if ~ischar(par.Label)
        error 'Value for Label is invalid: Must be character'
    end

    ind = strmatch(lower(par.Label),valid); %#ok

```

```

if isempty(ind) || (length(ind)>1)
    error(['Invalid Action: ',par.Label])
end
par.Label = valid{ind};
end
% Return == 'selected' by default
if isempty(par.Return)
    par.Return = 'selected';
else
    valid = {'selected', 'unselected'};
    if ~ischar(par.Return)
        error 'Value for Return is invalid: Must be character'
    end

    ind = strmatch(lower(par.Return),valid); %#ok
    if isempty(ind) || (length(ind)>1)
        error(['Invalid Action: ',par.Return])
    end
    par.Return = valid{ind};
end
% Verify == 'off' by default
if isempty(par.Verify)
    par.Verify = 'off';
else
    valid = {'on', 'off'};
    if ~ischar(par.Verify)
        error 'Value for Verify is invalid: Must be character'
    end

    ind = strmatch(lower(par.Verify),valid); %#ok
    if isempty(ind) || (length(ind)>1)
        error(['Invalid Action: ',par.Verify])
    end
    par.Verify = valid{ind};
end
% BrushSize == 0.05 by default
if isempty(par.BrushSize)
    par.BrushSize = 0.05;
else
    if (length(par.BrushSize)>1) || (par.BrushSize<=0) || (par.BrushSize>par.MaxBrush)
        error 'Brushsize must be scalar, and 0 < BrushSize <= 0.25'
    end
end
% Ignore == [] by default
if ~isempty(par.Ignore) && any(~ishandle(par.Ignore))
    error 'Ignore must be empty, or a data handle'
end
end % check_params
% =====
% Included subfunction - parse_pv_pairs
% =====
function params=parse_pv_pairs(params,pv_pairs)
% parse_pv_pairs: parses sets of property value pairs, allows defaults
% usage: params=parse_pv_pairs(default_params,pv_pairs)
%

```

```

% arguments: (input)
% default_params - structure, with one field for every potential
%                   property/value pair. Each field will contain the default
%                   value for that property. If no default is supplied for a
%                   given property, then that field must be empty.
%
% pv_array - cell array of property/value pairs.
%             Case is ignored when comparing properties to the list
%             of field names. Also, any unambiguous shortening of a
%             field/property name is allowed.
%
% arguments: (output)
% params    - parameter struct that reflects any updated property/value
%             pairs in the pv_array.
%
% Example usage:
% First, set default values for the parameters. Assume we
% have four parameters that we wish to use optionally in
% the function examplefun.
%
% - 'viscosity', which will have a default value of 1
% - 'volume', which will default to 1
% - 'pie' - which will have default value 3.141592653589793
% - 'description' - a text field, left empty by default
%
% The first argument to examplefun is one which will always be
% supplied.
%
% function examplefun(dummyarg1,varargin)
% params.Viscosity = 1;
% params.Volume = 1;
% params.Pie = 3.141592653589793
%
% params.Description = '';
% params=parse_pv_pairs(params,varargin);
% params
%
% Use examplefun, overriding the defaults for 'pie', 'viscosity'
% and 'description'. The 'volume' parameter is left at its default.
%
% examplefun(rand(10),'vis',10,'pie',3,'Description','Hello world')
%
% params =
%     Viscosity: 10
%         Volume: 1
%             Pie: 3
%     Description: 'Hello world'
%
% Note that capitalization was ignored, and the property 'viscosity'
% was truncated as supplied. Also note that the order the pairs were
% supplied was arbitrary.
nrv = length(pv_pairs);
n = nrv/2;
if n~=floor(n)
    error 'Property/value pairs must come in PAIRS.'

```

```

end
if n<=0
    % just return the defaults
    return
end
if ~isstruct(params)
    error 'No structure for defaults was supplied'
end
% there was at least one pv pair. process any supplied
propnames = fieldnames(params);
lpropnames = lower(propnames);
for i=1:n
    p_i = lower(pv_pairs{2*i-1});
    v_i = pv_pairs{2*i};

    ind = strmatch(p_i,lpropnames,'exact');
    if isempty(ind)
        ind = find(strncmp(p_i,lpropnames,length(p_i)));
        if isempty(ind)
            error(['No matching property found for: ',pv_pairs{2*i-1}])
        elseif length(ind)>1
            error(['Ambiguous property name: ',pv_pairs{2*i-1}])
        end
    end
    p_i = propnames{ind};

    % override the corresponding default in params
    params = setfield(params,p_i,v_i); %#ok

end
end % parse_pv_pairs

```